Nonequilibrium fluctuations of a Brownian particle

Juan Ruben Gomez-Solano

Laboratoire de Physique
de l'École Normale Supérieure de Lyon

ENS DE LYON

THÈSE DE DOCTORAT

présentée par

Juan Rubén GOMEZ-SOLANO

pour l'obtention du grade de

Docteur de l'École Normale Supérieure de Lyon

Spécialité : **Physique**

Nonequilibrium fluctuations of a Brownian particle

Thèse soutenue publiquement le 8 Novembre 2011 devant un jury composé de:

Sergio CILIBERTO	Directeur de thèse
Artyom PETROSYAN	Co-encadrant
Udo SEIFERT	Président
Félix RITORT	Rapporteur
Olivier DAUCHOT	Rapporteur
Krzysztof GAWĘDZKI	Examinateur

Contents

Introduction

The study of *small systems* has attracted much attention in recent years due to the development of experimental techniques to probe physical properties at micro- and nano-scales in physics, chemistry, material science, biology and medicine. For instance, *optical* and *magnetic tweezers* have allowed one to mechanically manipulate micron-sized particles to measure very weak interactions in colloids, to stretch living cells, or used as mechanical probes to measure rheological properties of very tiny samples of complex fluids. Nanoscopic objects such as nanotubes and biomolecules can be handled and probed by *atomic force microscopy* (AFM) micro-cantilevers. See figure 1(a) for two specific examples. On the other hand, new sophisticated micro and nanotechnologies are being currently developed (figure 1(b)). Some examples are *microelectromechanical systems* (MEMS) and lab-on-a-chip technologies, designed to run experiments with mesoscopic objets by means of micron-sized actuators, sensors and minute flows integrated in a single small device. The second relevant example of such nanotechnologies are synthetic *molecular motors*. They are conceived to operate as highly efficient nanomachines capable of generate rectified motion and do work based on the functioning of proteins responsible for the motion in living cells.

The systems cited in the previous examples share two important features:

- At these small lengthscales, the influence of the random collisions of the molecules surrounding the micro and submicrometric objects is non-negligible. Then **fluctuations** of quantities such as positions, velocities and energies are significant.

- **Nonequilibrium conditions** are commonplace due to nonconservative forces and time dependent drivings exerted by the experimental apparatus, external flows and gradients imposed at the boundaries or nonstationary conditions because of the initial preparation of the system.

Hence the physics of small systems requires to quantify the role of these two factors in the performance of such small objects. However, this is not a trivial task using the standard tools of thermodynamics and equilibrium statistical mechanics. Thermodynamics deals only with a phenomenological approach of energy exchanges (heat and work) for *equilibrium processes*, i.e. performed at an infinitely slow rate. A refinement is possible thanks to equilibrium statistical mechanics, which provides a theoretical framework to study the average behavior of thermodynamic bulk variables of macroscopic systems (composed of $\gtrsim 10^{23}$ particles) in thermal equilibrium from microscopic properties of the constituent atoms and molecules. It admits the statistical description of nonequilibrium states very close to thermal equilibrium through the so-called *fluctuation-dissipation theorem* [4]. This theorem provides an expression, which links the statisitical properties of the spontaneous fluctuations of a system in thermal equilibrium to the response to a weak external field. For example, it predicts mobilities of colloidal suspensions subjected to external shear from the measurement of diffusion coefficients done at thermal equilibrium. For an electric (magnetic) material, the fluctuation-dissipation theorem allows one to determine the equilibrium statistical properties of electric polarization (magnetization) fluctuations by the measurement of

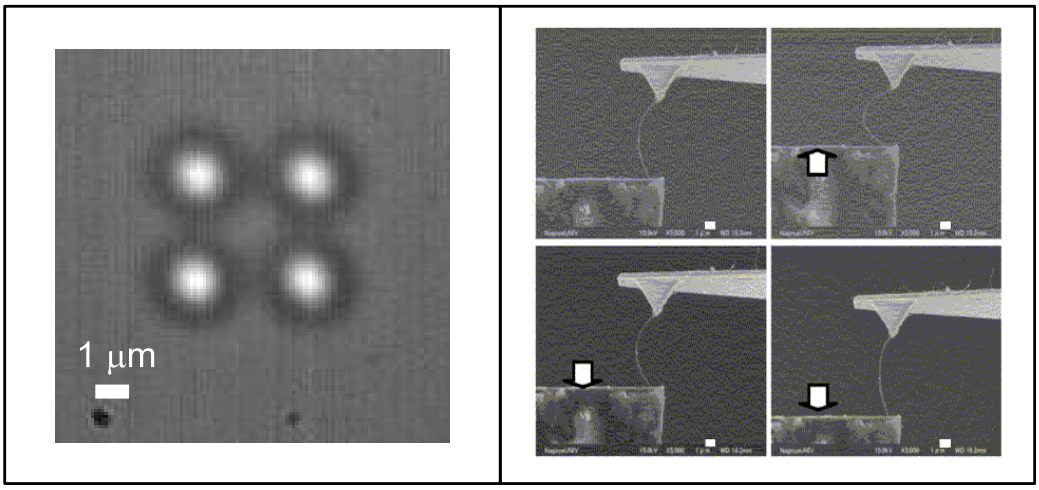

(a)

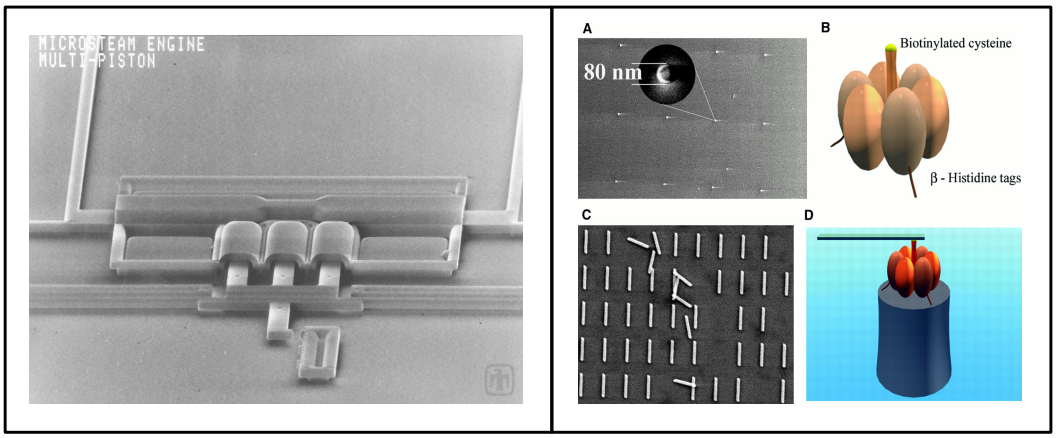

(b)

Figure 1: (a) Left panel: square array of silica microspheres (diameter 2 μm) suspended in water using optical tweezers. Right panel: nanotube (length 6.055 μm, diameter 133 nm) buckled by an AFM cantilever. Image taken from [1]. (b) Left panel: Triple-piston (5 μm) MEMS steam engine. Water inside the three compresion cylinders is heated by electric current and vaporizes, pushing the piston out. Image taken from [2]. Right panel: (D) Schematic diagram of an F_1-ATPase biomolecular-motor-powered nanomechanical device, composed by (A) a Ni post (height 200 nm, diameter 80 nm), (B) the F_1-ATPase molecular motor and (C) a nanopropeller. Image taken from [3].

susceptibilities. Nonetheless, thermodynamics and equilibrium statistical mechanics fail to describe adequately the behavior of the observables of a system as fluctuations and nonequilibrium conditions become dominant. Taking into account these limitations, recent progress in statistical mechanics of processes far from thermal equilibrium has been achieved in parallel during the last 20 years. There are roughly two kinds of theoretical relations that have been derived under certain hypothesis to statistically describe nonequilibrium processes: *fluctuation relations* and *generalized fluctuation-dissipation (response) relations*.

1. Fluctuation Relations (FR)

They describe symmetry properties of fluctuating energy exchanges and entropy production for processes arbitrarily far from equilibrium. Then they can be regarded as generalizations of the laws of thermodynamics to nonequilibrium fluctuating processes. More specifically:

Jarzynski, Crooks and Hatano-Sasa relations [5, 6, 7]

They provide statistical identities for the work done during arbitrarily fast *nonequilibrium* transformations between two *equilibrium* states and their relation with the variation of free energy between the same equilibrium states. Let us illustrate these relations with a simple example represented in figure 2(a).

We consider a small particle moving in a viscous fluid at fixed temperature T, with a viscous friction coefficient γ. The particle motion is confined by a harmonic potential of stiffness k and centered at x_0:

$$U_k(x) = \frac{k(x - x_0)^2}{2}.$$

The particle position x fluctuates around the position of the potential minimum x_0 because of the thermal fluctuations provided by the molecules of the surrounding fluid. For a constant value of k, the particle is in thermal equilibrium with the fluid and the probability distribution of x is determined by the Boltzmann distribution

$$\rho_k(x) \propto \exp\left[-\frac{U_k(x)}{k_B T}\right].$$

We consider two constant values of the potential stiffness: $k = k_1$ and $k = k_2$ with $k_1 < k_2$ fixing two different equilibrium states 1 and 2, respectively. We focus on a fast variation of the stiffness following a given protocol $k(t)$ in the time interval $t_1 \leq t \leq t_2$ between the two equilibrium states, i.e. $k(t_1) = k_1$ and $k(t_2) = k_2$. During this nonequilibrium process, a given amount of work W is done on the particle to perform the time variation of k. W is a random variable because it depends on the stochatic

evolution of the particle position[1]. Specifically

$$\begin{aligned} W &= -\int_{x(t_1)}^{x(t_2)} kx\,\mathrm{d}x, \\ &= -\frac{1}{2}\int_{t_1}^{t_2} k(t)\frac{\mathrm{d}}{\mathrm{d}t}\left[x(t)^2\right]\,\mathrm{d}t, \\ &= -\frac{1}{2}[k_2 x(t_2)^2 - k_1 x(t_1)^2] + \frac{1}{2}\int_{t_1}^{t_2} \dot{k}(t)x(t)^2\,\mathrm{d}t. \end{aligned}$$

The second term on the right-hand side of the third line represents the work irreversibly dissipated during a single stochastic realization in this nonequilibrium process:

$$W_{diss} = \frac{1}{2}\int_{t_1}^{t_2} \dot{k}(t)x(t)^2\,\mathrm{d}t.$$

The Hatano-Sasa relation states that for an infinite number of realizations of the same dynamical protocol $k(t)$ between the two equilibrium states at k_1 and k_2, the following identity holds [7]:

$$\left\langle \exp\left[\int_{t_1}^{t_2} \dot{k}(t)\partial_k \ln \rho_k(x_t)\,\mathrm{d}t\right]\right\rangle_k = 1,$$

where the brakets $\langle \ldots \rangle_k$ denote a dynamical average over the infinite number of realizations of $k(t)$ and the function $\partial_k \ln \rho_k$ must be evaluted along each stochastic realization of x. It turns out that the integral between the square brakets of the exponential is equal to $-W_{diss}/(k_B T)$. The Hatano-Sasa identity holds for any protocol $k(t)$ at any rate satisfying the boundary conditions imposed by the two equilibrium states.

The Jarzynski equality relates the stochastic work W_{diss} done during the dynamical process $k(t)$ with the free energy difference $\Delta F = F_2 - F_1$ between the two equilibrium states 1 and 2 [5]:

$$\left\langle \exp\left(-\frac{W_{diss}}{k_B T}\right)\right\rangle_k = \exp\left(-\frac{\Delta F}{k_B T}\right).$$

Therefore, unlike classical thermodynamics, this FR allows one to compute equilibrium free energies from the measurement of the nonequilibrium work done at any rate bewteen two equilibrium states. For the specific example illustrated in figure 2(a), the free energy difference is $\Delta F = 0$. Therefore, the Hatano-Sasa relation and the Jarzynski equality yield the same expression.

Finally, the Crooks relation measures the asymmetry of the distribution P of the work done from the equilibrium state 1 to the equilibrium state 2 with respect to the distribution P' of the work done during the backward process from 2 to 1 [6]:

$$\frac{P(W_{diss})}{P'(-W_{diss})} = \exp\left(\frac{W_{diss} - \Delta F}{k_B T}\right).$$

[1]Note that the work W corresponds to the *classical* work, which differs by boundary terms from the *stochastic* work W_{diss} involved in the FRs.

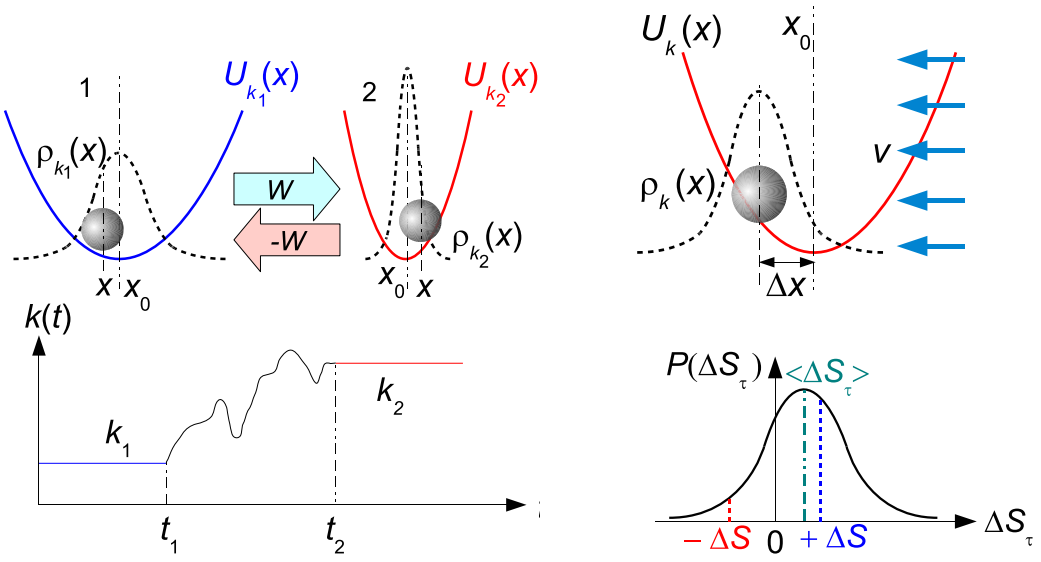

(a) (b)

Figure 2: (a) Schematic representation of a nonequilibrium process to illustrate the Hatano-Sasa, Jarzynski and Crooks relations. A particle immersed in a viscous fluid and confined by a harmonic potential is subjected to a nonequilibrium transformation between two equilibrium states 1 and 2. This is done by varying in time the potential stiffness k between the values k_1 and k_2 in the time interval $[t_1, t_2]$. During this process a given amount of work W is done. (b) Schematic representation of a nonequilibrium steady state to illustrate the fluctuation theorem. A particle is confined by a harmonic potential in a fluid in laminar flow moving at speed v. During a time τ a given amount of entropy ΔS_τ is produced. The asymmetry of the distribution of the fluctuations of ΔS_τ is quantified by the fluctuation theorem.

The Crooks relation, formulated as a theorem, is usually regarded as the general result from which the Jarzynski equality derives.

Fluctuation theorem [8, 9, 10, 11]

This FR quantifies the relative probability of observing positive values of the entropy production with respect to rare negative values for a system driven into a nonequilibrium steady state. In particular, it implies that the mean value of the total entropy production of a system in a nonequilibrium steady state is always positive.

Following the example of the particle confined by the harmonic potential, we now consider that the fluid around the particle flows at constant speed v, see figure 2(b). Therefore the flow constantly drags the particle with a force $\gamma(\dot{x}-v)$, which is balanced in average by the restoring force $-k(x-x_0)$ of the harmonic potential. This gives rise to an average displacement $\Delta x = \gamma v/k$ of the particle position with respect to x_0. This

is a nonequilibrium state because a finite amout of energy is externally provided to the system by the flow. Such a nonequilibrium state is statistically invariant under time translations, then it is a nonequilibrium steady state. In this case the distribution of x is given explicitly by

$$\rho_k(x) \propto \exp\left[-\frac{k(x+\Delta x)^2}{2k_BT}\right].$$

Due to the constant energy dissipation by the particle to sustain the nonequilibrium steady state, a nonzero amount of entropy is always produced in average. It can be shown that the *total* entropy change along a stochastic realization of x during a time interval $[0,\tau]$ is [11]

$$\Delta S_\tau = -k_B \ln \frac{\rho_k(x_\tau)}{\rho_k(x_0)} + \frac{Q_\tau}{T},$$

where Q_τ is the heat dissipated into the fluid during the same time interval. Since x and Q_τ are stochastic variables, ΔS_τ is also stochastic: there can be rare events where entropy decreases ($\Delta S_\tau < 0$) instead of the most common events where it increases ($\Delta S_\tau > 0$). The fluctuation theorem quantifies the relative probability of observing a negative value $\Delta S_\tau = -\Delta S$ with respect to the probability of observing a positive value $\Delta S_\tau = \Delta S$:

$$\frac{P(-\Delta S)}{P(\Delta S)} = \exp\left(-\frac{\Delta S}{k_B}\right).$$

Then $\langle \Delta S_\tau \rangle \geq 0$ in agreement with the second law of thermodynamics. See Appendices A and B for a more detailed overview on the fluctuation theorem.

Due to its apparent validity under rather general hypothesis, FRs have been subject to intensive theoretical, numerical and experimental investigations. See [12] and references therein for a descriptive review on experimental tests of FRs. But more importantly for applications, they have successfully provided useful information in small systems, otherwise inaccessible using the standard tools of equilibrium statistical mechanics. For instance, using the the Jarzynski and Crooks relations it is possible to measure free energies of single biomolecules by perfoming nonequilibrium stretching experiments [13, 14]. A second recent example is the use of the fluctuation theorem to estimate the mean torque exerted by chemical reactions on a molecular motor protein from fluctuation measurements [15]. Hence, they are turning from merely theoretical relations into useful quantitative tools in experiments and simulations to study the *thermodynamics* of small systems.

2. Generalized fluctuation-dissipation relations (GFDR)

Similar to the equilibrium formula given by the fluctuation-dissipation theorem, they establish a link between the spontaneous fluctuations of a system in an unperturbed state away from thermal equilibrium and the linear response to a weak perturbation around the same nonequilibrium state. Then they offer the possibility to determine the response of a system to complex time dependent perturbations by means of the

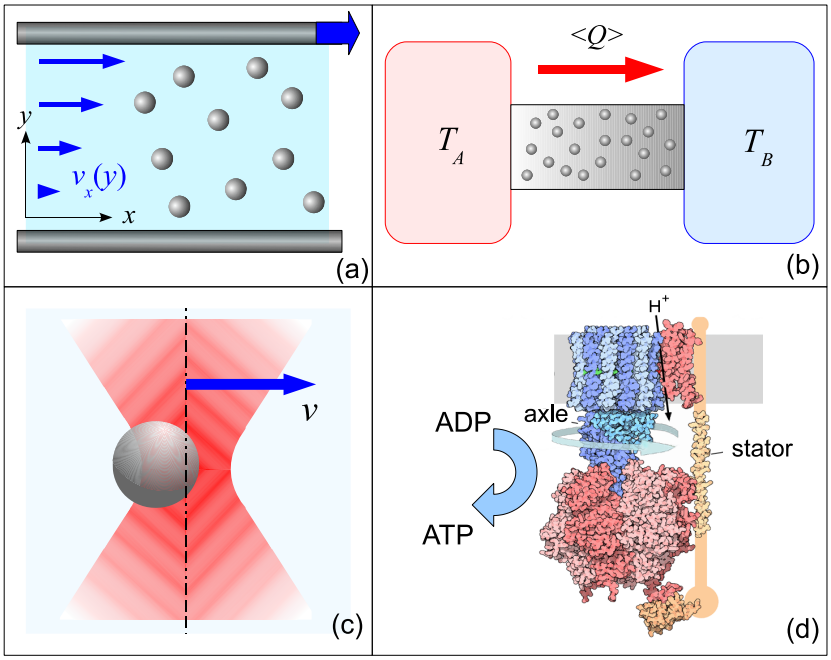

Figure 3: Examples of systems in nonequilibrium steady states: (a) Colloidal suspension in stationary shear flow $v_x(y)$. (b) System conducting heat $\langle Q \rangle$ between two reservoir at unequal temperatures $T_A > T_B$. (c) Brownian particle dragged by the potential created by an optical trap moving at constant speed v. (d) Rotary molecular motor enzyme (ATPase) pumped by the chemical synthesis of ATP. The central shaft (blue) rotates unidirectionally during the synthesis.

measurement of unperturbed nonequilibrium fluctuating quantities. Conversely, statistical properties of nonequilibrium fluctuations can be probed through the measuments of response functions to weak external fields. There are two important unperturbed nonequilibrium cases where GFDRs have been derived:

I. Nonequilibrium steady states [16, 17, 18, 19, 20, 21, 22, 23, 24]

This case corresponds to systems subjected to nonconservative forces, time-dependent drivings or energy or mass fluxes but with time-invariant probability distributions. GFDRs have been derived mainly for Markovian dynamics, i.e. when the time evolution depends only on present values but not on the previous history of the system. Some examples of nonequilibrium systems that are naturally in steady states are colloidal particles driven by optical traps, sheared suspensions, molecular motors and systems connected to reservoirs at different temperatures or chemical potentials (figure 3). In all of theses cases, energy in injected into the system and at the same time the system itself dissipates heat into the environment in order to maintain a stationary state.

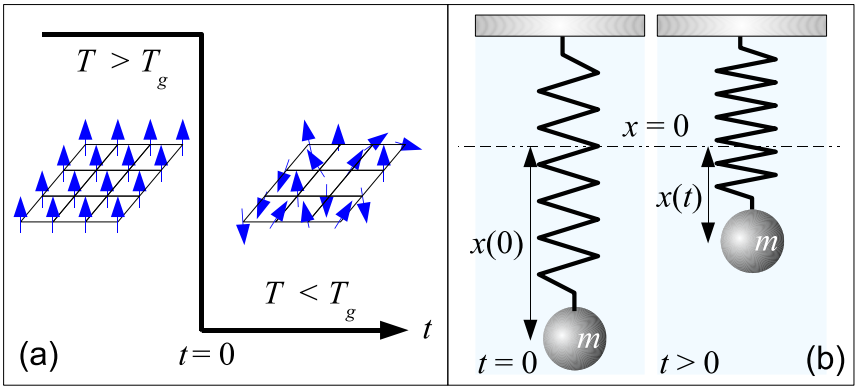

Figure 4: Examples of systems in nonstationary states relaxing to thermal equilibrium: (a) spin system quenched at time $t = 0$ from a ferromagnetic phase at high temperature ($T > T_g$) to a disordered spin glass phase at low temperature ($T < T_g$). Its magnetic properties slowly evolve in time for $t > 0$. (b) Damped anharmonic oscillator in a fluid at temperature T with friction coefficient γ. A mass m attached to a nonlinear spring is released with an initial energy $E(x(0), \dot{x}(0)) \gg k_B T$ at time $t = 0$. The position $x(t)$ of the mass at $t > 0$ is in a transient state before reaching the equilibrium mean value $\langle x(t) \rangle = 0$ for $t \gg m/\gamma$.

II. Nonstationary states [25, 26, 22, 27, 28]

This case concerns systems with relaxational or transient dynamics after an initial preparation of the system in a metastable configuration (figure 4). A special case of GFDRs have been derived for systems rapidly quenched into a metastable state from above to below a critical temperature and slowly relaxing towards thermal equilibrium states [25, 26]. Some examples are glasses quenched below the glass transition temperature T_g and thermoreversible gels quenched below the gelation temperature. A closely related relaxational process occurs for systems quenched near a critical point, for instance liquids crystal subjected to an abrupt decrease of an applied electric field up to a critical value [29]. Other kinds of GFDRs describe transient Markovian dynamics of systems subjected to a fast variation of a control parameter, prepared in a nonequilibrium initial condition or in contact with a nonstationary bath [22, 27, 28]. For instance, for a damped anharmonic oscillator in contact with a thermal bath, this type of GFDRs describes the fluctuations and response around the transient state after releasing the oscillator from a high-energy E configuration ($E \gg k_B T$). In both cases, the energy excess of the initial configuration must be dissipated into the environment in order for the system to reach thermal equilibrium.

GFDRs have been also studied theoretically, numerically and experimentally, albeit to a much lesser extent than FRs. This is because GFDRs have been formulated in more specific cases and from very different physical approaches involving quantities that are not always easily accessible in experiments. Moreover, most of the few

experimental tests so far only provide a qualitative picture of the relation between nonequilibrium fluctuations and response. They only measure the *violation* of the fluctuation-dissipation formula provided by equilibrium statistical mechanics without any clear interpretation of the origin of this deviation.

Motivation and outline of the thesis

Motivated by the extensive studies on FRs for systems under simple nonequilibrium conditions[2], the first goal of the present thesis is to perform a careful and comprehensive analysis of GFDRs in simple experiments on small systems that can be carried out under very well controlled conditions. We aim to keep the experimental systems as minimal as possible (e.g. a single relevant degree of freedom) but with enough nonequilibrium features and complexity in order to gain a clear physical understanding of the measured quantities. Such a kind of experimental control can be achieved in the manipulation of a single micron-sized particle embedded in a fluid by the forces exerted by a tigthly focused laser beam (optical traps). Strong nonequilibrium conditions can be imposed to the system either by nonconservative forces exterted by the laser beam or by the initial condition of the fluid surrounding the particle. In chapter 1 we describe the setup and the techniques based on optical traps that we use to conduct our experimental study. Then, the thesis is divided into two parts in order to focus on the study of two different kinds of nonequilibrium systems:

I. In the first part we address the study of fluctuations and linear response of a Brownian particle driven into a periodic nonequilibrium steady state by a nonconservative force exterted by a scanning laser beam. We first present in chapter 2 an overview of the theoretical derivation of the different GFDRs for nonequilibrium steady states. Then in chapter 3 we describe the experiment where the quantities involved in the different GFDR formulations can be accurately measured. Unlike previous experimental approaches, we do not attempt to measure only the violations of the classical equilibrium fluctuation-dissipation relation, but we determine the exact relation between fluctuations and response. Then a detailed analysis allows us to get a physical interpretation of these GFDTs and to quantify the role of currents due to the nonequilibrium nature of the system.

II. The second part deals with a Brownian particle in a bath prepared in an initial out-of-equilibrium condition and slowly relaxing towards an equilibrium state (physics aging). We measure the nonequilibrium spontaneous fluctuations of the particle trapped by optical tweezers and the linear response to an external perturbation exerted through the motion of the optical trap. With the purpose of quantifying the extent of the nonequilibrium nature of the system as it relaxes, we also measure the fluctuations of the heat exhanged between the Brownian

[2]For example, electrical circuits under external currents, harmonic oscillators driven by magnetic torques, colloidal particles dragged by optical tweezers, etc. either in transient and steady states resulting from time-dependent drivings [12].

particle and the bath. We study the statistical properties of these fluctuations in the context of the fluctuation theorem. We conduct this experimental study in two different relaxing media surrounding the Brownian particle: a colloidal glass (Laponite, chapter 4) and a thermoreversible gel after a fast quench (gelatin, chapter 5). In this way we are able to contrast the different experimental results taking place at different length and timescales. Then we can identify the fundamental features of fluctuations and response for a nonequilibrium sytem slowly relaxing to thermal equilibrium.

At first sight, the two different descriptions of nonequilibrium fluctuations and linear response for the systems addressed in parts I and II seem two be dissimilar and at the same time uncorrelated with the quantities measured in the context of FRs. Hence, our second goal is to find out whether or not there are underlying measurable quantities connecting these formulations. Once again, due to our minimal but sufficiently complex experiments we are able to identify such a quantitative link. It turns out that the total entropy production, or equivalently the probability or irreversible heat currents, play a unifying role between the different formulations of GFDRs and with FRs either in steady states or nonstationary states relaxing towards thermal equilibrium. Then throughout the present thesis we show that the "violation" of the equilibrium fluctuation-dissipation formula for both kinds of nonequilibrium systems is actually quantified by the total entropy production. This entropy can be experimentally measured by the tiny amounts of heat that must flow to sustain the nonequilibrium state and that satisfy the properties imposed by FRs.

Chapter 1

Optical traps

In this chapter we present a brief overview on the physics of optical tweezers. Then we describe two different optical trap setups used to perform the experiments on trapped micron-sized particles described throughout the thesis. We also detail the experimental techniques implemented for the calibration and the detection of each apparatus.

1.1 The physics of optical tweezers

Optical traps (tweezers) consist on the use of radiation pressure of light in order to trap and manipulate micron-sized objects in a stable way with forces ranging from femto to piconewtons. For ordinary light, the force exerted by radiation pressure is very small. For example, the radiation pressure P of sunlight (intensity $I \approx 1\,\mathrm{kW\,m^{-2}}$) on an object of reflection coefficient R is $P = (1+R)I/c$, where c is the speed of light. Then, in the ideal case $R = 1$ (total reflection) the maximum force that can be exerted on a surface $S = 1\,\mu\mathrm{m}^2$ is

$$F = 2\frac{IS}{c} \sim 10\,\mathrm{aN}.$$

However, for real materials ($R < 1$) the force is even weaker than the previous value. On the other hand, the force needed to drag a spherical particle of the same size through water at a speed of $1\,\mu\mathrm{m\,s^{-1}}$ is ~ 10 fN, i.e. 1000 times stronger than the maximum force exerted by the radiation pressure of sunlight. Therefore, optical tweezers require a large photon flux like that provided by a laser highly focused to the diffraction limit in order to manipulate micron-sized objects. The first attempts to accomplish optical trapping date back to the work of Ashkin in 1970 [30], one decade after the invention of laser. In these early experiments, micron-sized particles suspended in water could be accelerated and trapped by the radiation pressure of two opposing horizontal beams focused inside the sample (see figure 1.1(a)). Nevertheless, the first experimental realization of a stable optical trap using a single vertical beam was achieved until 1986 [31] (figure 1.1(b)). This is the basic experimental configuration implemented in most of the modern optical traps. Unlike the two opposing-beam system, the single-beam trap relies on a large gradient force exerted by the focused beam on the trapped particle towards the center

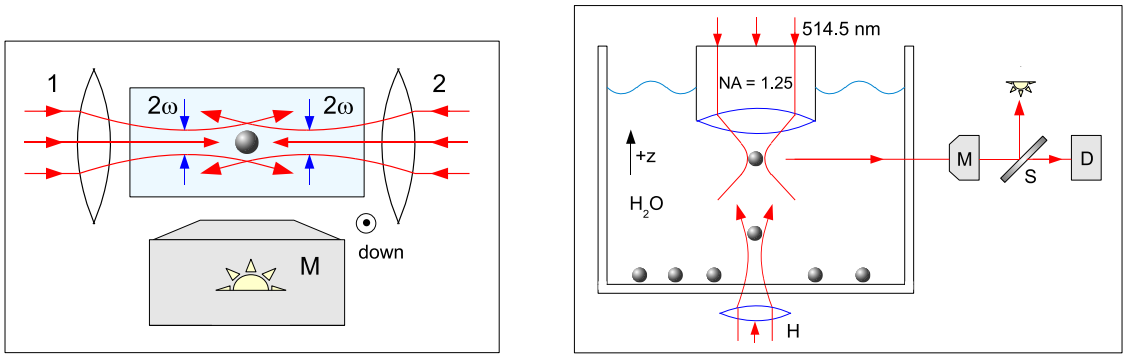

(a) (b)

Figure 1.1: (a) Sketch of the first experimental appartus [30] designed to trap a micro-sized particle embedded in water by the radiation pressure of two opposing laser beams ($\lambda = 514.5$ nm) focused by two lenses to obtained a waist $\varpi = 6.2\,\mu$m. The trapped particle is detected by a microscope (M). (b) Sketch of the first single-beam optical trap [31] created by means of an argon laser, tighly focused by a high-numerical-aperture objective ($NA = 1.25$) to the diffraction limit (waist $\varpi \approx \lambda$). A second laser (H) is used to lift the particles to the focus of the upper trapping beam. Trapped particles are visualized by a microscope (M) and the 90° scattered light is sent to a detector (D) by a beam splitter (S).

of the focus. Then the particle is confined to the well of a potential created by the focused beam. We explain the origin of this gradient force in the following.

The principle

We consider a spherical dielectric particle of radius r and refractive index n_p (dielectric constant ϵ_p) embedded in a fluid of refractive index $n_m < n_p$ (dielectric constant ϵ_m). The particle is close to a Gaussian laser beam of wavelength λ, tightly focused to the diffraction limit at $z = 0$ in the fluid and propagating in the vertical direction $+z$ opposite to gravity (see figure 1.2). The spatial intensity profile of this kind of beam can be approximated in cylindrical coordinates as

$$I(\rho, z) = I_0 \exp\left(-\frac{\rho^2}{2\varpi_\rho^2} - \frac{z^2}{2\varpi_z^2}\right), \tag{1.1}$$

where ϖ_ρ and ϖ_z are the size of the beam waist in the radial and axial directions, respectively. On the other hand, for a highly focused beam the main contribution of the force exerted by the electromagnetic field on the surface of the particle is of electrostatic dipolar origin. Then the interaction energy between the particle and the electrostatic field E can be expressed as

$$U = -\frac{1}{2}\int E_0 P \,\mathrm{d}V, \tag{1.2}$$

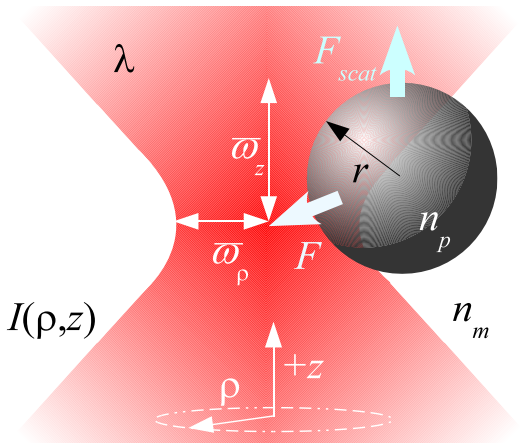

Figure 1.2: Schematic representation of a dialectric spherical particle close to a Gaussian laser beam tightly focused to the diffraction limited spot. The intensity profile $I(\rho, z)$ around the focus is given approximately by equation (1.1). The radiation pressure exerted by the beam results in two forces acting on the particle: a restoring force F due to the intensity gradient directed to the focus center ($\rho = 0, z = 0$) and a scattering force F_{scat} directed forward along the beam propagation $+z$.

where P is the dipolar density of the particle induced by the field E in presence of the particle and E_0 is the unperturbed electrostatic field in the absence of the particle. If the particle is made of an isotropic linear material, the dipolar density is proportional to electrostatic field

$$P = \frac{\epsilon_p - \epsilon_m}{4\pi} E.$$

In addition, if $|\epsilon_p - \epsilon_m| \ll 1$ (weak polarization), E can be approximated by E_0. Since the intensity of the unperturbed electrostatic fields is proportional to E_0^2

$$I = \frac{\epsilon_m E_0^2}{8\pi},$$

then the interaction energy (1.2) is approximately

$$U(\rho, z) = -2\pi\alpha \int_0^{\rho} \int_{-\infty}^{z} I(\rho', z')\, \rho'\, \mathrm{d}\rho'\, \mathrm{d}z', \tag{1.3}$$

where the parameter

$$\alpha = \frac{\epsilon_p}{\epsilon_m} - 1 \approx \frac{n_p^2}{n_m^2} - 1,$$

measures the refractive index mismatch between the particle and the surrounding medium. By inserting the expression of the Gaussian beam profile (1.1) into equation (1.3) and taking the spatial derivatives, one finds the radial F_ρ and axial F_z components

of the force $F = -\nabla U$ exerted by the electromagnetic field. For an isotropic focused Gaussian beam ($\varpi \equiv \varpi_\rho = \varpi_z$), an analytical expression of the isotropic force $F(\varrho)$ as a function of $\varrho = \sqrt{\rho^2 + z^2}$ can be readily found [32]

$$F(\varrho) = \alpha I_0 \varpi^2 4\pi \exp\left(-\frac{r^2+\varrho^2}{2\varpi^2}\right)\left[\frac{r\varrho}{\varpi^2}\cosh\left(\frac{r\varrho}{\varpi^2}\right) - \sinh\left(\frac{r\varrho}{\varpi^2}\right)\right], \tag{1.4}$$

For distances ϱ sufficiently small with respect to r, equation (1.4) yields a harmonic restoring force

$$F(\varrho) = -k\varrho, \tag{1.5}$$

whith an effective spring constant (*stiffness*)

$$k = \frac{\alpha I_0}{\varpi^2}\frac{4\pi r^3}{3}\exp\left(-\frac{r^2}{2\varpi^2}\right), \tag{1.6}$$

whereas for distances much larger than the beam waist, F vanishes. Note that according to equation (1.6), the focused beam actually acts as an attractive potential because $\alpha > 0$. Then when a particle is very close to the beam focus, its motion is confined by an approximately harmonic potential well

$$U(\varrho) = \frac{1}{2}k\varrho^2.$$

For particles smaller than the beam waist $r < \varpi$, the stiffness is almost proportional to the volume of the particle $4\pi r^3/3$ whereas for large particles $r > \varpi$, the stiffness decreases as the particle radius increases. For the anisotropic case $\varpi_\rho < \varpi_z$, which is the most common in real Gaussian beams, a cumbersome calculation yields the analytical expressions for the stiffness k_ρ and k_z of the radial $F_\rho = -k_\rho\rho$ and axial $F_z = -k_z z$ components of the restoring force with $k_\rho > k_z$ (see the analytical expression derived in [32]). However, these expressions are not very useful in practice because they require to measure the precise values of the beam waists ϖ_ρ, ϖ_z and the local value of the intensity I_0 inside the chamber containing the trapped particle. Instead, it is easier to implement in experiments some calibration techniques either to reconstruct the potential energy of the particle in the focused beam or to measure directly the values of k_ρ and k_z, as described in detail in subsections 1.2.2 and 1.3.3.

Effect of photon scattering

It should be noted that according to equation (1.1) the gradient of the intensity ∇I is proportional to I_0/ϖ^2. The stiffness k of resulting harmonic force is also proportional to I_0/ϖ^2 (see equation (1.6)). Then the origin of the attractive force exerted by the beam is the intensity gradient created by the Gaussian profile: the larger the gradient the stronger the trapping force. The maximum gradient that can be achieved in practice occurs when the beam is focused to the diffraction limited spot (waist $\varpi \approx \lambda$). However, this is not the only force exerted by the focused beam. Due to the scattering of the

laser photons when passing through the particle, there is an additional nonconservative force which pushes the particle forward along the beam propagation [33, 34, 35, 36]. For small particles $r \ll \lambda$, the scattering force is $F_{scat} \sim I_0 \lambda^2 \alpha^2 (r/\lambda)^6$ [34]. As $\varpi \approx \lambda$ for a diffraction limited laser spot and the maximum gradient force that can be exerted on the particle is $F_{max} \sim \alpha I_0 \varpi^2 (r/\varpi)^3$, then the ratio between the scattering and the maximum harmonic force behaves as

$$\frac{F_{scat}}{F_m} \sim \alpha \left(\frac{r}{\lambda}\right)^3 .$$

Since $\alpha < 1$ in most of the experimental conditions, in general the scattering force is much smaller than the trapping gradient force. When $r \approx \lambda$, F_{scat} can become non-negligible, slightly displacing the particle towards the direction of the beam propagation but it is exactly balanced by the vertical component F_z of the trapping force. However, this approximation is only valid when the laser is focused to the diffraction limit. Otherwise the waist is $\varpi > \lambda$ so that the ratio F_{scat}/F_m becomes proportional to ϖ/λ. In such a case the scattering force dominates for sufficiently large ϖ and the particle is pushed away from the focus in the direciton of the beam propagation. Finally, for large particles ($r \gg \lambda$), the scattering force is $F_{scat} \approx 2\pi\alpha^2 I_0 \varpi^2$ [32] whereas the maximum gradient force is $F_m \approx 2\pi\alpha I_0 \varpi^2$ (see equation (1.4)). Consequently the ratio between F_{scat} and F_m scales as

$$\frac{F_{scat}}{F_m} \approx \alpha,$$

regardless of the value of λ. In this case the trapping gradient force also dominates over the scattering force if the beam is focused to the diffraction limit $\varpi \approx \lambda$.

We now proceed to describe two different custom-built setups that we used in order to realize the optical trapping of microspheres of radius $r = 1\,\mu$m following the previous physical ideas. Note that this particle size is comparable to the laser wavelength.

1.2 Single-trap setup

The first experimental setup consists on the creation of a single optical trap. The setup is sketched in figure 1.3. The beam of a single-mode diode laser (Lumics, $\lambda =$ 980 nm) is guided by an optical fiber and collimated by a telescope to a dichroic mirror (DM2). The power of the diode laser is controlled by a computer. The collimated beam is reflected by DM2 and directed to the entrance of an oil-immersion microscope objective (Leica, 63×, high numerical aperture $NA = 1.4$). The objective tightly focuses the beam to the diffraction limited spot (waist $\varpi \approx \lambda$) inside a transparent cell containing the microbeads to be trapped. The sample cell is fixed to a piezoelectric stage (NanoMax-TS MAX313M) by means of a rigid holder to avoid the mechanical vibrations of the glass plates making up the cell, as shown in figure 1.3.

The cell basically consists of a microscope slide and a coverslip separated by a plastic spacer of inner diameter 15 mm $\leq 2R \leq$ 20 mm and thickness 1 mm $\leq L \leq$ 3

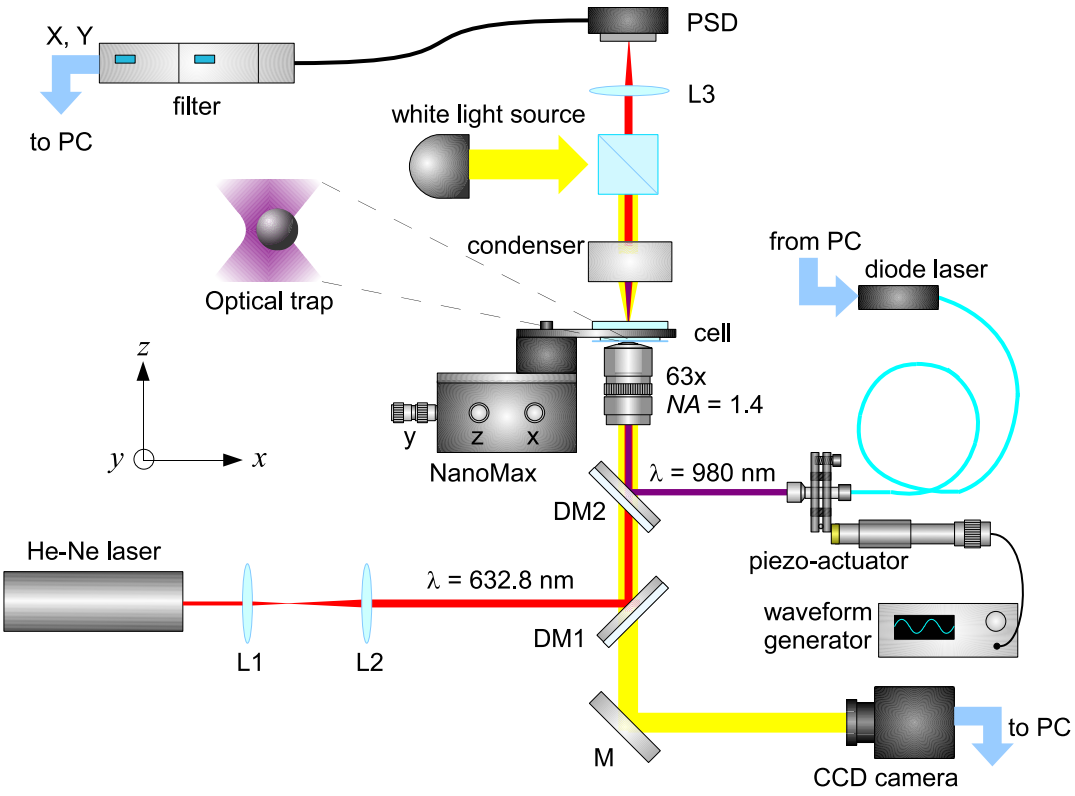

Figure 1.3: Diagram of the single-trap setup. L1 and L2 are the lenses of a beam expander, M a mirror, DM1 and DM2 are dichroic mirrors. See section 1.2 for a detailed explanation.

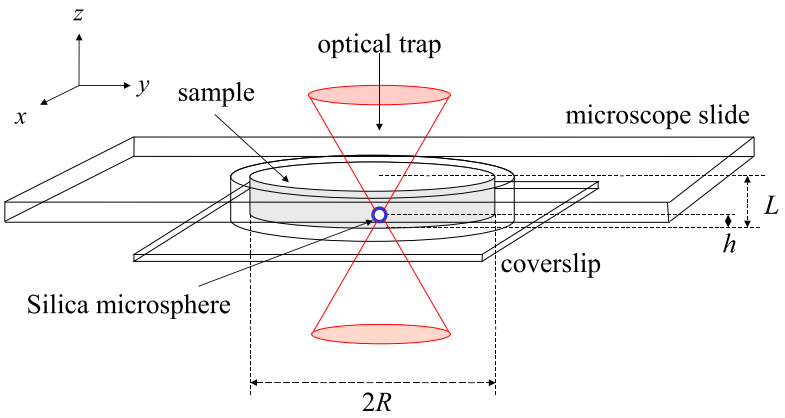

Figure 1.4: Schematic representation of the sample cell.

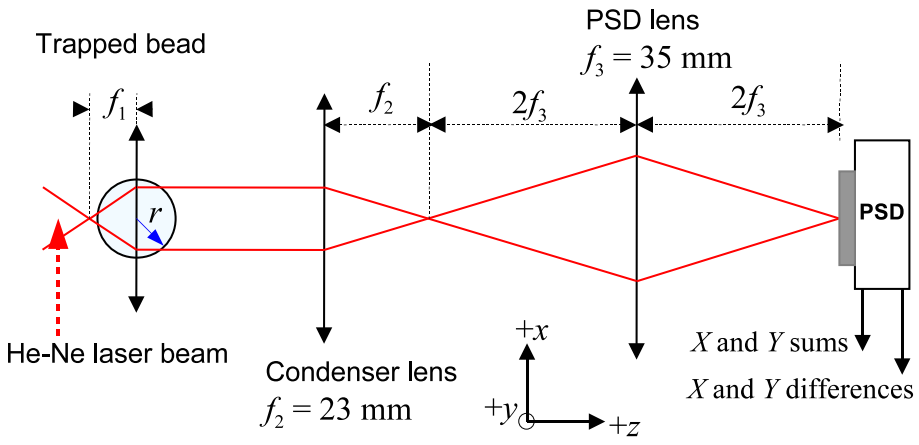

Figure 1.5: Diagram of the PSD detection system for the single-trap setup. See subsection 1.2.1 for a detailed explanation.

mm. The cell is put with the microscope slide on top fixed to the piezoelectric stage in such a way that the optical trap is created at a few microns 10 μm $\lesssim h \lesssim$ 25 μm from the inner coverslip surface, as schematized in figure 1.4. As the detailed description of the cell depends on the special features of the experiment, they will be given in the respective chapters.

The particles are dispersed in the fluid inside the cell at very low concentration (volume fraction $\sim 10^{-6}$). Hence, the piezoelectric stage is used to facilitate the trapping process: the sample cell can be slowly displaced a few microns in 3D by the micrometer screws x, y and z to put the particles close to the beam focus. With the purpose of visualizing the trapping process of a particle, the beam of a white light source is guided by a fiber and focused in the sample cell by a condenser lens (focal distance $f_2 = 23$ mm). Then the resulting contrast image is magnified by the same microscope objective used to create the optical trap. The image passes through the dichroic mirrors DM2, DM1 and then it is reflected by the mirror M to be detected by a CCD Camera. The whole setup is mounted on an optical table (Melles Griot) in order to get rid of external mechanical vibrations that perturb the sample cell and the position of the optical trap. In addition, the components of the trapping system are enclosed in a Plexiglas box fixed to the optical table surface to insulate the optical trap from acoustic noise. Once a particle is trapped by the focused beam, its position in the xy plane (perpendicular to the beam propagation in $+z$) is tracked with a resolution better than 1 nm using the following detection system.

1.2.1 Detection

The detection of the position of the trapped particle is based on a position sensitive detector system (see figures 1.3 and 1.5). For this purpose, in addition to the trapping beam we use a He-Ne laser (Melles Griot, $\lambda = 632.8$ nm). The Gaussian beam of the

He-Ne laser is magnified by a beam expander created by two lenses (L1 and L2) to fill completely the microscope objective entrance (diameter 10 mm). The collimated He-Ne beam is focused by the same microscope objective very close but not exactly in the focus of the trapping beam. A trapped bead of radius $r = 1\,\mu$m and refractive index n_p in a fluid of refractive index n_m acts as a microlens of effective focal length

$$f_1 = \frac{mr}{2(m-1)^2},$$

where $m = n_p/n_m$. Hence, the He-Ne beam must be focused close to the focal plane of the trapped bead, as shown in figure 1.5. In this way, when the bead barycenter is exactly located at f_1 from the focus of the He-Ne beam, the rays refracted by the bead emerge parallel to the $+z$ direction. Then the lens array formed by the condenser and L3 (shown in figure 1.5) allows one to obtain a final laser spot focused at a distance f_2+4f_3 from the center of the condenser. Thanks to the focus created by this lens array, the intensity of the He-Ne spot at the distance $f_2 + 4f_3$ is almost independent of the z position of the trapped bead. The spot is detected by a duolateral position sensing diode (PSD, DL100-7PCBA3) of square active area 10 mm×10 mm which measures the relative displacement of the laser spot centroid with respect to its own centroid. The optical system is aligned in such a way that the laser spot centroid is located exactly in the PSD centroid in the absence of the trapped bead[1]. In the presence of a bead, fluctuations around its the mean position in the xy plane deflect the resulting laser spot from the centroid of the PSD.

Data processing

When the laser spot impinges on the photodiode, currents are created and collected by electrodes located at opposite edges. The currents collected at each edge are converted into voltages (X_1, X_2 along x and Y_1, Y_2 along y) that are processed in order to provide the difference outputs $X_1 - X_2$, $Y_1 - Y_2$ and the sum outputs $X_1 + X_2$, $Y_1 + Y_2$. The differences are then externally normalized by the sums to obtain the centroid coordinates of the He-Ne spot

$$X = \frac{X_1 - X_2}{X_1 + X_2}, \quad Y = \frac{Y_1 - Y_2}{Y_1 + Y_2}.$$

For small displacements of the trapped bead with respect to the the focus center, the PSD response is linear. Then the instantaneous particle position $(x(t), y(t))$ at time t is proportional to the position $(X(t), Y(t))$ of the laser spot centroid

$$x(t) = AX(t), \quad y(t) = BY(t),$$

[1] In the absence of the trapped bead acting as a collimator, the He-Ne spot on the PSD surface is very large.

where the proportionality constants A, B must be determined by calibration of the apparatus[2]. The voltage signal (X, Y) is filtered by a low-pass filter (Stanford SR640) with a cutoff of 4 kHz in order to avoid aliasing. Finally, the filtered voltage signals X, Y are received by a data acquisition board (National Instruments PCI-MIO-16XE-10, 16-bit, 100 kS/s) with an adapted module (National Instruments SC-2040) for simultaneous sampling. The data processing and analysis is done using home-made LabVIEW and MATLAB programs, respectively.

1.2.2 Calibration

Without loss of generality, in the following analysis we will focus on a single coordinate x of the trapped particle. The calibration of x (in meters) and the restoring force exerted by the focused beam is done following the standard methods reported in the literature [37, 38, 39]. A suitable method is chosen according to the nature of the fluid where the micron-sized particles are suspended.

Viscous fluid

We first consider the case of a spherical Brownian particle of radius r in a Newtonian fluid (e.g. water or glycerol) of known viscosity η and trapped by the focused beam. The parameters to be determined are A and the optical trap stiffness k in the x direction for small displacements ($x < r$), see equations (1.5) and (1.6). If the fluid is in thermal equilibrium with the environment (temperature T), a simple method can be implemented by means of the measurement of the spontaneous fluctuations of x [37]. For a micron-sized particle in a Newtonian fluid, the inertia and the Reynolds number are negligible (see more details in section 1.4). Then, the time evolution of the fluctuations of x can be described by the first order Langevin equation

$$\gamma \dot{x} = -kx + \zeta, \tag{1.7}$$

where $\gamma = 6\pi\eta r$ is the viscous drag coefficient of the particle in the fluid and ζ is a white noise process of zero mean and delta-correlated in time $\langle \zeta_t \zeta_s \rangle = 2k_B T \gamma \delta(t - s)$ which models the random collision of the fluid molecules with the trapped particle. By taking the Fourier transform of x

$$\hat{x}(f) = \int_{-\infty}^{\infty} x(t) e^{-2\pi i f t} \, \mathrm{d}t$$

one can compute the *power spectral density*[3] of x, defined as

$$S_x(f) = \langle |\hat{x}(f)|^2 \rangle = \langle \hat{x}(f)^* \hat{x}(f) \rangle.$$

[2] The conversion factors A and B from V to m slightly change from one sample to another because of the dependence of the He-Ne beam deflexion on the optical path travelled through the cell and the sample. Then they must be determined independently for each sample.

[3] The power spectral density quantifies the power content of a stationary signal at a given frequency.

where $\langle \ldots \rangle$ is an infinite ensemble or time average. From equation (1.7) the analytical expression of $S_x(f)$ as a function of the frequency f is

$$S_x(f) = \frac{k_B T}{\gamma \pi^2 (f^2 + f_c^2)}, \tag{1.8}$$

where the *corner frequency* f_c, defined by $S_x(f_c) = S_x(0)/2$ (see figure 1.6), is given by

$$f_c = \frac{k}{2\pi\gamma}. \tag{1.9}$$

On the other hand, the power spectral density of the unconverted voltage signal X must be related to $S_x(f)$ by

$$S_X(f) = \frac{1}{A^2} S_x(f) = \frac{k_B T}{A^2 \gamma \pi^2 (f^2 + f_c^2)}. \tag{1.10}$$

Therefore, by performing a linear fit of the experimental signal: $S_X^{-1} = af^2 + b$, the conversion factor A and the trap stiffness are given in terms of the fitting parameters a and b and the known quantities T, η and r by

$$A = \sqrt{\frac{a k_B T}{6\pi^3 \eta r}}, \quad k = \sqrt{\frac{b}{a}} 12\pi^2 \eta r, \tag{1.11}$$

Figure shows an example of this calibration procedure for a spherical silica particle ($r = 1\,\mu$m) embedded in an aqueous solution of glycerol at 60 wt % and trapped by the $\lambda = 980$ nm laser kept at a fixed power $P = 30$ mW. The experimental power spectrum of x is shown as a solid blue line whereas the Lorentzian profile (1.8) determined by the linear fit of S_X^{-1} as a function of f^2 is shown as a thick solid line. The conversion factor from X to x and the trap stiffness k are computed using equations (1.11): $A = 350$ nm V^{-1}, $k = 4.8$ pN μm^{-1}, corresponding to a corner frequency $f_c = 5.4$ Hz.

Viscoelastic fluid

The calibration of the optical trap when the particle is embedded in a viscoelastic fluid is more delicate because in general a model for the is viscoelasticity of the fluid is unkown a priori. This requires to perform an additional *active* driving of the particle to take into account its response in presence of the viscoelastic medium. In practice this is realized by driving in time the position $x_0(t)$ of the optical trap by means of the mechanical modulation of the laser beam. A feedback piezo actuator (Thorlabs DRV517) is attached to the output of the optical fiber by a spring support, as shown in figure 1.3. 1 V of DC voltage applied to the actuator results in a constant mechanical displacement $x_0 = 150$ nm of the x position of the beam focus. Then upon applying a sinusoidal voltage to the actuator $V(t) = V_0 \sin(2\pi f_d t + \phi)$ at fixed frequency f_d using

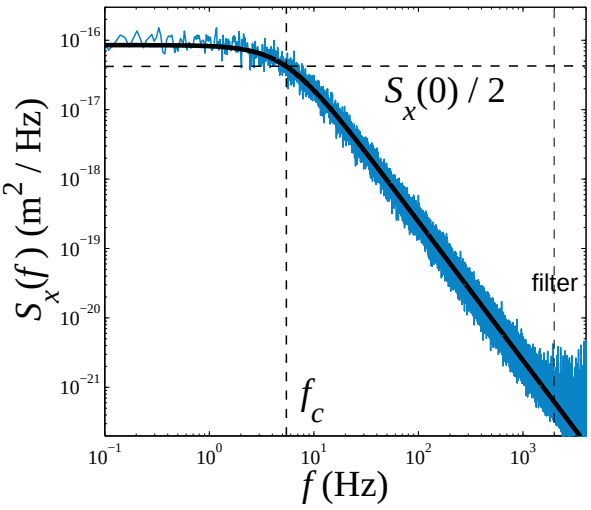

(a)

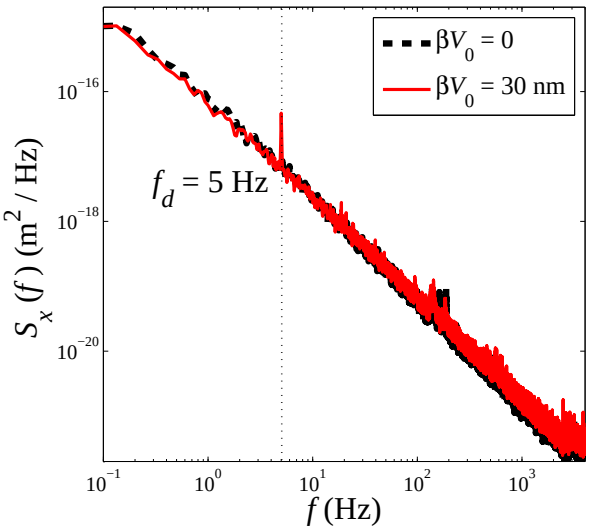

(b)

Figure 1.6: (a) (a) Power spectral density of x (blue line) for a trapped silica particle in an aqueous glycerol solution at 60 wt %. Black line: Lorentzian profile (1.8) computed using the calibration parameters $A = 350$ nm V^{-1}, $k = 4.8$ pN μm^{-1}. The vertical dashed lines show the position of the corner frequency $f_c = 5.4$ Hz and the cutoff frequency of the low-pass filter. (b) Power spectral density of a silica particle in an aqueous solution of gelatin at 10 wt %, measured without (black dashed line) and with a sinusoidal driving (red solid line) of the trap position x_0 at frequency $f_d = 5$ Hz and amplitude $\beta V_0 = 30$ nm. In both cases the particle (radius $r = 1\,\mu$m) is trapped by the $\lambda = 980$ nm diode laser focused at $h = 20\,\mu$m above the lower wall of the sample cell (see figure 1.3) at constant power $P = 30$ mW.

a waveform generator (Agilent 33220A), the position of the optical trap is driven in time as

$$x_0(t) = \beta V_0 \sin(2\pi f_d t + \phi), \tag{1.12}$$

where ϕ is the initial phase and $\beta = 150\,\mathrm{nm\,V^{-1}}$ is the conversion factor from the applied voltage to the resulting focus displacement. It can be shown that the conversion factor A from the PSD voltage signal X to x is[4]

$$A = \left[\mathrm{Re} \frac{\langle \hat{X}(f_d) \rangle}{\hat{x}_0(f_d)} \right]^{-1}, \tag{1.13}$$

where $\hat{X}$ is the Fourier transform of X measured in presence of the the sinusoidal driving x_0 at frequency f_d. On the other hand, once the parameter A is computed, for a fluid in thermal equilibrium with the environment[5] at temperature T and the trapped particle in equilibrium with the fluid, using the fluctuation-dissipation theorem (see section 2.1 of chapter 2 and [39]) the stiffness of the optical trap can be determined by the expression

$$k = 4 k_B T \frac{\mathrm{Re}\{R_L(f_d)\}}{S_x(f_d)}. \tag{1.14}$$

In equation (1.14), S_x is the power spectral density of x measured at equilibrium in absence of external driving ($x_0 = 0$) and $\mathrm{Re}\{R_L(f_d)\}$ is the real part of the active spectrum of the laser driving, defined as

$$R_L(f_d) = \mathrm{i} \frac{\langle \hat{x}(f_d) \rangle}{2\pi f_d \hat{x}_0(f_d)},$$

with $\hat{x}$ the Fourier transform of the particle trajectory driven at frequency f_d. Figure 1.6(b) shows the application of this calibration technique for a particle trapped in a viscoelastic medium: an aqueous solution of gelatin at 10 wt %. The experimental conditions of the trapping laser are the same as in figure 1.6(a) for glycerol. However, in this case due to the viscoelasticity of the medium, the power spectral density of the spontaneous fluctuations of x (black dashed line) is not Lorentzian. We also plot the spectrum (red solid line) obtained upon applying the sinusoidal driving (1.12) to the trap position x_0 at frequency $f_d = 5$ Hz and amplitude $\beta V_0 = 30$ nm. The spectra without and with the active driving of x_0 overlap at all frequencies except for $f = f_d$ at which there is a peak due to the sinusoidal excitation. Since no higher-order harmonics

[4] Strictly speaking, this expression is valid only for sufficiently large values of k. In practice the value of A obtained by this method can be checked by comparison with the value obtained by imaging: the variance of x, $\langle \delta x^2 \rangle_{\Delta t}$ must be computed over a given time window Δt obtained by image particle tracking. Then it follows that $A = \sqrt{\langle \delta x^2 \rangle_{\Delta t} / \langle \delta X^2 \rangle_{\Delta t}}$, with $\langle \delta X^2 \rangle_{\Delta t}$ the variance of the voltage signal X under the same experimental conditions.

[5] In the experiment described in chapter 5, the fluid is out-of-equilibrium but this technique is still valid if one assumes that for sufficiently short timescales, an equilibrium-like dynamics at temperature T is experimentally probed. Then this calibration method can be carried out by applying a high-frequency driving. The validity of the hypothesis is checked a posteriori.

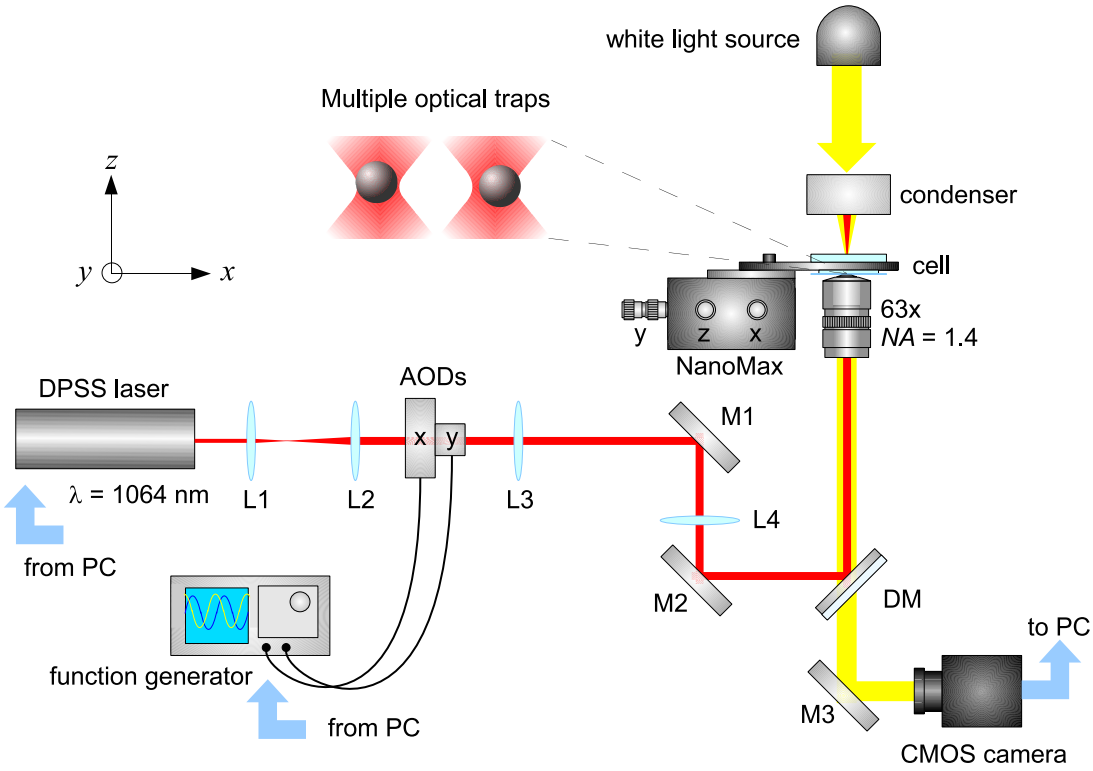

Figure 1.7: Diagram of the multiple-trap setup. L1, L2, L3 and L4 are lenses, M1, M2 and M3 mirrors and DM a dichroic mirror. See section 1.3 for a detailed explanation.

are created, we check in this way that the response of x is linear. The conversion factor from X to x, computed using equation (1.13), is $A = 260$ nm V^{-1}. The trap stiffness, computed using equation (1.14), is $k = 4.3$ pN μm^{-1}. Note that even when the laser power is the same in figures 1.6(a) and 1.6(b), the values of A and k are different because of their dependence on the refractive index of the medium.

1.3 Multi-trap setup

We now describe the second setup designed to create simultaneously multiple optical traps either static or moving in space and time. Figure 1.7 sketches this multi-trap system. A diode pumped solid state laser (Laser Quantum, Nd:YAG $\lambda = 1064$ nm) is magnified by a beam expander (lenses L1 and L2) to obtain a 2 mm diameter collimated beam. This diameter is necessary to optimize the efficiency of the XY acousto-optic deflectors (see subsection 1.3.1). The diameter of the beam which emerges from the second acousto-optic deflector output is magnified again to 10 mm and directed by two mirrors (M1 and M2) and a discroic mirror (DM) to fill completely an oil-immersion

microscope objective (Leica, 63×, $NA = 1.4$). This high-numerical-aperture objective tightly focuses the infrarred beam to the diffraction limit inside the sample cell which contains a fluid with suspended microbeads to be trapped. Similar to the single-trap system, here the cell is also fixed to a piezoelectric stage (NanoMax-TS MAX313M) by a rigid holder to avoid mechanical vibrations and to realize the trapping of the particles by the micrometric displacement of the cell in 3D. The cell is illuminated with white light by a condenser lens (focal distance $f = 23$ mm) to visualize the particles in the focal plane of the objective. Then the image is magnified by the same microscope objective. The image passes through the dicroic mirror DM and it is sent by the mirror M3 to a CMOS camera (Mikrotron MC1310) for high-speed image acquisition (see details in subsection 1.3.2). The setup is mounted on an optical table (Melles Griot) and enclosed in a Plexiglas box to avoid external mechanical vibrations and acoustic noise that would otherwise highly perturb the motion of the trapped particles. The laser power, the electric signal of the function generator sent to the XY acousto-optic deflector system and the data processing are controlled by a data acquisition board (National Instruments PXI-6259, 16-bit, 2.8 MS/s) using home-made LabVIEW programs whereas the image and data analysis is performed using MATLAB.

1.3.1 Acousto-optic deflectors

The creation of multiple independent optical traps is accomplished using an XY acousto-optic deflector (AOD) system (AA Opto-electronic). This AOD system is specially designed for a $\lambda = 1064$ nm laser. The beam trajectory can be slightly deflected by a single AOD, before being focused by the objective. As represented in figure 1.8(a), an acoustic wave is created in the crystal (TeO_2) inside the AOD by means of a piezoelectric transducer working at frequency $F = 75$ MHz. In this way the crystal acts as a diffraction grating because of the spatial variation of the refractive index. The speed of the acoustic wave in the TeO_2 crystal is $v = 650$ m s^{-1}. Consequently, at $F = 75$ MHz the beam is deflected with respect to the undeflected trajectory ($F = 0$) an angle Φ_0 given by

$$\Phi_0 = \frac{\lambda}{v} F.$$

The crystal is cut in such a way that in reality the deflected beam at the 1st diffracted order at $F = 75$ MHz emerges parallel to the incident beam from the AOD output with an efficiency $\approx 80\%$[6]. The deflexion angle can be varied in time by modulating in time the frequency of the electrical signal sent to the transducer by an arbitrary function generator (Tektronix AFG3102) an amount ΔF around F. Therefore, the final time-dependent deflexion angle with respect to Φ_0 is given by

$$\Delta\phi = \frac{\lambda}{v} \Delta F.$$

[6]The efficiency of an AOD is defined as the ratio between the intensity of the undeflected beam and the intensity of the 1st order diffracted beam, see figure 1.8(a).

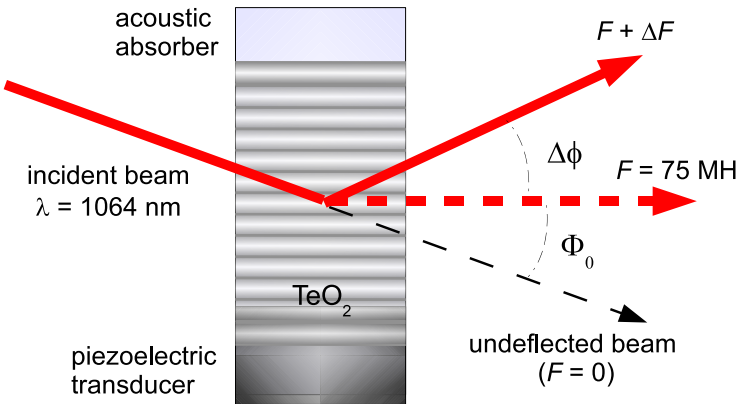

(a)

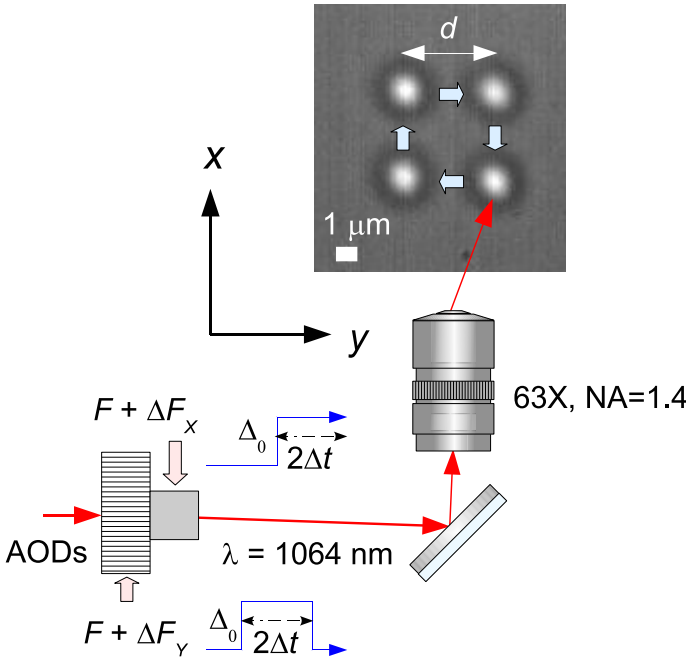

(b)

Figure 1.8: (a) Schematic representation of the deflexion of the infrarred laser beam by the spatial variation of the TeO_2 refractive index inside an AOD. The effective deflexion angle $\Delta\phi$ is controlled by the frequency $F + \Delta F$ of an acoustic wave created by a piezoelectric transducer and absorbed on the opposite side. (b) Schematic representation of the creation of 4 independent optical traps by the 2D scan of the trapping beam according to a step-like frequency modulation (1.15) of two AODs in series. The blue arrows on the snapshot indicate the actual scanning direction of the focused beam on the vertices of the square ($d = 4.5\,\mu$m).

The maximum deflexion angle of the 1st order diffracted beam that can be achieved in our experimental system is $\Delta\phi = \pm 24.6$ mrad corresponding to $\Delta F \pm 15$ MHz. In the experimental XY AOD system two AODs are coupled perpendicularly in series in the x and y directions, see figure 1.7. Then the final deflexion angle of the beam can be controlled in two dimensions through the simultaneous modulation of the frequencies ΔF_X and ΔF_Y, respectively. For a wavelength $\lambda = 1064$ nm of the trapping beam, a constant frequency modulation $\Delta F_X = 1$ MHz produces an angular deflexion $\Delta\phi = 1.6$ mrad. This results in a displacement $\Delta x = 1.65\,\mu$m of the trap position in the x (equivalently for the y direction). Then the creation of multiple optical traps can be easily realized through the high-frequency beam scan at different positions inside the sample cell. The scanning rate must be large enough in order to avoid a significant diffusive motion of the particle through the surrounding medium during the absence of the beam. For instance, figure 1.8(b) shows a snapshot of four particles trapped (in water) by means of the high-frequency scan (10 kHz) of the single $\lambda = 1064$ nm laser at four different positions on the focal plane of the trapping beam inside the sample cell. This is achieved by performing the following periodic frequency modulation of the AOD system

$$\Delta F_X(t) = \Delta_0 \Theta(t - 2\Delta t), \quad \Delta F_Y(t) = \Delta F_X(t - \Delta t), \quad 0 \leq t \leq 4\Delta t, \tag{1.15}$$

where Θ is the Heaviside step function, $\Delta t = 25\,\mu$s is the time spent by the scanning beam at each square vertex and $4\Delta t = 100\,\mu$s is the period of the modulation. During the absence of the trapping beam ($3\Delta t = 75\mu$s) each particle freely diffuses less than 6 nm in water, i.e. its Brownian motion is effectively confined by the harmonic potential created by the focused beam during the time Δt. The step frequency modulation $\Delta_0 = 2.73$ MHz corresponds to a separation distance between two adjacent optical traps of $d = 4.5\,\mu$m. This method based on a scanning laser beam is used in the experiments described in chapters 3 and 4.

1.3.2 Detection

The position of the particles trapped by the multi-trap system are dermined by image acquisition and processing. We use simple optical microscopy with a halogen lamp as the light source, as shown in figure 1.7. In order to avoid heating of the sample cell, this light is guided by a fiber. The light is focused inside the sample cell by means of a condenser lens ($f = 23$ mm) and then the contrast image of the bright particle in a dark background is magnified by the same microscope objective used to create the optical trap. The output images are detected using a high-speed CMOS camera (Mikrotron MC1310, full resolution of 1280×1024 pixels) with an adapted doubler lens. The sampling rate can be varied up to 118 frames per second at full resolution and up to 1000 frames per second in reduced frame size. Hence, the smallest measurable timescale (the time elapsed between successive positions of the particle) for this detection system corresponds to 1 ms and the highest accessible frequency is 500 Hz. The images are recorded in AVI format for further image processing. Accurate

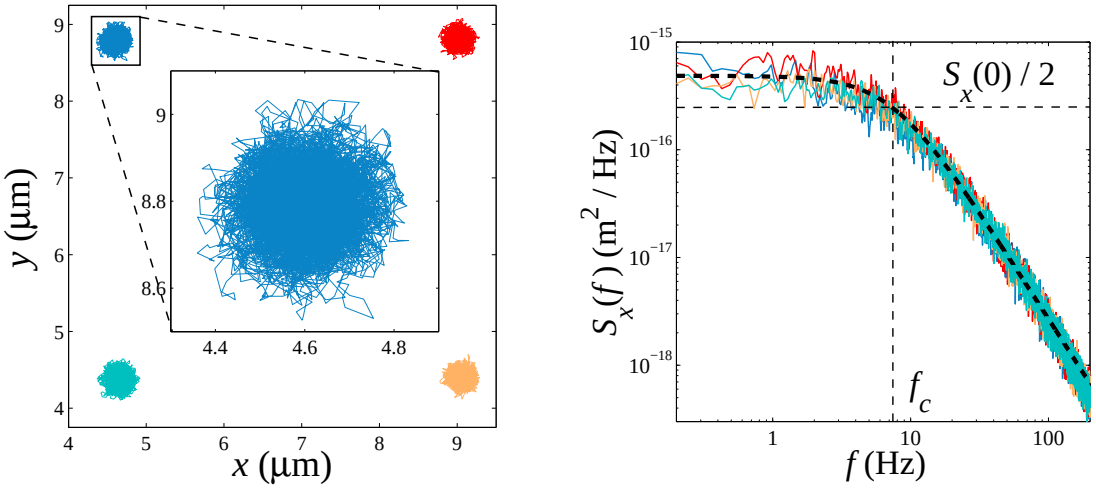

(a) (b)

Figure 1.9: (a) Examples of 2D trajectories of the four trapped particles shown in figure 1.8(b) obtained by means of the the particle tracking method of the intensity barycenter [40] for an image sampling rate of 500 frames per second. Inset: expanded view of one of the tracked trajectories. (b) Power spectral densities of the x coordinate of the four trapped particles shown in figure 1.8(b) (shown as solid lines in different colors). Thick dashed line: Lorentzian profile (1.8) computed using the calibration value $f_c = 7.5$ Hz for the corner frequency.

particle tracking is achieved using a MATLAB-based software package freely distributed for non-commercial use [40]. This software is based on a polynomial fit Gaussian weight method to locate the coordinates (x, y) of the barycenter of the intensity distribution on the image. The coordinates (x, y) correspond to the particle barycenter on the focal plane perpendicular to the direction of the laser beam propagation. The combination of this tracking method with the spatial resolution given by the camera (1 pixel = 103 nm, measured using a calibration grid with 200 lines per mm) leads to a spatial precision better than 10 nm for the tracked position of the particle. Even when the temporal and spatial resolution of this detection system are lower than that of the PSD system (subsection 1.2.1), the adventage here is that the positions of several particles can be tracked simultaneously. This can not be done with the PSD system. Besides, the resolution of the imaging procedure is enough for the experiments described in chapters 3 and 4. Figure 1.9(a) shows an example of this tracking procedure for the four trapped particles shown in figure 1.8 for an image sampling rate of 500 frames per second. The laser power is kept constant at 20 mW. Note that the Brownian motion of each trapped particle is isotropic in the xy plane due to the very low ellipticity (1:1.03) of the cross section of the trapping laser beam.

1.3.3 Calibration

We use calibration methods for the optical trap stiffness similar to those presented in section 1.2.2. The only difference here is that using the imaging technique for detection we can measure the actual particle position x (in meters). As mentioned before, using a calibration grid with 200 lines per mm placed in the focal plane of the microscope objective, we determine the conversion factor between the number of pixels on the detected image and the corresponding length in meters. We find 1 pixel = 103 nm for the experimental configuration sketeched in figure 1.7. Unlike the conversion factor A needed for the PSD system (subsection 1.2.1), the conversion factor from pixels to meters is fixed so it can be measure only once povided that the experimental setup is not modified. In this case the trap stiffness k can be also computed using equation (1.11) by means of the linear fit $S_x^{-1} = af^2 + b$. Figure shows the application of this calibration technique to the fours particles trapped by the four potential wells created by the scanning beam of figure 1.8(b) for a laser power $P = 20$ mW. As the spectra of the x coordinates of the four trapped particles are Lorentzian (1.8) and overlap, we check that the AOD frequency modulation (1.15) actually generates four harmonic potentials with the same stiffness. Then the linear fit yields the mean values $k = 0.85\,\mathrm{pN}\,\mu\mathrm{m}^{-1}$ for the trap stiffness and $f_c = 7.5$ Hz for the corner frequency. Similarly, for a viscoelastic fluid equation (1.14) can be directly used to compute k from the active measurement of R_L and the passive measurement of the power spectral density of the particle position at fixed frequency f imposed by the external driving.

1.4 Microrheology

One of the various applications of optical traps is to measure local rheological properties of tiny samples ($\sim 1\,\mu$l) of soft matter. In this kind of measurements the trapped microbeads embedded in the fluid of interest are used as mechanical probes to reconstruct the viscoelasticity of the surrounding medium. *Microrheology* is the generic term to call this kind of experimental techniques. Let us exemplify some microrheology techniques in the simplest case of a single spherical microbead. For a complete and modern review on microrheology, see reference [42].

We consider a viscoelastic fluid characterized by the *shear modulus* G. This quantity is a generalization of the concept of viscosity and accounts for energy storage and dissipation by the fluid. The shear modulus is defined as the ratio between the shear stress F/A applied to a volume of the fluid and the corresponding shear strain $\Delta x/l$ in response to the stress

$$G = \frac{F/A}{\Delta x/l},$$

as schematized in figure 1.10(a). In general G is a complex quantity. For example, for an oscillatory shear applied to the fluid at constant frequency f, the shear modulus can be splitted as

$$G(f) = G'(f) + \mathrm{i}G''(f).$$

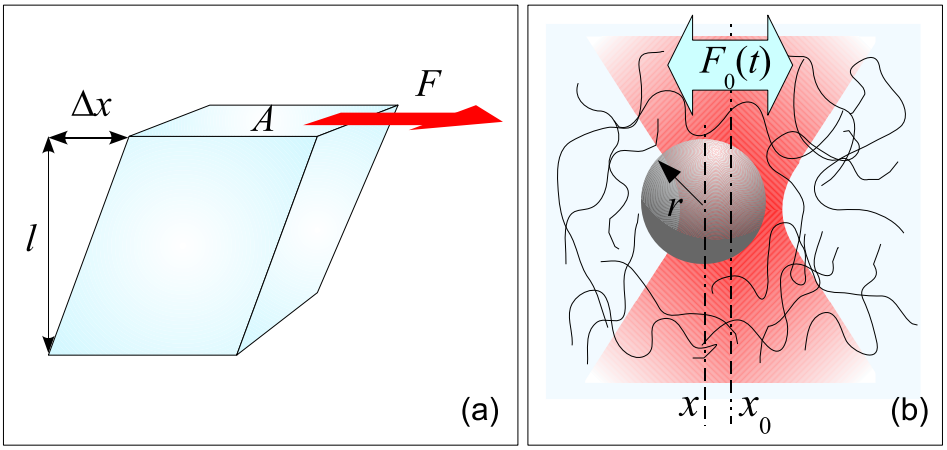

Figure 1.10: (a) Schematic representation of a shear stress applied to a viscoelastic fluid by means of a force F exerted to the upper surface A and the resulting shear strain $\Delta x/l$. (b) Schematic representation of a microrheology technique. A microbead in an optical trap is subjected to: the restoring harmonic force of the trap, the viscoelastic drag force of the surrounding fluid and the fluctuating force due to the thermal motion of the fluid microstructure (represented as filaments). An external time-dependent force $F_0(t)$ can be applied to the particle through the active driving of the trap position x_0.

The real $G'(f)$ and the imaginary $G''(f)$ parts are called the storage and the loss modulus and mesure the energy stored and dissipated by the fluid per unit volume, respectively, due to the shear. We now consider a spherical Brownian particle of radius r embedded in this viscoelastic fluid and confined by the harmonic potential of an optical trap, as represented in figure 1.10(b). For the typical acquisition frequencies in optical tweezers, inertial effects are negligible in the dynamics of the particle. For example, for a $r = 1\,\mu$m silica particle (mass $m \sim 1 \times 10^{-14}$ kg) immersed in water, the viscous drag coefficient is $\gamma \sim 1 \times 10^{-8}\,\mathrm{kg\,s^{-1}}$. Indeed, inertial effects are important only for frequencies

$$f \gtrsim \frac{\gamma}{m} \sim 1\,\mathrm{MHz},$$

very far from the frequency range accessible by the PDS system (subsection 1.2.1) or by image processing (subsection 1.3.2). On the other hand, the typical speed of the particle associated to its Brownian motion is

$$v \sim \sqrt{\frac{k_B T}{m}} \sim 100\,\mu\mathrm{m\,s^{-1}}.$$

Then the order of magnitude of the Reynolds number of a Brownian particle in water (dynamic viscosity $\eta \sim 1 \times 10^{-3}$ Pa s) is

$$Re \sim \frac{mv}{\eta r^2} \sim 10^{-3}.$$

Such a small value means that the presence of the particle does not perturb the laminar flow around it. Taking into account these two observations, the dynamics of the position x of a trapped particle in a viscoelastic fluid can be modeled by the first order Langevin equation

$$\int_{-\infty}^{t} \Gamma(t-s)\dot{x}(s)\,\mathrm{d}s = -kx(t) + F_0(t) + \zeta(t), \tag{1.16}$$

where the function $\Gamma(t-s)$, called the *memory kernel*, weights the past viscoelastic effects of the medium at time $s \leq t$ on the present motion of the particle at time t. Then the convolution of Γ with $\dot{x}$ represents the effective viscoelastic drag force acting on the particle. Taking into account that $Re \ll 1$, the Fourier transform of the memory kernel is simply related to the shear modulus $G(f)$ of the fluid by the following expression

$$\hat{\Gamma}(f) = 6\pi r \mathrm{i}\frac{G^*(f)}{2\pi f}. \tag{1.17}$$

The term $-kx$ in the Langevin equation is the harmonic force exerted by the optical trap; $F_0(t)$ represents an external time-dependen force applied to the particle; and ζ is a stochastic force of zero mean which models the random collisions of the fluid microstructure (e.g. molecules, chains, clusters) with the trapped particle. The external force is chosen depending on the nature of the fluid (equilibrium or nonequilibrium). Then, the goal of microrheology is to extract G from the measurement of x. Microrheology techniques can be classified into two categories according of the choice of the external force ($F_0(t) = 0$ or $F_0(t) \neq 0$):

1.4.1 Passive microrheology

In passive microrheology (PMR), an optical trap acts as a passive element ($F_0(t) = 0$) keeping fixed the mean position of the bead while measuring the spontaneous fluctuations of $x(t)$. This kind of technique is suitable for fluids in thermal equilibrium at constant temperature T. In such a case, the statistical properties of the stochastic force ζ in equation (1.16) are not arbitrary but they are linked to the memory kernel Γ by the fluctuation-dissipation theorem (see section 2.1). Specifically, the power spectral density of ζ satisfies the relation

$$\begin{aligned} \langle|\hat{\zeta}(f)|^2\rangle &= 4k_BT\mathrm{Re}\{\hat{\Gamma}(f)\}, \\ &= 12rk_BT\frac{G''(f)}{f}. \end{aligned} \tag{1.18}$$

On the other hand, when an external force is applied to the particle, the response of the system contains information on the shear modulus because of the fluid strain. A quantity which measures the response to small external forces is the *linear response function*. See subsection 2.1.2 for a formal definition of linear response function. The storage and loss moduli of the fluid are related to the Fourier transform $\alpha = \alpha' + \mathrm{i}\alpha''$

of the linear response function by the expressions

$$\begin{aligned} G'(f) &= \frac{1}{6\pi r}\frac{\alpha'(f)-k}{|\alpha(f)|^2}, \\ G''(f) &= -\frac{1}{6\pi r}\frac{\alpha''(f)}{|\alpha(f)|^2}. \end{aligned} \tag{1.19}$$

Since the particle is in thermal equilibrium with the fluid, the fluctuation-dissipation theorem is valid for x. Using this fact and equations (1.16) and (1.18), it can be shown that the power spectral density of x is related to the shear modulus of the fluid by

$$\langle|\hat{x}(f)|^2\rangle = \frac{2k_BT}{\pi f}\frac{6\pi rG''(f)}{[k+6\pi rG'(f)]^2+[6\pi rG''(f)]^2}.$$

Then, the imaginary part α'' can be indirectly computed from the power spectral density $\langle|\hat{x}(f)|^2\rangle$:

$$\alpha''(f) = \frac{\pi f\langle|\hat{x}(f)|^2\rangle}{2k_BT}. \tag{1.20}$$

The real part α' can be reconstructed from α'' using the the Kramers-Kronig relations

$$\alpha'(f) = \frac{2}{\pi}P\int_0^\infty \frac{\xi\alpha''(\xi)}{\xi^2+f^2}\,\mathrm{d}\xi, \tag{1.21}$$

where P stands for the principal part of the integral. Therefore the viscoelastic properties of the fluid can be completely determined by the measurement of the Brownian motion of a trap particle using equations (1.19), (1.20) and (1.21), without applying any shear stress, provided that it is in thermal equilibrium.

1.4.2 Active microrheology

Active microrheology (AMR) involves the active driving of the trapped particle by an external force ($F_0(t) \neq 0$). In the experiments presented in this thesis, F_0 is exerted by the oscillatory motion of the position x_0 of the optical trapped. This is realized using the piezo actuator in the single-trap (subsection 1.2.2) or the XY AOD system in the multi-trap setup (subsection 1.3.1). The particle displacement x is response to this time-dependent driving must be simultaneouly measured to probe the viscoelasticity of the fluid. Due to the time-dependent displacement of the trap position, the effective optical trapping force at time t is

$$-k[x(t)-x_0(t)] = -kx(t)+F_0(t),$$

where we take $F_0(t) = kx_0(t)$. From equations (1.16) and (1.17) it can be shown that the storage and loss moduli are given by the expressions

$$\begin{aligned} G'(f) &= \frac{1}{6\pi r}\left[\mathrm{Re}\left(\frac{\hat{F}_0(f)}{\langle\hat{x}(f)\rangle_{F_0}}\right)-k\right], \\ G''(f) &= \frac{1}{6\pi r}\mathrm{Im}\left(\frac{\hat{F}_0(f)}{\langle\hat{x}(f)\rangle_{F_0}}\right), \end{aligned} \tag{1.22}$$

where $\hat{x}$ and $\hat{F}_0$ are the Fourier transforms of x and F_0, respectively. The average $\langle \ldots \rangle_{F_0}$ must be computed over a large number of independent realizations of the force F_0. The ratio $\langle \hat{x}(f) \rangle_{F_0} / \hat{F}_0(f)$ in equation (1.22) is the Fourier transform of the linear response function (see subsection 2.1.2). The only restriction for equation (1.22) to be valid is that the maximum value of F_0 must be chosen small enough to avoid a nonlinear response of x because:

1) a large displacement of x_0 can push the particle barycenter out of the harmonic part of the trapping potential ($|x - x_0| \gtrsim r$);

2) a large shear strain of the surrounding fluid can induce nonlinear viscoelastic effects on the particle motion.

A general criterion is that the energy injected by the external driving must be comparable or smaller than the thermal fluctuating energy $k_B T$ provided by the fluid molecules, i.e.

$$\max\{x_0\} \lesssim \sqrt{\frac{k_B T}{k}}.$$

However, for a more precise determination of the regime where equation (1.22) is valid, the linearity between $\langle \max\{x\} \rangle_{F_0}$ and $\max\{F_0\}$ must be checked for different values of $\max\{x_0\}$ at constant k.

Note that, unlike PMR, for AMR no assumptions are made on the properties of the fluctuating force ζ of equation (1.16). Therefore this approach is valid either for equilibrium or out-of-equilibrium fluids [43]. The rheological properties of a broader class of soft materials can be probed by AM provided that the stiffness k of the optical trap is known in order to quantify the external force F_0 in equation (1.22). In chapters 4 and 5 we implement AMR to measure the time evolution of the shear modulus of two complex fluids initially prepared in a nonequilibrium state and relaxing to a solid-like phase.

Part I

Fluctuations and response around a NESS

Chapter 2

Generalized fluctuation-dissipation relations around a NESS

2.1 The fluctuation-dissipation theorem

2.1.1 Historical overview

The fluctuation-dissipation theorem has played a very important role in statistichal mechanics from the historical point of view. Indeed, the fundamental idea of relating equilibrium fluctuations with dissipation dates back to study of Brownian motion done by Einstein [44], Smolochowski [45], Langevin [46] and Perrin [47] at the beginning of the 20th century. Their work focused on the statistical description of the random motion of colloidal particles suspended in fluids, as represented in figure 2.1(a). This led to the celebrated Stokes-Einstein formula relating the diffusivity D of a Brownian particle in a fluid at temperature T with its mobility μ upon applying an external force

$$\begin{aligned} D &\equiv \lim_{t\to\infty} \frac{\langle x(t)^2\rangle - \langle x(t)\rangle^2}{2t}, \\ &= k_B T \mu, \end{aligned} \tag{2.1}$$

where $k_B = 1.38 \times 10^{-23}$ J K^{-1} is the Boltzmann constant and $x(t)$ denotes the position of the particle at time t in thermal equilibrium with the fluid. The mobility is determined slightly out of equilibrium by applying a weak external force F, measuring the resulting mean speed of the particle $\langle \dot{x}\rangle_F$ in this perturbed state and taking the ratio $\mu = \langle \dot{x}\rangle_F / F$. Hence equation (2.1) provides a direct link between the equilibrium fluctuations of the position x of the colloidal particle, quantified by D, with a response function, μ. These fluctuations are a result of the random collisions of the surrounding molecules of the fluid, that are small compared to the colloidal particle but the particle itself is small enough to perceive them. The mobility quantifies also the dissipation rate into the fluid due to the external force: it is given by the inverse of the viscous drag coefficient γ: $\mu = 1/\gamma$. For a spherical particle of radius r in a viscous fluid of

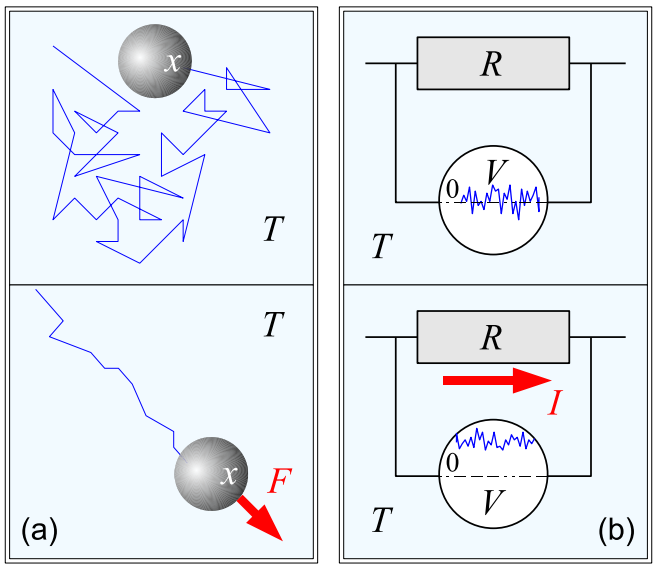

Figure 2.1: Examples of processes linked by the fluctuation-dissipation theorem (2.16): (a) Upper panel: free Brownian motion of a colloidal particle in a viscous fluid at constant temperature. Lower panel: motion of the particle dragged in the fluid by a constant external force F. (b) Upper panel: thermal voltage noise with zero mean in a resistor kept at constant temperature. Lower panel: non-zero mean voltage induced by a constant current I applied across the resistor.

dynamic viscosity η, the drag coefficient is $\gamma = 6\pi\eta r$, then equation (2.1) reads

$$D = \frac{k_B T}{6\pi r \eta}.$$

Therefore equation (2.1) represents an early fluctuation-dissipation relation for the Brownian motion derived more than a century ago.

The second representative example of a fluctuation-dissipation relation is that provided by the works of Johnson [48] and Nyquist [49] in 1928 on the thermal noise in a resistor (resistance R), see figure 2.1(b). This noise appears as a fluctuating voltage of zero mean value $\langle V \rangle = 0$ in absence of any external applied field and is generated by the thermal agitation of the electric charges in the resistor. In this case, the fluctuation-dissipation relation reads

$$\frac{\langle V^2 \rangle}{\Delta f} = 4 k_B T R, \tag{2.2}$$

where T is the temperature, $\langle V^2 \rangle$ is the mean square value of the thermal equilibrium fluctuations of V measured over a frequency bandwidth Δf. The left-hand side of equation (2.2) is measured at thermal equilibrium whereas the right-hand side is determined by perturbing the system: R measures the linear response of the mean voltage

$\langle V \rangle_I \neq 0$ induced when applying an external current I: $R = \langle V \rangle_I / I$. In analogy with the role of the mobility in Brownian motion, the resistance also quantifies the dissipation into the bath due to the external current applied to the resistor.

The particular equations (2.1) and (2.2) motivated to put the relation between spontaneous fluctuations at thermal equilibrium and dissipation (or equivalently the response) in a more fundamental context. In this way, Onsager proposed his famous *regression hypothesis*: "the relaxation of macroscopic disturbances is governed by the same laws as the regression of spontaneous microscopic fluctuations in an equilibrium system" [50]. The regression hypothesis was demonstrated some years later with the formulation of the fluctuation-dissipation theorem done in 1951 by Callen and Welton [4]. Some closely related formulae are the Green-Kubo relations [51, 52] that allow one to compute general transport coefficients (e.g. mobility, thermal conductivity, shear viscosity, etc.) from the measurement of the right equilibrium correlation functions. In the following subsections we present the standard derivation of the fluctuation-dissipation theorem for systems slightly perturbed around a thermal equilibrium state.

2.1.2 Linear response function

Before going directly into the derivation of the fluctuation-dissipation formula, we first formally specify what we mean by linear response function. We consider an observable O describing a physical quantity of the system, e.g. position, velocity, energy, etc. In general this is a function of the degrees of freedom q of the system: $O = O(q)$. We assume that this observable has a constant value O_0 when the system is unperturbed at time $s < t_0$. Then, at time $s = t_0$ we switch on a time-dependent perturbation $h(s)$ to the system so that the value of O changes from the original value O_0. The system is said to be in the linear response regime if the resulting value of the observable at time t upon applying the perturbation can be expressed as the convolution

$$O(q_t) = O_0 + \int_{-\infty}^{t} R(t-s)h(s)\,\mathrm{d}s. \tag{2.3}$$

The function R in equation (2.3) is called the *linear response function* and it takes into account the fact that the current value of O at time t depends not only on the present value of $h(t)$, but also on past values. Hence the linear response function weights the previous values of $h(s)$ on the resulting $O(q_t)$. If a system is in the linear response regime, equation (2.3) provides an operational definition of the linear response function as a functional derivative

$$R(t-s) = \left[\frac{\delta O(q_t)}{\delta h(s)}\right]_{h=0}. \tag{2.4}$$

We point out that equation (2.3) is only an approximation of the response of real physical systems. It represents an excellent approximation in the regime where the relevant degrees of freedom exhibit linear dynamics (e.g. for mechanical harmonic oscillators and RLC circuits). In such a case the response of O can be completely

characterized by the single function R. If the dynamics of the degrees of freedom is nonlinear, then one must consider the general expression of the response provided by the Volterra expansion

$$O(q_t) = O_0 + \sum_{n=1}^{\infty} \frac{1}{n!} \int_{-\infty}^{t} \dots \int_{-\infty}^{t} K_n(t-t_1, \dots, t-t_n) h(t_1) \dots h(t_n) \, \mathrm{d}t_1 \dots \mathrm{d}t_n, \quad (2.5)$$

where the kernel functions K_n are generalizations of the linear response function R that take into account nonlinear interactions in the system. In particular $R = K_1$ is the first order term in the Volterra expansion (2.5). Even when in general the response of nonlinear systems is formally expressed as a multiple nonlinear convolution, their observables can still exhibit linear response of the form (2.3) provided that the perturbation h is small enough so that the higher order terms $\mathcal{O}(h^2)$ in equation (2.5) are negligible compared to the linear order term. On the other hand, if the system is stochastic and the perturbation is small enough, then the deterministic values of $O(t)$ in equation (2.3) must be replaced by the mean values $\langle O(q_t) \rangle_h$, where $\langle \dots \rangle_h$ stands for an ensemble average performed over an infinite number of independent realizations of the same dynamical perturbation h.

In the linear response regime the function R can be determined in a straightforward way. Upon applying a delta perturbation at time $s = 0$: $h(s) = h_0 \delta(s)$, equation (2.3) directly yields the linear response function in terms of the unperturbed and perturbed mean values of the observable

$$R(t) = \frac{\langle O(q_t) \rangle_h - \langle O(q_t) \rangle_0}{h_0}, \quad h(s) = h_0 \delta(s). \quad (2.6)$$

In practice, it is always easier and more reliable to implement a Heaviside perturbation at time $s = 0$: $h(s) = h_0 \Theta(s)$, instead of a delta perturbation. The Heaviside procedure yields the *integrated* linear response function

$$\begin{aligned} \chi(t) &= \int_0^t R(t-s) \, \mathrm{d}s, \\ &= \frac{\langle O(q_t) \rangle_h - \langle O(q_t) \rangle_0}{h_0}, \quad h(s) = h_0 \Theta(s), \end{aligned} \quad (2.7)$$

defined over a time interval $[0, t]$. Then, once the integrated linear response function is determined by measuring the deviation between the perturbed and unperturbed mean values of the observable, it follows that $R(t) = \mathrm{d}\chi(t)/\mathrm{d}t$.

2.1.3 Derivation for Hamiltonian systems

We now present a simple but rather illustrative derivation of the fluctuation-dissipation formula for a system described by a set of degrees of freedom q and an unperturbed Hamiltonian $H_0(q)$. The system is in contact with a thermostat at fixed temperature

$T = (k_B\beta)^{-1}$. In this case the mean value of an observable $O(q)$ is determined by the Boltzmann distribution

$$\rho^0_{eq}(q) = \frac{\exp\left[-\beta H_0(q)\right]}{\int \exp\left[-\beta H_0(q)\right]\, \mathrm{d}q}, \tag{2.8}$$

and reads

$$\langle O(q)\rangle_0 = \int \rho^0_{eq}(q) O(q)\, \mathrm{d}q. \tag{2.9}$$

We focus on the relation between the spontaneous fluctuations of $O(q)$ with the linear response function when weakly perturbing the system. For this we now assume that from time $-\infty$ to time $t = 0$ the system is subjected to a weak external constant perturbation h such that the corresponding perturbed Hamiltonian can be written as $H_0(q) - hV(q)$, where $V(q)$ is the variable conjugate to h with respect to the energy. The perturbation is suddenly switched off at time $t = 0$, i.e.

$$h(s) = h\Theta(-s), \tag{2.10}$$

with Θ the Heaviside step function. Then the mean value of the observable for $t \geq 0$ is given by

$$\langle O(q_t)\rangle = \int \mathrm{d}q' \int \mathrm{d}q\, \rho_{eq}(q) P(q', t|q, 0) O(q'), \tag{2.11}$$

where P is the transition probability from the state at time $t = 0$ to the new state with $h = 0$ at time t and $\rho_{eq}(q)$ is the Boltzmann distribution (2.8) for the perturbed Hamiltonian $H_0(q) - hV(q)$. For a sufficiently small value of h, $\rho_{eq}(q)$ can be expressed at linear order as[1]

$$\rho_{eq}(q) = \rho^0_{eq}(q)[1 + \beta h V(q)] + \mathcal{O}(h^2). \tag{2.12}$$

Next, by inserting equation (2.12) into (2.11), one obtains the mean value of the observable after switching off the perturbation

$$\langle O(q_t)\rangle = \langle O(q)\rangle_0 + \beta h \langle O(q_t)V(q_0)\rangle_0, \tag{2.13}$$

On the other hand, using the definition of linear response function, equation (2.3) reads

$$\langle O(q_t)\rangle = \langle O(q)\rangle_0 + h\int_t^\infty R(s)\mathrm{d}s, \tag{2.14}$$

for the Heaviside perturbation (2.10) of the Hamiltonian. Then, the comparison of equations (2.13) and (2.14) implies that the linear response function R and the equilibrium correlation function $\langle O(q_t)V(q_0)\rangle_0$ are linked by the formula

$$k_B T R(t) = -\frac{\mathrm{d}\langle O(q_t)V(q_0)\rangle_0}{\mathrm{d}t}. \tag{2.15}$$

Finally, taking into account the stationarity property at thermal equilibrium:

$$\langle O(q_{t-s})V(q_0)\rangle_0 = \langle O(q_t)V(q_s)\rangle_0,$$

[1] Without loss of generality, we assume that $\langle V(q)\rangle_0 = 0$.

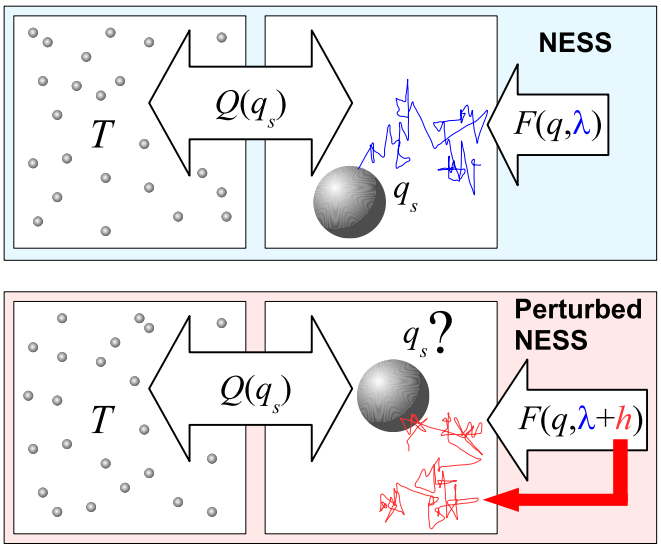

Figure 2.2: Schematic representation of the system studied in section 2.2. Upper panel: Nonequilibrium steady state of a system in contact with a thermal bath at temperature T and subjected to a total force F. Lower panel: perturbed NESS resulting from a small time-dependent variation h of the control parameters λ of the system.

equation (2.15) can be written in the general form

$$k_B T R(t-s) = \partial_s \langle O(q_t) V(q_s) \rangle_0. \tag{2.16}$$

Equation (2.16) is the general formula of the fluctuation-dissipation theorem for systems weakly perturbed around an equilibrium state.

2.2 Fluctuations and linear response around a NESS

Strictly speaking, the fluctuation-dissipation formula (2.16) is valid only to describe the linear response of systems in thermal equilibrium with a bath. This is because one of the hypothesis for its derivation is that there exists a Hamiltonian which determines the time evolution of its degrees of freedom. If such a Hamiltonian does not exist, then equation (2.16) does not necessarily hold. One example of this situation occurs when there are nonconservative forces acting on the system. In this section we focus on the case where the unperturbed system is out of equilibrium due to external nonconservative or time-dependent forces but its statistical properties are time-invariant, i.e. the system is in a nonequilibrium steady state (NESS). In a NESS, energy is constantly injected into the system by the external forces but at the same time the system irreversibly dissipates heat into the environment.

We consider a system in contact with a thermal bath at fixed temperature T. The system is described by a finite number n of microscopic degrees of freedom $q = \{q^i, i =$

$1, \ldots, n\}$, as sketched in the upper panel of figure 2.2. It can exchange an amount of heat $Q(q_s)$ with the bath which depends on the instantaneous configuration q_s at time s. In addition, it is subjected to a force F that depends on the degrees of freedom q and on the control parameters λ. This force is allowed to be time-dependent through the control parameters $\lambda(t)$ and to have a nonconservative component, i.e. it can be splitted as

$$F(q, \lambda(t)) = -\nabla U(q, \lambda(t)) + G(q),$$

where U is the potential that represents the Hamiltonian part of the dynamics. G is the nonconservative component of the force, i.e. it can not be expressed as the gradient of a potential function. The hypothesis for the formulations of the generalized fluctuation-dissipation relations are the following:

- The system is in a NESS: the probability density function of the degrees of freedom, $\rho_0(q)$, is time-invariant and the time correlation functions exhibit time-translation invariance. If the nonconservative force G is non-zero then $\rho_0(q)$ is different from the Boltzmann density $\rho^0_{eq}(q)$ of equation (2.8).

- The dynamics is Markovian, i.e. the system does not have any memory on past events. Its time evolution depends only on present values.

- The bath itself is at thermal equilibrium so the fluctuation-dissipation relation (2.16) locally holds for the degrees of freedom of the bath.

According to the previous hyphotesis, we assume that the degrees of freedom of the system exhibit diffusive dynamics, i.e. their time evolution can be modeled by a first order Langevin equation

$$\dot{q}^i = -\Gamma^{ij}\partial_j U(q) + G^i(q) + \zeta^i, \tag{2.17}$$

where Γ is a symmetric matrix which accounts for the dissipation into the bath. ζ is a stochastic process of zero mean and covariance $\langle \zeta^i_t \zeta^j_s \rangle = 2k_B T \Gamma^{ij} \delta(t-s)$ that models the random interaction with the bath. Some typical examples of real stochastic dynamics modeled by equation (2.17) are: the position of an overdamped Brownian particle driven by a moving optical trap in a fluid, the particle coordinates of a sheared colloidal suspension, the rotational degrees of freedom of a molecular motor and the voltage of a RC electronic network. We first focus on the fluctuations of an observable $O(q)$ of the system and then on the linear response function of $O(q)$ to a small external perturbation h of the control parameters λ, as depicted in the lower panel of figure 2.2. We briefly outline the physical ideas used for the derivation of the generalized fluctuation-dissipation relations (GFDRs) reported in the literature for a system with the features previously described.

2.2.1 Lagrangian formulation [20, 53]

In this approach, we consider that the mean value of an observable $O(q)$ evolves in time according to the equation

$$\partial_t \langle O(q_t) \rangle = \langle (LO)(q_t) \rangle, \tag{2.18}$$

where the linear operator L is called the generator of the process (2.17) and is explicitly given by $L = [-\Gamma \nabla U + G] \cdot \nabla + \beta^{-1} \nabla \cdot \Gamma \nabla$ for the diffusive process (2.17). The adjoint operator $L^\dagger$ determines the time evolution of the probability density of q: the Fokker-Planck equation associated to (2.17) can be written as

$$\partial_t \rho = L^\dagger \rho = -\nabla \cdot j, \tag{2.19}$$

where the probability current j is defined as

$$j = [-\Gamma \nabla U + G]\rho - \beta^{-1} \Gamma \nabla \rho. \tag{2.20}$$

Then we introduce the *mean local velocity*:

$$v = \frac{j}{\rho}, \tag{2.21}$$

which allows us to write equation (2.19) in the hydrodynamical form of an advection equation

$$(\partial_t + v \cdot \nabla)\rho = 0. \tag{2.22}$$

In general, equation (2.19) can not be solved analytically except for some special cases. For simplicity, here we focus on the situation when there is a single degree of freedom q and the system is in a NESS, then the density ρ is the time independent NESS density $\rho_0(q)$ and equation (2.19) implies that j is constant. In such a case the density and the current admit an analytical expression derived in [54] and the mean local velocity is proportional to the inverse of the NESS density:

$$v_0(q) = \frac{j}{\rho_0(q)}. \tag{2.23}$$

On the other hand, we consider a time dependent perturbation h_s to the potential starting at time $s = 0$:

$$U_s(q) = U(q) - h_s V(q), \tag{2.24}$$

In this case, the mean value of the observable can be expressed in terms of the nonstationary density of the perturbed process $\rho_t(q)$, as

$$\langle O(q_t) \rangle_h = \int \rho_t(q) O(q) \, \mathrm{d}q. \tag{2.25}$$

With the purpose to derive a GFDR from equation (2.25), a perturbative analysis must be performed to obtain an expression for ρ_t at linear order in h_s. This is done using

the expression of the generator L with the perturbation (2.24) and the expression of the current (2.20). Next, the resulting expression of $\rho_t(q)$ must be inserted in equation (2.25). Finally, taking the functional derivative of equation (2.25) with respect to h_s, a long but straightforward calculation leads to the GFDR

$$k_B T R(t-s) = \partial_s \langle O(q_t) V(q_s) \rangle_0 - \langle O(\theta_t) v_0(q_s) \partial_q V(q_s) \rangle_0. \tag{2.26}$$

Note that equation (2.26) relates the correlations measured in the unperturbed NESS with the response function like the fluctuation-dissipation relation around thermal equilibrium (2.16). However a new term appears involving a NESS correlation function with the mean local velocity v_0. Therefore it generalizes equation (2.16) so that the second term on the right-hand side of (2.26) can be regarded as nonequilibrium additive correction. This term vanishes at thermal equilibrium because in that case the current is $j = 0$. This is the so-called *detailed balance* condition. Then the GFDR (2.26) reduces to the equilibrium form (2.16).

In analogy with the simplicity gained in hydrodynamics when describing fields in the Lagrangian frame of a flow, equation (2.26) gains a simple form in the Lagrangian frame of the mean local velocity v_0 (2.23). The advection equation for the density (2.22) implies that when measuring the fluctuations and the linear reponse of the observables $\tilde{O}(\tilde{q})$ that are frozen in that frame, then they satisfy the equilibrium-like formula

$$\langle \tilde{O}(\tilde{q}_t) \tilde{V}(\tilde{q}_s) \rangle_0 = k_B T R_L(t,s), \tag{2.27}$$

where the tilde stands for the quantities measured in the Lagrangian frame and R_L is the response measured in that frame as well. Equation (2.27) is close to the equilibrium form (2.16) except for the lack of the translational time invariance because of the transformation $q \to \tilde{q}$. It can be formally shown that upon passing to the Lagrangian frame the dynamics of $\tilde{q}$ is nonstationary but it exhibits an equilibrium-like picture: the detailed balance condition holds ($j = 0$) and the corresponding probability density $\tilde{\rho}(\tilde{q})$ is invariant and coincides with the NESS density measured in the Eulerian (laboratory) frame, $\tilde{\rho} = \rho$.

2.2.2 Entropic-frenetic formulation [22, 55, 56]

A second approach to the relation between fluctuations and response around a NESS is based on symmetry properties of the fluctuations. The starting point is the description of the system in terms of the weight $\mathrm{P}(q_s)$ of space-time paths giving the state q_s of the system at time $0 \leq s \leq t$. Therefore, if the system is initially at time $s = 0$ in a NESS of density $\rho_0(q)$, the probability of finding the system in the state q_s is given by

$$\mathrm{P}(q_s) = \mathrm{P}(q_s|q_0)\rho(q_0),$$

where $\mathrm{P}(q_s|q_0)$ is a conditional path probability of q_s provided that the trajectory starts at q_0. In this way, the average of an observable $O(q)$ can be written simply as

$$\langle O(q_s) \rangle = \int_{q_s} \mathrm{dP}(q_s) O(q_s), \tag{2.28}$$

where $\int_{q_s}$ stands for the integration over all the possible paths arriving at q_s at time $s \leq t$. Now we consider the dynamical process when applying the perturbation to the potential (2.24). According to equation (2.28) the average value of the observable at time $t \geq 0$ is

$$\langle O(q_s)\rangle_h = \int_{q_s} \mathrm{dP}^h(q_s) O(q_s). \tag{2.29}$$

The weight along the perturbed trajectories P^h in equation (2.29) can be written in terms of an action A which relates P^h to the weight P^0 of the unperturbed NESS process. The action A is defined by

$$\mathrm{P}^h(q_s) = \exp[-A(q_s)]\mathrm{P}^0(q_s). \tag{2.30}$$

The central idea in this formulation is to decompose the action into a time symmetric Ψ and a time anti-symmetric Σ component:

$$A = \frac{\Psi - \Sigma}{2},$$

given respectively by

$$\Psi(q_s) = A((\theta q)_s) + A(q_s), \quad \Sigma(q_s) = A((\theta q)_s) - A(q_s). \tag{2.31}$$

In equation (2.31), θ is the time-reversal operator: $(\theta q)_s = q_{t-s}$. For diffusive processes like those modeled by equation (2.17) and for a perturbation of the form (2.24), the time symmetric term over a time interval $[0, t]$ is given by [22, 55]

$$\Psi(q_t) = \beta \int_0^t LV(q_s) h_s \mathrm{d}s. \tag{2.32}$$

Ψ is called the excess in *dynamical activity* due to the perturbation h_s. It quantifies how frenetic is the perturbed process with respect to the uperturbed one. The functional derivative of equation (2.32) with respect to h_s, $\beta LV(q)$, is called *frenesy* and can be regarded as a generalized escape rate of a stochastic trajectory of the particle from a given phase space point. In equation (2.32), LV is an observable computed by applying the generator of the process L to the variable $V(q)$ conjugate to the perturbation h with respect to the energy, see equation (2.24). On the other hand, the time anti-symmetric term is proportional to the entropy excess with respect to the unperturbed process produced by the perturbation

$$\Sigma(q_t) = \beta \left[h_t V(q_t) - h_0 V(q_0) - \int_0^t \dot{h}_s V(q_s) \mathrm{d}s \right]. \tag{2.33}$$

The derivation of the corresponding fluctuation-dissipation formula proceeds as follows. The expressions (2.32) and (2.33) are inserted in equation (2.30). Then the resulting expression for the path weight P^h is used to compute at linear order in h_s the mean

value $\langle O(\theta_t)\rangle_h$ given by equation (2.29). Finally, by taking the functional derivative of the resultant expression with respect to h_s one obtains the GFDR

$$k_B T R(t-s) = \frac{1}{2}[\partial_s \langle O(q_t)V(q_s)\rangle_0 - \langle O(q_t)LV(q_s)\rangle_0], \tag{2.34}$$

Unlike equation (2.26), this alternative GFDR does not involve explicitly the NESS density $\rho_0(q)$. It only involves dynamical quantities through the generator L. It is important to remark that this formulation is not restricted to diffusive processes in NESS. It is also valid in more general cases, i.e. systems with inertial degrees of freedom and nonstationary states, provided that the generator L is known.

2.2.3 Probability density formulation [17, 21, 24]

A third generalized approach to fluctuations and linear response around NESS exploits directly the properties of the NESS density ρ_0 with no need for a specific model of the dynamics. In this case we must consider the explicit dependence of ρ_0 on the control parameters of the system: $\rho_0(q,\lambda)$. We define a generalized potential

$$\Phi(q,\lambda) = -\ln \rho_0(q,\lambda). \tag{2.35}$$

Note that the generalized potential $\Phi(q,\lambda)$ reduces to $\beta U(\theta)$ when $\rho_0(q,\lambda)$ is the Boltzmann density (2.8), as happens with zero nonconservative forces in equation (2.17). Then, we consider the Hatano-Sasa relation, which provides a general identity for the transition between either equilibrium or nonequilibrium steady states for Markovian systems [7]. When the system is subjected to a time-dependent variation of the control parameters $\lambda(s)$ during the time interval $[0,t]$, then the Hatano-Sasa identity reads

$$\left\langle \exp\left[-\int_0^t \dot{\lambda}_\alpha(s)\frac{\partial\Phi(q_s,\lambda(s))}{\partial\lambda_\alpha}\right] \mathrm{d}s \right\rangle_\lambda = 1, \tag{2.36}$$

where the average $\langle\ldots\rangle_\lambda$ denotes the average over an infinite number of independent realizations of the dynamical process $\lambda(s)$. In order to derive a fluctuation-response relation from equation (2.36) we consider a small perturbation of the control parameter $h_s = \lambda(s) - \lambda_0$, around the value $\lambda_0 = \lambda(0)$ which fixes an initial NESS at time $s = 0$. Then, a straightforward perturbative analysis of equation (2.36) at linear order in h_s yields the generalized fluctuation-dissipation relation [21]

$$\begin{aligned} R_\rho(t-s) &= -\partial_s \left\langle \frac{\partial\Phi(q_t,\lambda_0)}{\partial\lambda}\frac{\partial\Phi(q_s,\lambda_0)}{\partial\lambda}\right\rangle_0, \\ &= -\partial_s \langle O_\rho(q_t)O_\rho(q_s)\rangle_0, \end{aligned} \tag{2.37}$$

where O_ρ is an observable fixed by the choice of the perturbation h

$$\begin{aligned} O_\rho(q) &= \frac{\partial\Phi(q,\lambda_0)}{\partial\lambda}, \\ &= -\frac{\partial \ln\rho_0(q,\lambda_0)}{\partial\lambda}, \end{aligned} \tag{2.38}$$

whereas R_ρ is the linear response function of this special observable with respect to h_s

$$R_\rho(t-s) = \left[\frac{\delta\langle O_\rho(q_t)\rangle_h}{\delta h_s}\right]_{h=0}. \tag{2.39}$$

We now contrast the structure of equation (2.37) with the previous formulations. Since this formulation is valid for any Markovian system in a NESS with no need for the system to be in contact with a thermal bath, then equation (2.37) does not involve the prefactor k_BT like equations (2.26) and (2.34). Therefore, this formulation covers a broader class of systems in NESS. On the other hand, it should be noted that the previous formulations relate the linear response of *any* observable of interest $O(q)$ due to a fixed perturbation h with correlation functions involving $O(q)$ and the observable $V(q)$ fixed by the choice of h. However, in the case of equation (2.37) there is no freedom to choose the observable of interest. The only observable appearing in this GFDR is $O_\rho(q)$, which is determined by the perturbed parameter according to equation (2.38).

We point out that it is possible to generalize equation (2.37) for the fluctuations and response of any observable $O(q)$ using a detailed version of the Hatano-Sasa identity (2.36), as demonstrated in [24]. The final GFDR for $O(q)$ reads

$$R(t-s) = -\partial_s\langle O(q_t)O_\rho(q_s)\rangle_0, \tag{2.40}$$

which involves a correlation between the observable of interest $O(q)$ and the observable $O_\rho(\lambda)$ defined in equation (2.38). As it turns out that equation (2.40) is closely related to the stochastic entropy formulation described in the following subsection, we do not present more details on its derivation.

2.2.4 Stochastic entropy formulation [23]

Finally, an alternative and unifying approach to fluctuations and linear response around a NESS for the diffusive systems that we consider in this chapter is based on *stochastic thermodynamics*. This formulation provides a conceptual framework to describe fluctuating energy exchanges taking place at thermal equilibrium or in simple nonequilibrium conditions. The fundamental idea is to extend the concepts of work, heat and entropy to single stochastic trajectories so it represents a refinement of the laws of thermodynmics. A brief overview on the main concepts of stochastic thermodynamics for overdamped diffusive processes is given in Appendix C. For a vast study on stochastic thermodynamics, see references [57, 58, 59, 60, 61, 62]. In particular, the second law of thermodynamics can be extended to a single stochastic realization q_t of a Markovian process like that model by equation (2.17) by introducing the concept of *stochastic entropy*

$$S_{st}(q_t) = -k_B \ln \rho(q_t, t). \tag{2.41}$$

In equation (2.41), $\rho(q_t, t)$ is the solution of the Fokker-Planck equation (2.19) evaluated along the stochastic trajectory q_t, hence it depends on the initial condition q_0 at time

$t = 0$. This terms accounts for the entropy produced by the stochastic time evolution of the configuration of the system. Hence, the *total* entropy production rate $\dot{S}_{tot}(q_t)$ during a single realization q_t is the sum of two contributions. The first one is the usual entropy production rate $\dot{S}_m(q_t) = \dot{Q}(q_t)/T$ associated to the instantaneous power $\dot{Q}(q_t)$ dissipated into the environment. The second contribution is the stochastic entropy production rate $\dot{S}_{st}(q_t)$:

$$\dot{S}_{tot}(q_t) = \dot{S}_m(q_t) + \dot{S}_{st}(q_t). \tag{2.42}$$

The derivation of the GFDR in the framework of stochastic thermodynamics proceeds as follows. First, the generator L^h of the diffusive process (2.17) perturbed according to equation (2.24) must be expressed at linear order in h_s in terms of the generator of the unperturbed NESS process: L: $L_s^h = L + h_s L^1$. This yields the following expression for the linear reponse function of an observable $O(q)$

$$R(t-s) = \int O(q) \exp[L(t-s)] L^1 \rho_0(q) \, \mathrm{d}q. \tag{2.43}$$

By performing a perturbative calculation of the Fokker-Planck equation (2.19) at two different NESS densities $\rho_0(q)$ and $\rho_0(q) + h\rho_1(q)$, one finds the following relation at lineat order in h

$$L\rho_1(q) = -L^1\rho_0(q).$$

On the other hand, using the definition of the stochastic entropy (2.41) we have

$$\partial_h S_{st}|_{h=0} = -k_B \rho_1(q)/\rho_0(q).$$

By inserting the previous two expressions into equation (2.43), we can readily obtain the GFDR

$$k_B R(t-s) = \langle O(q_t) X(q_s) \rangle_0, \tag{2.44}$$

where

$$X(q) = -\partial_h \dot{S}_{st}(q)|_{h=0}, \tag{2.45}$$

is the variable conjugate to the perturbation h with respect to the *stochastic entropy production rate*. It has to be noted that equation (2.44) reduces to the equilibrium fluctuation-dissipation relation (2.16) around thermal equilibrium because in such a case the *total* entropy production rate is zero $\dot{S}_{tot}(q_t) = 0$ for any stochastic trajectory q_t due to the detailed balance. Consequently, the stochastic entropy production rate is simply related to the time derivative of the potential energy: $\dot{S}_{st} = -\dot{U}/T$. Then it follows that $X(q) = \dot{V}(q)/T$, where V is the variable conjugate to h with respect to the potential energy so we recover the equilibrium formula (2.16).

2.3 Conclusion

The generalization of the fluctuation-dissipation theorem around a NESS for systems with Markovian dynamics has been achieved in recent years from different theoretical

approaches. The different GFDRs link correlation functions of the spontaneous fluctuations of the observable of interest in the unperturbed NESS with the linear response function of this observable due to a small external time-dependent perturbation. Most of the formulations involve a term which quantifies the broken detailed balance in a NESS, i.e. the presence of currents between the system and the bath. The observables involved in the different formulations (e.g. mean local velocities, dynamical activity, stochastic entropy production, etc.) are not unique but they are equivalent in the sense that they lead to the same values of the linear response function. From a fundamental point of view in statistical mechanics it is of primary importance to have a clear physical interpretation of the connection between these apparently different GFDRs. From the practical point of view this is an important issue as well because one can choose a suitable GFDR for the system of interest depending on the accessible observables in an experiment. For this purpose, in the chapter 3 we detail an experiment that allows us to get a clear physical interpretation of the connection between the different GFDRs previously described in this chapter.

Chapter 3

Brownian particle in a viscous thermal bath

In this chapter we describe an experiment in order to illustrate in a very clear way the generalization of the fluctuation-dissipation relation around nonequilibrium steady states (NESS) for systems with Markovian dynamics. In the experiment a micron-sized particle is embedded in a Newtonian fluid (water) and its Brownian motion is confined to a circular trajectory by scanning optical tweezers. A rotating laser beam exerts on the particle a periodic conservative force plus a constant nonconservative one resulting in the minimal non-trivial experimental realization of a NESS for a stochastic system with a single relevant degree of freedom. We performed independent measurements of the spontaneous NESS fluctuations of the position of the particle and the linear response function after slightly perturbing the NESS. The experimental data is analyzed in the context of the different generalized fluctuation-response formulae described in the previous chapter.

3.1 Description of the experiment

3.1.1 Sample preparation

We prepared a dilute solution (volume fraction 10^{-6}) of silica spherical particles (Polysciences Inc., radius $r = 1\,\mu$m) in ultrapure water. A small volume of this solution was introduced into a special transparent cell schematized in figure 3.1. The cell was made of a small plastic chamber (length 22 mm, width 22 mm, thickness 2.5 mm) sandwiched between a microscope slide and a coverslip and glued together with photopolymer adhesive. The chamber is made up of two reservoirs separated by a second coverslip. The reservoirs are connected by a small hole (diameter 1 mm) in this coverslip. The lower reservoir is filled with ultrapure water without beads whereas the upper reservoir is filled with the solution. The experiment was performed at room temperature

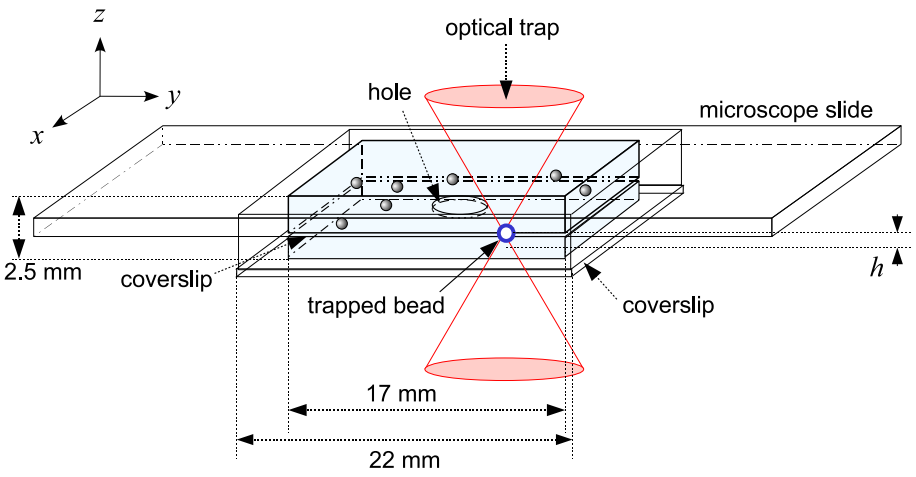

Figure 3.1: Schematic representation of the sample cell.

$T = 20.0 \pm 0.5°\text{C}$ at which the dynamic viscosity of water is

$$\eta = 1.002 \mp 0.010 \times 10^{-3}\,\text{Pa s},$$

and consequently the viscous drag coefficient and the bare diffusion coefficient of the particle are

$$\begin{aligned} \gamma &= 6\pi r\eta &&= 1.89 \times 10^{-8}\,\text{kg s}^{-1}, \\ D_0 &= \tfrac{k_B T}{\gamma} &&= 2.14 \times 10^{-13}\,\text{m}^2\,\text{s}^{-1}, \end{aligned}$$

respectively.

The cell was placed in the multi-trap setup described in chapter 1. A single spherical bead is trapped in the upper reservoir by the focused beam of the $\lambda = 1064$ nm laser. Then the bead is carefully dragged through the hole into the lower reservoir up to a distance of a few millimeters from the hole. This is in order to avoid the perturbations created by the presence of neighboring particles. In this way the experiment can be performed using the same bead for several hours. Once isolated, the particle is detected by imaging, as described in subsection 1.3.2 of chapter 1, at sampling rate of $f_s = 150$ Hz and exposure time of $1/300$ s.

3.1.2 Toroidal optical trap

The Brownian motion of a the particle trapped in the lower chamber is confined to a torus using the XY AOD system described in subsection 1.3.1. A frequency modulation is applied simultaneously to the acoustic wave created in each AOD, as represented in figure 3.2). We choose sinusoidal modulations ΔF_X and ΔF_Y in the x and y directions, respectively, given by

$$\Delta F_X(t) = \Delta F \cos(2\pi f_R t + \alpha), \quad \Delta F_Y(t) = \Delta F \sin(2\pi f_R t + \alpha), \tag{3.1}$$

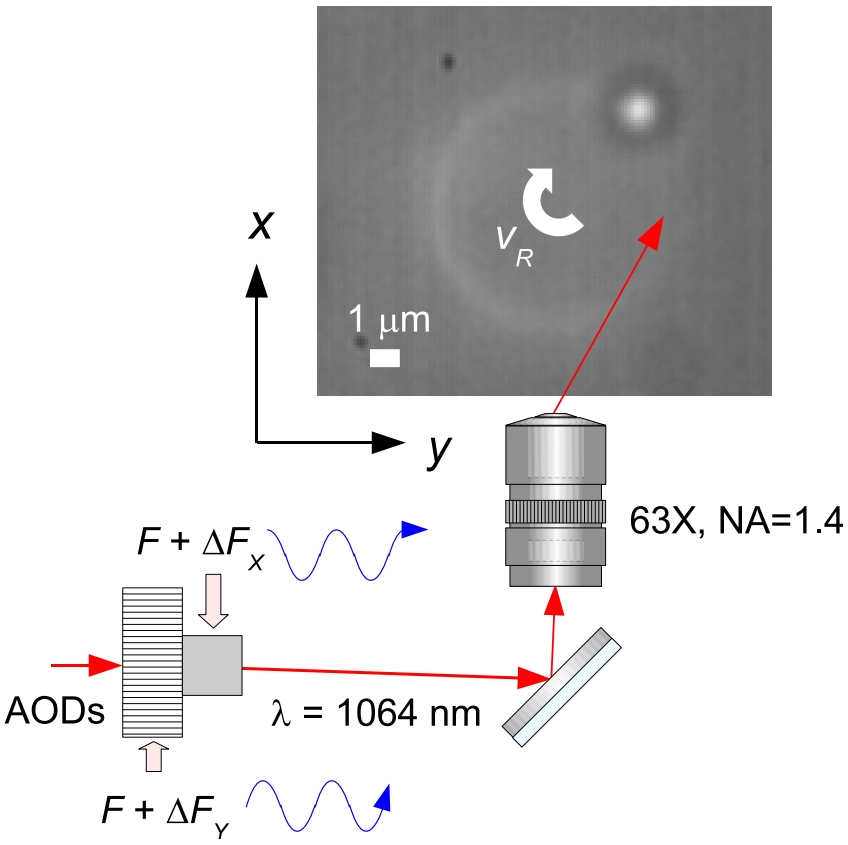

Figure 3.2: Diagram of the creation of a toroidal optical trap using the XY AOD system described in subsection 1.3.1. The red arrows represent the path of the laser beam. The snapshot shows the actual rotation direction (at speed v_R) of the scanning beam along the circular trajectory created inside the sample cell after being tightly focused by the microscrope objective.

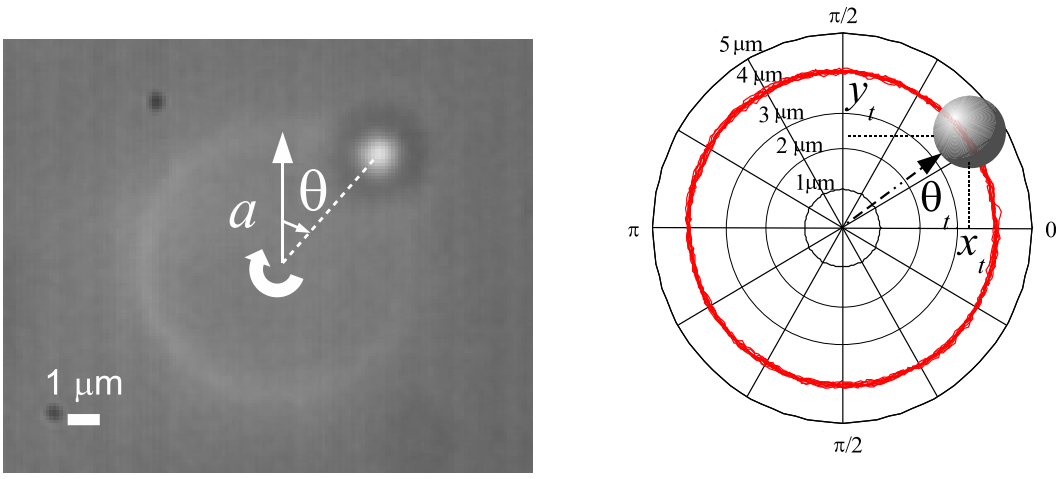

(a) (b)

Figure 3.3: (a) Snapshot of the Brownian particle in the toroidal optical trap. The vertical arrow indicates the position $\theta = 0$ whereas the curled arrow shows the direction of rotation of the scanning laser beam. (b) Example of a typical 2D trajectory (red line) on the plane of the circle described by the scanning beam for the experimental conditions (3.5), extracted using the image processing technique described in subsection 1.3.2. The instantaneous angular position θ_t is computed using equation (3.7).

where $\Delta F = 2.5$ MHz (corresponding to $\Delta\phi = 4$ mrad), f_R is the modulation frequency and α is an initial constant phase. In this way the beam focused inside the sample cell scans a circular trajectory of radius $a = 4.12\,\mu$m and angular position

$$\theta_b(t) = 2\pi f_R t + \alpha,$$

on the plane perpendicular to the beam propagation at a rotation frequency f_R. Figure 3.3(a) sketches this experimental configuration on a snapshot. The resulting rotation speed of the scanning focus along the circle of radius a is

$$v_R = 2\pi a f_R. \tag{3.2}$$

For a fixed value P of the laser power, the value of v_R is chosen according to the experimental conditions that one needs to impose to the particle by tuning the value of f_R. Three different nonequilibrium regimes occur depending on the value of v_R [63]:

(a) At small rotation speed ($v_R \lesssim 500\,\mu\mathrm{m\,s^{-1}}$ for a laser power of $P = 30$ mW), the particle is constantly dragged by the scanning optical trap along the circle at the same speed v_R. This is because the mean viscous drag force on the particle γv_R is balanced by the harmonic trapping force $k\Delta s$ so that the particle follows the trap center with a mean spatial delay $\Delta s = \gamma v_R/k$.

(b) At sufficiently large rotation frequencies ($500\,\mu\mathrm{m\,s^{-1}} \lesssim v_R \lesssim 10\,\mathrm{mm\,s^{-1}}$ for $P = 30$ mW) the speed of the scanning trap is so high that the viscous drag force exerted on the particle quickly exceeds the maximum optical trapping force $F_{max}(P)$ that can be achieved at a fixed laser power P, i.e.

$$v_R > \frac{F_{max}(P)}{\gamma}. \tag{3.3}$$

Consequently, at each rotation the beam only drags the particle a small distance δs along the circle before reaching the condition (3.3). Then the particle is released by the trap and undergoes 3D free diffusion during a time $\approx f_R^{-1}$. The beam eventually drags again the particle in the next rotation. In this regime the free-diffusion length $l_D = \sqrt{(D_0/f_R)}$ is comparable or smaller than δs so the particle moves along the circle at discrete steps δs with a mean constant speed $v_p = [\delta s/(2\pi a)]v_R < v_R$ in the direction of the beam rotation. Then the Brownian particle motion is effectively confined to a torus of major radius a and minor radius l_D. It can be shown that $\delta s \sim v_R^{-2}$ and then $v_p \sim v_R^{-1}$. Therefore as v_R increases the mean particle motion along the circle slows down and the discrete steps become smoother. This is the regime of interest for the experiment as explained in the following. Note that since $\delta s \sim v_R^{-2}$ and $l_D \sim v_R^{-1/2}$ there is a transition to a third regime dominated by diffusion ($l_D \gg \delta s$) as v_R increases.

(c) At very large rotation speed ($v_R \gtrsim 10\,\mathrm{mm\,s^{-1}}$ for $P = 30$ mW) the free diffusion of the particle during the time $\approx f_R^{-1}$ dominates over the discrete mean drag by

the scanning trap, i.e. $l_D \gg \delta s$. However the particle motion is still confined to the torus because of the radial attractive effect of the optical trap at each rotation so that it undergoes free diffusion along the circle with diffusion coefficient D_0.

The scanning laser beam is focused at $h \approx 10\,\mu$m above the inner bottom surface of the cell. At this distance, the hydrodynamic correction $\delta\gamma$ to the drag coefficient of the particle due to the presence of the coverslip surface is [64, 65]

$$\frac{\delta\gamma}{\gamma} \approx \frac{9}{16}\frac{r}{h} \approx 0.06, \tag{3.4}$$

which is small enough to neglect hydrodynamic interactions between the Brownian particle and the walls. For this value of h there is a good compromise between negligible hydrodynamic interactions and small optical aberrations of the scanning beam focus that increase as h increases. The experimental parameters

$$\begin{aligned} P &= 30\,\mathrm{mW}, \\ f_R &= 200\,\mathrm{Hz}, \\ v_R &= 5.2\,\mathrm{mm\,s^{-1}}, \end{aligned} \tag{3.5}$$

are chosen to work in the intermediate regime (b) where the particle rotates along the circle with a nonvanishing mean speed $v_p < v_R$. For these values the diffusion length of the particle and the mean displacement δs dragged by the beam at each rotation are

$$\begin{aligned} l_D &\lesssim 30\,\mathrm{nm}, \\ \delta s &\approx 18\,\mathrm{nm}. \end{aligned} \tag{3.6}$$

Since l_D is three orders of magnitude smaller than the circumference of the circle $2\pi a = 25.89\,\mu$m, the angular position of the particle barycenter θ (measured modulo 2π with respect to the circle center of the toroidal trap) is the only relevant degree of freedom of the dynamics, as shown in figure 3.3(b). The instantaneous value θ_t at time t is computed from the tracked particle coordinates (x_t, y_t)

$$\theta_t = \mathrm{arctan2}\left(\frac{y_t}{x_t}\right). \tag{3.7}$$

For the experimental values (3.5) of f_R and P, the particle moves along the circle at mean constant spead

$$v_p \approx 3.5\,\mu\mathrm{m\,s^{-1}} \ll v_R. \tag{3.8}$$

The nonequilibrium dynamics of θ_t in this experimental configuration is somehow trivial because in average it increases linearly in time (figure 3.4(a)) whereas its probability density function is uniform: $\rho(\theta) = (2\pi)^{-1}$ (figure 3.4(b)). In addition, as the dynamics of θ takes place in 1D and is stationary, the corresponding Fokker-Planck equation is

$$0 = \partial_t \rho(\theta) = -\partial_\theta j, \tag{3.9}$$

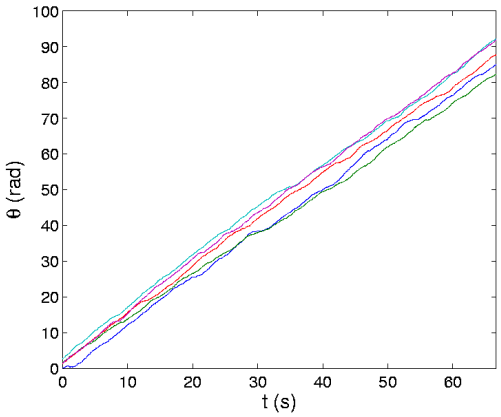

(a)

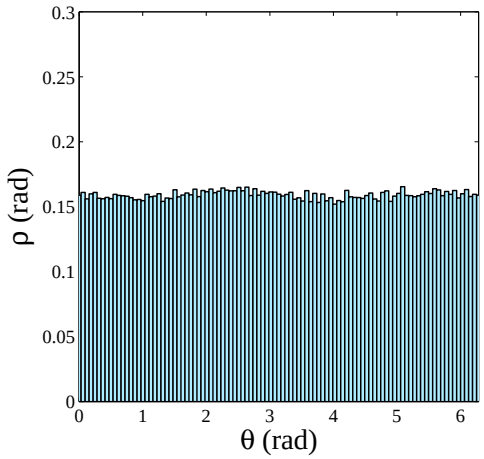

(b)

Figure 3.4: (a) Example of particle trajectories θ_t (not measured modulo 2π) showing the linear motion at mean constant speed for the experimental parameters (3.5). (b) Probability density function of the particle position when moving at mean constant speed for the experimental parameters (3.5). The experimental profile of ρ is close to the uniform distribution $\rho(\theta) = (2\pi)^{-1}$.

where j is the probability current. In general, for Brownian motion the probability current can be expressed in terms of the probability density ρ, the total force f_{tot} acting on the particle, the mobility μ and the diffusivity D, as

$$j = \mu f_{tot}\rho - D\ \nabla\rho.$$

Consequently, for the experimental conditions (3.5) the diffusive term $D\nabla\rho$ vanishes and the current is simply

$$j = \mu f_{tot}\rho. \tag{3.10}$$

From equations (3.9) and (3.10) we conclude that for constant P and f_R the probability current j and the mean value of f_{tot} are constant. This is because for a sampling frequency $f_s = 150$ Hz smaller than the rotation frequency $f_R = 200$ Hz the single discrete kicks δs at each rotation of the scanning laser can not be resolved separetely[1]. In other words, the fast particle dynamics taking place during the time $\delta s/v_R \approx 3.5\,\mu$s inside the harmonic potential of the optical trap, is coarse-grained in a time $f_s^{-1} = 6.7$ ms. Therefore the effective dynamics of θ can be simply regarded as the the result of a mean constant force f

$$\begin{aligned} f &= \langle\langle f_{tot}\rangle\rangle, \\ &= \frac{\gamma a j}{\rho(\theta)}, \\ &= \gamma v_p > 0. \end{aligned} \tag{3.11}$$

In equation (3.11), $\langle\langle \ldots \rangle\rangle$ represents the coarse-grain spatio-temporal average. Because of the periodic constraint of the particle motion on the circle, the driving force f satisfies the condition

$$\int_0^{2\pi} f\,\mathrm{d}\theta > 0. \tag{3.12}$$

Then, there does not exist any function $g(\theta)$ satisfying $f = -\partial_\theta g(\theta)$ and $g(0) = g(2\pi)$, i.e. f is *nonconservative*. The nonequilibrium nature of the system is due to the presence of this nonconservative force. Note that the value of f can be equivalently varied by tuning either f_R or P. Hence f is the single control parameter in this experimental configuration. For the experimental values (3.5), the value of the nonconservative force f estimated by means of equation (3.11) is

$$f \approx 70\,\mathrm{fN}. \tag{3.13}$$

In order to have a second independent control parameter and to create a nonlinear particle motion, the nonconservative force f is supplemented by a conservative component in the following way. The laser power is sinusoidally modulated in time

$$P(t) = P_0 + P_m \sin(2\pi f_R t + \alpha), \tag{3.14}$$

[1]Since $f_s < f_R$, aliasing due to single kick events is not a concern for the acquisition and processing of the time series θ_t.

sinchronously with the AOD frequency modulation (3.1) at f_R. In the experiment the values of the power offset P_0 and the power modulation amplitude were kept at

$$\begin{aligned} P_0 &= 30\,\mathrm{mW}, \\ P_m &= 2.1\,\mathrm{mW}. \end{aligned} \tag{3.15}$$

The position of the scanning beam evolves in time as $2\pi f_R t + \alpha$ along the circle, hence at each angular position θ on the circle the laser power does not change in time. This configuration gives rise to a static periodic intensity profile

$$I(\theta) = I_0 + I_m \sin(\theta + \alpha). \tag{3.16}$$

Since the laser intensity along the circle depends on θ according to (3.16), the effective force f which slightly drags the particle at each rotation also becomes position dependent: it is proportional to $I(\theta)$. Then

$$\begin{aligned} f(\theta) &= f_0 + f_m \sin(\theta + \alpha), \\ &= f_0 - \frac{1}{a}\partial_\theta U(\theta). \end{aligned} \tag{3.17}$$

In equation (3.17), $f_0 = const.$ is the nonconservative component due to the laser intensity offset I_0. $f_m \sin(\theta + \alpha)$ is the conservative component due to the modulation $I_m \sin(\theta + \alpha)$. This conservative component can be derived from the nonlinear periodic potential

$$U(\theta) = f_m a \cos(\theta + \alpha).$$

In this way a second independent control parameter, f_m, can be tuned by changing the power modulation amplitude P_m. A typical time series of θ_t representing the nonlinear particle motion due to the static intensity profile (3.16) obtained for the experimental values (3.15) of the power modulation (3.14) is shown in figure 3.6(b). Note that even when a potential barrier is created due to the static intensity profile of the toroidal optical trap, the particle is able to explore the whole circle because of the presence of the nonconservative force f_0 and the thermal fluctuations provided by the water molecules. Then the resulting nonequilibrium dynamics of the particle, studied in detail in the following sections, is statistically periodic and stationary with a nonvanishing probability current $j > 0$.

3.2 Model

In this section we study carefully the nonequilibrium dynamics and the statistics of the angular position of the particle θ subjected to the laser power modulation (3.14) in the toroidal optical trap. We first analyze the different relevant forces acting on the Brownian particle in the direction of θ for the experimentally accessible timescales:

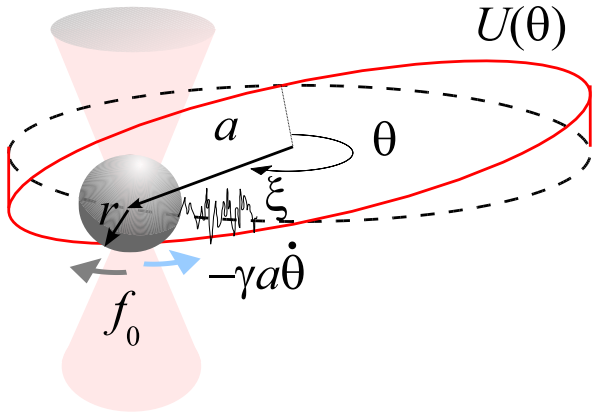

Figure 3.5: Diagram of the relevant forces acting on the Brownian particle in the toroidal optical trap: the nonconservative force f_0 (gray arrow), the viscous drag force $-\gamma a\dot{\theta}$ (blue arrow), the conservative force which derives from the periodic potential $U(\theta)$ (red solid line) and the stochastic force ξ (broken line). See text for explanation.

- The viscous drag force due to the surrounding water: $-\gamma a\dot{\theta}$. In this case one can safely use the expression $\gamma = 6\pi r\eta$ for the viscous drag coefficient of the particle because the Reynolds number of the water flow induced by the particle motion is negligible ($Re \sim 10^{-3}$, see section 1.4).
- The constant nonconservative force due to the mean "kick" done by the scanning trap at mean intensity I_0 during each rotation: f_0.
- The conservative force due to the static spatial modulation of the intensity profile (3.16): $-\partial_\theta U(\theta)/a$, where $U(\theta)$ is the corresponding periodic potential.
- The stochastic force resulting from the thermal motion of the water molecules: ζ. As hydrodynamic coupling effects between the particle and the walls are negligible and the sampling frequency of the particle motion is low enough ($f_s = 150$ Hz) to probe viscoelastic effects of water, then ξ can be modeled as a white noise process[2] of zero mean and covariance $\langle \xi_t \xi_s \rangle = 2k_B T\gamma\delta(t-s)$.

Two additional forces act on the particle motion, nevertheless they are completely negligible for the dynamics of θ for the following reasons:

- The inertial force $ma\ddot{\theta}$: the mass of the silica particle is so small ($m = 1 \times 10^{-14}$ kg) that one would need to resolve frequencies $\gtrsim \gamma/m \sim 1$ MHz in order to

[2]This model for the stochastic force ξ is based on the hypothesis that the presence of the particle and the laser does not perturb the local statistical properties of the thermal bath, i.e. detailed balance locally holds *for the water reservoir*. This hypothesis is justified by the fact that: 1) the temperature rise around the particle due to the light absorption by water is less than 1 K, 2) the Reynolds number of water due to the particle motion is negligible ($Re \sim 10^{-3}$). Therefore the water reservoir actually plays the role of an equilibrium thermal bath.

measure values of $ma\ddot{\theta}$ comparable to the viscous drag force. Then inertia is negligible in the dynamics of θ because the highest accessible frequency in the experiment is 75 Hz.

- A nonconservative force in the direction of the beam propagation due to the light scattered by the particle, as explained in section 1.1. This nonconservative force becomes significant only for the particle dynamics in the direction of the beam propagation when the trapping laser power is extremely weak ($P \lesssim 2$ mW) and when the particle is continuously trapped for several minutes, as discussed in [41]. In our experiment the particle is not continuously trapped by the scanning beam, the laser power is not small ($P_0 = 30$ mW) and we focus on a single degree of freedom on the plane almost perpendicular to the beam propagation ($\angle 89.8°$). Then this force is fully negligible for the dynamics of θ.

Then, according to the previous force picture, the dynamics of θ, restricted to the domain $[0, 2\pi)$, can be modeled by the first-order Langevin equation

$$\gamma a\dot{\theta} = -\frac{1}{a}\partial_\theta U(\theta) + f_0 + \xi, \tag{3.18}$$

as sketched in figure 3.5. Equation (3.18) can be conveniently written in the form

$$\dot{\theta} = -\partial_\theta A\phi(\theta) + F + \zeta, \tag{3.19}$$

where

$$\begin{aligned} A &= \frac{\max\{U(\theta)\}}{\gamma a^2}, \\ \phi(\theta) &= \frac{U(\theta)}{\max\{U(\theta)\}}, \\ F &= \frac{f_0}{\gamma a}, \end{aligned} \tag{3.20}$$

are the normalized potential amplitude, the dimensionless potential profile ($\max\{\phi(\theta)\} = -\min\{\phi(\theta)\} = 1$) and the normalized nonconservative force, respectively, and ζ is a white noise process satisfying

$$\begin{aligned} \langle \zeta_t \rangle &= 0, \\ \langle \zeta_t \zeta_s \rangle &= 2D\delta(t-s), \\ D &= \frac{k_B T}{\gamma a^2}, \end{aligned} \tag{3.21}$$

where $D = D_0/a^2 = 1.26 \times 10^{-2}\,\mathrm{rad}^2\,\mathrm{s}^{-1}$ is the angular diffusion coefficient along the circle for the coordinate θ. The periodic nonlinear first-order Langevin equation (3.19) has been theoretically studied in the context of simple nonequilibrium steady states for

overdamped diffusion processes[3] [54, 66]. For $F, A, D > 0$, the Fokker-Planck equation associated to (3.19) for the probability density function ρ of θ reads

$$\begin{aligned} \partial_t \rho &= -\left[F - \partial_\theta A\phi(\theta)\right] \partial_\theta \rho + D\partial_\theta^2 \rho, \\ &= -\partial_\theta j, \end{aligned} \tag{3.22}$$

where the corresponding probability current is given by

$$j = \left[F - \partial_\theta A\phi(\theta)\right] \rho - D\partial_\theta \rho, \tag{3.23}$$

At thermal equilibrium ($F = 0$) the diffusive contribution $D\partial_\theta \rho$ to the current in equation (3.23) is exactly balanced by the drift term $-\partial_\theta A\phi(\theta)\rho$ so that the detailed balance condition holds: $j = 0$. In such a case the stationary solution of equation (3.22) is given by the the Boltzmann density

$$\begin{aligned} \rho_{eq}(\theta) &= \frac{1}{Z} \exp\left[-\frac{A\phi(\theta)}{D}\right], \\ Z &= \int_0^{2\pi} \exp\left[-\frac{A\phi(\theta)}{D}\right] \mathrm{d}\theta. \end{aligned} \tag{3.24}$$

On the other hand, when the particle is driven out of equilibrium by a constant non-conservative force $F > 0$, equation (3.22) admits a stationary solution $\rho_0(\theta)$ with a constant non-zero probability current $j = \left[F - \partial_\theta A\phi(\theta)\right] \rho_0(\theta) - D\partial_\theta \rho_0(\theta) > 0$. The density $\rho_0(\theta)$ in this nonequilibrium steady state is different from the Boltzmann density $\rho_{eq}(\theta)$ of equation (3.24). The analytical expression of $\rho_0(\theta)$ was derived in [54, 67] and reads

$$\begin{aligned} \rho_0(\theta) &= \frac{1}{Z} \int_0^{2\pi} \exp\left[\frac{W(\nu,\theta)}{D}\right] \mathrm{d}\nu, \\ Z &= \int_0^{2\pi} \int_0^{2\pi} \exp\left[\frac{W(\nu,\theta)}{D}\right] \mathrm{d}\nu \, \mathrm{d}\theta, \end{aligned} \tag{3.25}$$

where $\gamma a^2 W(\nu,\theta)$ is the work performed by the deterministic forces $-A\phi(\theta)$ and F along the positively oriented path $\nu \to \theta$ on the circle

$$W(\nu,\theta) = A[\phi(\nu) - \phi(\theta)] + \begin{cases} (\theta - \nu)F & \text{for } \nu \leq \theta \\ (2\pi - \nu + \theta)F & \text{for } \nu > \theta \end{cases}, \tag{3.26}$$

whereas the analytical expression of the probability current is

$$j = \frac{D}{Z}\left[\exp\left(\frac{2\pi F}{D}\right) - 1\right]. \tag{3.27}$$

[3] When periodicity modulo 2π is not imposed ($0 \leq \theta < +\infty$), it describes the Brownian motion of a particle in a tilted potential $A\phi(\theta) - F\theta$. In such a case the probability density function of θ is not normalizable.

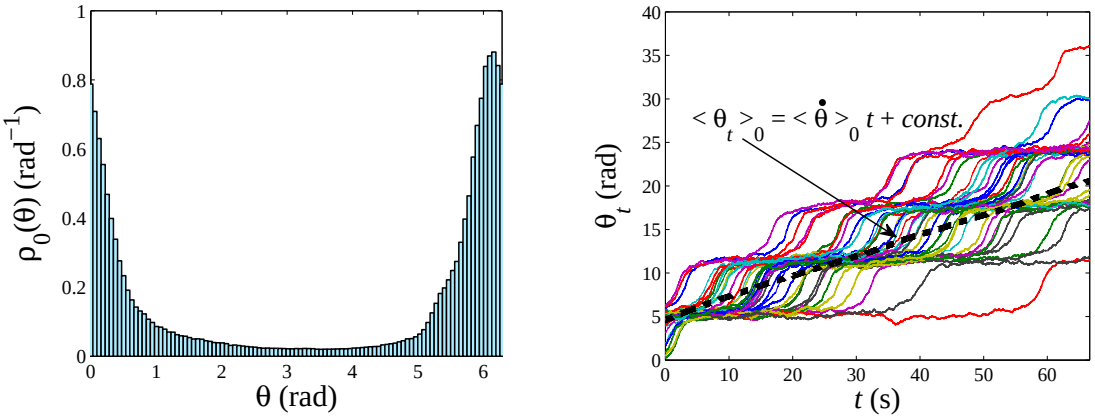

(a) (b)

Figure 3.6: (a) Probability density function ρ_0 of the angular position θ of the Brownian particle in NESS. (b) Examples of stochastic trajectories θ_t (not measured modulo 2π) used to compute the global mean velocity $\langle\dot{\theta}\rangle_0$ and the current j from the linear fit of the NESS average $\langle\theta_t\rangle_0$.

In the experiment, F and A can not be directly measured to compute $\rho_0(\theta)$ and j using equations (3.25) and (3.27), respectively. Instead, $\rho_0(\theta)$ and j can be easily determined from the tracked time series θ_t of the particle position. In figure 3.6(a) we show the experimental profile of the probability density $\rho_0(\theta)$ for the values (3.15) of the parameters of the power modulation. This was done from the histogram of θ_t computed over a time window of 66.67 s and averaged over 200 independent initial conditions. We checked that for these fixed values of P_0 and P_m, the experimental profile of $\rho_0(\theta)$ does not depend on the length of the time window used to compute the histogram provided that the whole circle $[0, 2\pi)$ is sampled. In this way the stationarity of the dynamics of θ for constant $A, F, D > 0$ was verified. Note that unlike the case of the particle dynamics at constant power ($P_m = 0$) where $\rho_0(\theta) = (2\pi)^{-1}$ (figure 3.4(a)), a very small power modulation $P_m/P_0 = 0.07$ gives rise to a highly inhomogeneous motion reflected in a large peak of $\rho_0(\theta)$. This indicates the presence of a large potential barrier of heigth $2A$ created by the laser power modulation. On the other hand, the probability current given by

$$j = \frac{\langle\dot{\theta}\rangle_0}{2\pi}, \tag{3.28}$$

where $\langle\dot{\theta}\rangle_0$ is the global mean velocity of the particle computed over a time and an ensemble average in the nonequilibrium steady state, then it has a constant value. The experimental value of $\langle\dot{\theta}\rangle_0$ was calculated from the slope of the linear fit of the mean angular position $\langle\theta_t\rangle_0 = \langle\dot{\theta}\rangle_0 t + const.$ of the particle which was obtained after averaging the 200 independent time series θ_t (not taken modulo 2π), as sketched in figure 3.6(b). The experimental value of the probability current is $j = 3.76 \times 10^{-2}\,\mathrm{s}^{-1}$.

This corresponds to a mean rotation period along the circle of $j^{-1} = 26.6$ s for the particle.

3.2.1 Calibration

We now proceed to determine the experimental values of the parameters A and F and the potential profile $\phi(\theta)$ involved in the Langevin model of equation (3.19). For this purpose we use the method described in [68] and successfully used in [69, 70, 71]. This method exploits the measured probability current j and the density $\rho_0(\theta)$ in a nonequilibrium steady state to reconstruct then actual effective energy landscape of the dynamics. Dividing equation (3.23) by ρ_0 and integrating over the interval $[0, \theta]$, one obtains an expression for the potential profile at each position $0 \leq \theta < 2\pi$ in terms of ρ_0 and j

$$A\phi(\theta) = -D \log \rho_0(\theta) + \int_0^\theta \left[F - \frac{j}{\rho_0(\theta')} \right] \mathrm{d}\theta', \tag{3.29}$$

Equation (3.29) still involves the unknown quantity F. An expression for F can be found by noting that the periodicity of the functions ϕ and ρ_0 and equation (3.29) imply: $A\phi(2\pi) = A\phi(0) = -D \log \rho_0(0) = -D \log \rho_0(2\pi)$. Then evaluating equation (3.29) at $\theta = 2\pi$

$$F = \frac{j}{2\pi} \int_0^{2\pi} \rho_0(\theta)^{-1} \, \mathrm{d}\theta. \tag{3.30}$$

The experimental value of F computed using equation (3.30)

$$F = (0.850 \pm 0.004) \, \mathrm{rad\,s^{-1}}, \tag{3.31}$$

corresponding to a nonconservative force $f_0 = 66.0 \pm 0.3$ fN, in good agreement with the rough estimate ≈ 70 fN done using equation (3.11) for the toroidal trap at constant laser power. Using the value (3.31) in equation (3.29), we obtain the experimental profile of the periodic potential $U(\theta) = \gamma a^2 A\phi(\theta)$ where the value of the normalized potential amplitude is

$$A = (0.870 \pm 0.013) \, \mathrm{rad^2\,s^{-1}}, \tag{3.32}$$

The experimental errors of F and A in (3.31) and (3.32) are estimated in the following way. We take into account that the RMS noise of the laser power used in the multi-trap setup (section 1.3) is 0.5%. As the mean force exerted by the scanning beam is proportional to the laser intensity, the main source of error ΔF for F comes from the fluctuations ΔP of the mean laser power P_m, i.e.

$$\frac{\Delta F}{F} = \frac{\Delta P}{P_m} \approx 0.005.$$

On the other hand, according to equation (3.29), the error ΔA in the computation of A depends on the experimental error $\Delta\eta/\eta = 0.01$ of the water viscosity due to the small

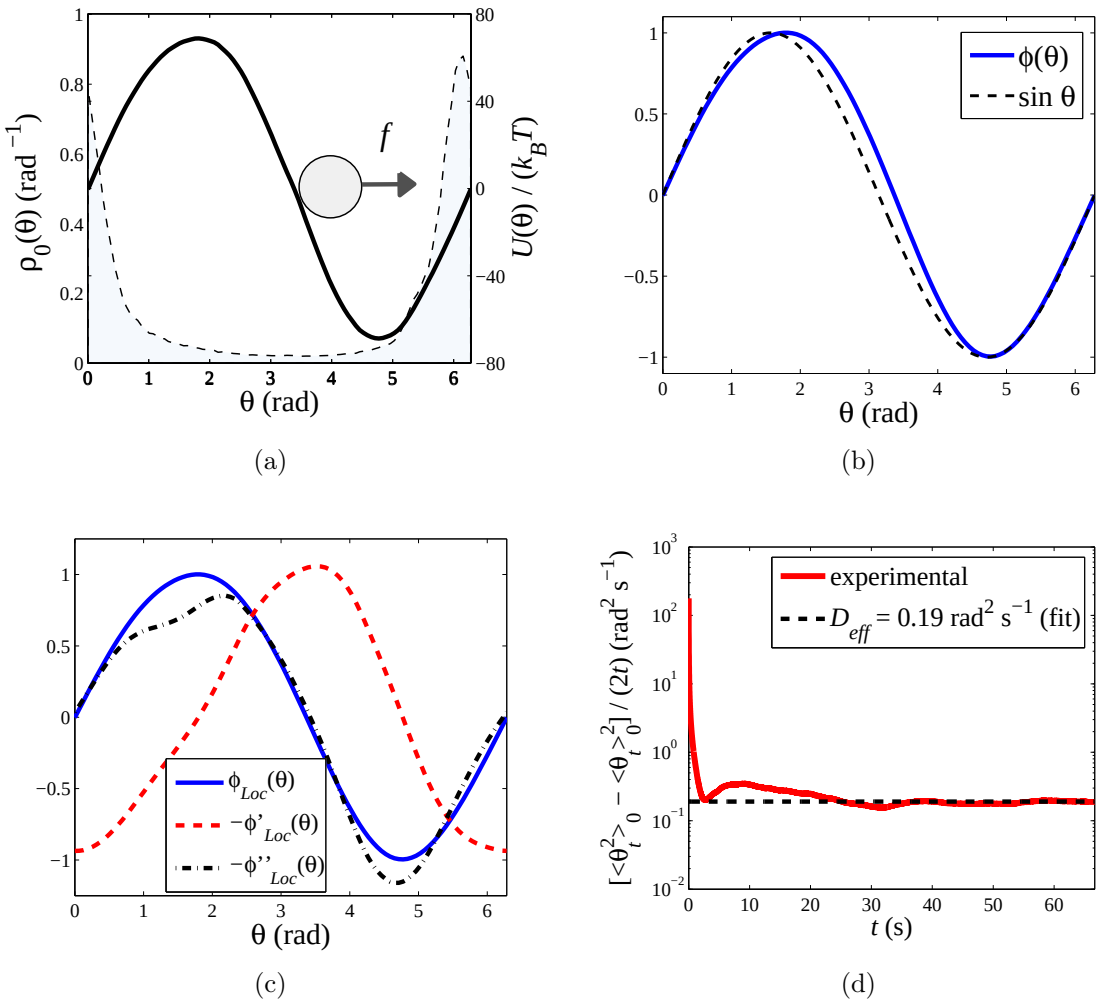

Figure 3.7: (a) Experimental potential profile (solid line) and probability density function of θ (dashed line) for the NESS generated by the nonconservative force f. (b) Dimensionless potential profile $\phi(\theta)$ compared to the sine function. (c) Third-order polynomial fit $\rho_{Loc}(\theta)$ of the potential profile $\phi(\theta)$ around each value of *theta* and its first two derivatives. (d) Effective diffusion coefficient D_{eff} of the Brownian particle in NESS (black dashed line) computed from the asymptotic value of its mean square displacement (red solid line).

temperature variation (0.5°C) during the experiment, plus the error of F. Therefore we obtain

$$\frac{\Delta A}{A} = \frac{\Delta \eta}{\eta} + \frac{\Delta F}{F} \approx 0.015.$$

In figure 3.7(a) we plot $U(\theta)$ showing that even a small sinusoidal power modulation of 7% of the mean power gives rise to a large potential barrier of several times the thermal agitation energy: $\gamma a^2 A = \max\{U(\theta)\} = (68.8 \pm 1.0) k_B T$. In addition, despite the sinusoidal form of the power modulation (3.14), the resulting dimensionless potential profile $\phi(\theta)$ is periodic but not perfectly sinusoidal as shown in figure 3.7(b). It is slightly distorted as a result of unavoidable experimental static defects, e.g. optical aberration. The non-sinusoidal distortion is more evident when computing the spatial derivatives of $\phi(\theta)$, as shown in figure 3.7(c) for the profile of the first two derivatives $\phi'(\theta)$ and $\phi''(\theta)$. These derivatives are computed from a local polynomial fit ϕ_{Loc} of ϕ around each value of $\theta \in [0, 2\pi)$. As this small static distortion is accurately quantified by the calibration method then it is not a major concern for the forthcoming data analysis. In figure 3.7(a) we plot simultaneously the NESS probability density $\rho_0(\theta)$. Note that at thermal equilibrium ($F = 0$) the particle motion would be tightly confined in a region of size $\Delta\theta = \sqrt{(k_B T/(A\gamma a^2))}$ centered around the potential minimum $\theta_m \approx 3\pi/2$ rad according to the Boltzmann density $\rho_{eq}(\theta)$ of equation (3.24). However, for the current nonequilibrium experimental conditions this maximum is shifted in the positive direction of θ by the nonconservative force $F > 0$. Besides, the particle is able to go beyond the large potential barrier and explore the whole circle due to the combined effect of the thermal fluctuations and F. Since the experimental value of the nonconservative force is slightly smaller than the maximum conservative force A: $(F - A)/A \approx -0.02$, the particle stays a long time around the maximum of the probability density ($\theta \approx 6$ rad) before completely overcoming the maximum of the potential barrier located at $\theta \approx 1.8$ rad by a sufficiently large thermal fluctuation. In this way the stochastic nature of the dynamics is highly enhanced: the effective diffusivity of the system, defined as

$$D_{eff} = \lim_{t\to\infty} \frac{\langle \theta_t^2 \rangle_0 - \langle \theta_t \rangle_0^2}{2t}, \tag{3.33}$$

is very close to its maximum value occuring at $F = A$ [72, 73]. Indeed, the experimental value of the effective diffusion coefficient defined by equation (3.33) is $D_{eff} \approx 0.19$ rad^2 s^{-1}, as depicted in figure 3.7(d). This value is 15 times larger than the value of the bare diffusion coefficient $D = 1.26 \times 10^{-2}$ rad^2 s^{-1}.

3.3 Direct measurement of linear response function

We are interested now in studying the integrated linear response function χ of the particle defined in equation (2.7), after weakly perturbing the nonequilibrium steady state previously described. For experimental simplicity we consider a step perturbation to the potential amplitude

$$A \to A + \delta A, \tag{3.34}$$

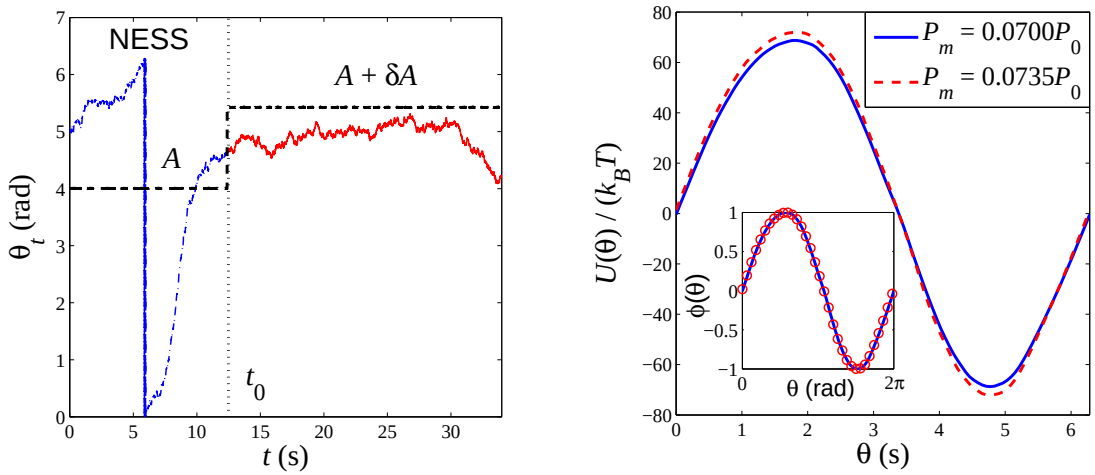

(a) (b)

Figure 3.8: (a) Example of a trajectory θ_t before (blue dotted-dashed line) and after (red solid line) applying the step perturbation (3.34) to the potential amplitude at time t_0. For $t < t_0$ the system is in an initial NESS at A whereas for $t > t_0$ it is in a nonstationary transient regime toward a new NESS at $A + \delta A$. (b) Experimental potential profiles $U(\theta)$ at two different values of the power modulation P_m keeping fixed the value of the mean power at $P_0 = 30$ mW. Inset: Dimensionless profile $\phi(\theta)$ normalized by the corresponding potential amplitude: $\gamma a^2 A = 68.8 k_B T$ (solid line) and $\gamma a^2 (A + \delta A) = 72.2 k_B T$ ($\circ$).

so that the perturbation and its conjugate variable with respect to the energy are $h = -\delta A$ and $V(q) = \phi(\theta)$, respectively. It should be noted that *the dynamics of* θ *is strongly nonlinear* as the particle undergoes the periodic potential $A\phi(\theta)$ but for sufficiently small values of δA *the response around the initial NESS* can still be linear. In the experiment, 500 times series of duration 100 s were specially devoted for the determination of χ. During each interval of 100 s the step perturbation (3.34) was implemented from time t_0 to $t_0+\Delta t$ with $0 < t_0 < 66.67$ s and $\Delta t = 33.33$ s by suddenly switching the laser power modulation P_m (3.14) from 7% to 7.35% of the mean power $P_0 = 30$ mW, as depicted in figure 3.8(a) By keeping constant P_0 during the switch we ensure that the value of F remains also constant. The experimental value of the perturbation ($\delta A = 0.05A$) is determined from independent NESS measurements of the amplitude of $U(\theta)$ at $P_m = 0.0735P_0$ and subtracting the original NESS measurement at $P_m = 0.0700P_0$ (shown in figure 3.8(b) respectively) as described in the previous section. We verify that for both values of P_m the corresponding dimensionless potential profile $\phi(\theta)$ remains unchanged so no distortion is induced by the step perturbation of the power modulation, as shown in the inset of figure 3.8(b). In this way, we extract 500 *perturbed* trajectories $\{\theta_t^{\delta A}\}$ of duration $\Delta t = 33.33$ s starting at time t_0, like that plotted in red in figure 3.8(a), randomly sampled from the initial NESS. As $\Delta t > j^{-1} = 26.6$ s, we ensure that after switching off the perturbation the system has attained a NESS before the beginning of the next step perturbation.

We focus on the measurement of the linear response of a given observable $O(\theta)$. Formally, the integrated linear response function of $O(\theta)$ at time $t \geq 0$ due to the step perturbation (3.34) starting at time $t = 0$ is given by

$$\chi(t) = \frac{\langle O(\theta_t)\rangle_{\delta A} - \langle O(\theta_t)\rangle_0}{-\delta A}. \tag{3.35}$$

In equation (3.35) the average $\langle \ldots \rangle_{\delta A}$ is performed over an ensemble of an infinite number of independent realizations of the dynamical process δA whereas the average $\langle \ldots \rangle_0$ is computed over the initial NESS distribution $\rho_0(\theta)$. Hence, some care is needed in practice because the direct computation of the experimental $\chi(t)$ using equation (3.35) exhibits a number of technical difficulties:

- First, one requires an extremely large number of independent realizations of δA to resolve χ as the perturbation $\delta A\phi(\theta)$ must be chosen very weak, typically comparable or smaller than the thermal fluctuations $\sim k_BT$ of the energy injected by the environment.

- Second, a vanishingly small Heaviside perturbation $\delta A\phi(\theta)$ to the initially unperturbed potential $A\phi(\theta)$ is ideally required. Otherwise spurious effects quickly bias the measurement of χ, specially when the system is strongly non-linear. For instance, a small error in the initial condition at t_0 may largely propagate as t increases.

For the experimental conditions (3.15) of the system the energy variation due to the perturbation is $\gamma a^2 \delta A = 3.44 k_B T$, this is small enough to be in the linear response

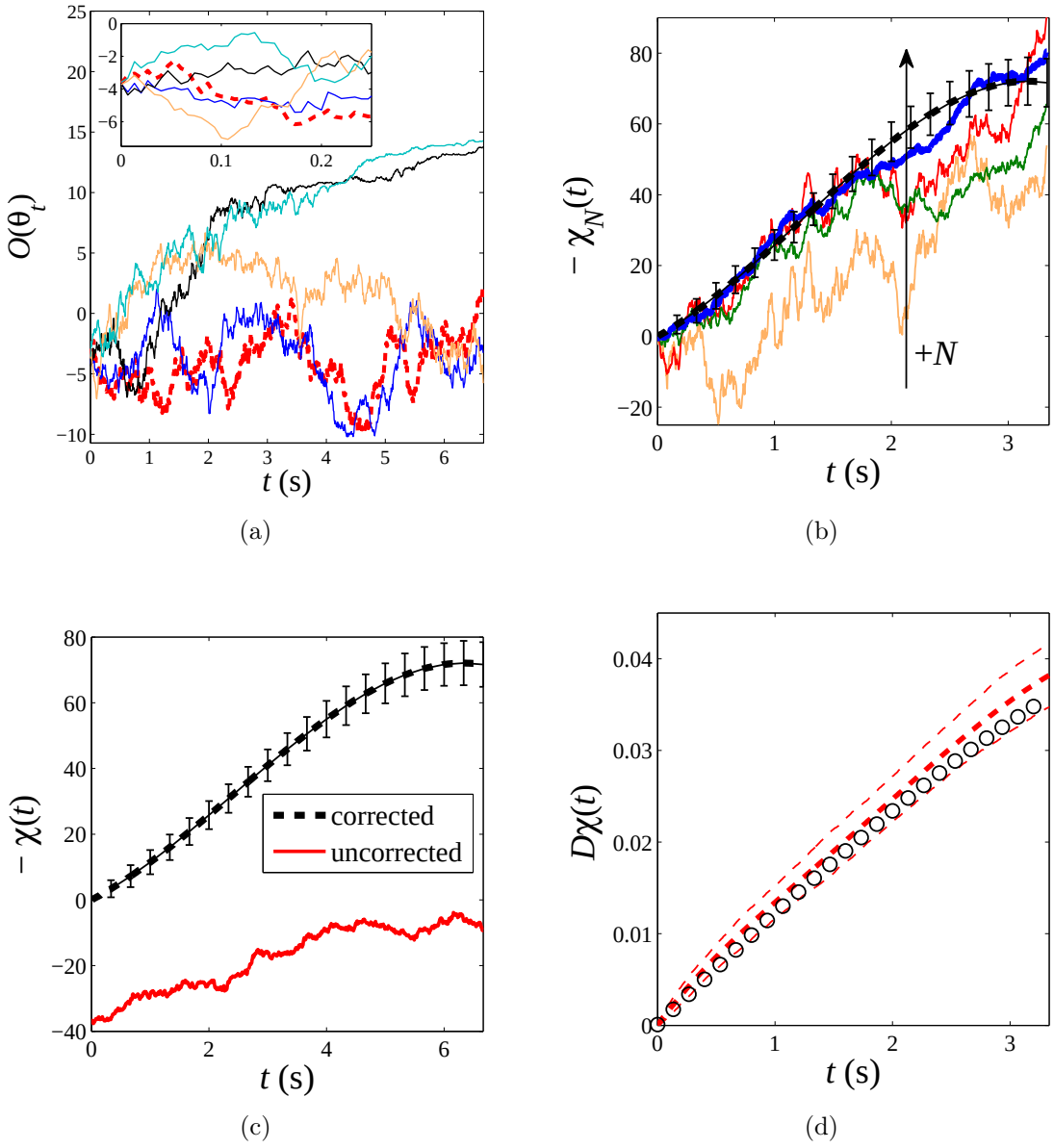

Figure 3.9: (a) Examples of a perturbed trajectory $O^{\delta A}(\theta_t)$ (red dashed line) and four unperturbed ones $O(\theta_t)$ (continuous lines) satisfying the condition (3.38) to estimate the linear response function using equation (3.37). Inset: expanded view at short time. (b) Estimate of $-\chi(t)$ by $-\chi_N(t)$ defined in equation (3.39) for $N = 50, 100, 250, 500$ and $L = 1$ (solid lines) and $N = 500$, $L = 200$ (black dashed line). (c) Comparison of $-\chi_N(t)$ for $N = 500$ and $L = 200$ (black dashed line) with the poor estimate of $-\chi(t)$ done with thecuncorrected arithmetic average (red continuous line). (d) Experimental integrated response function $\chi(t)$ of the observable $O(\theta) = \phi(\theta)$ measured upon applying the step perturbation (3.34) at two different values of δA: $\delta A = 0.05A$ (thick red dashed line) and $\delta A = -0.07A$ ($\circ$). The thin dashed lines represent the error bars.

regime, as shown further. However, since a finite number $N = 500$ of independent realizations of δA are sampled, tha average $\langle \ldots \rangle_\delta$ in equation (3.35) is not perfectly computed. Note that by definition $\chi(t)$ must satisfy the initial condition $\chi(0) = 0$ because the step perturbation starts at time $t = 0$ from an initial NESS described by the density $\rho_0(\theta)$. Then depending on the observable $O(\theta)$ the error of the initial condition $\chi(0) = 0$ may be non-negligible because the initial inhomogeneous NESS density is not properly sampled at the beginning of each realization of δA. This error can propagate because of the nonlinear dynamics of θ. In order to avoid the problem of the propagation of the initial finite sampling error, instead of using the arithmetic average $N^{-1}\sum_{j=1}^{N}(\ldots)$ to estimate the formal average $\langle \ldots \rangle_{\delta A}$ in equation (3.35), one can define an estimator $\chi_N(t)$ satisfying the initial condition $\chi_N(0) = 0$. In this way the propagation of the initial error is supressed at the beginning. An intuitive way to define χ_N can be outlined from the usual protocol to compute the integrated response function according to equation (3.35)

$$\chi(t) = \frac{\langle O^{\delta A}(\theta_t)\rangle_{\delta A} - \langle O(\theta_{t+t^*})\rangle_0}{-\delta A}. \tag{3.36}$$

In equation (3.36) $O^{\delta A}(\theta_t) \equiv O(\theta_t^{\delta A})$ denotes the observable measured during the perturbed process and in practice is computed using the perturbed times series $\{\theta_t^{\delta A}\}$. The time t^* is chosen such that $O^{\delta A}(\theta_0) = O(\theta_{t^*})$. The time $t = 0$ corresponds to the instant t_0 when the step perturbation δA is switched on. Note that equation (3.36) is justified by the fact that in the case of an infinite number of samples $\langle O^{\delta A}(\theta_0)\rangle_{\delta A} = \langle O(\theta_t)\rangle_0$ for all t because of the time translational invariance of the NESS. In contrast, when N is finite it is useful to take into account that in equation (3.36) $\langle \ldots \rangle_{\delta A}$ and $\langle \ldots \rangle_0$ are performed independently: the first on the perturbed trajectory $O^{\delta A}(\theta_t)$ and the second on the unperturbed ones $O(\theta_{t+t^*})$, specifically

$$\chi_N(t) = \frac{1}{-\delta A}\left[\frac{1}{N}\sum_{j=1}^{N} O_j^{\delta A}(\theta_t) - \frac{1}{L}\sum_{k=1}^{L} O_k(\theta_{t+t^*})\right], \tag{3.37}$$

where, for each $O^{\delta A}(\theta_t)$, L is the number of unperturbed trajectories such that

$$O_k(\theta_{t^*}) = O_j^{\delta A}(\theta_0). \tag{3.38}$$

Therefore equation (3.37) can be rewritten as

$$\chi_N(t) = \frac{1}{-\delta A}\frac{1}{N}\sum_{j=1}^{N}\left[\frac{1}{L}\sum_{k=1}^{L}\delta O_{jk}(\theta_t)\right], \tag{3.39}$$

where $\delta O_{jk}(\theta_t) \equiv O_j^{\delta A}(\theta_t) - O_k(\theta_{t+t^*})$ is the instantaneous difference between a perturbed trajectory $O_j^{\delta A}(\theta_t)$ and an unperturbed one $O_k(\theta_{t+t^*})$. An example of this procedure is depicted in figure 3.9(a) for the observable $O(\theta) = -\partial_A \ln \rho_0(\theta)$. We focus here on this observable because the normalization of the NESS density ideally implies

that $\langle O(\theta)\rangle_0 = 0$. Then, according to equation (3.36) it is strongly subjected to the propagation of the initial error if the estimate of $\langle O(\theta_t)\rangle_0$ at $t = 0$ is poor. For a given perturbed trajectory $O_j^{\delta A}(\theta_t)$ (thick dashed red line) obtained after performing δA, one must look for an unperturbed trajectory $O_k(\theta_{t+t^*})$ such that $O_j^{\delta A}(\theta_0) = O_k(\theta_{t^*})$ like those shown by solid lines.

In this way $\delta O_{jk}(\theta_0) = 0$ by construction and the estimator defined by equation (3.37) satisfies the initial condition $\chi_N(0) = 0$. Moreover, for $N, L \to \infty$, $\chi_N(t)$ converges to $\chi(t)$ defined by equation (3.35) because the conditional average over the L unperturbed trajectories in equation (3.39) converges to the NESS average $\langle \ldots \rangle_0$. In figure 3.9(b) we show $\chi_N(t)$, computed using equation (3.39), for different values of N and fixed $L = 1$ (solid lines) and $L = 200$ (dashed line), for the observable $O(\theta) = -\partial_A \ln \rho_0(\theta)$. As N increases for $L = 1$ the curves converge to a single profile which must correspond to that of $\chi(t)$ ideally given by equation (3.35). The additional condition average done for $L = 200$ smoothes the slightly fluctuating profile for $N = 500$ and $L = 1$ (thick solid blue line) resulting in the thick dashed solid line. Besides, the subensemble of 200 unperturbed trajectories allows one to estimate the statistical error of the computation of $\chi(t)$ through the standard deviation, as shown by the error bars $\pm\sigma_\chi(t)$ in figures 3.9(b) and 3.9(c). For comparison we plot in figure 3.9(c) the raw estimate of $\chi(t)$ using directly the arithmetic average $N^{-1}\sum_{j=1}^{N}(\ldots)$ to compute $\langle \ldots \rangle_{\delta A}$ in equation (3.35) for the same $N = 500$ perturbed trajectories $O_j^{\delta A}(\theta_t)$ without correcting the effect of the initial sampling. In this case the propagation of the initial error of $\chi(0)$ gives rise to a very poor estimate of the integrated response function for $t > 0$.

Finally we check whether for the finite perturbation $\delta A = 0.05A$ the response of the system around the NESS is linear. Two different measurements of $\chi(t)$ at $\delta A = 0.05A$ and $\delta A = -0.07A$ were performed following the numerical protocol previously described. In figure 3.9(d) we show the results for the observable $O(\theta) = \phi(\theta)$. Within the experimental error bars $\pm\sigma_\chi(t)$ the experimental integrated response function $\chi(t)$ is the same. The independence of $\chi(t)$ with respect to δA experimentally demonstrates that the system is actually in the linear response regime with respect to δA at least for $|\delta A| \leq 0.07A$.

As we have studied in detail how to estimate correctly the linear response function using a finite number of data, we can now analyze its relation with the fluctuations of the corresponding observable measured in the nonequilibrium steady state.

3.4 Generalized fluctuation-dissipation relations

3.4.1 Lagrangian approach

We first study the relation between the fluctuations of a periodic observable in the NESS and the linear response function around this NESS in the context of the Lagrangian approach described in subsection 2.2.1. This formulation is based on the concept of

local mean velocity, defined by

$$v_0(\theta) = \frac{j}{\rho_0(\theta)}. \tag{3.40}$$

The comoving frame of $v_0(\theta)$ represents the Lagrangian frame of the probability flow, in analogy with a real hydrodynamic flow. For the particle in the toroidal optical trap, $v_0(\theta)$ corresponds to the mean velocity of the particle at a given position θ on the circle. In other words, $v_0(\theta)$ is given by the conditional average of the instantaneous velocity of the particle $\dot{\theta}$ provided that the particle is located at θ: $v_0(\theta) = \langle\dot{\theta}|\theta\rangle_0$. In figure 3.10(a) we plot the experimental mean local velocity as a function of θ for the nonequilibrium steady state described in section 3.2. $v_0(\theta)$ can be readily determined from the direct measurement of j and $\rho_0(\theta)$ using equation (3.40). Since v_0 is proportional to the inverse of ρ_0, it attains its maximum value where ρ_0 is minimum corresponding to the the position on the circle that is rarely explored because the particle moves very fast. Conversely, v_0 reaches its minimum where the motion slows down and the particle stays pinned longtime around the maximum of ρ_0, before being activated by: 1) a sufficiently large thermal fluctuation or 2) more likely by a series of small fluctuations acting in the same direction.

We focus on the fluctuations of the periodic observable $O(\theta) = \phi(\theta)$ which is proportional to the potential energy $U(\theta)$ of the particle in the toroidal optical trap: $\phi(\theta) = U(\theta)/(\gamma a^2 A)$. At thermal equilibrium the mean value of this observable would be $\langle\phi(\theta)\rangle_{eq} = -1 + k_B T/(2\gamma a^2 A) = -0.993$ which corresponds to the average potential energy of the particle in the minimum of the potential well with depth $U_0 = \gamma a^2 A$ given by the equipartition relation $\langle U(\theta)\rangle_{eq} = -U_0 + k_B T/2 = -68.3 k_B T$. However, due to the nonequilibrium conditions of the system the experimental value of the NESS average is $\langle\phi(\theta)\rangle_0 = -0.068$ corresponding to an average potential energy $\langle U(\theta)\rangle_0 = -4.7 k_B T$.

The fluctuations of $\phi(\theta)$ can be characterized by the two-time autocorrelation function, defined by the NESS average $\langle\ldots\rangle_0$ as

$$\begin{aligned} C_0(t) &= \langle\phi(\theta_0)\phi(\theta_t)\rangle_0, \\ &= \langle\phi(\theta_u)\phi(\theta_{u+t})\rangle_0, \end{aligned} \tag{3.41}$$

where the initial time u in the second equality can be chosen arbitrarily because of the stationarity of the system. Then, in practice, an additional time average of equation (3.41) is performed over a time window $[0, t_{max}]$ [4] in order to improve the statistics of the autocorrelation function of $O(\theta)$

$$C(t) = \frac{1}{t_{max}} \int_0^{t_{max}} \langle\phi(\theta_u)\phi(\theta_{u+t})\rangle_0, \mathrm{d}u. \tag{3.42}$$

The experimental profile of $C(t)$ is plotted in figure 3.10(b). It exhibits oscillations due to the periodicity of the observable $O(\theta)$ and it decays in a timescale of the order of the

[4] The only restriction in the choice of t_{max} is that the ensemble of averaging intervals $[\theta_0, \theta_{t_{max}}]$ must cover the whole circle $[0, 2\pi)$ to sample correctly the steady state.

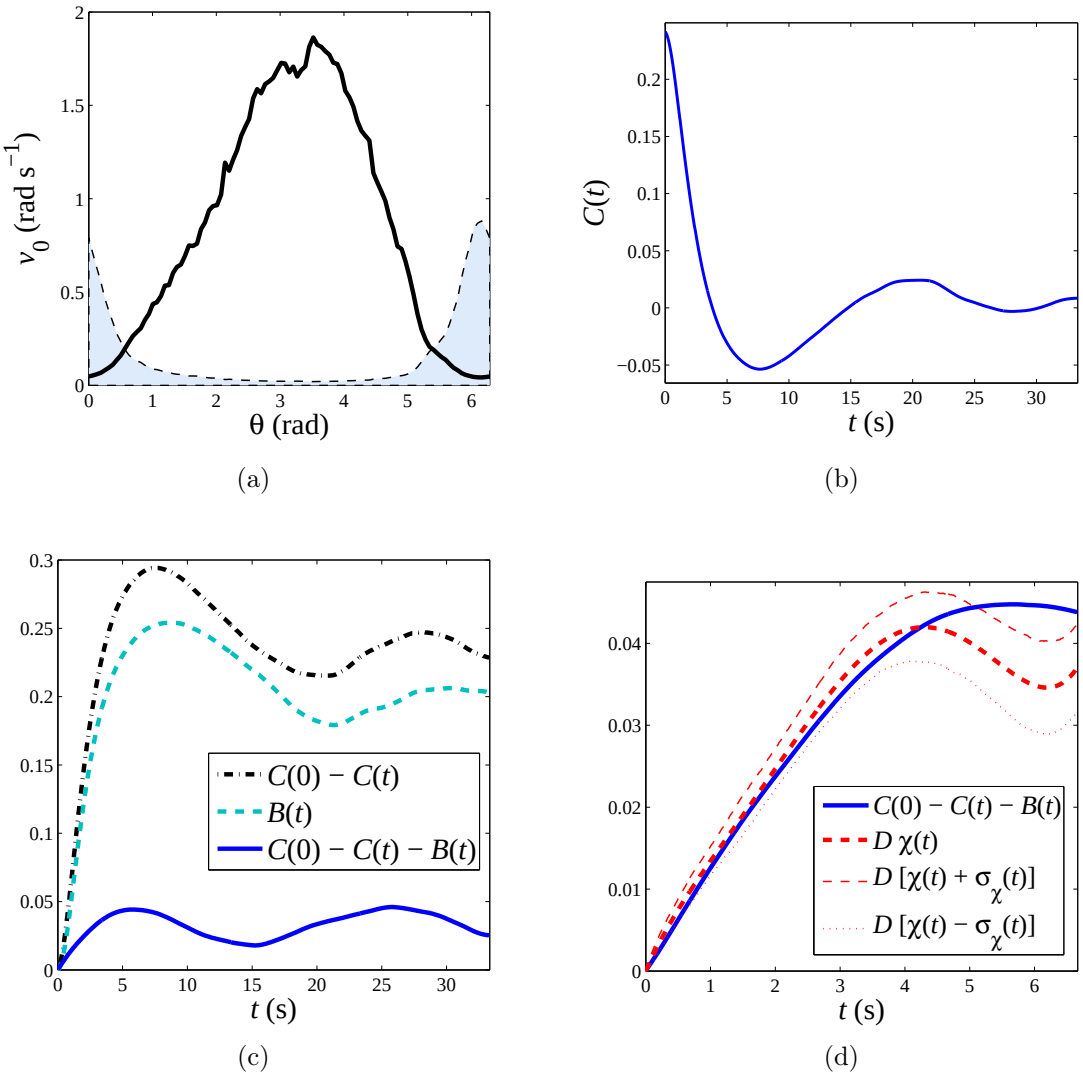

Figure 3.10: (a) Mean local velocity v_0 (solid line) and NESS density ρ_0 (dashed line) as functions of θ. (b) Autocorrelation function of the observable $O(\theta) = \phi(\theta)$ as a function of the time lag t. (c) Comparison between the different terms on the left hand side of equation (3.43) involving spontaneous NESS fluctuations. (d) Comparison between the experimental left-hand side and right hand-side of the theoretical modified fluctuation-dissipation relation (3.43).

mean rotation period of the particle: $\tau_r \sim j^{-1} = 26.6$ s. Because of the presence of the nonvanishing current j the particle motion becomes strongly correlated: the relaxation timescale of the fluctuations of $O(\theta)$ is much larger than the relaxation time that would be observed at thermal equilibrium. In such a case one would obtain $\tau_r = (2A/\text{rad}^2)^{-1}$ $= 0.57$ s.

Next, we establish the connection between the spontaneous NESS fluctuations of $O(\theta)$ characterized by $C(t)$ with the linear response function $\chi(t)$ of $O(\theta)$ at time $t \geq 0$ after performing the dynamical step perturbation of the potential amplitude A at time $t = 0$, as described in Subsection 2.2.1. According to the Lagrangian formalism, the integral version of the modified fluctuation-response relation (2.26) for the observable $O(\theta)$ when following this procedure reads

$$C(0) - C(t) - B(t) = D\chi(t). \tag{3.43}$$

The term $B(t)$ in equation (3.43) is given by

$$\begin{aligned} B(t) &\equiv \int_0^t b(t-s)\,\mathrm{d}s, , \\ &= \int_0^t \langle O(\theta_t) v_0(\theta_s) \partial_\theta \phi(\theta_s) \rangle_0 \,\mathrm{d}s, \end{aligned} \tag{3.44}$$

and takes into account the violation of the usual fluctuation-dissipation theorem around thermal equilibrium due to the broken detailed balance for NESS, reflected in the mean local velocity v_0. Then $B(t)$ can be regarded as a nonequilibrium corrective term of the fluctuation-dissipation theorem so that at thermal equilibrium $B(t) = 0$. Note that this corrective term must be measured in the unperturbed NESS. To determine $B(t)$ for the observable $O(\theta) = \phi(\theta)$ in the current nonequilibrium experiment we first compute the correlation function $b(t-s) = \langle \phi(\theta_t) v_0(\theta_s) \partial_\theta \phi(\theta_s) \rangle_0$ in equation (3.44) using the instantaneous values of the mean local velocity shown in figure 3.10(a). The instantaneous values of the spatial derivative $\partial_\theta \phi(\theta)$, which is a slightly distorted cosine function, is accurately computed using the polynomial fit of figure 3.7(c). In figure 3.10(c) we plot the resulting experimental profile of $B(t)$ using equation (3.44) where an additional average over a time window $[0, t_{max}]$ like in equation (3.42) was also performed because of the stationarity of the particle dynamics. As expected, due to the far from equilibrium conditions of the NESS experiment, the corrective term $B(t)$ is non-negligible compared to $C(0) - C(t)$: both are of the same order of magnitude for all $t \geq 0$. Then the difference $C(0) - C(t) - B(t)$, which represents and indirect measurement of the linear response function according to equation (3.43), is one order of magnitude smaller than the terms $C(0) - C(t)$ and $B(t)$ separately, as shown in figure 3.10(c). On the other hand, we perform the direct measurement of the integrated response function $\chi(t)$ for the observable $O(\theta) = \phi(\theta)$ computed following the dynamical procedure described by equation (3.39). The comparison between the right hand side and the left hand side of equation (3.43) is shown in figure 3.10(d), for the time lag interval $0 \leq t \leq 6.67$ s. As expected, the equilibrium-like relation

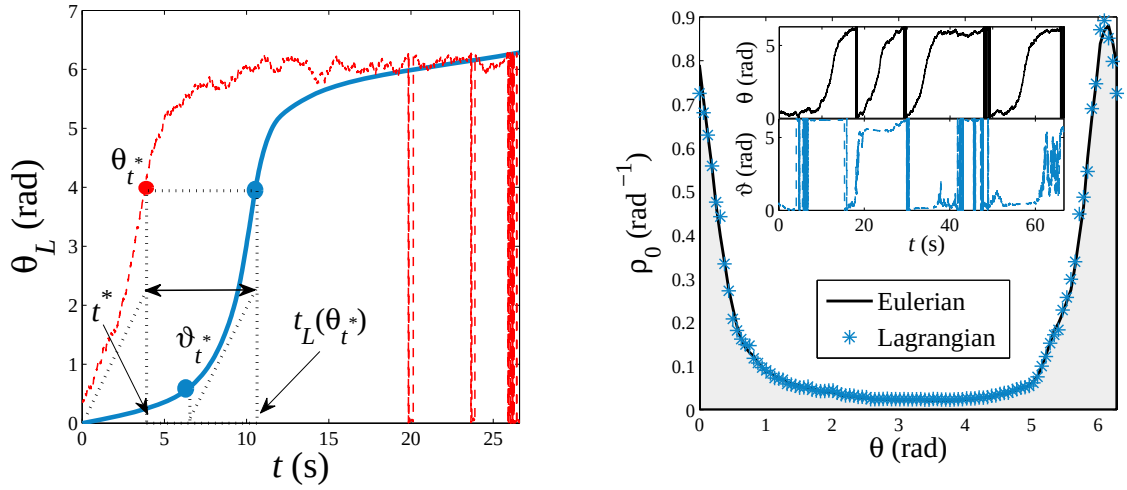

(a) (b)

Figure 3.11: (a) Lagrangian trajectory θ_L (blue solid line) of the comoving frame of the mean local velocity obtained by a numerical solution of equation (3.46) and a typical stochastic trajectory θ_t of the particle measured in the Eulerian frame (red dashed line). The figure sketches the linear transformation (3.47) applied to θ_t to obtain its values ϑ_t measured in the Lagrangian frame. (b) Probability density function of the particle position measured in the Eulerian (black solid line) and in the Lagrangian frame ($*$). Inset: Example of trajectory measured in the Eulerian (upper panel) and in the Lagrangian frame (lower panel).

provided by the usual fluctuation-dissipation theorem (2.16) is strongly violated in this NESS because of the broken detailed balance, with the correlation term $C(0) - C(t)$ being one order of magnitude larger than the response term $D\chi(t)$. However, with the corrective term $B(t)$ associated to the probability current subtracted, $C(0)-C(t)-B(t)$ shown in solid blue line in figure 3.10(c), becomes equal to $D\chi(t)$, as shown in the expanded view of figure 3.10(d). We observe that, within the experimental error bars, the agreement between both terms is quite good, verifying the integrated form of the modified fluctuation-dissipation relation (3.43). Equation (3.43) is checked only for the first ≈ 4 s because after this time the evaluation of $\chi(t)$ is affected by large errors associated to the finite sampling at $t = 0$ when the perturbation δA is switched on, as discussed in section 3.3. Indeed, for $t > 6.67$ s the difference between $D\chi(t)$ and $C(0) - C(t) - B(t)$ become increasingly significant with the error bars of $D\chi(t)$ comparable or larger than the mean values (not shown).

As mentioned in subsection 2.2.1, the validity of equation. (3.43) for the fluctuations of the angular position of the silica particle in NESS gains a transparent interpretation in the Lagrangian frame of the mean local velocity $v_0(\theta)$ along the circle. This is analogous to the simplicity gained in hydrodynamics when passing to the Lagrangian frame of the flow. One of the predictions of the Lagrangian analysis of systems in

NESS is that, although the trajectories in the Eulerian (laboratory) and the Lagrangian frame of $v_0(\theta)$ are quite different, their average probability density is the same in the two frames [53]. In order to check this unexpected theoretical prediction for the NESS experimental data, for each particle trajectory θ_t measured in the Eulerian frame we compute the corresponding one ϑ_t measured in the comoving frame of the mean local velocity $v_0(\theta)$. For this purpose we consider that a Lagrangian trajectory θ_L moving with $v_0(\theta)$, i.e. static with respect to the comoving frame of $v_0(\theta)$, evolves in time as

$$\frac{d\theta_L(t)}{dt} = v_0(\theta_L(t)). \tag{3.45}$$

Then by setting the initial condition $\theta_L(0) = 0$ without loss of generality, according to equations (3.45) and (3.40) the Lagrangian trajectory of $v_0(\theta)$ must satisfy at time $t \geq 0$ the equation

$$\begin{aligned} t &= \frac{1}{j}\int_0^{\theta_L(t)} \rho_0(\theta)\,\mathrm{d}\theta, \\ &= \frac{1}{j}P(\theta_L(t)), \end{aligned} \tag{3.46}$$

where P is the cumulative distribution function of the stochastic variable θ. Then equation (3.46) yields the function $t_L \equiv t(\theta_L)$ that must be inverted in order to find the time evolution of a Lagrangian trajectory (3.45). The period of the function $\theta_L(t)$ is $T \equiv t_L(2\pi) = j^{-1} = 26.6$ s which corresponds to the mean rotation period of the particle along the toroidal optical trap. Figure 3.11(a) shows the dependence of θ_L on t after inverting equation (3.46) for the experimental NESS data. Using this curve, the trajectories of the particle position ϑ_t measured in the Lagrangian frame are computed in the following way. For a given particle position θ_{t^*} measured in the Eulerian frame at time t^* one must find the point on the circle from which the Lagrangian flow would arrive at time t^* at θ_{t^*}. In other words, one must take the time $t_L(\theta_{t^*})$ when the Lagrangian trajectory θ_L is at θ_{t^*}. Then, the stochastic trajectory ϑ at time t is given by the nonlinear transformation

$$\vartheta_t = \theta_L([t_L(\theta_t) - t]) \tag{3.47}$$

where

$$[t_L(\theta_t) - t] = t_L(\theta_t) - t \mod T, \qquad 0 \leq [t_L(\theta_t) - t] < T, \tag{3.48}$$

as sketched in figure 3.11(a). This nonlinear transformation satisfies $\vartheta_t = \theta_L(0) = 0$ when the stochastic trajectory θ_t exactly matches $\theta_L(t)$. By construction, the transformed trajectories defined by equation (3.47) satisfy the initial condition $\vartheta_0 = \theta_0$. Note that due to the strongly nonlinear dynamics of θ_L (3.45), in general the stochastic process ϑ_t is nonstationary and it may look very different from the process θ_t. The inset of figure 3.11(b) points out the difference between a trajectory measured in the Eulerian frame and the same trajectory measured in the Lagrangian frame transformed

according to equation (3.47). Upon applying the nonlinear transformation (3.47) to the 200 experimental NESS time series θ_t and computing the histogram of the resulting tranformed time series, one obtains the probability density function $\varrho_0(\vartheta)$ of the stochastic variable ϑ. In figure 3.11(b) we plot $\varrho_0(\vartheta)$ (star symbols) and we compare it with $\rho_0(\theta)$ (solid line) showing that even when the stochastic processes θ_t and ϑ_t are completely different, the corresponding densities are the same. This results provides an experimental evidence that the passage to the comoving frame of the mean local velocity allows a rather complex nonequilibrium stationary dynamics like that modeled by equation (3.19) to exhibit a simple physical picture: an equilibrium-like nonstationary dynamics can be restored in this frame where detailed balance holds relative to the invariant density $\varrho_0(\vartheta)$, as described in chapter. Moreover this is in agreement with the experimental verification of the modified fluctuation-response formula (3.43). It turns out that when measuring the observables that are time independent in the Lagrangian frame of the mean local velocity, the term $B(t)$ vanishes because in that frame the probability current is zero. Therefore the fluctuations and the linear response are simply linked by the equilibrium-like formula

$$\partial_s C_L(t,s) = k_B T R_L(t,s), \tag{3.49}$$

where C_L and R_L are the autocorrelation function defined in equation (3.41) and the response function measured in the Lagrangian frame. Equation (3.49) is close to that of the equilibrium fluctuation-dissipation formula except for the lack of the time translation invariance of the functions involved due to the nonlinear coordinate transformation (3.47).

3.4.2 Entropic-frenetic approach

We now analyze the same experimental NESS time series θ_t and those $\theta_t^{\delta A}$ upon applying the dynamical perturbation (3.34) for the fluctuations and response of the same observable $O(\theta) = \phi(\theta)$ as before in the context of the entropic-frenetic approach described in Subsection 2.2.2. This formulation is based only on time-symmetric and anti-symmetric properties of the fluctuations and does not involve directly the probability density $\rho_0(\theta)$. For the dynamical perturbation of the potential amplitude (3.34) it involves the following quantities characterizing the NESS fluctuations of $O(\theta)$:

- The *entropic* term: this is related to the autocorrelation function $C(t)$ of $O(\theta)$, defined in equations (3.41) and (3.42). The origin of this term can be traced back to time-antisymmetric properties of the fluctuations and can be regarded as a correlation function between $O(\theta)$ and the excess of entropy $\gamma a^2 \delta A \phi(\theta)/T$ produced by the heat dissipated into the thermal bath due to perturbation δA with respect to the NESS.

- The *frenetic* term: this is a term related to the time-symmetric part of the action defined for the perturbed process with respect to the unperturbed NESS process

(see Subsection 2.2.2), namely the excess of dynamical activity or *frenesy*. The frenesy can be regarded as a generalized escape rate of a stochastic trajectory of the particle from a given phase space point $(\theta, \dot{\theta})$. For the driven diffusion of the particle on the toroidal optical trap, the instantaneous value of the frenesy at time s associated to the perturbation (3.34) is given by

$$\psi(\theta_s) = \frac{1}{D} L\phi(\theta_s), \tag{3.50}$$

where

$$L = [F - A\partial_\theta \phi(\theta)]\partial_\theta + D\partial_\theta^2, \tag{3.51}$$

is the generator of the Langevin dynamics (3.19). The integrated excess in dynamical activity

$$\Psi(t) = \int_0^t \psi(\theta_s)\delta A \, \mathrm{d}s, \tag{3.52}$$

quantifies how frenetic is the motion in the perturbed process with respect to the unperturbed one during a time interval $[0, t]$. The frenetic term can be regarded as a correlation function between $O(\theta)$ and the frenesy $\psi(\theta)$ given by equation (3.50).

Specifically, in the integrated version of the fluctuation-dissipation relation (2.34) provided by this formulation, $h = -\delta A$ is the perturbation and $V(\theta) = \phi(\theta)$ is the observable conjugated to the perturbation with respect to the energy. Then equation (2.34) reads in this case

$$\frac{E(t) + K(t)}{2} = D\chi(t), \tag{3.53}$$

where the entropic and frenetic terms are explicitly given by the expressions

$$E(t) = C(0) - C(t), \tag{3.54}$$

$$\begin{aligned} K(t) &= -\frac{D}{\delta A}\langle O(\theta_t)\Psi(t)\rangle_0, \\ &= -D\int_0^t \langle O(\theta_t)\psi(\theta_s)\rangle_0 \, \mathrm{d}s, \\ &= -\int_0^t \langle [\phi(\theta_t)(F - A\phi'(\theta_s))\phi'(\theta_s) + D\phi''(\theta_s)]\rangle_0 \, \mathrm{d}s, \end{aligned} \tag{3.55}$$

respectively. In equation (3.53) the integrated linear response function $\chi(t)$ is the same as defined in equation (3.35) for the observable $O(\theta) = \phi(\theta)$ because we focus on the same perturbation protocol (3.34). It is clear that in this approach we need to know accurately the potential profile $\phi(\theta)$ because the integrand of equation (3.55) involves the instantaneous values of its first two derivatives $\phi'(\theta)$ and $\phi''(\theta)$. In order to take into account the non-sinusoidal distortion of the potential profile in the computation

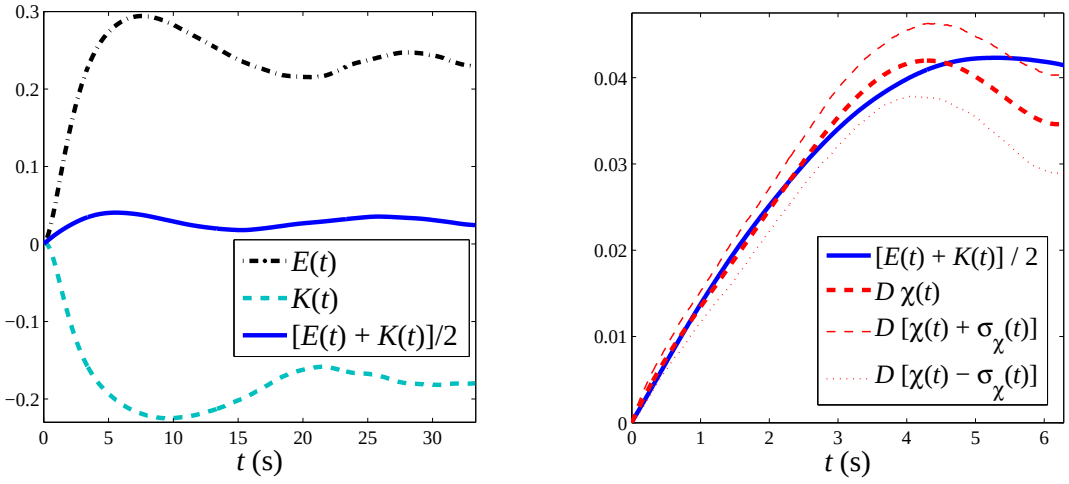

(a) (b)

Figure 3.12: (a) Comparison between the experimental entropic term (black dotted-dashed line), the frenetic term (turquoise dashed line), and their average (solid blue line) appearing on the left-hand side of equation (3.53) for the Brownian particle in a NESS. (b) Comparison between the experimental left-hand side (solid blue line, measured at NESS) and the right-hand side (red dashed line, obtained by the dynamical protocol (3.34)) of equation (3.53).

of $K(t)$, we use the local polynomial fit of ϕ and its derivatives shown in figure 3.7(c). Then the instantaneous value of $\phi^{(n)}(\theta_t)$ at time t $(n = 0, 1, 2)$ is approximated by $\phi^{(n)}_{Loc}(\theta_t)$ either for an unperturbed or a perturbed trajectory.

The resulting experimental curves $E(t)$ and $K(t)$ as functions of the integration time t are plotted in figure 3.12(a). At thermal equilibrium ($F = 0$) one should find that $E(t) = K(t)$ for all $t \geq 0$ because of the time reversibility and stationarity of the two-time correlations leading to the equilibrium fluctuation-dissipation relation $D\chi(t) = E(t)$. On the other hand, in the present case $K(t)$ reaches negative values of the same order of magnitude as the positive values of $E(t)$. This reflects the experimental conditions far from thermal equilibrium of the system. The curve for $K(t)$ represents the first experimental result concerning the direct measurement of the dynamical activity along a trajectory. The average of these two quantities $[E(t)+K(t)]/2$ is one order of magnitude smaller. This average agrees very well with the direct measurement of the integrated linear response function $\chi(t)$ within the experimental error bars $\pm\sigma_\chi$, as shown in figure 3.12(b). All is consistent with the analysis performed in the previous section, but the approach here is quite different. Here we measure directly explicit correlation functions $E(t)$ and $K(t)$ without recourse to and indeed without need for the expression for the stationary distribution $\rho_0(\theta)$. Note that in this case the experimental density profile $\rho_0(\theta)$ (and not its analytical expression) is used in practice only for calibration purposes to determine the experimental parameters A and F and

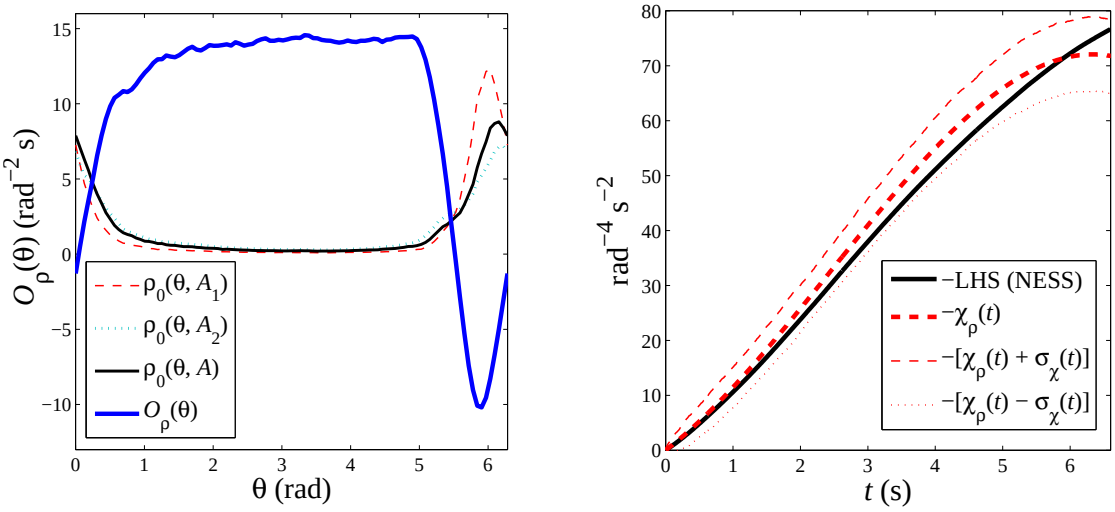

(a) (b)

Figure 3.13: (a) NESS probability density function of θ measured at three different values of the potential amplitude: $A = 0.87$ rad^2 s^{-1}, $A_1 = A + 0.05A$ and $A_2 = A - 0.07A$ and fixed $F = 0.85$ rad s^{-1}. The experimental profile of the observable $O_\rho(\theta)$ defined in equation (3.57) is computed as a discrete time derivative using these NESS densities. (b) Comparison between the experimental left-hand side (black solid line) and the right-hand side (red dashed line) of the generalized fluctuation-dissipation relation (3.56).

the profile of $\phi(\theta)$. Once these parameters are known the data analysis necessary to compute $E(t)$ and $K(t)$ completely relies on the dynamics, i.e. the measurement of the time series θ_t.

3.4.3 Probability density approach

This alternative approach to fluctuation-response around a stationary state, derived from the Hatano-Sasa relation (see Subsection 2.2.3), exploits the properties of the stationary density $\rho_0(\theta)$ without any need of a model for the dynamics of the system. It only requires the knowledge of the local dependence of $\rho_0(\theta)$ on the control parameter that is perturbed to determine the linear response function around a given NESS. In the present experiment this parameter is the potential amplitude A. Then we take adventage of the calibration procedure described in subsection in order to know the dependence of the NESS probability density on A:

$$\rho_0(\theta, A) = \rho_0(\theta) \text{ at fixed } A,$$

like the three density profiles at different values of A shown in figure 3.13(a). Then, according to this formulation the generalized fluctuation-dissipation relation for the

perturbation procedure (3.34) reads

$$\langle O_\rho(\theta_t)O_\rho(\theta_0)\rangle_0 - \langle O_\rho(\theta_t)O_\rho(\theta_t)\rangle_0 = \chi_\rho(t). \tag{3.56}$$

Equation (3.56) involves an observable directly related to the density ρ_0 that is fixed by the choice of the perturbed parameter A

$$O_\rho(\theta) = -\partial_A \ln \rho_0(\theta, A). \tag{3.57}$$

In practice this observable is computed as a discrete three-point derivative of $-\ln \rho_0(\theta, A)$ at two different NESS around that at $A = 0.87$ rad^2 s^{-1}. The experimental profile of $O_\rho(\theta)$ is shown in figure 3.13(a) (blue solid line). The left-hand side of equation (3.56) involving the autocorrelation function of this observable measured in NESS is plotted in figure 3.13(b) (black solid line).

On the other hand, the integrated response function on the right hand side of equation (3.57) is explicitly given by

$$\chi_\rho(t) = \frac{\langle O_\rho(\theta_t)\rangle_{\delta A} - \langle O_\rho(\theta_t)\rangle_0}{\delta A}. \tag{3.58}$$

Upon applying the protocol described in section to estimate the averages in the numerator of equation (3.58) from a finite number of realizations of δA, one obtains the experimental response curve $\chi_\rho(t)$ shown in figure 3.13(b) (red dashed line). Once again, the data verifies the generalized fluctuation-response formula (3.56) even when it involves the autocorrelation function of an observable (3.57) different from those used in the previous formulations (3.43) and (3.53). This result verifies the fact that the experimental conditions of the Brownian particle in the toroidal optical trap fulfill the hypothesis needed for the validity of equation (3.56): the degrees of freedom of system (the position of the Brownian particle) have Markovian dynamics in a steady state and the perturbation δA is small enough to be in the linear response regime. In addition, note that provided that these assumptions are verified, no information on the properties of the bath (e.g. D) or on the model of the system explicitly appears in equation (3.56). The only price to pay for this simple fluctuation-response description is that the NESS density ρ_0 has to be accurately mesured as a function of the main control parameter A, which implies additional NESS measurements. Otherwise the observable (3.57) can not be computed properly.

We point out that, as explained in Subsection 2.2.3 the Hatano-Sasa-based fluctuation-dissipation relation (3.56) can be regarded as a special case of the more general formula derived in [24] (see equation (2.40)). This general formulation involves also the measurement of the observable (3.57) in NESS. However, unlike equation (3.56) which is restricted to the linear response of the special observable $O_\rho(\theta)$, the more general relation (2.40) allows one to compute the response function $\chi(t)$ for any observable $O(\theta)$. Then we can exploit this generality to compare directly the probability density approach with the Lagrangian and the entropic-frenetic ones. Once again we focus on the fluctuations and the linear response of the potential energy observable $O(\theta) = \phi(\theta)$

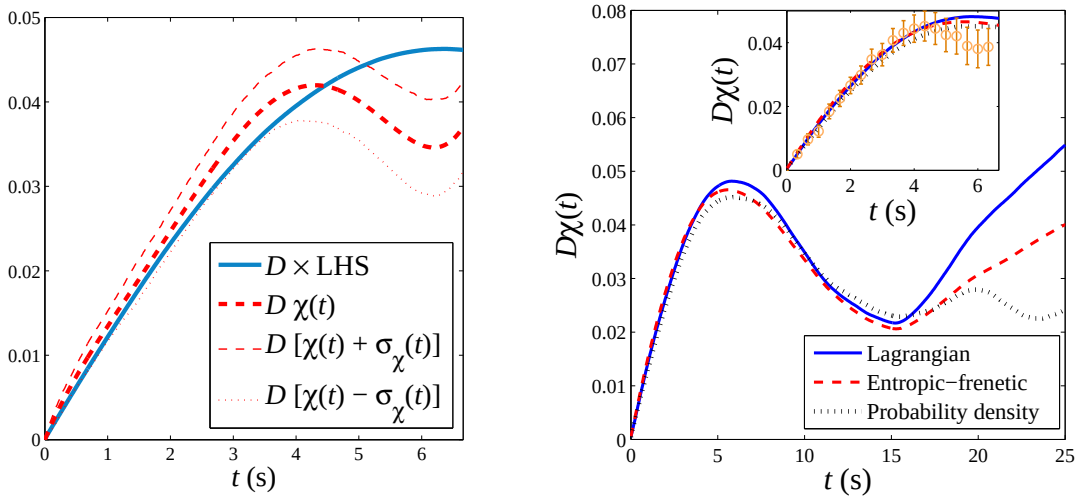

(a) (b)

Figure 3.14: (a) Comparison between the experimental left-hand side (blue solid line) and right-hand side (red dashed line) of equation (3.59). (b) Comparison between the experimental unperturbed NESS terms involved in the different fluctuation-dissipation formulations to estimate indirectly the integrated linear response function $\chi(t)$. Inset: expanded view at short time lags compared to the direct measurement of $\chi(t)$ ($\circ$) by performing the dynamical perturbation of A (3.34).

when perturbing in time A according to the procedure (3.34). In such a case the integrated GFDR (2.40) reads

$$\langle \phi(\theta_t) O_\rho(\theta_t) \rangle_0 - \langle \phi(\theta_t) O_\rho(\theta_0) \rangle_0 = \chi(t), \tag{3.59}$$

where the integrated response function $\chi(t)$ of $\phi(\theta)$ is different from $\chi_\rho(t)$ defined in equation (3.58). In figure 3.14(a) we plot the left-hand side of equation (3.59) computed using the unperturbed NESS trajectories θ_t. We also show the integrated response function $\chi(t)$ already computed in the previous formulations. As expected, the generalized fluctuation-dissipation formula (3.59) is verified within the experimental error bars of the response $\chi(t)$. However, in this approach the computation of the NESS correlation term (left-hand side of equation (3.59)) is more subjected to experimental errors than the Lagrangian and the entropic-frenetic approaches. This is because of the computation of the observable $O_\rho(\theta)$ in equation (3.57) using a discrete derivative. The initial numerical error done in this approximation gives rise to a slightly worse agreement between the NESS correlation and the response of equation (3.59) compared to that of figures 3.10(d) and 3.12(b).

In figure 3.14(b) we compare the unperturbed NESS quantity on the left-hand side of the fluctuation-dissipation relation (3.59) with those that appear in the Lagrangian (3.43) and the entropic-frenetic (3.53) approaches to estimate the linear response function. Even when the observables involved the corresponding NESS correlation functions are completely different, the agreement between the three experimental curves is excellent for $t \lesssim 20$ s. Then for $t \gtrsim 20$ s they exhibit deviations that increase as t increases. Nevertheless, these deviations are induced by the computation of the discrete time integrals (3.44) and (3.55) and the discrete derivative (3.57). Indeed, the very fact that the excellent agreement between the three curves for $t \lesssim 20$ s and with the direct measurement of $\chi(t)$ for $t \lesssim 4$ s (inset of figure 3.14(b), circles) indicates that this is only a numerical artifact. This agreement represents an experimental test of the equivalence of the three different generalized fluctuation-dissipation approaches around a NESS previously presented. In the following section we discuss in detail the physical interpretation of this equivalence for the Brownian particle in the toroidal optical trap.

3.5 Discussion

We now discuss the relation between the different GFDRs presented in the previous section. Due to the minimal non-trivial nature of the NESS experiment, a very simple and transparent interpretation of the link between these relations is possible. The intuitive starting point for this discussion is the formulation based on stochastic thermodynamics as it represents the extension of thermodynamic concepts to small systems. See subsection 2.2.4 and Appendix C for a more detailed derivation of the equations presented in this section. We recall that the fundamental observable in this approach is the stochastic entropy production S_{st}. For the NESS dynamics of the particle position θ, the instantaneous value of the stochastic entropy at time s along a specific trajectory

θ_s is by definition

$$S_{st}(\theta_s) = -k_B \ln \rho_0(\theta_s). \tag{3.60}$$

According to stochastic thermodynamics, the stochastic entropy (3.60) can be expressed as the difference between the total entropy production S_{tot} minus the entropy production of the medium S_m: $S_{st} = S_{tot} - S_m$. For the driven diffusion on the circle modeled by the Langevin equation (3.19), the total entropy production rate reads

$$\begin{aligned} \dot{S}_{tot}(\theta_s) &= \frac{v_0(\theta_s)\gamma a^2 \dot{\theta}_s}{T}, \\ &= \frac{\gamma a^2 v_0(\theta_s)}{T}\left[-A\partial_\theta\phi(\theta_s) + F + \zeta_s\right]. \end{aligned} \tag{3.61}$$

whereas the entropy production rate due to the power dissipated into the thermal bath is given by

$$\dot{S}_m(\theta_s) = -\frac{\gamma a^2}{T}\frac{\mathrm{d}}{\mathrm{d}s}\left[A\phi(\theta_s) - F\theta_s\right]. \tag{3.62}$$

Then, by taking the derivative with respect to A in equations (3.61) and (3.62) one finds that the variable conjugate to the perturbation $A \to A + \delta A$ with respect to the stochastic entropy production rate, defined in equation (2.45), is

$$X(\theta) = \frac{\gamma a^2}{T}\left[\dot{\phi}(\theta) - v_0(\theta)\partial_\theta\phi(\theta)\right]. \tag{3.63}$$

Finally, by inserting the variable $X(\theta)$ of equation (3.63) into the stochastic entropy fluctuation-dissipation formula (2.44) we recover the differential form of the formulae (3.43) and (3.44) provided by the Lagrangian formulation

$$DR(t-s) = \partial_s\langle\phi(\theta_t)\phi(\theta_s)\rangle_0 - \langle\phi(\theta_t)v_0(\theta_s)\partial_\theta\phi(\theta_s)\rangle_0. \tag{3.64}$$

We stress that even when both approaches are theoretically equivalent, the observables involved in the NESS correlation functions are not the same. In the first case, in order to measure directly the variable $X(\theta)$ one must determine the dependence of the NESS density ρ_0 on the control parameter A. Then at fixed A one must compute the time derivative of the stochastic entropy $-k_B \ln \rho_0(\theta_s, A)$ evaluated along each stochastic trajectory θ_s:

$$\dot{S}_{st}(\theta_s) = \frac{\mathrm{d}[-k_B \ln \rho_0(\theta_s, A)]}{\mathrm{d}s}.$$

Then it follows that the instantaneous value at time s of the variable $X(\theta)$ involved in the GFDR (2.44) is operationally given by the formula

$$X(\theta_s) = k_B\partial_A\left[\frac{\mathrm{d}[\ln \rho_0(\theta_s, A)]}{\mathrm{d}s}\right].$$

However, in general the direct measurement of X is difficult in experiments if the system of interest has many coupled degrees of freedom because one should need to measure

their joint probability density. In addition, even if the joint density is experimentally accessible, one must perform several measurements to determine its dependence on the control parameter used in the perturbation protocol. By contrast, if the dynamics of the system can be modeled in terms of the perturbed control parameter, the stochastic entropy production can be expressed in terms of observables of the model itself and the mean local velocity, like in equations (3.61) and (3.62). Note that in this way there is no need to determine the dependence of the NESS on A. Both approaches involve the autocorrelation function of the observable $\phi(\theta)$ because this term accounts indirectly for the dissipation with respect to the perturbation as in the equilibrium fluctuation-dissipation theorem (2.16). On the other hand, the corrective term involving the mean local velocity quantifies the nonequilibrium nature of the system. This term is closely related to the heat that must be irreversibly dissipated to maintain the NESS. In the first case, it can be interpreted as the existence of a nonvanishing *total* entropy production rate (3.62) with $\langle \dot{S}_{tot} \rangle_0 > 0$ due to the broken detailed balance of the dynamics. In the second case, it can be regarded as the existence of a probability current (3.23), similar to a hydrodynamic current, generated by the nonconservative force F.

Now we discuss the connection with the entropic-frenetic approach based on symmetry arguments. Causality implies that at time $t < s$, before perturbing the initial NESS, the impulse response is zero: $R(t-s) = 0$. Then for the generalized fluctuation-dissipation relation (2.34) to be valid for all s and t, one needs

$$\begin{aligned} \partial_t \langle \phi(\theta_s)\phi(\theta_t)\rangle_0 &= \langle \phi(\theta_s) L \phi(\theta_t)\rangle_0 \ \text{ for } t < s, \\ &= \langle \phi(\theta_t) L^\dagger \phi(\theta_s)\rangle_0, \end{aligned} \tag{3.65}$$

where $L^\dagger$ is the adjoint operator of L. The last equality in (3.65) holds because $L^\dagger$ generates the time-reverse process, so $L \to L^\dagger$ upon interchanging the indices t and s. Then by subtracting equation (3.65) from the differential form of equation (3.53)

$$DR(t-s) = \frac{1}{2}\left[\partial_s \langle \phi(\theta_t)\phi(\theta_s)\rangle_0 - \langle \phi(\theta_t) L \phi(\theta_s)\rangle_0\right], \tag{3.66}$$

the entropic-frenetic fluctuation-dissipation formula (3.66) can be rewritten as

$$\begin{aligned} DR(t-s) &= \frac{1}{2}[\partial_s \langle \phi(\theta_t)\phi(\theta_s)\rangle_0 - \partial_t \langle \phi(\theta_t)\phi(\theta_s)\rangle_0] - \\ &\quad \frac{1}{2}\langle \phi(\theta_t)(L - L^\dagger)\phi(\theta_s)\rangle_0. \end{aligned} \tag{3.67}$$

For a NESS, the time translational invariance implies that

$$\partial_s \langle \phi(\theta_t)\phi(\theta_s)\rangle_0 = \partial_s \langle \phi(\theta_{t-s})\phi(\theta_0)\rangle_0 = -\partial_t \langle \phi(\theta_t)\phi(\theta_s)\rangle_0,$$

so the first term on the right-hand side of equation (3.67) becomes equal to the NESS quantity $\partial_s \langle \phi(\theta_t)\phi(\theta_s)\rangle_0$. This is exactly the term associated to the correlation between the observable of interest and the conjugate variable to the entropy production rate of

the medium $\propto \dot{\phi}$ according to equation (3.62), i.e. the entropy excess with respect to the perturbation. On the other hand, the second correlation function on the right hand side of equation (3.67) represents the correction due to the fact that the unperturbed system is in a nonequilibrium state. At equilibrium this term vanishes due to the time-reversibility of the dynamics: $O(\theta_t)LO(\theta_s) = O(\theta_t)L^\dagger O(\theta_s)$, recovering the equilibrium fluctuation-dissipation relation (2.16). However, for the driven diffusion on the circle (3.19) in a NESS, the second term on the right-hand side of equation (3.67) reflects the breakdown of the time-reversal symmetry by the nonzero value of F. In this case the generator L and its adjoint operator is $L^\dagger$ satisfy [22, 55]

$$L - L^\dagger = 2v_0(\theta)\partial_\theta. \tag{3.68}$$

By substituting the expression (3.68) of the operator $L - L^\dagger$ into equation (3.66), we recover the previous generalized fluctuation-dissipation formula (3.64). Note that in the entropic-frenetic approach, the NESS correction can be regarded as a measure of the time irreversibility and of the broken detailed balance of the system since the operator $L - L^\dagger$ does not annihilate the last correlation function of equation (3.67).

Finally, the relation between the stochastic entropy approach and that based on the probability density is straightforward. It turns out that the variable $X(\theta)$ involved in the NESS correlation function of the former is closely related to the observable $O_\rho(\theta)$ defined in equation (3.57) because for every stochastic trajectory θ_s we have

$$\begin{aligned} X(\theta_s) &= k_B\partial_A\left[\frac{\mathrm{d}}{\mathrm{d}s}[-\ln\rho_0(\theta_s, A)]\right], \\ &= k_B\frac{\mathrm{d}}{\mathrm{d}s}[-\partial_A\ln\rho_0(\theta_s, A)], \\ &= k_B\frac{\mathrm{d}O_\rho(\theta_s)}{\mathrm{d}s}. \end{aligned} \tag{3.69}$$

Accordingly, in the present experiment we actually measured the stochastic entropy production along the trajectories of the Brownian particle following the probability density approach. Then we were able to directly probe the stochastic-entropy-based GFDR (2.44) without recourse to any model of the dynamics but only the experimental measurement of the probability density at different values of A. Once again, we point out that this approach is suitable only when the NESS joint probability density of the degrees of freedom of interest can be accurately measured as a function of the perturbed control parameter (e.g. systems with a single degree of freedom or linear systems with multiple degrees of freedom). Otherwise the stochastic entropy production observable X is not easily accessible in experiments.

According to the previous discussion sketched from our simple nonequilibrium experiment, in general a suitable approach can be chosen to measure the fluctuations or the linear response around a NESS depending on the accessible observables. In table 3.1 we summarize the main features of each formalism and some particular examples when they can be relevant for experimental measurements:

Table 3.1: Generalized fluctuation-dissipation relations around a NESS

Formulation	Main features	Relevant examples
Stochastic thermodynamics	•Thermodynamic interpretation. •No model needed provided that the NESS density can be accurately determined as a function of the control parameters.	• Linear systems with many degrees of freedom (e.g. harmonic chains). •Driven diffusive processes with a single degree of freedom (e.g. molecular motors).
Lagrangian	•*Hydrodynamic* interpretation. •Equilibrium-like form in the Lagrangian frame of the mean local velocity. •Model of dynamics and NESS density are required.	•Driven diffusive processes with a finite number of of degrees of freedom and known interacting potentials (e.g. simple sheared polymer suspensions).
Entropic-frenetic	•Symmetry interpretation. •No explicit knowledge of the NESS density is required provided that the generator of the dynamics is known.	•Nonlinear stochastic systems with several degrees of freedom (e.g. coupled anharmonic oscillators in contact with baths at different temperatures).

It is interesting to note that besides the broad freedom in the choice of the observables depending on the experimental conditions, new observables satisfying GFDRs can be constructed in the following way. If there is a set of n observables $\{\Upsilon_j, j = 1, \ldots, n\}$ satisfying

$$R(t-s) = \langle O(\theta_t)\Upsilon_j(\theta_s)\rangle,\ j = 1, \ldots, n, \tag{3.70}$$

then any linear combination

$$Y(\theta) = \frac{\sum_{j=1}^{n} a_j \Upsilon_j(\theta)}{\sum_{j=1}^{n} a_j}, \tag{3.71}$$

also satisfies a GFDR of the form (3.70), [23]. This remarkable result can be ilustrated by the experimental data of the Brownian particle in the toroidal optical trap. By choosing the observables

$$\Upsilon_1(\theta) = \dot{\phi}(\theta) - v_0(\theta)\partial_\theta\phi(\theta), \quad \Upsilon_2(\theta) = \frac{1}{2}\dot{\phi}(\theta) - \frac{1}{2}L\phi(\theta),$$

appearing in the Lagrangian and the entropic-frenetic formulae (3.64) and (3.66), respectively, we can define the new observable

$$\begin{aligned} Y(\theta) &= 2\Upsilon_2(\theta) - \Upsilon_1(\theta), \\ &= -D[\partial_\theta^2\phi(\theta) + \partial_\theta \ln \rho_0(\theta)\partial_\theta\phi(\theta)]. \end{aligned} \tag{3.72}$$

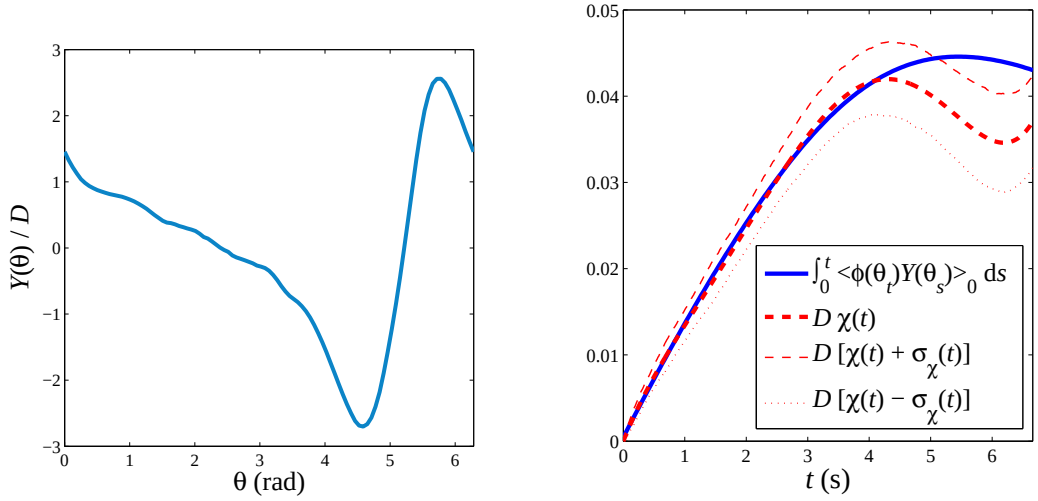

(a) (b)

Figure 3.15: (a) Experimental profile of the observable $Y(\theta)$ defined in equation (3.72). (b) Comparison between the direct measurement of the integrated linear response function $\chi(t)$ and the integral of the NESS correlation function on the right-hand side of equation (3.73).

where we have used the explicit expressions of $v_0(\theta)$ and L. Unlike the observables $\Upsilon_1(\theta)$ and $\Upsilon_2(\theta)$, the observable $Y(\theta)$ only involves diffusive terms. The experimental profile of $Y(\theta)$ for the Brownian particle in the toroidal optical trap is shown in figure 3.15(a). Then the corresponding form of the fluctuation-response formula must read

$$\begin{aligned} R(t-s) &= \frac{1}{D}\langle\phi(\theta_t)Y(\theta_s)\rangle_0, \\ &= -\langle\phi(\theta_t)[\partial_\theta^2\phi(\theta_s) + \partial_\theta \ln\rho_0(\theta_s)\partial_\theta\phi(\theta_s)]\rangle_0, \end{aligned} \tag{3.73}$$

that does not depend explicitly on the control parameters A, F, D of Langevin model but only the potential profile and the NESS density. In figure 3.15(b) we plot the result for the integrated version of equation (3.73) using the independent measurement of the NESS unperturbed and the perturbed particle trajectories following the Heaviside procedure (3.34). The generalized fluctuation-dissipation formula (3.73) is also verified by the experiment even when the NESS correlation function contains the term $\partial_\theta\rho_0(\theta)$ that does not explicitly appear in the previous formulations. The experimental validity of (3.73) is in agreement with the linear property previously discussed. This property might be very useful in more general situations when an observable can not be easily determined in practice, but a suitable linear combination can restore the generalized-fluctuation dissipation relation into a more accessible form.

3.6 Application example

We illustrate the usefulness of the application of the previous generalized fluctuation-response formulations to study the temporal behavior of the mean potential energy of the particle $\langle U(\theta_t)\rangle_h$ under small external perturbations h_s more intricate than a simple Heaviside function. This is done without carrying out the different physical realizations of h_s using only the unperturbed NESS time series θ_t of the particle position. We concentrate on a sinusoidal perturbation starting at time $s = 0$

$$h_s = h_0 \sin(2\pi f s), \tag{3.74}$$

either to the phase or to the amplitude of the potential around the steady state.

As all the parameters (A, F, D) describing the Langevin dynamics of the particle (3.18) are known, in the following analysis we will follow the entropic-frenetic approach. First, we consider the case of a small phase perturbation

$$\alpha_s = \alpha_0 \sin 2\pi f_0 s, \quad \alpha_0 \ll 1. \tag{3.75}$$

Then, the static potential is perturbed in time as

$$\begin{aligned} A\phi(\theta) &\to A\phi(\theta + \alpha_s), \\ &\approx A\phi(\theta) + A\phi'(\theta)\alpha_s, \end{aligned} \tag{3.76}$$

so that $h_0 = -A\alpha_0$ in equation (3.74) and the variable conjugate to the perturbation $h_s = -A\alpha_s$ is $V = \phi'(\theta)$. According to the generalized relation (2.34), one can determine the integrated response function $\chi(t)$ of the energy observable $O(\theta) = \phi(\theta)$ through the NESS quantity $[E(t) + K(t)]/(2D)$ by using the right V, Q and the generator L (3.51). The resulting curves $E(t)$, $K(t)$ and $[E(t) + K(t)]/(2D)$ are plotted in figure 3.16(a). Next, by definition the experimental impulse response function $R(t-s)$ is simply given by

$$\begin{aligned} R(t-s) &= \partial_t \chi(t-s), \\ &= \frac{\partial_t E(t-s) + \partial_t K(t-s)}{2D}. \end{aligned} \tag{3.77}$$

The impulse response function (3.77) must be convolved with $h_s = -A\alpha_s$ given by equation (3.74)

$$\langle \phi(\theta)\rangle_h = \langle \phi(\theta)\rangle_0 + \int_0^t R(t-s) h_s \, \mathrm{d}s, \tag{3.78}$$

in order to obtain the mean value of $\phi(\theta)$ upon switching on the sinusoidal phase perturbation. In this way we find that the mean potential energy of the particle oscillates around the NESS value $\langle U(\theta)\rangle_0 = -4.7 k_B T$ as shown by the dashed blue line in figure 3.16(b) for $\alpha_0 = 0.05$ rad and $f = 1$ Hz. The oscillations of $\langle U(\theta_t)\rangle$ (blue dashed line) exhibit a slow transient ($\sim$ 15 s), which corresponds to the relaxation time of the NESS correlations, see figure 3.10(b). At this excitation frequency f, as t

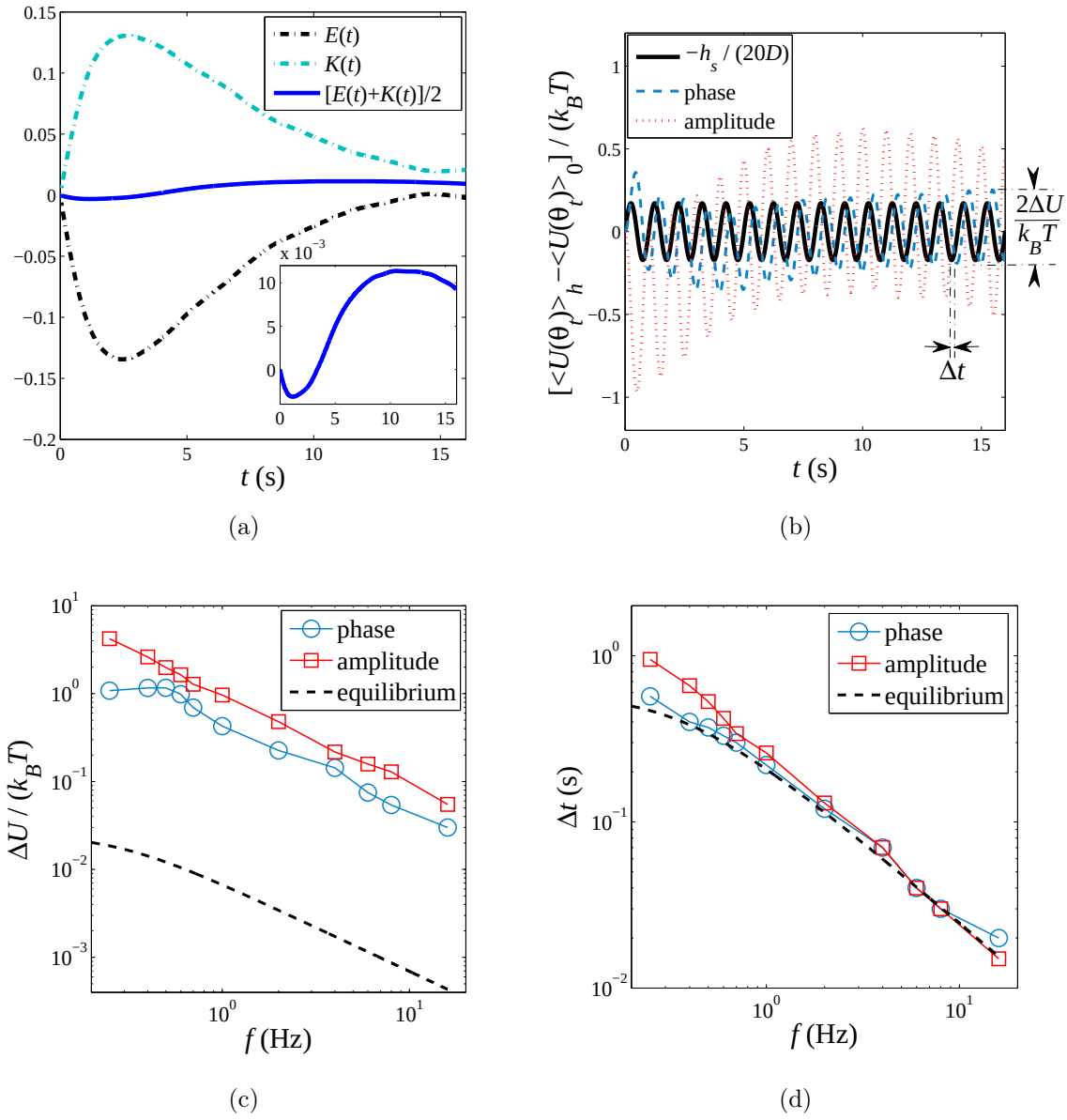

Figure 3.16: (a) Integrated response function of the observable $O = \phi(\theta)$ for a small perturbation of the potential phase around a NESS as a function of the integration time t computed through the unperturbed NESS quantity $[E(t)+K(t)]/2$. Inset: expanded view of $[E(t) + K(t)]/2$. (b) Sinusoidal time-dependent perturbation $-h_s$ (solid black line) of the static potential $A\phi$. Resulting mean potential energy of the Brownian particle for a phase perturbation (dashed blue line) and an amplitude perturbation (dotted red line) for $-h_0/A = 0.05$ and $f = 1$ Hz. (c) Asymptotic values of the oscillation amplitude of the potential energy and (d) the delay time with respect to $-h_s$ for each kind of perturbation. The black dashed lines represent the values that would be obtained around thermal equilibrium ($F = 0$), given by equations (3.82) and (3.83).

increases the oscillations settle around $\langle U(\theta)\rangle_0$ with constant amplitude $\Delta U \approx 0.2 k_B T$ and delay time[5] $\Delta t \approx 0.23$ s with respect to $-h_s$ (black solid line). This value of Δt corresponds to a phase shift of $2\pi f \Delta t = 1.45$ rad between the oscillatory perturbation $-h_s$ and the resultant $\langle U(\theta_t)\rangle$.

We now consider a sinusoidal time-dependent perturbation to the potential amplitude:

$$\delta A_s = \delta A_0 \sin(2\pi f s). \tag{3.79}$$

In this case, the the perturbation parameter h_0 in equation (3.74) is $h_0 = -\delta A_0$ and the variable conjugate to the perturbation with respect to the energy is $V(\theta) = \phi(\theta)$. We choose the amplitude perturbation (3.79) with the same strength ($-h_0/A = 0.05$) and frequency ($f = 1$ Hz) as the phase perturbation (3.75). Following the same procedure using the experimental values of $[E + K]/(2D)$ shown in figure 3.12(c), we find a different qualitative behavior of $\langle U(\theta_t)\rangle_h$. In figure 3.16(b) we show that at the beginning of the perturbation the mean potential energy (dotted red line) responds in the opposite direction of the perturbation $-h_s$. Then, there is a transient regime for $0 < t \lesssim 15$ s due the nonequilibrium nature of the unperturbed steady state. As t increases, $\langle U(\theta)\rangle_h$ relaxes to a periodic behavior with oscillations around the NESS value $\langle U(\theta)\rangle_0$ of constant amplitude $\Delta U \approx 0.5 k_B T$ and a delay time $\Delta t \approx 0.26$ s with respect to the perturbation $-h_s$. This delay time corresponds to a phase shift of $2\pi f \Delta t = 1.63$ rad.

For both types of perturbations we can write the asymptotic dependence of $\langle U(\theta_t)\rangle_h$ on $t \gtrsim 15$ s as

$$\langle U(\theta_t)\rangle_h = \langle U(\theta_t)\rangle_0 \pm \Delta U \sin[2\pi f(t - \Delta t)], \tag{3.80}$$

where the positive and negative signs stand for the phase and amplitude perturbations, respectively. Hence, in both cases the dynamics of the system settles into a new oscillatory nonequilibrium state around the original NESS for $t \gtrsim 15$ s. Note that this new state can be regarded as a NESS when the time is measured in multiples of $1/f$. The values of ΔU and Δt in equation (3.80) depend on the excitation frequency f. In figures 3.16(c) and 3.16(d) we show this dependence. We now compare these far-from-equilibrium results with those that would be obtained when applying the oscillatory h_s (3.74) around the corresponding situation at thermal equilibrium ($F = 0$). In such a case the particle motion would be tightly confined to the harmonic part of the potential around the minimum $\theta_m = 3\pi/2$: $\phi(\theta) \approx -1 + (\theta - \theta_m)^2/(2\,\mathrm{rad}^2)$. After some algebra using this approximation one finds the expression for $\langle U(\theta_t)\rangle_h$ when perturbing the system in thermal equilibrium

$$\langle U(\theta_t)\rangle_h = \langle U(\theta_t)\rangle_0 \pm \Delta U\{\sin[2\pi f(t - \Delta t)] + e^{-2\bar{A}t} \sin 2\pi f \Delta t\}, \tag{3.81}$$

where $\langle U(\theta_t)\rangle_0 = -68.3 k_B T$ and

$$\Delta U = -\frac{h_0}{\bar{A}} \frac{k_B T}{2(1 + \pi^2 f^2/\bar{A}^2)^{1/2}}, \tag{3.82}$$

[5] The delay time Δt is a result of the retarded response of the particle in a viscous medium (water) due to the periodic perturbation.

$$\Delta t = \frac{1}{2\pi f} \arctan\left(\frac{\pi f}{\bar{A}}\right), \tag{3.83}$$

either for a phase (positive sign) or an amplitude (negative sign) perturbation. In equations (3.81), (3.82) and (3.83), $\bar{A}$ represents the value of the potential amplitude $A = 0.87\,\mathrm{rad}^2\,\mathrm{s}^{-1}$ expressed in units of inverse time, i.e. $\bar{A} = 0.87\,\mathrm{s}^{-1}$. Note that for $t \gg (2\bar{A})^{-1}$, equation (3.81) exhibits the same qualitative behavior as (3.80). Nevertheless in this case the decay time of the initial equilibrium steady state ($(2\bar{A})^{-1} = 0.57$ s) is two orders of magnitude smaller than that of the initial NESS (~ 15 s) previously described. We plot the curves given by equations (3.82) and (3.83) in figures 3.16(c) and 3.16(d), respectively, for the same values of the parameters h_0 and A as before. Unlike the behavior close to equilibrium, the oscillation amplitude ΔU strongly depends on the perturbed parameter around the non-equilibrum steady state: it is more sensitive to amplitude perturbations than to phase perturbations. In addition, the far-from-equilibrium values are two orders of magnitude larger than that given by equation (3.82). By contrast, the delay time Δt is not significantly affected by the far-from-equilibrium nature of the system. It is almost independent of F and of the type of perturbation and it converges to equation (3.83) as the excitation frequency f increases.

3.7 Conclusion

We have experimentally studied the relation between spontaneous fluctuations and linear response of an observable related to the potential energy of a Brownian particle in a toroidal optical trap. The experimental data is analyzed in the context of various and apparently dissimilar GFDRs theoretically derived for NESS. We show that when taking into account the nonequilibrium corrections of the equilibrium fluctuation-dissipation theorem due to the broken detailed balance of the experiment, these GFDRs are verified by the data. The nonequilibrium corrections quantify the role of the probability current in a NESS, which is closely related to the rate of the total entropy produced by the system to remain in a stationary state. The simplicity of the system allows us to examine in detail the physical interpretation of the different terms involved in such formulations, the relation between them and their accessibility from the experimental point of view. Besides, we gain insight into the understanding and application of these GFDRs. Our experiment, perfomed under very well controlled conditions, reveals that the indirect determination of the linear response function by means of the measurement of the right NESS correlation functions is less time-consuming, more accurate and more flexible than the direct perturbation of the NESS. Similar ideas are expected to be applicable to more complex small systems where fluctuations are important and NESS are the natural unperturbed states.

Part II

Nonequilibrium fluctuations in an aging bath

Chapter 4

Brownian particle in a Laponite colloidal glass

4.1 Fluctuations and linear response for aging systems

Systems in a nonstationary state slowly relaxing towards thermal equilibrium are a second example for which the relation between spontanoeus fluctuations and linear response is not necessarily described by the fluctuation-dissipation relation (2.16). This is because nonvanishing currents are present in the form of energy or matter flows from the system to the environment during the relaxation process so the detailed balance condition is not fulfilled. Due to the complexity of the nonstationarity and the intricate microscopic structure, there is no general framework to describe the fluctuation-response relations for these out of equilibrium situations.

Glasses are the typical examples of slowly relaxing systems that have been studied extensively over the past years in the context of fluctuation-dissipation theory. They are microscopically arrested systems after a quench from an ergodic phase (e.g. an ordinary liquid in equilibrium with the environment) above a certain temperature, called the glass transition temperature T_g, to a non-ergodic phase (e.g. a supercooled liquid) below T_g. In figure 4.1(a) we represent the usual thermodynamic picture of glassy dynamics. After a quench into the non-ergodic phase, the system is initially in a metastable state in one of the local minima of its complex potential energy landscape. Below T_g the potential barriers become so large that the system remains trapped in the initial minimum, identified as one of the possible microscopic amorphous configurations of a glass. Then, the dynamical evolution consists in a rather short equilibration inside the minima followed by jumps between different minima that are well-separated in time. Physically, these jumps correspond to the structural rearrangements of mesoscopic regions in the system that allow it to relax to a new phase in equilibrium with the new temperature T of its surroundings. During the relaxation the system explores different metastable states before reaching the global minimum corresponding to the final

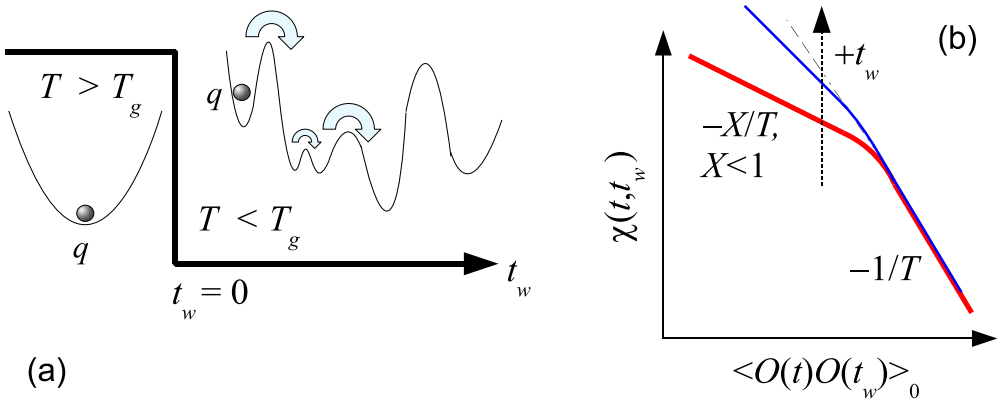

Figure 4.1: (a) Schematic representation of the relaxation process of a glassy system, depicted as a sphere, through its potential energy landscape after being initially trapped in a metastable configuration due to a quench from above to below T_g. (b) Diagram of the typical fluctuation-dissipation plot for mean field models of structural glasses. As t_w increases the curve gets closer to the equilibrium straight line of slope $1/T$ (dotted-dashed line).

equilibrium configuration. However, depending on the quench depth the time needed to reach equilibrium may be extremely large, typically much larger than the timescales accessible in the experiments. During this process there is a continuous energy release from the frustrated regions in the system that relax to more stable configurations to the environment. Since the system is non-ergodic during the relaxation, there is no invariance under time translations and then its physical properties depend on the time elapsed after the quench: t_w. The slow time evolution of the physical properties (e.g. viscosity) is known as *aging*. For a complete theoretical review on the glass transition and its connection with experiments, see [74] and references therein.

The concept of *effective temperature* is a useful attempt to develop a statistical description of the relation between fluctuations and response to external fields for aging systems. This is based on the usual relation (2.16) given by the fluctuation-dissipation theorem for systems slightly perturbed around a thermal equilibrium state. For an aging system the equilibrium temperature that appears as a constant prefactor on the left-hand side of equation (2.16) is replaced by introducing a function $X(t, t_w)$, called the fluctuation-dissipation ratio, which depends both on the age t_w of the system and on the measurement time $t \geq t_w$

$$k_B T R(t, t_w) = X(t, t_w) \partial_{t_w} C(t, t_w), \tag{4.1}$$

where T is the temperature of the environment. Unlike equation (2.16), the time translational invariance is not allowed for an aging system because of the nonstationarity. Then the linear response function $R(t, t_w)$ and the autocorrelation function of the observable of interest $C(t, t_w) = \langle O(q_t) O(q_{t_w}) \rangle$ in equation (4.1) depend not only on the

difference $t - t_w \geq 0$ but on both times t and t_w separately. Here the brakets $\langle \ldots \rangle_0$ denote an average over an infinite number of realizations of the unperturbed aging state fixed by the times t_w and t. It is important to remark that due to the loose definition of $X(t, t_w)$, in general it depends on the observable O: it can be different for different observables. Then the effective temperature for the observable $O(q)$ is defined as

$$T_{eff}(t, t_w) = \frac{T}{X(t, t_w)}, \tag{4.2}$$

which in general is not expected to be equal to the equilibrium temperature T of the environment. Indeed, mean field models of structural glasses show that T_{eff} defined by equations (4.1) and (4.2) exhibits a non-trivial but simple structure for these kind of glassy systems. It turns out that in such a case, the fluctuation-dissipation ratio X can be expressed as a function of C only: $X(t, t_w) = X(C(t, t_w))$, with two asymptotic behaviors: $X(C) \to 1$ for small $t - t_w$ whereas $X(C) < 1$ for sufficiently large $t - t_w$. Then, when plotting the integrated version of equation (4.1) with the integrated response function:

$$\chi(t, t_w) = \int_{t_w}^{t} R(t, s)\, \mathrm{d}s,$$

versus $C(t, t_w)$, one must obtain a fluctuation-dissipation plot like that sketched in figure 4.1(b). This theoretical fluctuation-dissipation plot has been found in numerical simulations of glassy systems [75, 76] (e.g. Lennard-Jones glasses) and in some experiments on spin glasses [77, 78]. According to equation (4.2), the existence of two different slopes with negative values $-X/T$ indicates the presence of two different fluctuating processes determined by the value of T_{eff}. The slope $-1/T$ corresponds to $T_{eff} = T$ associated to the fast rattling fluctuations of the system. The negative slope with absolute value $< 1/T$ is the one associated to the slowest structural rearrangements that can be interpreted as an effective temperature larger than T. The value of this effective temperature decreases in time to T as the the system relaxes.

For this kind of glassy systems, it has been widely discussed that the function defined by equation (4.2) actually has the properties of a thermodynamic temperature in the sense that its two asymptotic values correspond to two different thermalization processes at two well-separated time scales [79]. In order to understand this, the idea is to couple a probe, described by an additional degree of freedom $x(t)$. This probe plays the role of the thermometer operating at frequency ω. Simple calculations show that the temperature probed in this way is [25]

$$T^x_{eff}(\omega, t_w) = \frac{\omega \langle |\hat{x}(\omega, t_w)|^2 \rangle}{4k_B \mathrm{Im}\{\hat{R}(\omega, t_w)\}}, \tag{4.3}$$

which is closely related to T_{eff} defined in equation (4.2). In equation (4.3), the hat denotes the Fourier transform of the corresponding quantity, computed over the time interval $t_w \leq t < \infty$. $\langle |\hat{x}(\omega)|^2 \rangle$ is the power spectral density of the fluctuations of x,

defined as the Fourier transform of the autocorrelation function at time t_w

$$\langle |\hat{x}(\omega, t_w)|^2 \rangle = \int_{t_w}^{\infty} \langle x(t) x(t_w) \rangle e^{-i\omega t} \mathrm{d}t, \tag{4.4}$$

whereas $\hat{R}(\omega, t_w)$ is the Fourier transform of the linear response function of x to an external time-dependent field f:

$$\hat{R}(\omega, t_w) = \frac{\langle \hat{x}(\omega, t_w) \rangle_f}{\hat{f}(\omega)}. \tag{4.5}$$

In equation (4.5), the average $\langle \hat{x}(\omega, t_w) \rangle_f$ is computed over a large number of independent realizations of f. If the probe is a harmonic oscillator, the mean value of the energy E of the probe measured at frequency ω is

$$\langle E \rangle = k_B T^x_{eff}(\omega, t_w), \tag{4.6}$$

Then in principle, equations (4.3) and (4.6) provide an experimental protocol to measure the function T_{eff} defined in equation (4.2) *for the aging glass* by means of the measurement of the ratio between the power spectrum and the linear response(4.3) or the energy fluctuations (4.6) of a small *probe*. This approach has been successfully implemented in numerical simulations of sheared supercooled liquids [80], where the effective temperature of a glassy system is probed by the Brownian motion of a small tracer in the glass. It is important to remark that in these numerical simulations the characteristic timescale of the tracer is tuned by varying its mass but its size is kept constant at the same value of the glass particles. Then the tracer is able to probe a low-frequency $T^x_{eff} > T$, provided that its length and timescales are comparable to those of the glassy structure. Otherwise the temperature perceived by the tracer is $T^x_{eff} = T$.

4.2 Fluctuations and response in Laponite suspensions

The experimental evidence of a low-frequency effective temperature higher than the bath temperature for structural and spin glasses is still an open problem. Therefore, several experimental works have recently attempted to look for the same effect in another kind of aging systems: *colloidal glasses*. Unlike structural or spin glasses, the formation of a colloidal glass does not require a temperature quench but only the packing of colloidal particles at a certain concentration in a solvent [81]. In particular, aqueous suspensions of clay *Laponite* have been studied as a prototype of colloidal glasses.

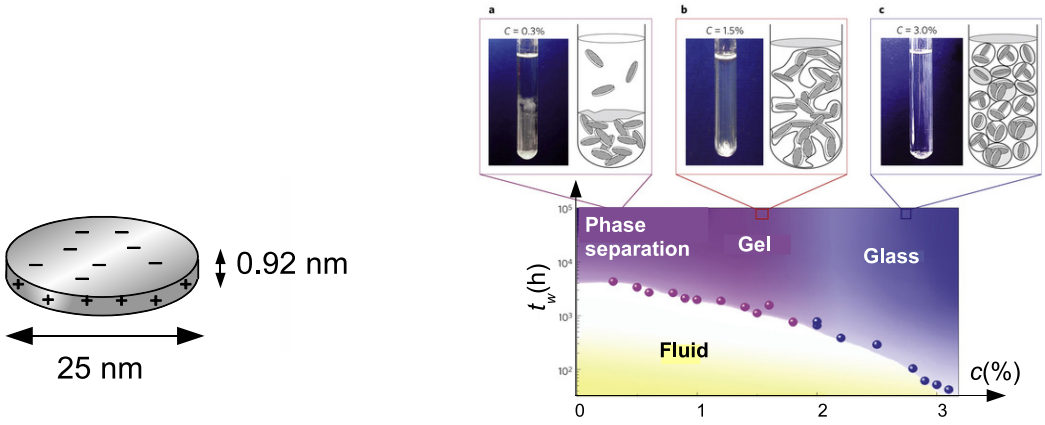

(a) (b)

Figure 4.2: (a) Sketch of a disc-shaped Laponite particle negatively charged on the surface and positively charged on the edge. (b) Experimental and numerical phase diagram of aqueous Laponite suspensions as a function of the concentration c and the time t_w elapsed after the preparation. Figure taken from [86]

4.2.1 Description of the system

Laponite is a synthetic clay widely used as a rheology-modifier in many technological applications: surface coatings, ceramic glazes, paints, household cleaners, personal care products, film former and to build optimized nanocomposites. It is formed by electrostatically charged disc-shaped particles of chemical formula

$$\mathrm{Na}^{+}_{0.7}[\mathrm{Si}_8\mathrm{Mg}_{5.5}\mathrm{Li}_{0.3}\mathrm{O}_{20}(\mathrm{OH})_4]^{0.7-}.$$

The size of these platelets is 1 nm (width) and 25 nm (diameter), as depicted in figure 4.2(a). When Laponite powder is mixed in water, the resulting suspensions exhibit a rich phase diagram due to the complex anisotropic electrostatic attraction and repulsion of Laponite platelets. At low concentrations $c \lesssim 3\%$ they display non-ergodic states that slowly evolve towards an equilibrium configuration. Depending on the concentration, phase-separated liquids, gels and glasses can be formed in these non-ergodic states, as shown in figure 4.2(b). In particular, for concentrations $2\% \lesssim c \lesssim 3\%$, aqueous Laponite suspensions form a *Wigner glass*. Unlike a gel, which is composed by connected particles forming a network, Laponite particles in the Wigner glass state remain spatially disconnected although arrested in a sort of empty cage. In this sense the localization length of the particles should be larger, or at least comparable to the particle size. Due to the dynamical arrest of the particles in an initial metastable state imposed by the electrostatic repulsion and the geometric constraints, Laponite suspensions exhibit physical aging. They undergo a transition from a viscous liquid phase into a viscoelastic phase in a few hours. Several properties of Laponite suspensions, such as viscoelasticity [82], translational and rotational diffusion [83] and optical susceptibility

[84], have been experimentally studied using rheology and dynamic light scattering. This techniques have allowed one to have a complete picture of the Laponite phase diagram as a function of the Laponite concentration and the ionic concentration which controls the strength of the electrostatic interactions [81, 85].

4.2.2 Overview on previous experimental results

Despite the well understood phase diagram of Laponite, the available results for the existence of an effective temperature T_{eff} different from the temperature T of the environment, are contradictory. Bellon *et al.* [87, 88, 89] performed an early experiment in order to measure T_{eff}. They reported an effective temperature from dielectric measurements indicating $T_{eff} \gg T$ for frequencies $f < 40$ Hz. On the other hand, the first rheological measurement of T_{eff} in Laponite was done by the same group using a rheometer sensitive to thermal fluctuations in the colloidal glass [88]. In this case it was found that T_{eff} was equal to the temperature of the environment. In principle, T_{eff} is expected to depend on the observable measured in the experiment, as discussed in section 4.1. Then in this chapter we focus only on rheological measurements where T_{eff} is determined by the measurement of the position of a probe immersed in the colloidal glass.

The rheological experiment described in [88] was a global bulk measurement so one may wonder whether a local experiment probing microscopic lengthscales gives or not the same results. This idea, in addition to the protocols (4.3) and (4.6) proposed for structural and spin glasses, motivated several experiments using *microrheology*. In this kind of experiments, a Brownian particle embedded in the fluid of interest is used as a mechanical probe to perform local rheological measurements, as described in detail in section 1.4. The goal is to measure whether the properties of the Brownian motion of the probe are affected by the fact that the surrounding fluid, acting as a bath, is out of equilibrium. Several microrheological experiments on Laponite solutions have been done by different groups using various techniques. However, the results on the behavior of T_{eff} are rather contradictory. Let us summarize them.

- Abou *et al.* [90], performed independent measurements of the free Brownian motion of a micron-sized bead and the response of the bead trapped by optical tweezers to an external force. Then using an alternative version of equation (4.3) they observed that T_{eff} increases in time from the value of the bath temperature to a maximum and then it decreases to the bath temperature.

- Jabbari-Farouji *et al.* [91] used a combination of *passive* and *active microrheology* techniques (see section 4.4) to measure the power spectral density of the fluctuations of a trapped micron-sized bead and the response of the trapped bead to an oscillatory force. Then, using directly equation (4.3) they computed T_{eff}. In this experiment no deviation of the effective temperature from the bath temperature was observed over several decades in frequency (1 Hz$-$10 kHz).

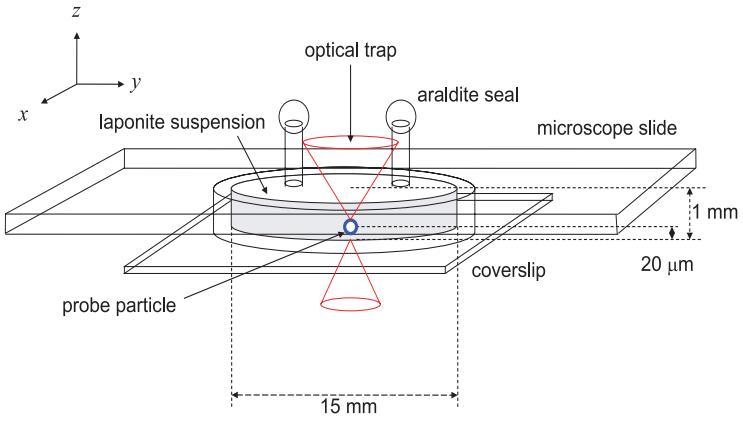

Figure 4.3: Diagram of the sample cell used during the experiment.

- Greinert *et al.* [92] adapted equation (4.6) to compute T_{eff} only by the measurement of the spontaneous fluctuations of the position of a particle trapped by optical tweezers at two different trapping stiffness without applying any time-dependent force. They found that the effective temperature increases monotonically in time after a few hours once the system becomes viscoelastic.

- Jabbari-Farouji *et al.* [93] confirmed that $T_{eff} = T$ for the frequency range of 1 Hz−10 kHz for Laponite suspensions in two different phases (glass and gel) all along the aging process.

Given the conflicting results previously described from the same kind of experimental techniques, in this section we compare them in order to understand where the difference may come from. Our purpose is to describe the results of the measurement of the Brownian motion of several particles inside a Laponite solution using a combination of different techniques proposed in previous references. We extend our measurement to frequencies one order of magnitude smaller than those reported in the literature. This is because an effective temperature higher than the bath temperature is expected to occur for the slowest structural modes of the colloidal glass. The measurements performed with several particles exploit the spatial homogeneity of the suspension and are of particular importance because they allow us to compare simultaneously passive and active microrheology techniques in the same sample.

4.3 Description of the experiment

4.3.1 Sample preparation

Physical properties of Laponite suspensions are very sensitive to the method used during their preparation [94]. Hence, a careful experimental protocol must be followed

in order to perform reproducible measurements of their aging properties. Laponite RD, the most frequently studied grade and the one studied in this work, is a hygroscopic powder that must be handled in a controlled dry atmosphere. The powder is mixed with ultrapure water, at a weight concentration which has been varied from 2.0 to 3.0%. The pH is adjusted to 10 in order to ensure chemical stability of the samples. At lower pH, the decomposition of clay particles occur. CO_2 absorption by water can modify the pH of the samples and then their aging properties. For these purposes, the preparation of the samples is done entirely within a glove box filled with circulating nitrogen. The suspension is vigorously stirred by a magnetic stirrer during 30 minutes. The resulting aqueous suspension is filtered through a 0.45 μm micropore filter in order to destroy large particle aggregates and obtain a reproducible initial state. The initial aging time ($t_w = 0$) is taken at this step. Immediately after filtration, a small volume fraction (10^{-6}) of silica microspheres (radius $r = 1\,\mu$m) is injected into the suspensions. The sample is placed in a ultrasonic bath during 10 minutes to destroy small undesired bubbles that could be present during the optical tweezers manipulation. The suspension is introduced in a sample cell which is sealed in order to avoid evaporation. The cell consists of a microscope slide and a coverslip separated by a cylindrical plastic spacer of inner diameter 15 mm, thickness 1 mm and glued together with photopolymer adhesive, as shown in Fig. 4.3. In this cell the inputs are sealed with araldite adhesive in order to avoid evaporation and direct contact with CO_2 from air.

4.3.2 Multi-trap system

The experiment is performed at room temperature ($22 \pm 1^\circ$ C) in the multi-trap setup described in section 1.3. Multiple probe particles have to be trapped in the same sample in order to perform simultaneously the passive and active microrheology measurements described in section 4.4. Since two trapped particles are needed for each technique, at least three different optical traps must be created simultaneously, as shown in figure 4.4. For passive measurements, two static traps of different stiffness are needed. We label the weakest trap as '1' while the strongest one as '2'. For active measurements, we need a static trap to measure the power spectral density of the fluctuations of the particle position. For convenience, we choose the same trap '2' for such a purpose. In addition, we need a trap with time-dependent position in order to measure the response of the probe to an external forcing. This trap is labeled as '3'. The separation distance between adjacent traps is set to $d = 9.3\,\mu$m. We checked that such distance is sufficiently large to avoid correlations between their motions. In the following, x defines the direction along which the position of trap '3' is oscillated in time, while y corresponds the perpendicular direction (see Fig. 4.4). For simplicity, all the calculations are done for the x coordinates only.

The creation of three independent optical traps on the $x - y$ plane is implemented by means of the XY AOD system described in subsection 1.3.1, This experimental configuration is shown in figure 4.4. The laser beam scans three different positions

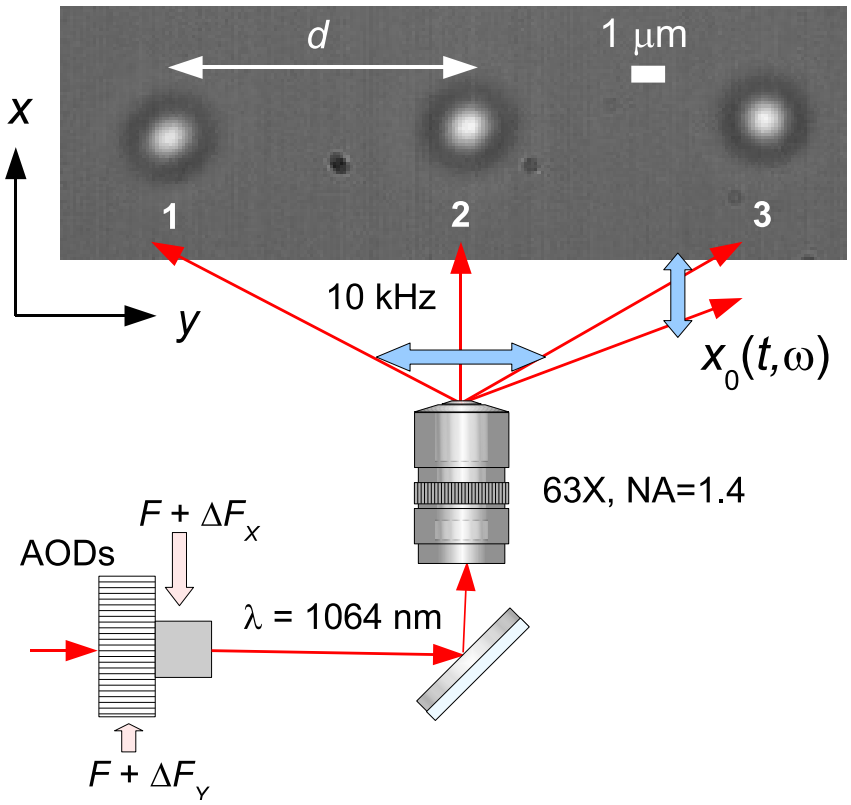

Figure 4.4: Diagram of the creation of three independent optical traps using the multi-trap system described in section 1.3. The traps are separated by a distance $d = 9.3\,\mu$m. The bright spots on the snapshot correspond to three trapped particles ($r = 1\,\mu$m).

along the y direction at a rate of 10 kHz by applying a two-step frequency modulation

$$\Delta F_Y(t) = \Delta_Y \left[\Theta(t-\Delta t) - 1 + \Theta(t-3\Delta t)\right],\ 0 \leq t \leq 5\Delta t,$$

to the Y AOD, where Θ is the Heaviside step function. We set $\Delta_Y = 5$ MHz and $\Delta t = 20\,\mu$s, corresponding to a separation distance $d = 9.3\,\mu$m between the traps and $\Delta t = 20\,\mu$s, $2\Delta t = 40\,\mu$s and $2\Delta t = 40\,\mu$s the time that the laser beam stays in the traps '1', '2' and '3', respectively. A slow oscillation $x_0(t,\omega)$ of the position of trap '3' is accomplished by deflecting the laser beam along x. This is done by applying the following frequency modulation to the X AOD

$$\Delta F_X(t,\omega) = \Delta F_0 \sum_{j=1}^{n} \sin(\omega_i t),$$

where n is the number of sinusoidal modes at frequency $\omega_i = 2\pi f_i$ $(i = 1,\ldots,n)$ that are studied simultaneously. In the experiment we set $\Delta F_0 = 60$ kHz corresponding to an oscillatory displacement of the trap '3' of the form

$$x_0(t,\omega) = A \sum_{j=1}^{n} \sin(\omega_i t), \tag{4.7}$$

where the amplitude of the displacement $A = 100$ nm is small enough to be in the linear response regime of the optical trap. The stiffness of each trap is proportional to the time that the laser beam stays in the corresponding position. We check that by selecting the ratio 20:40:40 for the visiting time of traps '1', '2' and '3', respectively we obtain a stiffness ratio of 20.7:39.7:39.6, respectively. Specifically the stiffness of the three traps are: $k_1 = 3.73$ pN/μm, $k_2 = 7.15$ pN/μm, $k_3 = 7.12$ pN/μm. The stiffness is measured using the power spectrum technique described in subsection 1.3.3.

4.4 Microrheology methods

Uisng the multi-trap configuration of figure 4.4, we perform *simultaneoulsy* two different methods to measure the effective temperature probed by the trapped particles. These methods are based in passive and active microrheology, see section 1.4.

4.4.1 Passive microrheology

The first method, proposed by Greinert *et al* [92], is based on passive microrheology (PMR). It exploits the generalized equipartition relation (4.6) valid for a small probe in a glassy systems [80]. The basic idea is the following. Since a Laponite suspension becomes viscoelastic as it ages, a particle in an optical trap of stiffness k is subjected to an additional force

$$F_e = -K_{Lap}(t_w)x,$$

due to the elasticity of the colloidal glass, where K_{Lap} denotes the effective elastic stiffness of the colloid. Then, in analogy with equation (4.6) for a harmonic oscillator, an effective temperature $T_{eff}(t_w)$ can be defined for the overdamped Brownian motion of the particle

$$\frac{k_B\, T_{eff}(t_w)}{k + K_{Lap}(t_w)} = \left\langle x^2 - \langle x \rangle^2 \right\rangle, \tag{4.8}$$

where brackets stand for average over a time window such that K_{Lap} is almost constant. In equation (4.8), $(k+K_{Lap})\left\langle x^2 - \langle x \rangle^2 \right\rangle/2$ represents the average value of the effective potential energy of the particle at time t_w due to the optical trapping force and the elastic force F_e exerted by the medium. Note that $K_{Lap}(t_w)$ and $T_{eff}(t_w)$ are global quantities that integrate the contribution of all frequencies. Hence, their measurements are strongly limited by the capability of detecting slow modes. Therefore, in practice the time average $\langle \ldots \rangle$ in equation (4.8) must be computed over a sufficiently large time window to detect the slowest structural rearrangements during the aging but at the same time sufficiently short to avoid a large variation of the viscoelasticity of the colloidal glass.

We consider the traps '1' and '2' in figure 4.4 with different stiffness: k_1 and k_2, respectively. At a given aging time t_w, we compute the variance of the position of the j-th particle ($j = 1, 2$):

$$\langle \delta x^2(t_w) \rangle_j = \langle x^2 - \langle x \rangle^2 \rangle_j,$$

over a time window $[t, t + \Delta\tau]$, where $t \geq t_w$. Different values of $\Delta\tau$ are used in the calculations: 3 s $< \Delta\tau <$ 25 s. One must be aware that the shortest time window of 3 s like the one used in [92] is not sufficiently long to take into account the role of low frequency fluctuations at late stages during aging. Consequently the variances can be underestimated in this regime, as noted by [96]. The values of the variance computed in each window $\Delta\tau$ are then averaged over a longer time interval $t_w \leq t \leq t_w + \Delta t$, with $\Delta t > \Delta\tau$. The value of Δt must be chosen sufficiently short to ensure that the viscoelasticity of the colloidal glass remains almost constant. Specifically, the variance of x for each trapped particle is computed as

$$\langle \delta x^2(t_w) \rangle_j = \frac{1}{\Delta\tau \Delta t} \int_{t_w}^{t_w+\Delta t} dt \int_{t}^{t+\Delta\tau} (x_j^2(t') - \langle x_j(t') \rangle^2) dt', \tag{4.9}$$

where we set $\Delta t = 50$ s and $j = 1, 2$ correspond to the variance measured for the particles trapped by '1' and '2', respectively. Assuming the equipartition relation equation (4.8) still holds in this out-of-equilibrium system, T_{eff} is computed as in [92]. The expressions of the effective temperature and of the Laponite elastic stiffness K_{Lap} are the following

$$k_B T_{eff}(t_w) = \frac{(k_2 - k_1)\langle \delta x^2(t_w) \rangle_1 \langle \delta x^2(t_w) \rangle_2}{\langle \delta x^2(t_w) \rangle_1 - \langle \delta x^2(t_w) \rangle_2}, \tag{4.10}$$

$$K_{Lap}(t_w) = \frac{k_1\, \langle \delta x^2(t_w) \rangle_1 - k_2 \langle \delta x^2(t_w) \rangle_2}{\langle \delta x^2(t_w) \rangle_1 - \langle \delta x^2(t_w) \rangle_2}. \tag{4.11}$$

This technique, although very simple, has several drawbacks that we will discuss in the next sections. Furthermore, being a global measurement, it has no control of what is going on at different timescales.

4.4.2 Active microrheology

The second method involves a combination of PMR and active microrheology (AMR). This is the approach followed in references [90, 91, 93]. It allows one to measure T_{eff} using equation (4.3) through the simultaneous measurement of the power spectrum of the spontaneous fluctuations of the particle position and the linear response function to an external force.

In our experiment, we apply an oscillatory force $f_0(t,\omega) = k_3 x_0(t,\omega)$ to the trapped particle at certain frequencies ω by means of the spatial modulation $x_0(t,\omega)$ of trap '3' given in equation (4.7). Next, we determine the Fourier transform of the linear response function R of x due to f:

$$\hat{R}(\omega, t_w) = \frac{\hat{x}(\omega, t_w)}{\hat{f}_0(\omega)}, \tag{4.12}$$

where the hat stands for the Fourier transform. As the system is in a nonstationary state, all the observables depend on t_w. Therefore for a fixed time t_w, the Fourier transforms in equation (4.12) must be computed over a time window $t_w \leq t \leq t_w + \Delta t$ according to [25]. We set $\Delta t = 50$ s in order to compare the results provided by this method with those obtained by the PMR method described in subsection 4.4.1. By taking into account that the effective Hookean force on the particle due the relative displacement $x(t) - x_0(t,\omega)$ with respect to the laser beam focus is $-k_3[x(t) - x_0(t,\omega)]$, the motion of the probe particle is described by the following Langevin equation

$$\int_{-\infty}^{t} \Gamma(t - t', t_w)\dot{x}(t')dt' + k_3[x - x_0(t,\omega)] = \xi(t), \tag{4.13}$$

where we have written the explicit dependence on the slow variable t_w due to the nonstationarity of the system. In frequency domain, equation (4.13) reads

$$-\mathrm{i}\omega\gamma(\omega, t_w)\hat{x} + [k_3 + K_{Lap}(\omega, t_w)]\hat{x} = \hat{f}_0(\omega) + \hat{\xi}(\omega), \tag{4.14}$$

where $\gamma(\omega, t_w)$ and $K_{Lap}(\omega, t_w)$ are real functions that represent separately the viscous and elastic[1] terms of the Fourier transform of the viscoelastic kernel Γ, i.e.

$$\hat{\Gamma} = \gamma + \mathrm{i}\frac{K_{Lap}}{\omega}.$$

[1]The frequency-dependent Laponite stiffness defined by equation (4.14) is different from the *global* Laponite stiffness defined by the equipartition relation (4.8). Nevertheless we will keep the same notation for both quantities throughout the chapter because both quantify the elasticity of the Laponite suspension and they exhibit the same qualitative behavior as a function of t_w.

On the other hand, the term $\hat{f}_0(\omega) = k_3\hat{x}_0(\omega)$ on the right-hand side of equation (4.14) is the force exterted by the acting driving of the trap position, whereas $\xi(t)$ is a stochastic process of zero mean and power spectral density

$$\langle|\hat{\xi}(\omega)|^2\rangle = 4k_BT_{eff}(\omega,t_w)\gamma(\omega,t_w),$$

representing the nonequilibrium collisions of the Laponite platelets with the probe. The relation between γ and K_{Lap} with the complex viscosity $\eta^* = \eta' - i\eta''$ and the shear modulus $G = G' + iG''$, usually measured in rheology experiments, is

$$\begin{aligned} \gamma &= 6\pi r\eta' &&= \frac{6\pi rG''}{\omega}, \\ K_{Lap} &= 6\pi r\omega\eta'' &&= 6\pi rG', \end{aligned} \tag{4.15}$$

Equation (4.14) leads to the following expression for the inverse of the linear response function of the particle

$$\frac{1}{\hat{R}(\omega,t_w)} = -\mathrm{i}\omega\gamma(\omega,t_w) + [k_3 + K_{Lap}(\omega,t_w)], \tag{4.16}$$

Therefore, by measuring directly the mechanical response of x to the applied external force at a given frequency, it is possible to resolve the viscosity and the elasticity of the colloidal glass at aging time t_w by means of the expressions

$$\frac{\omega\gamma(\omega,t_w)}{k_3} = \mathrm{Im}\left[\frac{1}{k_3\hat{R}(\omega,t_w)}\right], \tag{4.17}$$

$$\frac{K_{Lap}(\omega,t_w)}{k_3} = \mathrm{Re}\left[\frac{1}{k_3\hat{R}(\omega,t_w)}\right] - 1. \tag{4.18}$$

In our case, the position of trap '3' is oscillated in time along the x direction at three different frequencies $\omega = \omega_j, j = 1,2,3$ simultaneously according to

$$x_0(t,\omega) = A[\sin(\omega_1 t) + \sin(\omega_2 t) + \sin(\omega_3 t)], \tag{4.19}$$

where $f_1 = \omega_1/2\pi = 0.3$ Hz, $f_2 = \omega_2/2\pi = 0.5$ Hz, $f_3 = \omega_3/2\pi = 1.0$ Hz, and $A = 1.04 \times 10^{-7}$ m. These frequencies are one order of magnitude smaller than the lowest ones resolved in previous works using AMR [91, 93]. Therefore our study goes deeper into the slow timescales where T_{eff} could be different from T. Higher frequency sinusoidal oscillations ($\omega/2\pi = 2.0$, 4.0, 8.0 Hz) and different low-frequency ones (0.25, 0.75 Hz) are also checked in order to compare our results with different mechanical excitations of the probe at different frequencies.

The AMR method previously described allows one to determine directly the effective temperature of the colloidal glass probed by the Brownian particle using equation (4.3). First of all, we synchronize the input forcing signal $x_0(t,\omega)$ with the response of the

trapped bead $x(t)$. The Fourier transform of the response function is computed using equation (4.12) for a probe particle driven by trap '3'. On the other hand, we measure the power spectral density of the position fluctuations of the particle trapped by '2', i.e. in absence of the external driving. For this reason, traps '2' and '3' are created with the same stiffness.

4.5 Viscoelastic properties of the aging colloidal glass

We first present separately the results of the time evolution of viscosity and elasticity of the colloidal glass at low frequencies during aging. The time evolution of the dimensionless quantity $\omega\gamma/k_3$, linearly proportional to the dynamic viscosity η' of the suspension, is shown in Fig. 4.5(a). As expected, it increases continuously as the system ages. On the other hand, the evolution of the stiffness K_{Lap} is qualitatively different, as shown in Fig. 4.5(b). For $t_w < 300$ min, $K_{Lap} \approx 0$, revealing an entirely viscous nature of the Laponite suspension, while for $t_w > 300$ min it becomes viscoelastic, with K_{Lap} increasing dramatically in aging time from 0 to 10 times the stiffness of the second trap $k_2 = 7.15$ pN/μm. In order to compare our low-frequency AMR results with previous rheological measurements, we plot in figure 4.5(c) the time evolution of the modulus of the complex viscosity, given by $|\eta^*| = (\gamma^2 + K_{Lap}^2/\omega^2)^{1/2}/6\pi r$. We observe that $|\eta^*|$ increases, almost exponentially, two orders of magnitude during the first 500 minutes of aging. The behavior of $|\eta^*|$ is in good agreement with previous rheological measurements [95]. These results become more evident when protting the time evolution of the real G' and the imaginary G'' part of the shear modulus defined in equation (4.15), as shown in figures 4.5(d) and 4.5(e). During the first 300 s the quantity G''/ω, which is proportional to the viscosity is frequency independent but it increases more than six times. This shows a Newtonian behavior of the Laponite suspension that is verified by the fact that $G' = 0$ for this aging time interval. Then the system undergoes a rather abrupt transition and G' starts to increase continuously, becoming comparable to the values of G'' that become frequency-dependent. This result indicates a sharp transition from a purely viscous phase to a viscoelastic phase, as observed in bulk measurements [95]. On the other hand, the time $t_g \approx 300$ min at which the transition occurs at this concentration (2.8% wt) is consistent for both PMR and AMR, as shown in figure 4.5(b). We notice that AMR measurements are more accurate, leading to a very small data dispersion around the mean trend and allowing to resolve the aging time evolution for each frequency. Instead, according to equation (4.11) the global stiffness determined from PMR is very sensitive to the inverse of the difference $\langle \delta x^2 \rangle_1 - \langle \delta x^2 \rangle_2$. Indeed, as t_w increases, the relative difference between these two variances decreases, leading to increasingly large data dispersion for $t_w > 350$ min. .

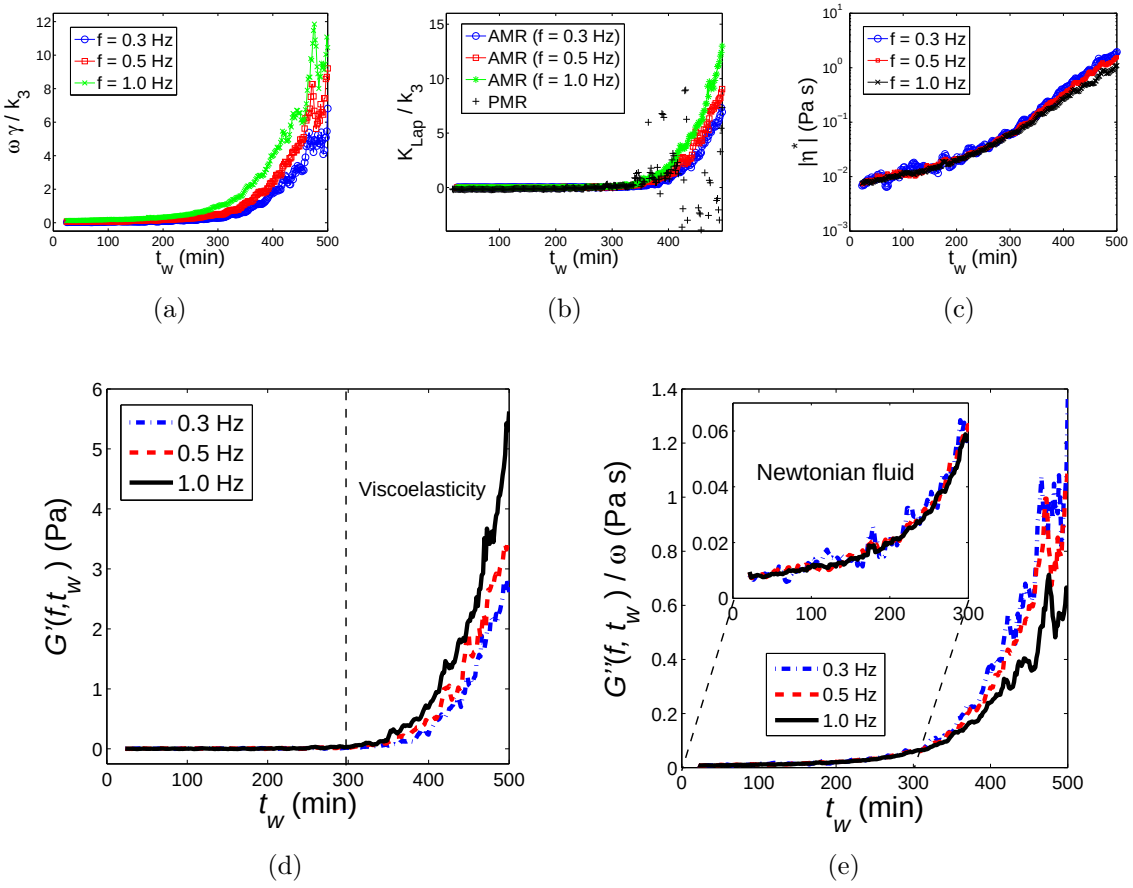

Figure 4.5: (a) Time evolution of the viscous drag coefficient γ obtained by means of AMR. (b) Time evolution of elasticity K_{Lap} obtained by PMR and AMR. (c) Time evolution of the modulus of the complex viscosity. (d) Time evolution of the real part G' of the shear modulus. The vertical dashed line indicates the transition to the viscoelastic phase which occurs at $t_w \approx 300\,\mathrm{min} \equiv t_g$ (e) Time evolution of the imaginary part G'' of the shear modulus. Inset: Expanded view for $0 < t_w \leq t_g$ showing the frequency independence of G''/ω. The measurements were performed at a Laponite concentration of 2.8 %wt.

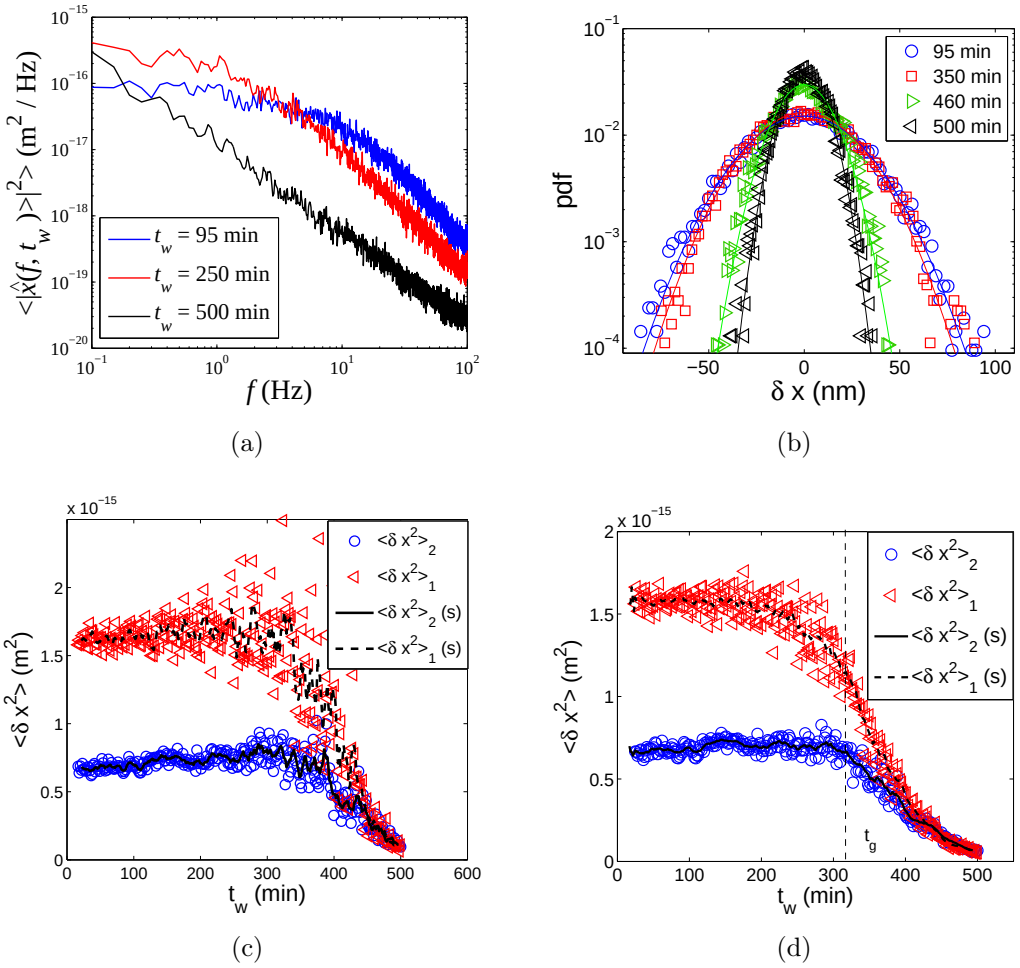

Figure 4.6: (a) Power spectral density of the fluctuations of x of a particle in trap '2' measured at different aging times t_w. As t_w increases the corner frequency of the spectrum is shifted to the left. (b) PDFs of δx at different t_w for particle '2'. (c) Time evolution of variances for particles '1' and '2' computed for $\Delta\tau = 25$ s. Labels (s) correspond to smooth curves (see text, Subsection 4.6.1). (d) Time evolution of variances computed for $\Delta\tau = 3$ s.

4.6 Nonequilibrium fluctuations and response

We fist study the statistical properties of the spontaneous fluctuations of $\delta x = x - \langle x \rangle$ for the particles trapped by '1' and '2' by means of the probability distribution and the variance of δx. This analysis is performed over the time windows Δt defined in equation (4.9). Some care is needed because the results could depend on the length of Δt. First, these analyzing windows cannot be made too large because the viscoelastic properties of Laponite evolve as a function of time. Second, Δt can not be chosen very short because long-lived fluctuations could be ignored in the analysis. Indeed, it turns out that as t_w increases, the slowest modes are the main contribution to the power content of the fluctuations: the corner frequency (see definition by equation (1.9) in section 1.2.2) of the power spectrum of x, decreases continuously mainly because of the increase of viscosity of the suspension, as shown in figure 4.6(a). At the end of the experiment, the power spectrum of x shows that the corner frequency is lower than 0.1 Hz. Since the variance of x is equal to the integral of the power spectrum over the whole frequency domain, then the resulting values can be underestimated as t_w increases. if Δt is chosen very short [96].

In order to avoid the previous problems, in equation (4.9) we use moving analyzing time windows of length $\Delta\tau = 25$ s along the large time interval of length $\Delta t = 50$ s. These values are sufficiently large to take into account the power of slow fluctuations. Figure 4.6(b) shows that fluctuations of δx are Gaussian, as checked by the corresponding Gaussian fits plotted as solid lines for clarity. Hence, the variance $\langle \delta x^2(t_w) \rangle$ is actually the only relevant quantity to characterize the spontaneous fluctuations of x. The aging time evolution of the variances $\langle \delta x^2 \rangle_1$ and $\langle \delta x^2 \rangle_2$ for particles '1' and '2' is shown in figure 4.6(c). For $t_w \lesssim 300$ min, both variances are quite constant whereas for $t_w \gtrsim 300$ min they decrease up to one order of magnitude at $t_w = 500$ min. The transition between these two regimes is kind of abrupt and occurs at $t_w \approx 300$. This time corresponds to the transition from a purely viscous liquid-like phase to viscoelastic glass at time $t_g = 300$ min according to the results presented in subsection 4.5. In figure 4.6(d) we also show the variances purposely computed for $\Delta\tau = 3$ s. Note that for this short analyzing time windows the variance is underestimated compared to the values shown in figure 4.7(b) for $\Delta t = 25$ s. Then, the time at which it starts to decrease apparently depends on the value of the trap stiffness and occurs before 300 min. Of course, this is only a result of inappropriate data analysis associated to the underestimate of the long-lived fluctutions. In subsection 4.6.1 the we show that this gives rise to artifacts resulting in an apparent sharp increase of T_{eff} for $t_g < t_w$ as that reported in [92].

On the other hand, frequencies as low as 0.1 Hz could be properly resolved using the AMR method. In figure 4.7(a) we plot a typical realization of the oscillatory force f_0, given by (4.19), resulting from the sum of three different modes $f = \omega/(2\pi) = 0.3, 0.5$ and 1.0 Hz. We also plot the displacement x of the particle '3' in response to this external force. In figure 4.7(b) we observe that the application of this f_0 leads to an increase of two orders of magnitude of its spectrum of x at the corresponding driving frequency

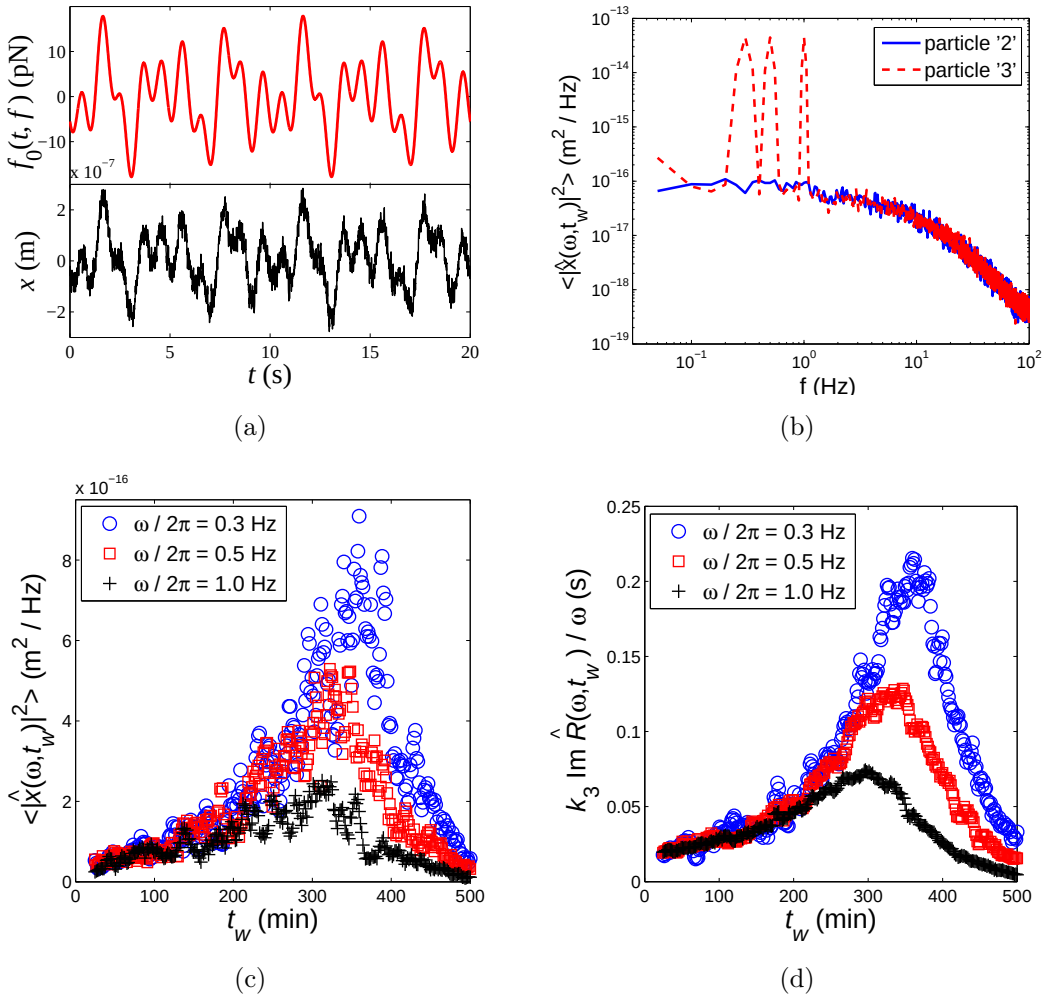

Figure 4.7: (a) Oscillatory force applied to particle '3' (upper panel) implemented by the particular waveform (4.19) and the resulting particle displacement (lower panel). (b) Spectra of x for particles '2' and '3' at $t_w = 95$ min. (c) Time evolution of the power spectral densities of the position fluctuations of particle '2' at three fixed frequencies. (d) Time evolution of the imaginary part of the Fourier transform of the response functions of particle '3' at the same frequencies fixed by the external driving.

ω. However no higher-order harmonics are excited, i.e. the system is in the linear response regime. Therefore, both the power spectral density and the response function could be measured with good frequency resolution in the case of AMR. Figure 4.7(b) also confirms the spatial homogeneity of the sample because the values of the power spectra at non-excited frequencies are the same for particles located in different places. This is consistent with the homogeneity of the glassy phase of Laponite discussed in [81]. Figure 4.7(c) shows the time evolution of the power spectral density for each frequency $\omega = \omega_j, j = 1, 2, 3$. The time behavior of $|\hat{x}(\omega, t_w)|^2$ is completely different from that of ergodic liquids at equilibrium. In such a case the value of $|\hat{x}(\omega, t_w)|^2$ is constant in time. We observe that the nontrivial shape of the power spectral density has a maximum which depends on the value of the corresponding frequency. Figure 4.7(d) shows the time evolution of the imaginary part of the Fourier transform of the response function $\hat{R}(\omega, t_w)$ at each frequency $\omega = \omega_j, j = 1, 2, 3$, calculated by means of equation (4.12). We observe the same behavior in time for each frequency, indicating that $|\hat{x}(\omega, t_w)|^2$ and $\mathrm{Im}\{\hat{R}(\omega, t_w)\}$ are related by a proportionality constant during aging. It has to be noted that the position of these maxima depend on the strength of the optical traps used to measure the response and fluctuations. These strengths are the same in our case whereas they are different in the experiment described in reference [90] where the spontaneous fluctuation measurements are performed on free particles ($k = 0$). The difference in the value of the stiffness induces a shift on the time position of these maxima which must be corrected in the data analysis. Small errors in this correction may of course induce an apparent anomalous maximum of T_{eff} as a function of t_w when computing the ratio between$|\hat{x}(\omega, t_w)|^2$ and $\mathrm{Im}\{\hat{R}(\omega, t_w)\}$, like the maximum of $T_{eff} > T$ reported in [90].

4.6.1 Effective temperature

The effective temperatures perceived by the Brownian probe determined by means of both PMR and AMR methods are shown in figures 4.8(a) and 4.8(b), respectively. We first show as black triangles the most reliable PMR results obtained by using an analyzing time window $\Delta\tau = 25$ s for the computation of the variances using equation (4.10). In order to find the mean trend of the aging time evolution of the scattered experimental variances shown in figure 4.6(c), we convolute these raw data with *smoothing* rectangular time windows of length $\delta\tau$. Note that these smoothing time windows are physically meaningless and we use them only as a tool to reduce the variability of experimental data around the actual mean trend. They must be chosen short enough to avoid a wrong determination of the mean trend for 300 min $< t_w$ since a large value of $\delta\tau$ would involve a moving time average of values that decrease continuously in aging time. The smoothed curves obtained by means of this procedure with $\delta\tau = 5$ min are also shown in figures 4.6(c) as solid and dashed lines. From these smooth curves we compute the effective temperature along aging by means of equation (4.10). In figure 4.8(a) we observe that for $t_w < 300$ min the effective temperature is very close to the bath temperature $T = 295$ K with very few data dispersion around

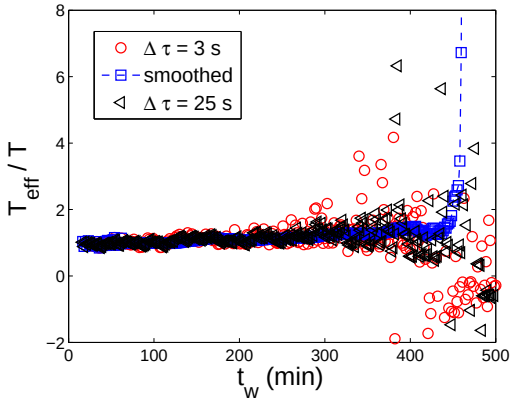

(a)

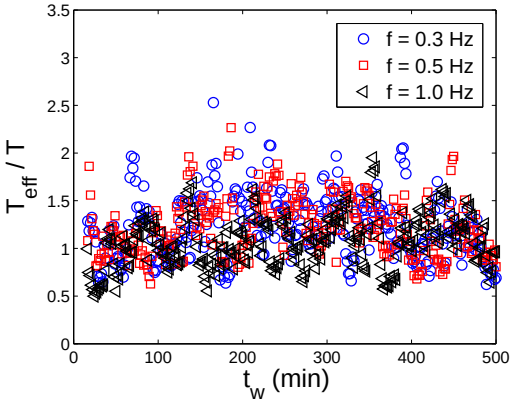

(b)

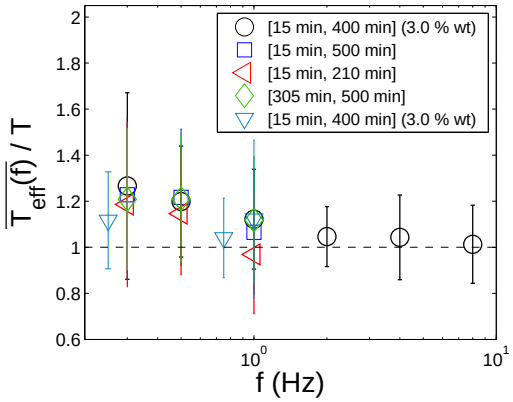

(c)

Figure 4.8: (a) Time evolution of effective temperatures probed by the Brownian particle during aging obtained by means of PMR (see text for symbols). (b) Time evolution of effective temperatures for different frequencies obtained by means of AMR. (c) Aging time average of the effective temperatures obtained by AMR for different frequencies. Error bars represent the standard deviation of the data shown in figure 4.8(b).

it, typically $\Delta T_{eff}/T_{eff} < 10\%$. This is due to the fact that at this aging stage the aqueous Laponite suspension behaves as a purely viscous liquid leading to small and constant data dispersion of $\langle \delta x^2 \rangle$. For 300 min $< t_w <$ 350 min, corresponding to the aging times when the elasticity of the suspension begins to become non-vanishing, the data variability increases ($\Delta T_{eff}/T_{eff} \approx 30\%$) but the mean value of T_{eff} remains close to T, revealing no anomalous increase like the one observed in [92] for $\Delta\tau = 3.3$ s. For 350 min $< t_w$ this method fails to give reliable results since we observe an increasingly large variability of the effective temperature leading even to negative values of T_{eff} due to the fact that the dispersions of $\langle \delta x^2 \rangle_1$ and $\langle \delta x^2 \rangle_2$ are comparable to or even larger than $\langle \delta x^2 \rangle_1 - \langle \delta x^2 \rangle_2$ in equation (4.10), as shown in figure 4.6(c).

Artifacts in the estimate of the effective temperature

Artifact due to analyzing time window

In order to identify the artifacts that can arise for PMR and give an explanation of the strange behavior of T_{eff} observed in previous PMR studies on Laponite [92], we first analyze the effect of using inappropriate short analyzing time windows. We purposely perform the analysis for a short time window $\Delta\tau = 3$ s (close to the one used in [92]), leading to the time evolution of the displacement variances shown in figure 4.6(d). In this case the transition point from the plateau to the decaying curve depends on the value of the stiffness of the optical trap. We observe that the transition occurs first (around $t_w = 250$ min) for the weakest trap ('1') than for the strongest one ('2') (around $t_w = 300$ min), indicating that the motion of a probe particle could be sensitive to the strength of the optical trap close to the glass transition. However, this is nothing but an artifact due to the use of a very short analyzing time window. Since the corner frequency of the power spectral density of displacement fluctuations depends linearly on the stiffness of the optical trap k, large underestimates of the corresponding variance occur first for the weakest trap, leading to such an apparent dependence on k. In fact, when using $\Delta\tau = 25$ s, there is no such a dependence as shown in figure 4.6(c). Even when smaller data variability is observed for $\Delta\tau = 3$ s than for 25 s, one must be aware that the latter case is more reliable than the former since longer lived modes are taken into account in a method which must integrate the contributions of as many frequencies as possible. The consequence of using such a short analyzing time window in that for 230 min $< t_w <$ 300 min an apparent systematic increase of T_{eff} is observed due to the significant underestimation of $\langle \delta x^2 \rangle_1$ with respect to $\langle \delta x^2 \rangle_2$, as shown in red circles in figure 4.8(a). For longer aging times, once again the large data dispersion of the values of the variances lead to extremely scattered values of T_{eff}.

Artifact due to data smoothing

A second artifact can arise easily due to wrong data smoothing. As explained previously, in order to find the mean trend of the aging time evolution of the scattered experimental variances computed at every t_w we convolute these raw data with *smooth-*

ing rectangular time windows. Figure 4.6(d) shows as solid and dashed lines the smooth curves obtained for a very long smoothing window ($\delta\tau = 16$ min). In this case, a curve smoother than the one shown in figure 4.7(b) for $\delta\tau = 5$ min is obtained but a worse trend is found for long aging times since in this regime the values of the variances significantly decrease during 16 min. The time evolution of the effective temperature computed with the smooth variances of figure 4.6(d) is shown as blue squares in figure 4.8(a). In this case the combined effects of wrong data analysis and smoothing lead to a fake sharp increase of T_{eff}.

Discussion on PMR method

It is important to point out that the global effective temperature $T_{eff}(t_w)$ introduced in equation (4.8) integrates the contribution of every local effective temperature $T_{eff}(\omega, t_w)$, but in practice it is limited to the accessible experimental timescales of 10 ms (the sampling period) and 25 s (the length of the analyzing time window), corresponding to the finite frequency range [0.04 Hz, 100 Hz]. Any possible violation in this frequency range should certainly lead to $T_{eff}(t_w) \neq T$. Consequently, by means of the PMR technique we verify in figure 4.8(a) that $T_{eff} = T$ is observed in this system even for frequencies as low as 0.04 Hz and for waiting times as long as 350 minutes when the elasticity of the suspension is zero or very small. For longer waiting times the large data variability using PMR hides any possible trend, but the direct measurement of the response function by means of AMR allows to overcome this problem showing that $T_{eff} = T$ even for 350 min $< t_w <$ 500 min, as shown in the following.

Discussion on AMR method

The AMR results for the effective temperature at different frequencies are shown in figure 4.8(b). We verify that there is no actual systematic increase of $T_{eff}(\omega, t_w)$ as the colloidal glass ages. The effective temperatures recorded by the probe particles at a given time scale $2\pi/\omega$ are equal to the bath temperature during aging even for the slowest modes studied with this method ($\sim 1/f_1 \approx 4$ s). Unlike PMR measurements, we find that the variability of the data is constant in aging time, which implies that AMR is a more reliable method even during the transition to the viscoelastic regime. In order to check if $T_{eff}(\omega, t_w) = T$ within experimental accuracy, we can compute the aging time average of $T_{eff}(\omega, t_w)$ over different aging time intervals $t_w \in [t_w^i, t_w^f]$

$$\overline{T_{eff}(\omega)} = \frac{1}{t_w^f - t_w^i} \int_{t_w^i}^{t_w^f} T_{eff}(\omega, t'_w) dt'_w, \tag{4.20}$$

for each frequency ω. Figure 4.8(c) shows the results of $\overline{T_{eff}(\omega)}$ with their respective error bars corresponding to the standard deviations of the data sets. For comparison, we also determine the effective temperature of the colloidal glass at 3.0% wt of Laponite (for which the suspension becomes viscoelastic at $t_g \approx 250$ min) for two different shapes of the external perturbation $f_0(t, \omega)$ (with sinusoidal modes $f = 0.3,\ 0.5,\ 1.0,\ 2.0,$

4.0 and 8.0 Hz, and $f = 0.25$, 0.75 and 1.0 Hz) without observing any deviation of the effective temperatures from the bath temperature within experimental accuracy. Note that the AMR method does not allow the determination of the local effective temperatures corresponding to frequencies as low as those detectable using PMR. This is due to large errors in the measurement of the response function at low frequencies. Nevertheless the time evolution of the effective temperature can be recorded at every single frequency all along the aging process with constant accuracy (data dispersion $\lesssim 30\%$) using the AMR method. These results reveal that no systematic increase or decrease of T_{eff} is observed even during the late aging stage when the elasticity of the colloidal glass is large. In addition, the use of the spectral analysis with very good low-frequency resolution allows the detection of the influence of external noise that could be present in the experiment. This is impossible in the case of the global quantities involved in PMR and could give rise to a bad determination of the effective temperature.

In summary, both microrheology techniques are complementary and we definitely conclude that $T_{eff} = T$ for this aging nonequilibrium system for 0.25 Hz $\leq f$ and $t_w \leq 500$ min. In other words, for these timescales the relation between the spontaneous fluctuations of the trapped particle and its response to an external perturbation are related like in equilibrium (2.16) even when the surrounding medium, the Laponite colloidal glass, is in a nonequilibrium regime.

4.7 Heat fluctuations

Finally, we study the properties of the fluctuations of the heat exhanged between the colloidal glass in the purely viscous regime ($0 < t_w \leq t_g \approx 300$ min) and the surroundings. This kind of analysis has been motivated by the recent experimental works focused on extreme fluctuations of injected and dissipated power in systems with harmonic linear [97, 98] and non-harmonic potentials [99, 100] within the context of fluctuation theorem (FT). See appendix A and references [12, 101] for a review on FT. The idea of using FT for theoretically studying the heat flux in aging systems was first proposed in [102, 103]. Let us summarize the main physical concepts that are behind this idea. Since nonequilibrium fluctuating forces due to the collisions of the colloidal glass particles inject energy into the micron-sized probe, in a given time lag τ a fraction of this energy must be dissipated in the form of heat Q_τ. Q_τ is a stochastic variable which can be either positive (heat received by the probe) or negative (heat transferred to the colloid). In an ergodic system acting as an equilibrium thermal bath at temperature T, the mean heat must vanish in the absence of any external forcing on the probe in order to satisfy the first law of thermodynamics. However, in a system out of equilibrium this situation is not necessarily fulfilled if detailed balance does not hold. A mean heat transfer $\langle Q_\tau \rangle \neq 0$ would be a fingerprint of an effective temperature of the colloidal glass $T_{eff}(\omega, t_w) \neq T$ during a time lag $\tau \approx 2\pi/\omega$. Hence, by investigating possible asymmetries in the probability density function (PDF) of Q_τ for different time

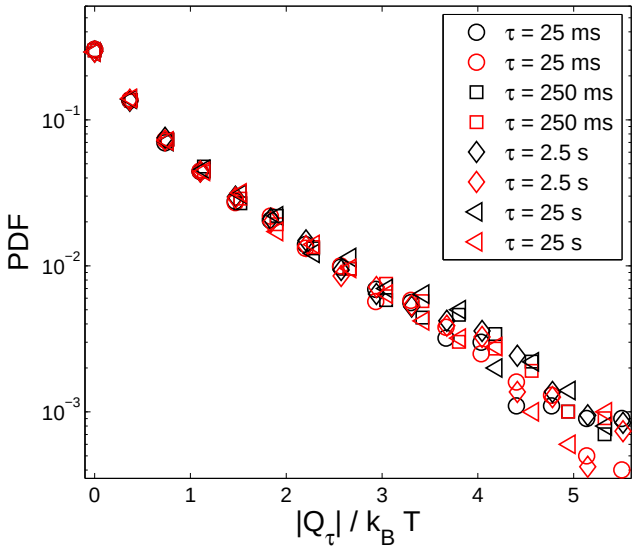

(a)

Figure 4.9: PDFs of $|Q_\tau(t_w)|$ at $t_w = 95$ min for different values of the time lag τ. The black symbols correspond to $Q_\tau \geq 0$ whereas the red ones to $Q_\tau \leq 0$.

lags and at different aging times, one could find possible values of T_{eff} different from T in the aging colloidal glass.

We are interested in the situation without any external forcing. Then we must set $x_0(t, \omega) = 0$ in equation (4.13). In order to calculate the heat transfer during a time lag τ, equation (4.13) is multiplied by $\dot{x}$ and integrated from t_w to $t_w + \tau$, which yields an extension of the first law of thermodynamics for the energy exchange process between the particle and the colloidal glass [104]

$$\Delta U_\tau(t_w) = Q_\tau(t_w), \tag{4.21}$$

In equation (4.21), the first term

$$\Delta U_\tau(t_w) = \frac{1}{2}k(x(t_w+\tau)^2 - x(t_w)^2) + \int_{t_w}^{t_w+\tau} \dot{x}(t)(K_t * x)(t, t_w)dt, \tag{4.22}$$

is the variation of the potential energy of the particle during the time interval $[t_w, t_w+\tau]$, whereas

$$Q_\tau(t_w) = \int_{t_w}^{t_w+\tau} \xi(t')\dot{x}(t')dt' - \int_{t_w}^{t_w+\tau} \dot{x}(t')(\gamma_t * \dot{x})(t, t_w)dt', \tag{4.23}$$

is the heat exchanged between the particle and the surrounding colloidal glass during the same time interval. In equations (4.22) and (4.23), $*$ stands for the convolution computed over $[t_w, t]$. Therefore the last two integrals in equations (4.22) and (4.23) account for the energy storage and loss, respectively, due to the evolving viscoelasticity

of the suspension. The terms $K_t(t, t_w)$ and $\gamma_t(t, t_w)$ are the inverse Fourier transforms of $\gamma(\omega, t_w)$ and $K_{Lap}(\omega, t_w)$ defined in subsection 1.4.2. Note that in general the calculation of Q_τ by means of the right-hand side of equation (4.22) requires a very good accuracy for the dependence of $K_{Lap}(\omega, t_w)$ on ω over a broad frequency range. Otherwise the convolution in equation (4.22) is underestimated. In practice this method is quite inaccurate for $t_w > t_g$ given the large experimental errors when computing K_{Lap} over a broad frequency range in the viscoelastic regime. However, for $t_w \leq t_g$ $K_{Lap}(\omega, t_w) = 0$ and $\gamma(\omega, t_w) = \gamma(t_w)$ as shown in subsection 4.5. Consequently, the storage term associated to the elasticity of the glass in equation (4.22) vanishes leading to a simply expression for the heat transfer

$$Q_\tau(t_w) = \frac{1}{2}k[x(t_w + \tau)^2 - x(t_w)^2]. \tag{4.24}$$

For a given waiting time t_w, we compute a data set $\{Q_\tau(t)\}_\tau$, with $t_w \leq t \leq 50$ s, using equation (4.24). Then the PDF of the heat at t_w is computed using this data set for different values of τ. The results are shown in figure 4.9 for $t_w = 95$ min. By plotting the PDF of the absolute value of Q_τ, we observe that it is strongly non-Gaussian. It has long tails decaying approximately as an exponential and it is symmetric with respect to the maximum value located at $Q_\tau = 0$ even for extreme fluctuations as large as $\pm 5 k_B T$. We verify this symmetry for different waiting times $t_w < 300$ min and for different time lags over four decades (25 ms $\leq \tau \leq$ 25 s). The absence of any asymmetry in the PDF of Q_τ confirms, in addition to the different methods described in the previous sections, that $T_{eff} = T$ for fluctuations taking place at time scales as slow as $\tau = 25$ s corresponding to frequencies ~ 0.04 Hz.

4.8 Discussion and Conclusion

We have experimentally studied the statistical properties of the Brownian motion of a bead inside a colloidal glass of Laponite during the transition from a viscous to a visoelastic state. We were specifically interested in understanding whether a $T_{eff} \neq T$ can be observed when the Brownian particle is inside an out of equilibrium bath, i.e. the Laponite suspension in this case. As already mentioned, this problem has been the subject of several measurements giving contrasting results. Our experimental results show not only that, within experimental errors, $T_{eff} = T$ at any time but they also indicate the reasons of the contrasting results. This was possible thanks to the use of multiple optical traps which allow us to apply simultaneously in the same evolving colloid active and passive microrheology techniques. Let us summarize the new main results of our investigation:

a) The use of multiple traps allows us to check simultaneously two microrheology techniques that had led to conflicting results in the past and to find the possible reasons of this contrast. We have interpreted the relation between the local and global quantities defined in previous works and explained why they must be consistent with each other. In section 4.6 we have shown that:

a.1) In the case of PMR the use of too short time windows to measure the variance of fluctuations and of too long time windows for data smoothing induces an anomalous increase of the T_{eff} at very long times. This artifact is suppressed if a more precise and unbiased data analysis is performed.

a.2) By means of AMR at very low frequencies never studied before we check that $T_{eff} = T$ for the micron-sized probe in the aging colloidal glass. An advantage of the AMR technique is that it also allows to resolve the slowly evolving viscosity and elasticity of the colloidal glass in order to observe its transition from a purely viscous fluid to a viscoelastic solid-like phase.

a.3) For the active microrheology method we have shown in figure 4.7 the existence of a maximum as a function of time for the fluctuation spectra and for the imaginary part of response function, such that the ratio of these two functions gives a constant T_{eff}. The position of these maxima depends on the strength of the optical traps used to measure the response and fluctuations. These strengths are the same in our case whereas they are different in the experiment reported in [90]. This difference in strength induces a shift in the time position of these maxima which must be corrected in the data analysis. Small errors in this correction may of course induce an anomalous time dependence of T_{eff}.

b) The use of a new method based on the PDF of heat fluctuations, section 4.7. This technique shows no measurable mean heat transfer between the aging colloidal glass and the environment even at long time scales. This is consistent with the results of passive measurements which show that T_{eff} is equal to T at any time even for very low frequencies ($\sim 10^{-2}$ Hz).

These results show that the effective temperature of the colloidal glass felt by the Brownian particle is always equal to the temperature of the environment during aging *for the timescales that we probed*. Furthermore they explain where the conflict between the various results reported in literature may come from. The relation between spontaneous fluctuations and linear response of the particle in the Laponite bath seems is very well described by an equilibrium-like relation as (2.16)

$$-\partial_t \langle x(t)x(t_w)\rangle = k_B T_{eff} R(t, t_w),$$

with $T_{eff} = T$ and $0 \leq t - t_w \lesssim 25$ s, except for the explicit dependence on the age of the system t_w This result suggests that slow structural rearrangements taking place at these timescales are equilibrated with the environment since our results show no increase of T_{eff}. This is in agreement with those of reference [88], based on bulk measurements, and those of Jabbari-Farouji *et al.* [83, 91, 93], who measured fluctuations and responses of the bead displacement in Laponite over a wide frequency range and found that T_{eff} is equal to T.

We stress the following important features of the experiment:

- The size of the Brownian probe is 2 orders of magnitude larger than the size of the Laponite platelets. Then it is unlikely that a structural rearrangement of a metastable configuration of the platelets can give rise to a sufficiently strong fluctuating force on the probe that could be interpreted as $T_{eff} > T$.

- The largest timescales probed by microrheology techniques are two orders of magnitude smaller than the typical timescale of the formation of the viscoelastic structure. Once again, it is unlikely that the probe particle is able to detect such slow fluctuations (provided that they are strong enough to perturb the Brownian motion) in a time two orders of magnitude smaller.

- The initial nonequilibrium condition of the suspension is not prepared by means of a temperature quench but by the unstable disordered packing of Laponite particles. Unlike structural or spin glasses, where the distance from thermal equilibrium of the system can be tuned by means of the quench depth, in the case of the Laponite colloidal glass there is no such a control on the initial condition.

Therefore, it is natural to conclude that the preparation of the initial condition of the Laponite colloidal glass drives the system only into a *weak* nonequilibrium state. In this way, as the system ages the energy flux from to the suspension to the environment slow down. Then, they are undetectable by the Brownian motion of the micron-sized probe. In addition, it is important to remark that even when the idea of measuring T_{eff} by means of the Brownian motion of a small probe in the glass is similar to the numerical simulations that report $T_{eff} > T$ in [80], the conditions are quite different. In such a numerical work, the tracer is able to probe a low-frequency $T_{eff} > T$, provided that its length and timescales are comparable to those of the glass. However, in our experimen the typical length and timescales of the probe particle are very different from those of the glassy structure. In other words, x is not coupled to the nonequilibrium dynamics of the relevant degrees of freedom of the colloidal glass. Hence x exhibits equilibrium-like statistical properties. This conclusion is in full agreement with recent numerical simulations on assembling polymers [105] that show no deviation of the equilibrium fluctuation-dissipation relation (2.16) if the measured observable is not coupled to the nonequilibrium degrees of freedom of the system.

Finally, we point out that our results are not in contrast with the very large values of $T_{eff} > T$ observed by dielectric measurements [87, 88, 89] and more recently by birefringence methods [106]. This is because, by definition, T_{eff} is in principle observable dependent, see equations (4.1) and (4.2). Indeed, according to the explanation provided by [105], the observables measured in this kind of experiments (electric impedance and polarization) are strongly coupled to the nonequilibrium degrees of freedom of the colloidal glass.

Chapter 5

Brownian particle in gelatin after a fast quench

5.1 Gelatin and the sol-gel transition

Gelatin is a thermoreversible gel obtained from denatured collagen which is the the building block of connective tissues of mammals. Collagen molecules are long chains (300 nm long and 1.5 nm in diameter) with a triple-helix structure stabilized by hydrogen bonds (see inset of figure 5.1). Then gelatin, which is obtained by hydrolyzation of collagen, has also a triple helical structure in aqueous solutions at low temperature. The formation of a network of cross-linked helical segments gives rise to an arrested state with elastic behavior, i.e. a *gel*. Upon heating up the gel phase above a temperature T_{gel} called the gelation temperature, the hydrogen bonds are disrupted and then aqueous gelatin solutions exhibit a random single-stranded coil structure resulting in a macroscopic viscous liquid phase (*sol*). This process is completely reversible: by cooling down the sol phase below T_{gel}, the renaturation of the native triple helices is thermodynamically favorable, then the triple helical network connected by single strands is formed by percolation of the long gelatin chains, as depicted in figure 5.1. The transition from the sol phase to the gel phase is called the *sol-gel* transition. The value of T_{gel} depends on the gelatin concentration of the aqueous solution: in general T_{gel} increases as the concentration increases. If the transition is induced by a quench from above to below T_{gel}, the system quickly becomes frustrated by topological constraints due to the competition of neighboring triple helices for the shared portions of the chains. Therefore after a quench the system displays physical aging: the physical properties of the aqueous gelatin solution evolve in time as the system undergoes the sol-gel transition. The aging strongly depends on the quench depth: the deeper the system is quenched, the faster the aging. Bulk rheological measurements show that gelatin samples quenched or ramped below T_{gel} share some common phenomenological features with glassy dynamics. For example, the rheological properties in both kinds of systems display scaling laws: the real part of the shear modulus, which quantifies the elasticity of the system, increases logarithmically as a function of the aging time

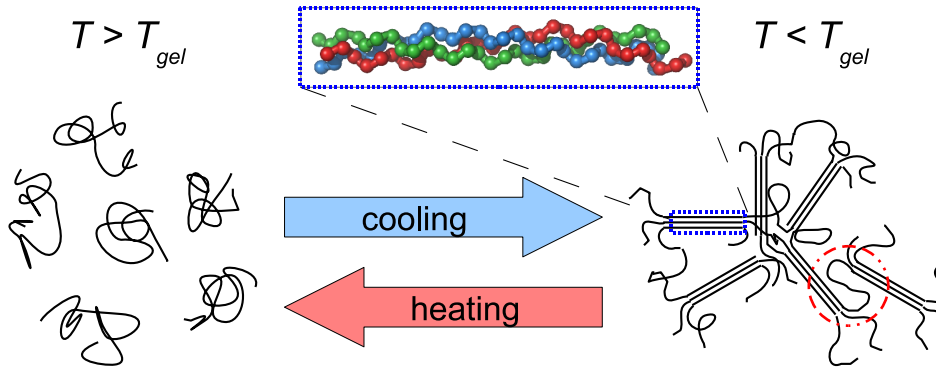

Figure 5.1: Schematic representation of the sol-gel transition of gelatin. Above the gelation temperature T_{gel}, the gelatin chains have a random single-stranded coil structure giving rise to a viscous liquid-like phase (sol). By cooling down below T_{gel} the single strands arrange in the triple-helix structure of the native collagen (inset). Then the network formed by percolation of these chains gives rise to a viscoelastic solid-like phase (gel). During this process the system becomes frustrated due to the competition of neighboring triple helices for the shared single strands, like the one enclosed by the red circle.

[107, 108]. The elasticity of gelatin solutions only depends on the helix concentration, i.e. the fraction of renatured triple helices with respect to the native collagen structure.

Unlike the Laponite colloidal glass, the key features of gelatin for our experiment are the following:

- The initial nonequilibrium condition of the bath can be accurately controlled by performing a temperature quench from above to below T_{gel}. Then the experiment can be repeated severeal times in order to compute ensemble averages.

- As the quench depth can be tuned by varying the power supplied to the gelatin gel, then the aging rate can be accelerated to be accessible for microrheological measurements using optical traps.

- The lengthscales of the gelatin chains (300 nm) and the resulting mesh size of the gel network after the quench are not negligible with respect to the Brownian particle size. Hence in principle the particle must be able to probe the nonequilibrium assemblage of the gel network after the quench.

Bearing in mind these features, the aqueous gelatin solution represents a good experimental system to conduct a careful study of the Brownian motion of a micron-sized particle in an out-equilibrium aging bath.

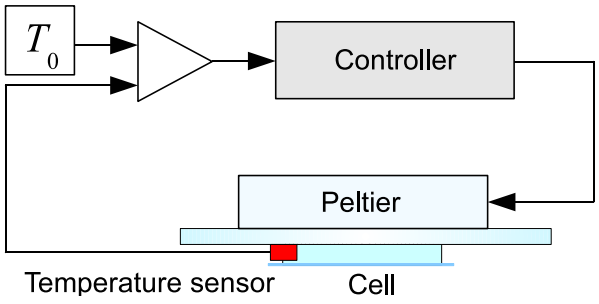

Figure 5.2: Diagram of the temperature feedback system used to keep the gelatin bulk inside the cell at $T_0 = 26 \pm 0.05°\text{C} < T_{gel}$.

5.2 Description of the experiment

We now proceed to describe the experimental setup that we implemented to perform a very fast quench of $\Delta T \approx 11$ K in less than 1 ms in a micron-sized region around a spherical Brownian particle trapped by optical tweezers. This quenching rate is 4 orders of magnitude faster than the typical rates that can be achieved in bulk rheological measurements. In this way we were able to impose strong nonequilibrium conditions to the gelatin sample and detect the influence of its nonequilibrium relaxational dynamics on the Brownian motion of the probe.

5.2.1 Sample preparation

In the experiment, we prepare an aqueous gelatin solution using a type-B pig skin gelatin powder. This type of gelatin is obtained from alkaline treatment during the denaturation of collagen. The sample is prepared at a weight concentration of 10 wt % following the usual protocol [109]: the powder is heated in water for 30 minutes at 60° C and gently stirred until obtaining a homogeneous transparent solution. At a concentration of 10 wt % the gelation temperature for this type of gelatin is $T_{gel} = 29°$ C. We keep the gelatin sample in the sol phase at $T = 36°\text{C}$ and a small volume fraction (10^{-6}) of silica microspheres (radius $r = 1\,\mu$m) is injected and homogeneously mixed in the solution. Then a tiny amount (0.3 ml) of the solution is introduced inside a cell made of a plastic chamber (inner diameter 15 mm, thickness 1 mm) sealed between a microscope slide and a coverslip, like that sketched in figure 1.4. The sample is aged at room temperature $\approx 26 \pm 1°\text{C}$ for several hours after the preparation in order to obtain a gel without quenching the sample.

5.2.2 Fast quenching method

Once the gelatin sample inside the cell is in the gel phase, it is placed in the single-trap setup described in detail in section 1.2. The temperature of the cell is measured using an AD590 thermal sensor placed on the lateral side of the chamber containing the gel. The sensor produces a current which is directly proportional to the temperature of the cell. This current is detected by the temperature control module (TCM-39032) of a modular laser diode controller (LDC-3900, ILX Lightwave) and converted into temperature units after calibrating the sensor. A Peltier element is put in contact with the microscope slide of the cell and connected to the temperature control module. In this way the temperature of the cell is controlled by current feedback of the Peltier element and the gelatin bulk is kept in the gel phase at constant temperature $T_0 = 26 \pm 0.05°\text{C} < T_{gel}$. An schematic diagram of the temperature feedback system is shown in figure 5.2. Next, one of the silica beads inside the gel is kept in the focal position of a tightly focused laser beam ($\lambda = 980$ nm) at a power of 20 mW and at a distance $h = 25\,\mu$m from the coverslip surface (see figure 5.3). At this power the laser produces on the particle an elastic force of stiffness $k = 2.9$ pN/μm. Starting from this condition, the power of the trapping laser is increased to $P = 200$ mW. Because of the light absorption by the water molecules of the solution, the temperature of the gel around the trapped particle increases an amount δT. A formula to estimate the temperature increase of a fluid by an optical trap was derived and experimentally checked in reference [110]. δT can be expressed in terms of P, λ, the attenuation coefficient of the fluid α and its thermal conductivity K

$$\delta T = \frac{P\alpha}{2\pi K}\left[\ln\left(\frac{2\pi h}{\lambda}\right) - 1\right], \tag{5.1}$$

Since the gelatin sample in our experiment is composed of 90% water, the value of δT at $h = 25\,\mu$m from the cell wall can be estimated by substituting in equation (5.1) the experimental values of P, λ, the attenuation coefficient $\alpha = 50$ m^{-1} and the thermal conductivity of water $K = 0.60$ W m^{-1} K^{-1}. This yields the value

$$\delta T \approx 12\,\text{K}.$$

Then the temperature around the trapped Brownian particle is $T_0 + \delta T = 38°$C, which is higher than T_{gel} [1]. As a result the gel melts and a liquid droplet is formed around the trapped bead inside the the solid gel bulk, as depicted in figure 5.3. The size of the melted droplet slightly depends on the time that the beam locally heats the gelatin. In order to avoid a significant damage to the surface smoothness of the bead by the continuous strong heating, we keep the power at $P = 200$ mW only for 180 s. For this heating time the final radius of the melted droplet is $a = 5\,\mu$m, measured in the

[1] The value 38°C of the temperature around the bead is checked by comparing the high-frequency side of the power spectrum of fluctuations of the position of the bead trapped by the focused laser at $P = 200$ mW with the spectrum obtained by trapping the bead at a very weak laser power (weak absorption) and heating the whole cell at 38° C by means of the power dissipated by an indium tin oxide coated microscope slide suject to an electric current.

plane xy perpendicular to the beam propagation. We determine this value of a in two different and independent ways:

a) After 180 s, we suddenly decrease the laser power to 20 mW, which is enough to keep the bead in the beam focus with a trapping stiffness of $k = 2.9\,\mathrm{pN}/\mu\mathrm{m}$. Then we slowly drag the bead across the liquid droplet by moving horizontally the whole cell using the piezoelectric stage of the single optical trap setup (see section 1.2). Since at this small power the temperature rise is only $\delta T \approx 1.2$ K according to equation (5.1), no additional amount of gel melts during the displacement of the cell. The radius $a = 5\,\mu$m is determined as the distance travelled by the dragged particle from its original position in the center of the droplet to the point where the optical trap is not able to drag it anymore because of the liquid-solid interface between the droplet and the gel bulk.

b) A second gelatin solution is prepared at 10 wt % with a relatively high concentration (volume fraction 10^{-3}) of small silica microspheres of radius $r = 0.225\,\mu$m and without $r = 1\,\mu$m beads. We repeat the heating procedure for 180 s to melt a droplet of the same size as before. In this case we use the small microspheres as tracers. In figure 5.4 we show two snapshots of this gelatin solution before and after locally heating with the laser. Most of the particles located inside the droplet undergo free Brownian motion and are eventually attracted to the beam focus whereas those outside the droplet stay almost immobile by the elastic gel network. In this way we check that $a = 5\,\mu$m.

Once that we melt the sol droplet for 180 s, the laser power is suddenly decreased again to 20 mW, as sketeched in figure 5.5(a). Since the thermal diffusivity of water is $\kappa = 1.4 \times 10^{-7}\,\mathrm{m^2\,s^{-1}}$, the time τ_κ needed for the heat to diffuse from the droplet to the bulk is

$$\tau_\kappa \sim \frac{a^2}{\kappa} \sim 2 \times 10^{-4}\,\mathrm{s}.$$

Hence, the temperature of the droplet is homogenized by heat diffusion into the bulk in less than 1 ms resulting in a very efficient quench of the gelatin around the trapped particle to the final temperature $T = 27.2°\mathrm{C} < T_{gel}$. At this final temperature the liquid inside the droplet undergoes aging because of the fast quench and it solidifies in about 1 hour to the surrounding gel phase. The particle, trapped in the center of the droplet by the harmonic potential created by the focused beam, is a probe of this relaxation dynamics. In the experiment we repeat this quenching procedure 60 times in order to perform the proper ensemble averages.

5.3 Microrheology

Immediately after the quench we record the time evolution of the x position of the trapped particle, see figure 5.3. The acquisition, done at 8 kHz, and the data processing are performed using the PSD system described in detail in subsection 1.2.1. Figure

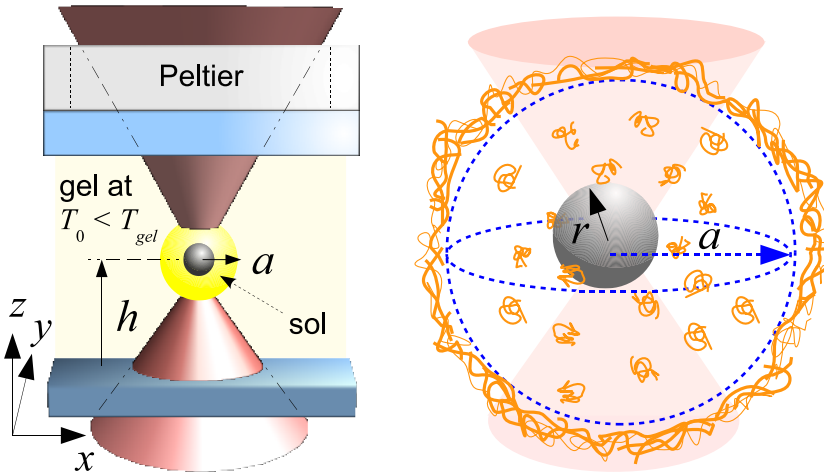

Figure 5.3: Left panel: schematic representation of the experimental setup to perform a fast local quench of the gelatin around a trapped Bronwian particle. A Peltier element with current feedback keeps the gelatin bulk in the gel phase at contant temperature $T_0 = 26 \pm 0.05$°C whereas a tightly focused laser beam locally rises the temperature to 36°C. Right panel: a droplet in the sol phase (radius $a = 5\,\mu$m) is melted around the trapped particle as a result of the local heating of the gel by the laser for 180 s. The liquid droplet is surrounded by the gel network.

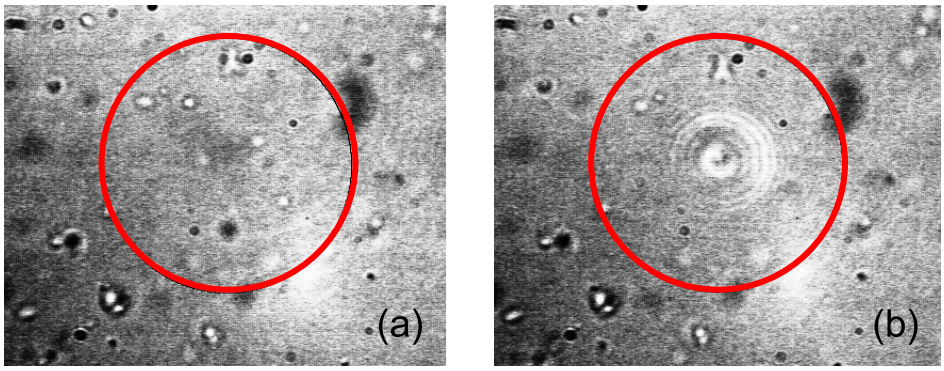

Figure 5.4: Snapshots of the gelatin solution (bulk temperature 26°C) with small tracers ($r = 0.225\,\mu$m) (a) before and (b) after locally heating during 180 s with the focused laser beam at $P = 200$ mW. The radius of the red circle is $a = 5\,\mu$m.

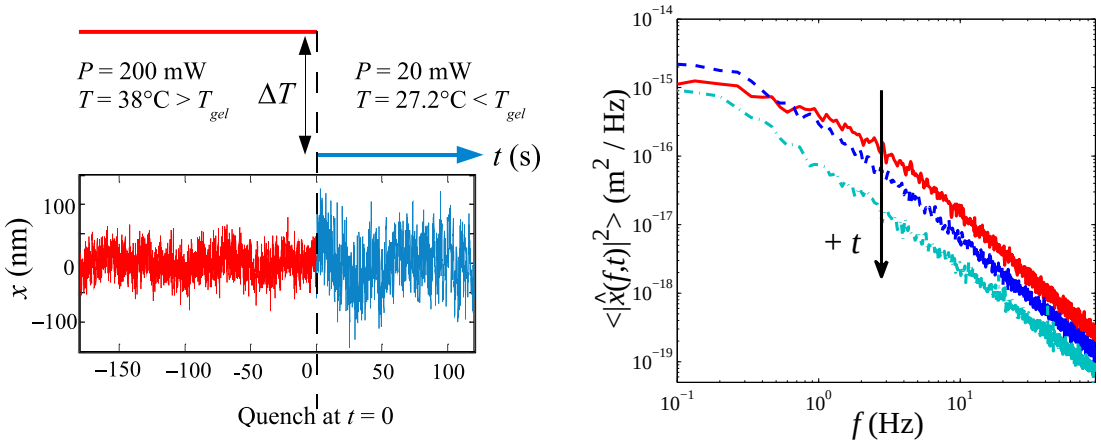

(a) (b)

Figure 5.5: (a) Diagram of the quench of the droplet from $T_0 = 38°C$ to $T = 27.2°C$ in less than 1 ms by suddenly decreasing the laser power from $P = 200$ mW to $P = 20$ mW. The lower panel shows the fluctuations of the position of the trapped particle before and after the quench. (b) Power spectral density of the fluctuations of x for the trapped bead measured over a time window $\Delta t = 15$ s at different times t after the quench: $0\,\text{s} \leq t \leq 15$ s (red solid line), $75\,\text{s} \leq t \leq 90$ s (blue dashed line), and $1200\,\text{s} \leq t \leq 1215$ s (turquoise dotted-dashed line).

5.5(a) shows the typical time evolution of x before and after the quench. Due to the aging process of the gelatin droplet, the time series of x is nonstationary. This is more evident in figure 5.5(b) where we plot the power spectral density $\langle|\hat{x}(f,t)|^2\rangle$ of x computed over a time window $[t, t+\Delta t]$ of length $\Delta t = 15$ s at different times t after the quench. The average $\langle\ldots\rangle$ is performed over 60 independent quenches. The high frequency side of the spectrum continuously decreases one order of magnitude during the first 20 minutes whereas the low frequency side exhibits a rather complex time evolution due the increasing viscoelasticity of gelatin during the gelation process.

In order to characterize the dynamics of x, we first perform active microrheology to determine the viscoelasticity of the gelatin droplet. See section 1.4 for the experimental details on microrheology. For this purpose we apply an external oscillating force $F(t, f)$ to the trapped bead

$$F(t, f) = F_0 \sin(2\pi f t). \tag{5.2}$$

at different driving frequencies $0.2\ \text{Hz} \leq f \leq 5$ Hz and fixed amplitude $F_0 = 87$ fN. In this way we resolve the storage $G'(f,t)$ and loss $G''(f,t)$ modulus of the droplet at different times t after the quench. Because of the relatively fast aging process shown in figure 5.5(b), the spectral analysis involved in the calculation of G' and G'' must be carried out over a short time window $[t, t+\Delta t]$ for each aging time t. In the following we set $\Delta t = 15$ s in all the calculations. This value of Δt is large enough to resolve the frequencies of the applied driving and at the same time it is short enough to avoid

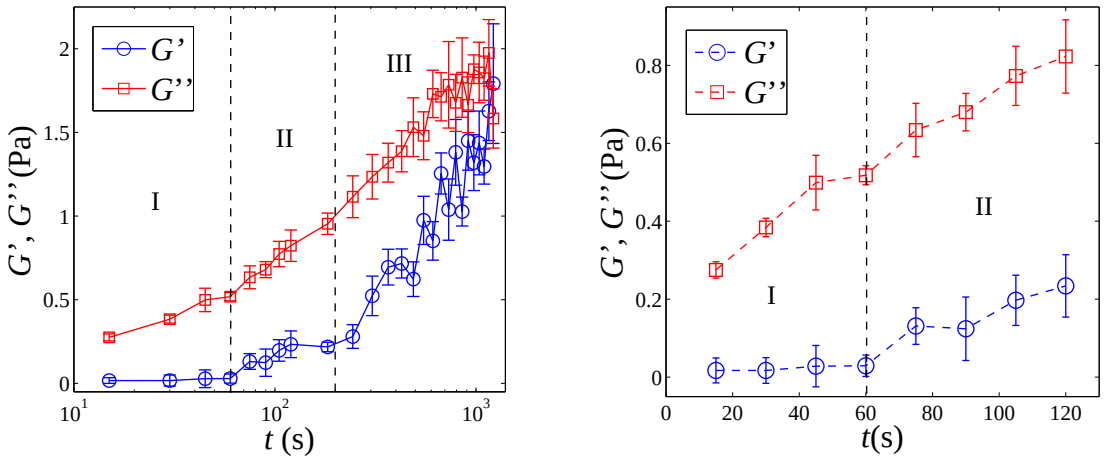

Figure 5.6: (a) Aging time evolution of the real G' and imaginary G'' part of the shear modulus of the gelatin droplet after the quench, measured at $f = 5$ Hz. (b) Expanded view of the aging time evolution of G' and G'' during the first 120 s.

a pronounced time evolution of the nonstationary signals that we measure. In figures 5.6(a) and 5.6(b) we plot the aging time evolution of G' and G'' computed at $f = 5$ Hz during the first 20 minutes after the quench. We can identify three different regimes:

I. For 0 s $\leq t \leq$ 60 s the storage modulus G' is completely negligible, whereas the loss modulus G'' increases continuously in time by a factor of almost two. In this aging regime, hightlighted in figure 5.6(b), it is expected that the gelatin droplet still behaves as a purely viscous liquid even when the final temperature of the quench is below T_{gel}, as verified further.

II. For 60 s $\leq t \leq$ 200 s, the loss modulus continuously increases and the storage modulus starts to increase slowly. This result shows that the droplet is in a transient regime towards the sol-gel transition where the gel network is not completely formed. Indeed, G' is still much smaller and it increases slower than G''.

III. For 200 s $\leq t \leq$ 1200 s, both G' and G'' reach a logarithmic growth $\sim \log t$ where G' increases faster than G''. This growth as t increases is similar to that reported in macroscopic bulk measurements [107, 109, 111, 112, 113] but taking place at much faster timescales because of the smallness of the gelatin droplet. Then the system is actully undergoing gelation providing evidence that the percolating gel network is already formed.

By measuring the time evolution of G' and G'' at different low frequencies ($f = 0.2, 0.5, 1.0$ and 5.0 Hz) we can reconstruct a picture of the relevant relaxation timescales of the fluid inside the droplet during the gelation process:

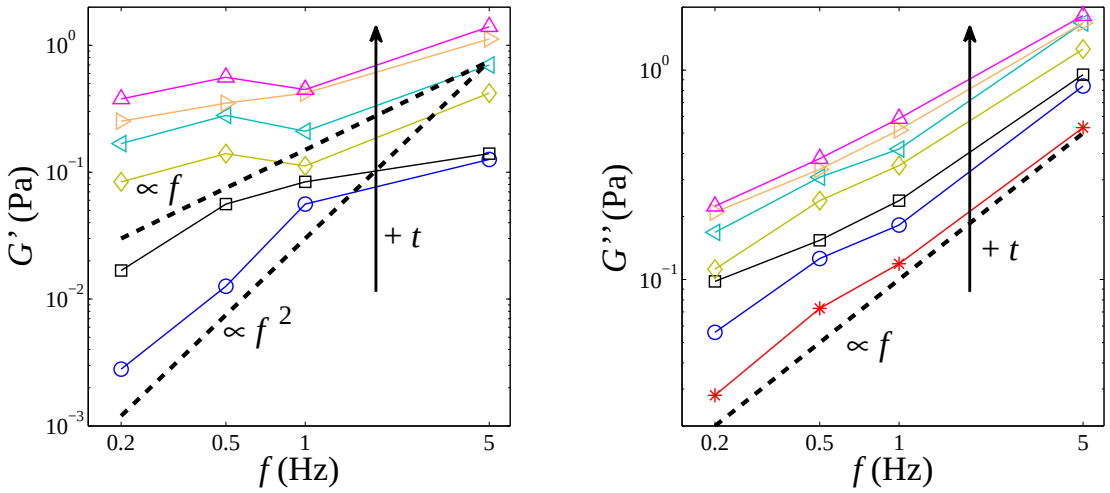

Figure 5.7: (a) Storage modulus of the gelatin droplet measured at different frequencies and at different times after the quench: $t = 120, 180, 300, 600, 900$ and 1200 s. For $t \leq 60$ s the mean values of G' are smaller than the statistical error bars indicating that they are completely negligible (not shown). (b) Loss modulus measured at different frequencies and at different times after the quench: $t = 60, 120, 180, 300, 600, 900$ and 1200 s.

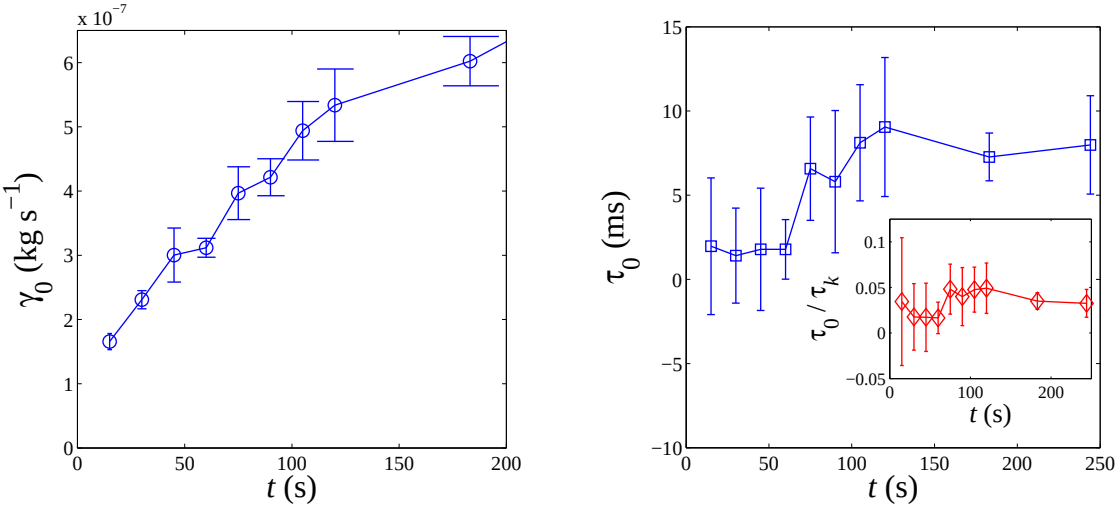

(a) (b)

Figure 5.8: (a) Aging time evolution of the viscous drag coefficient of the particle in the gelatin droplet during the first 200 s after the quench. (b) Aging time evolution of the largest relaxation time of the fluid inside the droplet. Inset: aging time evolution of the ratio between the largest relaxation time of the droplet and the relaxation time $\tau_k = \gamma_0/k$ of the position fluctuations of the trapped Brownian particle.

- In figures 5.7(a) and 5.7(b) we plot the low-frequency spectrum of G' and G'', respectively, at different times after the quench. We check that for the regime I ($0\ \text{s} \leq t \leq 60\ \text{s}$) the droplet is almost purely viscous because the mean value of G' is close to 0 and even smaller than the statistical errors for all the measured frequencies f. Besides, G'' is approximately proportional to f (dashed line in figure 5.7(b)), then the dynamic viscosity of the droplet $G''/(2\pi f)$ is frequency-independent but it increases as t increases. Therefore at this time scales the fluid inside the droplet behaves as a Newtonian fluid with a vanishing relaxation time.

- Next, in figure 5.7(a) we plot as dashed lines the curves $\propto f$ and $\propto f^2$. We observe that as $f \to 0$, the storage modulus displays an intermediate behavior between these two reference curves. Then we conclude that $G'(f,t) \to 0$ as $f \to 0$ in the regime II ($60\ \text{s} \leq t \leq 200\ \text{s}$). On the other hand, in figure 5.7(b) we observe that the loss modulus is roughly proportional to f. This behavior of $G = G' + \mathrm{i}G''$ can be approximately described by the Maxwell model for a viscoelastic fluid with a single relevant relaxation time[2] τ_0. Based on these experimental results we can estimate $\tau_0(t)$ at aging time t for both regimes I and II based on the Maxwell

[2]The relaxation time τ_0 represents the largest timescale at which a viscoelastic fluid is able to store energy at present time t starting from $t - \tau_0$. For timescales $\gg \tau_0$ the memory of this energy storage process is lost. In particular, for a Newtonian fluid $\tau_0 = 0$.

model for G' and G''

$$\begin{aligned} G'(\omega,t) &= \frac{\eta_0(t)\omega^2\tau_0(t)}{\omega^2\tau_0(t)^2+1}, \\ G''(\omega,t) &= \frac{\eta_0(t)\omega}{\omega^2\tau_0(t)^2+1}, \end{aligned} \tag{5.3}$$

where $\omega = 2\pi f$ and $\eta_0(t)$ is the zero-shear viscosity at time t. Using equation (5.3) we obtain an expression for τ_0 and for the viscous drag coefficient of the spherical bead

$$\gamma_0 = 6\pi r\eta_0,$$

in terms of the measured values of G' and G''

$$\begin{aligned} \tau_0 &= \frac{1}{\omega}\frac{G'}{G''}, \\ \gamma_0 &= 6\pi r\frac{G''}{\omega}\left[1+\left(\frac{G'}{G''}\right)^2\right]. \end{aligned} \tag{5.4}$$

In figures 5.8(a) and 5.8(b) we plot the time evolution of γ_0 and τ_0, respectively, during the first 200 s after the quench. γ_0 and τ_0 are estimated at $f = 5$ Hz using equation (5.4). As expected, τ_0 is very small (≈ 2 ms) with error bars even larger than the mean values during the first 60 s after the quench. Therefore, the droplet can be regarded as Newtonian fluid ($\tau_0 \approx 0$), at least for frequencies $f < 1/(2\pi\tau_0) \approx 80$ Hz in the regime I. Next, for 60 s $\leq t \leq$ 200 s the mean value of τ_0 becomes larger than the error bars and approximately four times the value found for the regime I. Hence, the fluid in the droplet can be actually modelled as a Maxwellian fluid with nonzero τ_0 in the regime II. In the inset of figure 5.8 we compare the values of τ_0 with the viscous relaxation time of the particle inside the optical trap

$$\tau_k = \frac{\gamma_0}{k}. \tag{5.5}$$

Since $\tau_0/\tau_k \leq 0.05$ even in the regime II, then the viscoelastic memory effects of the droplet taking place during τ_0 does not significantly affect the Brownian motion of the particle during the first 200 s, as shown further on.

- Finally, for the regime III (200 s $\leq t \leq$ 1200 s) G'' and mainly G' exhibit a complex frequency dependence. Unlike the Maxwellian behavior which satisfies $G' \to 0$ as $f \to 0$, in this regime G' seems to remain finite as $f \to 0$, as shown in figure 5.7(a). This is also in agreement with bulk measurements [111, 112] that report a nonzero storage modulus of constant value at very low frequencies. This low-frequency behavior corresponds that of an elastic solid with a continuous spectrum of relaxation times.

With the previous microrheological information of the gelatin droplet, we are able to study carefully in the following sections the nonequilibrium fluctuations of the trapped particle (with no external force $F(t)$) during the aging of the bath.

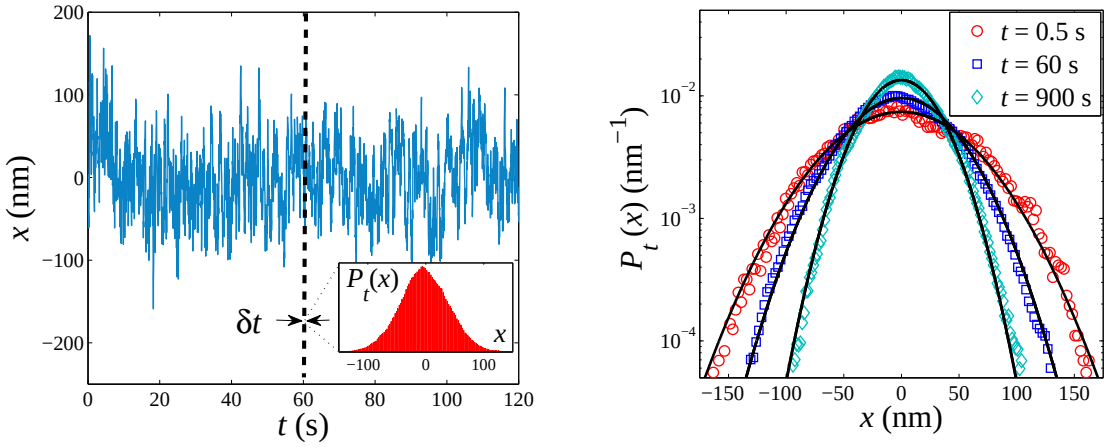

(a) (b)

Figure 5.9: (a) Time evolution of the particle position x after a given realization of the quench. The probability density function of x at time t, $P_t(x)$, is determined by computing the histogram of x over a short time window $\delta t = 0.1$ s around t and over 60 independent quenches. (b) Probability density function of x at different times t after the quench. The solid lines are Gaussian fits.

5.4 Spontaneous nonequilibrium fluctuations

In order to probe the statistical properties of the nonequilibrium fluctuations of x during the gelation of the droplet in absence of any external force, we first compute their probability density function $P_t(x)$ at time t after the quench. Since the stochastic process $x(t)$ is nonstationary, we compute $P_t(x)$ over 60 independent quenches and over a short time window $\delta t = 0.1$ s around each value of t to improve the statistics, as represented in figure 5.9(a). We find that $P_t(x)$ is Gaussian for all $t \geq 0$

$$P_t(x) = \frac{1}{\sqrt{2\pi\sigma_x(t)^2}} \exp\left(-\frac{x^2}{2\sigma_x(t)^2}\right), \tag{5.6}$$

as plotted in figure 5.9(b). Consequently, the statistical properties of x can be completely characterized by the variance $\sigma_x(t)^2$ computed at time t in the same way as $P_t(x)$. The time evolution of $\sigma_x(t)^2$ is plotted in figure 5.10. We now analyze in detail the behavior of $\sigma_x(t)^2$ according to the different aging regimes identified by active microrheology and the information that can be provided by this quantity. We carry out this analysis taking into account that the total potential energy of the trapped particle at time t is

$$U(t) = \frac{1}{2}kx(t)^2 + U_{stored}(t), \tag{5.7}$$

where $U_{stored}(t)$ is the energy stored by the surrounding gelatin chains in the droplet until time t.

Regime I

As the storage modulus is completely negligible in this regime, $U_{stored} = 0$. Then, the total energy of the Brownian particle is $U(t) = kx(t)^2/2$. At thermal equilibrium $U(t)$ should satisfy the equipartition relation

$$\langle U \rangle = \frac{1}{2} k_B T,$$

where T is the temperature of the bath. Then, the variance of x would be $\sigma_x(t)^2 = k_B T/k$ for all $t \geq 0$. However, we observe that immediately after the quench, $\sigma_x(t)^2$ is almost three times the equilibrium equipartition value $k_B T/k$, with $T = 300.4$ K the final equilibrium temperature of the droplet after the quench. This shows the presence of a stochastic force on the particle stronger than the thermal fluctuations provided by the fast thermal motion of gelatin chains. This force weakens monotonically as t increases so that $\sigma_x(t)^2$ reaches the equipartition value at $t \approx 20$ s and remains at this value for $t \gtrsim 20$ s. It must be noted that this relaxation timescale is two orders of magnitude larger than the initial viscous relaxation time of the particle:

$$\tau_k = \frac{\gamma_0(0)}{k} = 65\,\text{ms}.$$

Thus, the observed slow dynamics is not the result of the particle relaxation after the sudden change of the the optical trap stiffness during the quench but it is a real nonequilibrium effect due to transient formation of the gel network towards the sol-gel transition.

With the purpose to check this hypothesis, we perfom the same quenching procedure in a Newtonian fluid (glycerol 60 wt % in water) with the same viscosity of the initial sol phase of gelatin (9×10^{-3} Pa s). In figure 5.10 we also plot the time evolution of $\sigma_x(t)^2$ measured after the quench in glycerol. In this case, the particle dynamics must settle into an equilibrium state in a time $t \approx \tau_k = 65$ ms after the quench [114, 115]. Indeed in figure 5.10 we see that, in glycerol, $\sigma_x(t)^2 = k_B T/k$ for all t within the experimental accuracy. This confirms that no experimental artifact is present and that the observed dependence of $\sigma_x(t)^2$ in gelatin is a real nonequilibrium effect due to the sol-gel transition.

Regime II

Since $\sigma_x(t)^2$ has already relaxed to an equilibrium-like behavior in the previous regime, at first glance it should be expected that $\sigma_x(t)^2 < k_B T/k$ for 60 s $\leq t \leq$ 200 s because in this regime the storage modulus G' is nonzero compared to G'' (see figures 5.6 and 5.7). This implies that $U_{stored} > 0$, then

$$\sigma_x(t)^2 = \frac{2\langle U(t) - U_{stored}(t) \rangle}{k} < \frac{k_B T}{k}. \tag{5.8}$$

However, in figure 5.10 we observe that for 60 s $\leq t \leq$ 200 s, the value of $\sigma_x(t)^2$ remains constant and equal to the equipartition value $k_B T/k$ within the experimental accuracy.

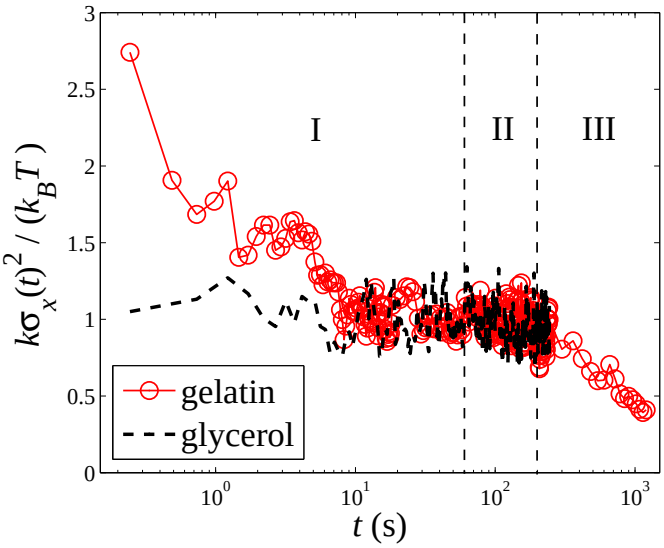

Figure 5.10: Time evolution of the variance of the particle position, normalized by the equilibrium equiparition value k_BT/k, after the quench in gelatin (∘) and glycerol (dashed line). The labels I, II and III correspond to the different aging regimes of the gelatin droplet found by active microrheology (see section 5.3).

Indeed, a simple calculation, based in the Langevin equation (1.16) and the Maxwell model (5.3) for the shear modulus of the droplet, shows that the variance of the particle position in this regime is

$$\sigma_x(t)^2 = \frac{k_BT}{k}\frac{1}{1+\frac{\tau_0(t)}{\tau_k(t)}}. \tag{5.9}$$

In equation (5.9), $\tau_0(t)$ and $\tau_k(t)$ are the largest relaxation time of the aging gelatin and the viscous relaxation time of the fluctuations of the trapped particle at time t, defined by equations (5.3) and (5.5), respectively. Therefore, the energy stored by the viscoelasticity of the gelatin chains is

$$\langle U_{stored}(t)\rangle = \frac{1}{2}k_BT\left[1-\frac{1}{1+\frac{\tau_0(t)}{\tau_k(t)}}\right], \tag{5.10}$$

In the inset of figure 5.8(b) we have shown that the ratio τ_0/τ_k is smaller than 0.05 during the first 200 s after the quench. Then, according to equation (5.10) U_{stored} represents in average less than 5% the total potential energy of the particle. In other words, the energy storage effect of the gelatin chains on the Brownian motion of the particle is negligible because the memory of the bath is erased in a timescale τ_0 much shorter than the time needed for the fluctuations of x to decorrelate. As $\tau_0/\tau_k \leq 0.05$, according to equation (5.9) the experimental value k_BT/k of the variance in this regime shows that the Brownian motion of the trapped particle behaves like in equilibrium with the thermal motion of the gelatin chains even when the droplet is aging.

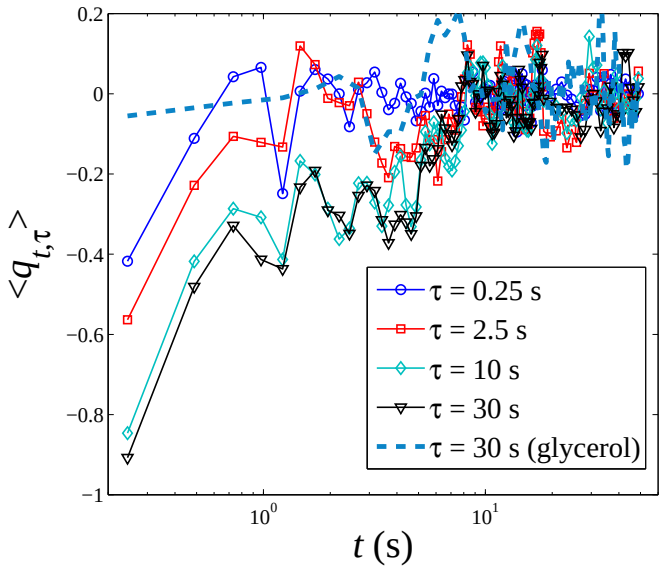

Figure 5.11: Mean value of the normalized heat $q_{t,\tau} = Q_{t,\tau}/(k_B T)$ computed at different times t after the quench and for different values of the time lag τ. The symbols correspond to the quench in gelatin whereas the dashed line corresponds to the quench in glycerol.

Regime III

In figure 5.10 we show that in this regime $\sigma_x(t)^2$ exhibits a different qualitative behavior: it decreases monotonically as t increases. This is in agreement with the microrheological measurements plotted in figures 5.6 and 5.7, where we show that the shear modulus has a complex frequency dependence with a non-negligible storage component $G' > G''$ as $f \to 0$. Then, equation (5.10) is not valid anymore in this regime because several relaxation timescales come into play due to the strong elastic behavior of the aging gelatin. As t increases, the gelatin droplet becomes stiffer and stiffer so the gel network around the particle stores a significant fraction of its total potential energy. Consequently, according to equation (5.8) $\sigma_x(t)^2$ becomes a decreasing function of t for $t > 200$ s. Note that this behavior is qualitatively similar to that observed for the Brownian particle in the Laponite colloidal glass (see chapter 4). Once the viscoelasticity of the bath starts to increase, the particle dynamics has an equilibrium-like behavior because the tipical relaxation times of the bath are much larger than that of the Brownian probe.

5.5 Heat fluctuations and the fluctuation theorem

We now focus on the statistical properties of the spontaneous energy fluctuations of the Brownian particle inside the aging droplet for the very first 200 s after the quench

(no external force). We concentrate in this time interval because we have shown in the previous section that in the regimes I and II the energy stored by the bath constitutes in average less than 5% of the total potential energy of the particle. Since the motion of the Brownian particle is overdamped, the instantanous value of its *total* energy at time t is given with an error smaller than 5% by

$$U_t = \frac{1}{2} k x_t^2.$$

As there is no external force acting to the particle, according to stochastic thermodynamics [61, 104] the heat exchanged between the particle and the bath during the time interval $[t, t+\tau]$ is equal to the variation $\Delta U_{t,\tau} = U_{t+\tau} - U_t$ of the total energy of the particle. Specifically

$$Q_{t,\tau} = \Delta U_{t,\tau} = \frac{k}{2}(x_{t+\tau}^2 - x_t^2), \tag{5.11}$$

where a positive (negative) value of $Q_{t,\tau}$ represents a heat fluctuation from (to) the bath to (from) the trapped particle. Therefore, the mean heat transferred during $[t, t+\tau]$ can be written in terms of the variance of x as

$$\langle Q_{t,\tau} \rangle = \frac{k}{2}[\sigma_x(t+\tau)^2 - \sigma_x(t)^2] \leq 0. \tag{5.12}$$

In fig. 5.11 we plot the ensemble average value of the heat (normalized by $k_B T$) using equation (5.12) and the experimental values of the variance σ_x^2 shown in figure 5.10. We observe the existence of a mean heat flux from the particle to the surroundings over the timescale τ because of the relaxation of $\sigma_x(t)^2$. Since the mean heat is an extensive variable, its absolute value increases as the measurement time τ increases. Note that at thermal equilibrium the mean heat would be $\langle Q_{t,\tau} \rangle = 0$ for all t and τ because of the detailed balance. The maximum value $|\langle Q_{t,\tau} \rangle| \approx k_B T$ takes place at $t = 0$ s and for 20 s $\lesssim \tau \lesssim$ 200 s. Non-negligible values of the mean heat compared to $k_B T$ persist for several seconds after the quench. Nevertheless, as t increases, $|\langle Q_{t,\tau} \rangle|$ decreases becoming negligible and experimentally undetectable for $t \gtrsim 20$ s. The nonvanishing mean heat flux $\langle Q_{t,\tau} \rangle / \tau$ is a strong signature that the detailed balance of the particle dynamics is broken by the assembling gelatin chains. However, as the bath is undergoing aging, the typical timescales of the dynamics slow down. Then the rate at which the heat flows from the system to the environement becomes undetectable by the Brownian probe which results in an apparent equilibrium-like behavior for $t \gtrsim 20$ s. For comparison, in figure 5.11 we also plot as a dashed line the mean heat computed at different times t after the quench in glycerol for the same large timescale $\tau = 30$ s. In this case $\langle Q_{t,\tau} \rangle = 0$ for all $t \geq 0$ within the experimetal accuracy because of the very fast equilibration of the bath and the particle after the quench.

Eq. (5.11) allows us to compute directly the fluctuations of $Q_{t,\tau}$ from the measurement of two instantaneous positions, x_t and $x_{t+\tau}$, at two different times t and $t+\tau$,

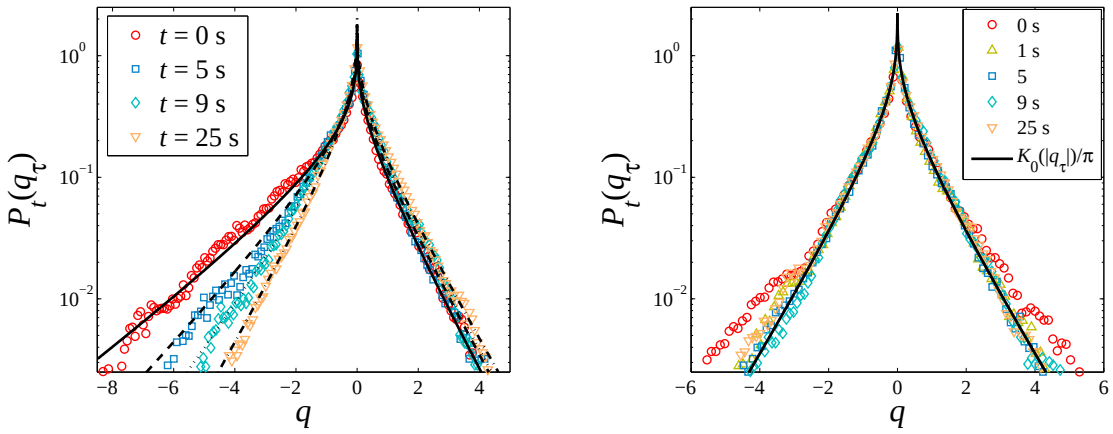

(a) (b)

Figure 5.12: (a) Probability density function of the normalized heat $q_{t,\tau}$ computed for $\tau = 30$ s at different times t after the quench in gelatin. The lines are computed using equation (5.21). (b) Probability density function of the normalized heat $q_{t,\tau}$ computed for $\tau = 30$ s at different times t after the quench in glycerol. The solid line corresponds to the theoretical equilibrium profile.

respectively[3]. The probability density function $P_t(q_\tau)$ of the normalized heat

$$q_{t,\tau} = \frac{Q_{t,\tau}}{k_B T},$$

is computed over the 60 quenches and over a short time window $\delta t = 0.1$ s around each t and $t + \tau$. We focus on a large value of τ in order to probe timescales comparable to the relaxation of the *nonthermal* fluctuations due to the early assemblage of the gel network. Figure 5.12(a) shows $P_t(q_\tau)$ at different times t after the quench for $\tau = 30$ s. $P_t(q_\tau)$ is highly non-Gaussian with a spike at $q_\tau = 0$ and slowly decaying tails for all the values of t. Immediately after the quench, $P_t(q_\tau)$ is strongly asymmetric with a long tail occurring at negative fluctuations. As t increases this asymmetry decreases and $P_t(q_\tau)$ becomes symmetric at $t \gtrsim 20$ s. Once again, we check that the long-lived asymmetry occurs because of the intricate nonequilibrium nature of the gelatin bath. In figure 5.12(b) we plot $P_t(q_\tau)$ with $\tau = 30$ s for the local quenches performed in glycerol. $P_t(q_\tau)$ quickly converges to the equilibrium profile and it is always symmetric with respect to $q_\tau = 0$.

A quantity commonly used to measure the asymmetry of the probability of observing positive and negative fluctuations of a given observable is the asymmetry function.

[3]This is not valid during the aging regime III because in such a case we have to take into account the particle history between t and $t+\tau$ and the exact form of the memory kernel Γ in equation (1.16). See equations (4.22) and (4.23) in chapter 4 for the analytical expression of $Q_{\tau,t}$ for a viscoelastic fluid with $G' > 0$.

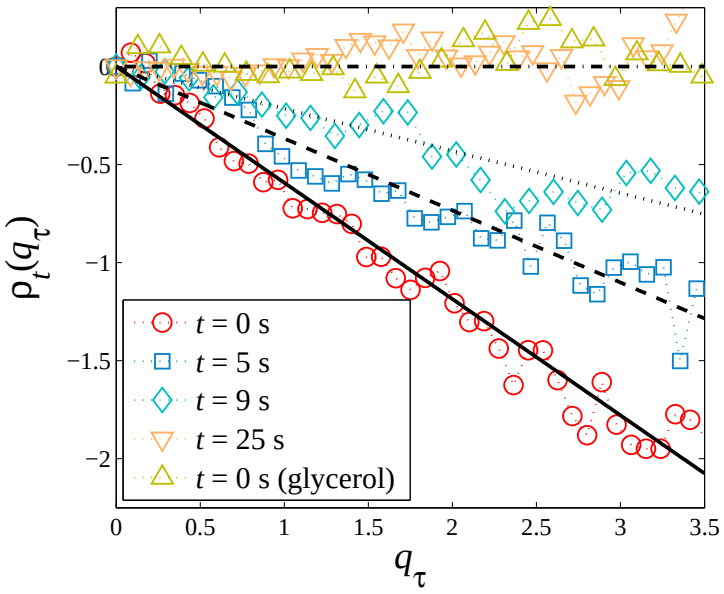

Figure 5.13: Asymmetry function of the probability density of the normalized heat fluctuations $q_{t,\tau}$ computed at different times t after the quench for $\tau = 30$ s. The straight lines are obtained using equations (5.23) and (5.24)

For the fluctuations of $q_{t,\tau}$ the asymmetry function is defined as

$$\rho_t(q_t) = \ln \frac{P_t(q_\tau)}{P(-q_\tau)}.$$

The function $\rho_t(q_\tau)$, computed from the $P_t(q_\tau)$ shown in figure 5.12(a), is plotted in figure 5.13. It is a linear function of its argument q_τ:

$$\rho_t(q_\tau) = -\Delta\beta_{t,\tau} q_\tau. \tag{5.13}$$

The slope $\Delta\beta_{t,\tau}$ decreases as t increases approaching the symmetric value $\Delta\beta_{t,\tau} = 0$ as $|\langle Q_{t,\tau}\rangle| \ll k_B T$. Equation (5.13), except for the time dependent $\Delta\beta_{t,\tau}$, is formally similar to equation (A.3) provided by the fluctuation theorem. These results are the first experimental evidence of this symmetry property for the heat fluctuations of a relaxing system similar to that studied theoretically for an aging spin glass in Ref. [116, 117]. For comparison, in figure 5.12(b) we plot $\rho_t(q_\tau)$ for the quench in glycerol at $t = 0$ and $\tau = 30$ s. In this case the heat exchange process is always symmetric because the bath quickly relaxes to thermal equilibrium in less than 1 ms after the quench and the particle equilibrates with this equilibrium bath in ≈ 65 ms. This result stresses the conclusion that the observed asymmetry in gelatin is really due to the intricate nonequilibrium nature of the bath. The relaxation of the strong nonequlibrium fluctuations of the assembling gelatin chains, which perturb the Brownian particle motion, can be interpreted as a heat flux towards the environment. This process becomes so slow during the aging that it is undetectable by the particle after 20 seconds.

5.5.1 Model

In the absence of a theory for these experimental results we need to estimate the prefactor $\Delta\beta_{t,\tau}$ to gain a physical interpretation of equation (5.13). We proceed to show that the asymmetry of $P_t(q_\tau)$ can be directly linked to the nonstationarity of the aging bath through the quantity σ_x. From equation (5.11), the probability density $P_{Q_{t,\tau}}$ of the heat fluctuations is equal to the probability density $P_{\Delta U_{t,\tau}}$ of the variation of the potential energy of the particle. Then, according to equation (5.11), $Q_{t,\tau}$ can be expressed as the difference of two random variables: $U_{t+\tau}$ and U_t. For τ much larger than the largest correlation time of these two variables, $P_{Q_{t,\tau}}$ can be written as a cross-correlation function

$$P_{Q_{t,\tau}}(Q) = \int_{-\infty}^{\infty} P_{U_{t+\tau}}(u+Q)P_{U_t}(u)\,\mathrm{d}u,$$

Then, the corresponding characteristic functions (their Fourier transforms) are

$$\hat{P}_{Q_{t,\tau}}(s) = \hat{P}_{U_{t+\tau}}(s)\hat{P}_{U_t}(-s), \tag{5.14}$$

where the probability density of the energy fluctuations $U_t = kx_t^2/2$ at time t can be expressed in terms of the probability density of the fluctuations of x_t. Taking into account the experimental fact that the fluctuations of x_t are Gaussian for all $t \geq 0$ (see figure 5.9(b)), we find the explicit expression of P_{U_t} using the formula for $P_{x_t}(x)$ given by equation (5.6)

$$P_{U_t}(U) = \frac{2}{\sqrt{4\pi k\sigma_x(t)^2}}\frac{1}{\sqrt{U}}\exp\left(-\frac{U}{k\sigma_x(t)^2}\right)\Theta(U), \tag{5.15}$$

where Θ is the Heaviside function. The Fourier transform of equation (5.15) is

$$\hat{P}_{U_t}(s) = \frac{1}{\sqrt{1+\mathrm{i}k\sigma_x(t)^2 s}}. \tag{5.16}$$

Then, from equation (5.14) we obtain the explicit form of the characteristic function of the heat fluctuations

$$\begin{aligned}\hat{P}_{Q_{t,\tau}}(s) &= \frac{1}{\sqrt{1+\mathrm{i}k\sigma_x(t+\tau)^2 s}}\frac{1}{\sqrt{1-\mathrm{i}k\sigma_x(t)^2 s}},\\ &= \frac{1}{\sqrt{\alpha_{t,\tau}+\left[\epsilon_{t,\tau}s-\mathrm{i}\frac{\Delta_{t,\tau}}{2}\right]^2}},\end{aligned} \tag{5.17}$$

where the parameters $\alpha_{t,\tau}$, $\epsilon_{t,\tau}$ and $\Delta_{t,\tau}$, that depend on t and τ, are

$$\begin{aligned}\alpha_{t,\tau} &= 1+\frac{1}{4}\left[\frac{\sigma_x(t)}{\sigma_x(t+\tau)}-\frac{\sigma_x(t+\tau)}{\sigma_x(t)}\right]^2,\\ \epsilon_{t,\tau} &= k\sigma_x(t+\tau)\sigma_x(t),\\ \Delta_{t,\tau} &= \frac{\sigma_x(t)}{\sigma_x(t+\tau)}-\frac{\sigma_x(t+\tau)}{\sigma_x(t)}.\end{aligned} \tag{5.18}$$

Equation (5.17) can be written in the form

$$\hat{P}_{Q_{t,\tau}}(s) = \frac{1}{\sqrt{\alpha_{t,\tau}}}\hat{g}\left(\frac{\epsilon_{t,\tau}}{\sqrt{\alpha_{t,\tau}}}s - \mathrm{i}\frac{\Delta_{t,\tau}}{2\sqrt{\alpha_{t,\tau}}}\right), \tag{5.19}$$

where $\hat{g}(y) = (1+y^2)^{-1/2}$. Therefore its inverse Fourier transform leads to the expression of the probability density of $Q_{t,\tau}$

$$P_{Q_{t,\tau}}(Q) = \frac{1}{\epsilon_{t,\tau}}g\left(\frac{\sqrt{\alpha_{t,\tau}}}{\epsilon_{t,\tau}}Q\right)\exp\left(-\frac{\Delta_{t,\tau}}{2\epsilon_{t,\tau}}Q\right). \tag{5.20}$$

The inverse Fourier transform $g(x)$ of the function $\hat{g}(y)$ has an analytical expression in terms of the zeroth-order modified Bessel function of the second kind

$$g(x) = \frac{K_0(|x|)}{\pi},$$

which allows us to write an explicit expression for the probability density function of the normalized heat $q_{t,\tau}$

$$P_t(q_\tau) = \frac{A_{t,\tau}}{\pi}K_0\left(B_{t,\tau}|q_\tau|\right)\exp\left(-\frac{\Delta_{t,\tau}A_{t,\tau}}{2}q_\tau\right), \tag{5.21}$$

with the time dependent parameters

$$\begin{aligned}
\Delta_{t,\tau} &= \frac{\sigma_x(t)}{\sigma_x(t+\tau)} - \frac{\sigma_x(t+\tau)}{\sigma_x(t)}, \\
A_{t,\tau} &= \frac{k_BT}{k\sigma_x(t)\sigma_x(t+\tau)}, \\
B_{t,\tau} &= A_{t,\tau}\sqrt{1+\frac{\Delta_{t,\tau}^2}{4}}.
\end{aligned} \tag{5.22}$$

In equation (5.21) the asymmetry of the density is completely determined by the parameter $\Delta_{t,\tau}$ in the exponential. At equilibrium $\Delta_{t,\tau} = 0$, $A_{t,\tau} = B_{t,\tau} = 1$ regardless of t and τ, so that one recovers the expression of the symmetric equilibrium profile $P_t(q_\tau) = K_0(|q_\tau|)/\pi$ with $\langle q_{t,\tau}\rangle = 0$ that was found in [118, 119]. In figure 5.12 for each experimental $P_t(q_\tau)$ we plot the prediction given by the analytical formula (5.21) using the respective experimental values of σ_x shown in figure 5.10. The excellent agreement confirms that our approach is suitable to describe the heat exchanges of the bead with the gelatin bath during the first 200 s after the quench.

From equation (5.21) we obtain the explicit expression for the asymmetry function of $q_{t,\tau}$

$$\begin{aligned}
\rho_t(q_\tau) &= \ln\frac{P_t(q_\tau)}{P_t(-q_\tau)}, \\
&= -\Delta\beta_{t,\tau}q_\tau,
\end{aligned} \tag{5.23}$$

where the prefactor $\Delta\beta_{t,\tau}$ is

$$\Delta\beta_{t,\tau} = \frac{k_B T}{k}\left[\frac{1}{\sigma_x(t+\tau)^2} - \frac{1}{\sigma_x(t)^2}\right]. \tag{5.24}$$

Hence, the linearity of $\rho_t(q_\tau)$ is analytically satisfied for all the values of the heat fluctuations and for all t even when $P(q_\tau)$ is strongly non-Gaussian. In figure 5.13 we plot the straight lines with the slope $\Delta\beta_{t,\tau}$ given by equation (5.24) and computed using the experimental values of σ_x. The good agreement with the experimental data shows that the asymmetry of the fluctuations of the heat exchanged between the Brownian particle and the bath verifies the fluctuation theorem.

Equations (5.23) and (5.24) gain a very intuitive interpretation if one introduces an equipartition-like relation for the particle motion for $0 \leq t \lesssim 200$ s:

$$\frac{1}{2}k_B T_{eff}(t) = \frac{1}{2}k\sigma_x(t)^2.$$

Here $T_{eff}(t)$ is the effective temperature perceived by the particle at time t due to its coupling with the nonequilibrium gelatin environment. It quantifies the total stochasticity provided to the particle by the motion of the neighboring gelatin chains. In this way the parameter $\Delta\beta_{t,\tau}$ can be written conveniently as

$$\Delta\beta_{t,\tau} = \left[\frac{1}{T_{eff}(t+\tau)} - \frac{1}{T_{eff}(t)}\right]T, \tag{5.25}$$

Equation (5.25) is formally equivalent to the expression (A.3) provided by the fluctuation theorem for the heat fluctuations of a system in contact with two thermostats at unequal temperatures. See appendix A for more details. Hence the quantity

$$\Delta S_{t,\tau} = -k_B \Delta\beta_{t,\tau} q_{t,\tau} \tag{5.26}$$

can be naturally identified as the entropy produced by the breakdown of the time-reversal symmetry due to the the effective temperature imbalance at two different times after the quench. As the gelatin droplet ages the mean entropy production rate $\Delta S_{t,\tau}/\tau$ slows down and the particle exhibits an equilibrium-like dynamics for the experimental timescales. We point out that unlike equation (A.3) derived in references [120, 121, 122, 123, 124, 125] for nonequilibrium *steady* states, equations (5.23) and (5.24) hold for a nonstationary regime created by the nonequilibrium bath (the aging gelatin droplet around the particle).

5.6 Nonequilibrium fluctuations and linear response

We now discuss the relation between entropy production, spontaneous fluctuations and response of the trapped particle in this out-of-equilibrium aging bath. From the results presented in chapters 3 and 4, it is clear that the there is a strong connection

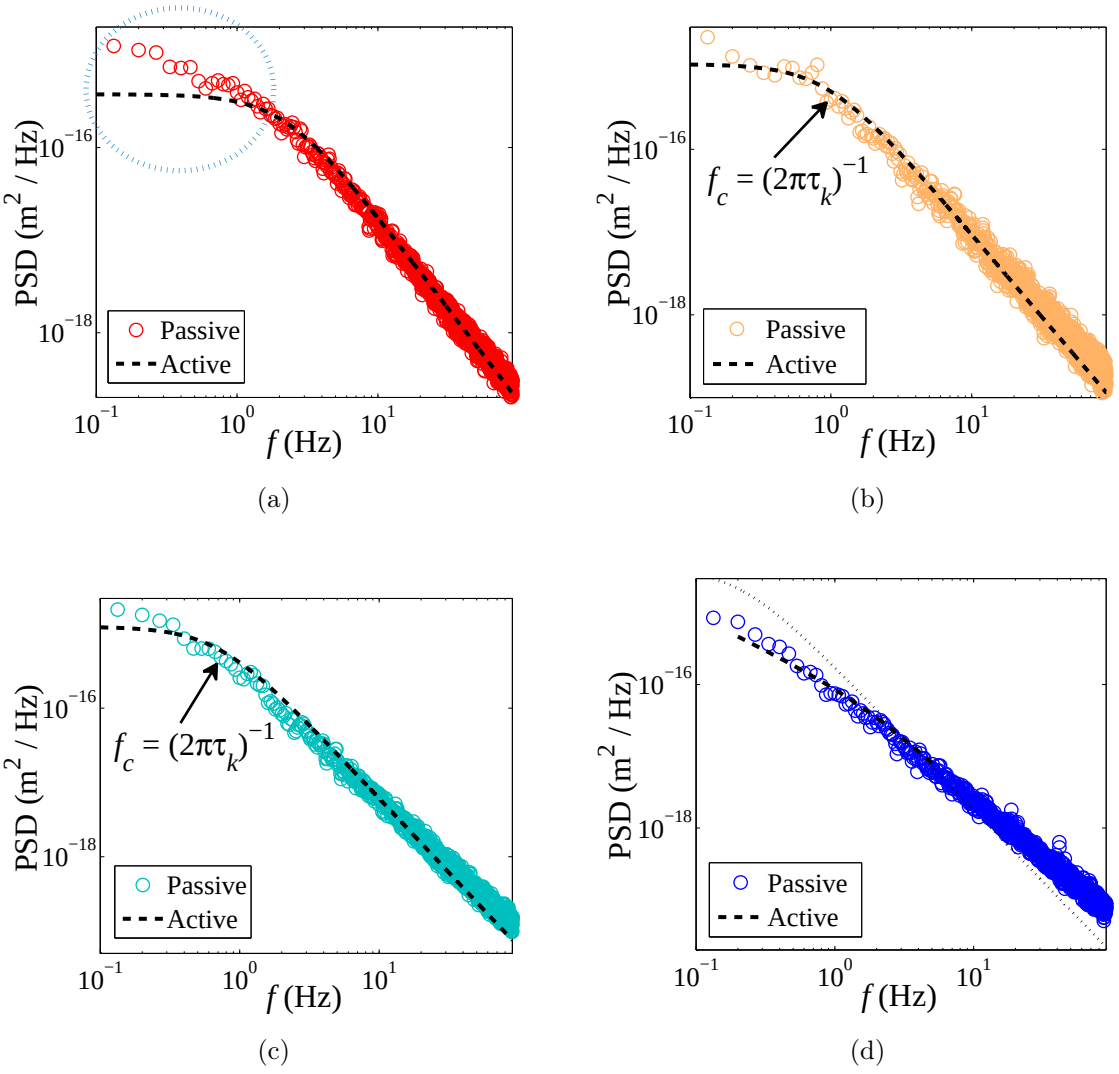

Figure 5.14: Passive ($\langle|\hat{x}(f,t)|^2\rangle$) and active ($2k_BT\mathrm{Im}\{\hat{R}\}/(\pi f)$) terms of equation (5.28) for the particle position x at different times after the quench: (a) $0 \leq t \leq 15$s, the dotted circle points out the low-frequency deviation from equation (5.28); (b) 30 s $\leq t \leq$ 45 s, the arrow indicates the position of the frequency f_c (5.30); (c) 75 s $\leq t \leq$ 90s; and (d) 1200 s $\leq t \leq$ 1215 s. The dotted line corresponds the Lorentzian curve obtained without taking into account the storage modulus G' of the gel.

between the deviations from the equilibrium fluctuation-dissipation relation (2.16) and the extent of the broken detailed balance. If energy fluxes or total entropy production take place at a very slow rate then the system exhibits an equilibrium-like behavior, i.e. fluctuations and response are related by equation (2.16) like the Brownian particle in the Laponite colloidal glass. On the other hand, if the rate is fast enough, then currents are non-negligible and deviations from equation (2.16) are significant, like in the case of the Brownian particle in the toroidal optical trap. In the case of gelatin, we found that there is a non-negligible heat flux comparable to k_BT from the particle to the bath during the first 20 seconds of the quench. The rate at which this heat flux takes place slows down as the gelatin ages. The heat $q_{t,\tau}$ times the prefactor $-\Delta\beta_{t,\tau}$ defined in equation (5.24) corresponds to the total entropy production during the time interval $[t, t+\tau]$. The breakdown of the detailed balance is reflected in the asymmetry $\Delta\beta_{t,\tau} > 0$, quantified by $\sigma_x(t)^2 - \sigma_x(t+\tau)^2 > 0$ or by introducing the effective temperature imbalance $T_{eff}(t) - T_{eff}(t+\tau) > 0$. Therefore it should be expected that a significant deviation of the equilibrium fluctuation-dissipation relation (2.16) will happen for the fluctuations and response of the trapped particle during the aging regime I of the gelatin droplet. In contrast, in the regimes II and III the fluctuation-dissipation relation (2.16) must be satisfied with the temperature T of the thermal bath. Indeed, we show in the following that our experimental results display such a kind of behavior.

As we performed the active microrheology measurements at fixed excitation frequency f, it is more convenient to study the fluctuations and linear response in frequency domain. According to equation (1.22), the Fourier transform of the linear response function of the particle position x to a perturbative time-dependent force is related to the shear modulus G of the gelatin droplet by

$$\hat{R}(f,t) = \frac{1}{6\pi r G^*(f,t) + k},$$

Then, the imaginary part, related to the additional dissipation of the particle due to an external force with respect to the unperturbed aging process, is

$$\mathrm{Im}\{\hat{R}(f,t)\} = \frac{6\pi r G''(f,t)}{[k + 6\pi r G'(f,t)]^2 + [6\pi r G''(f,t)]^2}. \tag{5.27}$$

Around thermal equilibrium, this *active* quantity is related to the *passive* power spectral density $\langle|\hat{x}(f,t)|^2\rangle$ of the fluctuations of x (no external force) by

$$\langle|\hat{x}(f,t)|^2\rangle = \frac{2k_BT}{\pi f}\mathrm{Im}\{\hat{R}\}. \tag{5.28}$$

Then, we proceed to compare the relation between $\langle|\hat{x}(f,t)|^2\rangle$ and $2k_BT\mathrm{Im}\{\hat{R}\}/(\pi f)$ in the different nonequilibrium aging regimes of the gelatin droplet.

In figure 5.14(a) we plot $\langle|\hat{x}(f,t)|^2\rangle$, computed over the time window $0 \leq t \leq 15$ s where a strong mean heat flux takes place (see section 5.5). On the other hand, taking

into account the active measurements of G (section 5.3), $\mathrm{Im}\{\hat{R}\}$ can be written in this regime as

$$\mathrm{Im}\{\hat{R}(f,t)\} = \frac{1}{2\pi\gamma_0(t)}\frac{f}{f^2+f_c(t)^2}, \tag{5.29}$$

where $f_c(t)$ is related to the inverse of the viscous relaxation time $\tau_k(t)$ (equation (5.5)) of the trapped particle at time t by

$$f_c(t) = \frac{1}{2\pi\tau_k(t)}. \tag{5.30}$$

In figure 5.14(a) we also plot the quantity $2k_BT\mathrm{Im}\{\hat{R}\}/(\pi f)$, which has a Lorentzian profile. As expected, an important deviation of equation (5.28) is observed for frequencies $f \lesssim 1$ Hz. Note that at frequencies $f \gtrsim 1$ Hz equation (5.28) is verified, indicating that the deviation is actually due to the slow structural assembalge of the gel. The spectral curves of figure 5.14(a) provide information on the timescales at which this phenomenon perturb the Brownian probe: $\gtrsim 1$ s. The extent of the deviation, i.e. the difference between the area below $\langle|\hat{x}(f,t)|^2\rangle$ minus the area below $2k_BT\mathrm{Im}\{\hat{R}\}/(\pi f)$ in figure 5.14(a), can be written as

$$\begin{aligned}\int_0^\infty \left[\langle|\hat{x}(f,t)|^2\rangle - \frac{2k_BT}{\pi f}\mathrm{Im}\{\hat{R}(f,t)\}\right]\mathrm{d}f &= \frac{k_B}{k}[T_{eff}(t)-T], \\ &= \frac{2|\langle Q_{t,\infty}\rangle|}{k},\end{aligned} \tag{5.31}$$

Similar to the generalized fluctuation-dissipation relation for NESS derived by Harada and Sasa [18], equation (5.31) hightlights the role of currents (or equivalently, total entropy production) in the relation between spontaneous fluctuations and linear response. In the present case, the right-hand side of equation (5.31) is closely related to such a current because it quantifies the heat excess that must irreversibly flow from the particle to the bath in order for the system to reach equilibrium at temperature T. Thus, the "violation" of the fluctuation-dissipation relation (5.28) in the form (5.31) can be interpreted as a measure of the heat that must be dissipated to reach an equilibrium state. This is in close analogy to the heat that must be dissipated into the medium to keep a NESS in the fluctuation-dissipation formulation developed in reference [18]. In figure 5.14(b) we plot the passive and active fluctuation-response terms in the regime I for the time window 30 s $\leq t \leq$ 45 s. We check that in this case the equilibrium-like equation (5.28) is satisfied with the final equilibrium temperature $T = 27.2°$C of the gelatin droplet. As discussed previously, this results is in good agreement with the fact that the mean heat flux becomes undetectable by the Brownian particle.

Figure 5.14(c) displays the passive power spectral density of x computed in the time interval 75 $\leq t \leq$ 90 s, i.e. in the regime II where G' starts to increase. Taking into account that the fluid can be characterized by a single relaxation time τ_0 in this

regime, the active term related to the linear response reads

$$\begin{aligned} \mathrm{Im}\{\hat{R}(f,t)\} &= \frac{\gamma_0(t)}{k^2}\frac{2\pi f}{1+4\pi^2[\tau_0(t)+\tau_k(t)]^2 f^2}, \\ &\approx \frac{1}{2\pi\gamma_0(t)}\frac{f}{f^2+f_c(t)^2}, \end{aligned}$$

where we have used the experimental fact that $\tau_0 \leq 0.05\tau_k$ (figure 5.8). Using the previous expression for the imaginary part of the response with the experimental values of γ_0 and f_c, in figure 5.14(c) we plot the active term $2k_BT\mathrm{Im}\{\hat{R}\}/(\pi f)$. In this case, the agreement between the left-hans side and the right-hand side of equation (5.28) is good verifying simultaneously that the system has relaxed to an equilibrium-like behavior and that the fluid has a single relaxation time much smaller than τ_k.

Finally, in figure 5.14(d) we plot the passive (circles) and active (dashed line) spectral terms computed in the time interval 1200 s $\leq t \leq$ 1215 s. In this case the large viscoelasticity of the gelatin droplet gives rise to the highly non-Lorentzian shape of both terms. For comparison, we also plot the Lorentzian profile (dotted line) that would be naïvely obtained using equation (5.29) without taking into account the contribution of the storage modulus G'. In the absence of an accurate model for the viscoelasticity of the droplet in this regime, we only plot the active term in the frequency range 0.2 Hz$\leq f \leq$ 5Hz at which the sinuosoidal external force was applied to the particle. Once again, we verifiy that an equilibrium-like fluctuation-dissipation relation (5.28) holds for the particle position x because of the smallness of the heat fluxes as the gelatin droplet ages.

5.7 Summary and conclusion

We have experimentally measured the fluctuations of the position of a trapped Brownian particle in a nonstationary bath, i.e. an aging gelatin after a very fast quench. This simple experiment has allowed us to understand several concepts formulated originally for NESS that can be naturally extended to nonstationary systems prepared away from thermal equilibrium and slowly relaxing towards an equilibrium state. We summarize the main points of this chapter:

(a) The use of gelatin as a nonequilibrium aging bath for a micron-sized particle let us actually probe the nonequilibrium transient formation of a gel because the typical length of the gelatin chains is not negiglible compared to the size of the Brownian probe.

(b) Thanks to our experimental setup based on optical tweezers, we were able to perform a very fast quench from above to below the gelation temperature of the sample in a micron-sized droplet melted around the trapped bead. In this way the gelation rate was accelerated with respect to the usual bulk experiments to achieve accessible timescales for the Brownian probe. Besides, we could perform

several independent quenches to compute ensemble averages, which was strictly required because of the nonstationarity of the system.

(c) By performing active microrheology we identified three different aging regimes during the gelation of the droplet. In particular, we found a very early regime during the first 60 s after the quench where the droplet rheologically behaves as a Newtonian fluid but it exhibits striking nonequilibrium effects on the Brownian motion of the trapped particle.

(d) We determined the statistical properties of the spontaneous fluctuations of the particle position in the absence of external time-dependent forces. We found that these fluctuations are Gaussian so they can be completely characterized by the variance. We found that this variance, which is a decreasing function of time, supplies additional information on the influence of the nonequilibrium fluctuations produced by the assembling gelatin chains.

(e) During the first 200 s after the quench we directly computed the heat exchanged between the trapped particle and the bath. We showed that the distribution of the heat has a strong asymmetry which is a decreasing funtion of the aging time. Using the experimental statistical properties of the fluctuations of x, we derived an analytical expression for this asymmetry and we showed that it satisfies a fluctuation relation similar to that for a thermal conductive system in a NESS in contact with two reservoirs at unequal temperatures. This is a remarkable result since the system studied here is nonstationary. We provided a clear interpretation to our results in terms of entropy production. This interpretation and the theoretical results reported for spin glasses [116, 117] (see appendix A), suggest that this fluctuation relation may appear as a very robust symmetry property of heat exchange processes in other kinds of relaxing systems.

(f) Finally, we discussed the connection between the mean heat flux from the particle to the bath with fluctuations and linear response. We checked that the extent of the "violation" of the equilibrium fluctuation-dissipation relation is closely related to the heat flux from the particle to the bath, or equivalently, to the entropy that is produced in order for the system to reach equilibrium. Therefore as the system ages, the relation between fluctuations and linear response behaves like in equilibrium.

Conclusion

Chapter 6

Conclusion and perspectives

The generalization of the fluctuation-dissipation theorem, to processes away from thermal equilibrium, and the fluctuation relations are important topics of great current interest in nonequilibrium statistical mechanics. They are particularly relevant to describe energy exchanges of small system wherein fluctuations and off-equilibrium conditions are common. The present dissertation describes three experiments that provide a clear understading on generalized fluctuation-dissipation relations derived from different theoretical approaches. It also shows, from an experimental perspective, how to connect quantitatively these concepts with heat flux and entropy production that are the quantities directly involved in the fluctuation theorem. This was possible thanks to our experimental study based on the Brownian motion of a single microbead confined by optical tweezers.

We summarize the main points and conclusions of each chapter:

- In chapter 1 we detailed two different optical tweezers that allowed us to carry out the experiments under very well controlled conditions. One of the most important features of these setups is that the relevant forces exerted on the particle by a highly focused laser beam can be accurately measured. External perturbative forces can be also applied to the trapped particle by driving the focus position or by tuning the laser power. In addition, the viscoelastic properties of the fluid surrounding the particle can be determined by microrheology. In this way a complete characterization of the forces of interest acting on the particle was achieved.

- In chapter 2 we presented a brief overview on different generalized fluctuation-dissipation formulations for Markovian systems in nonequilibrium steady states. We emphasized the main ideas behind the derivation of these relations in order to contrast their physical approaches involving different observables. Hence, we highlighted the importance of understanding the connection between these relations from the theoretical and experimental points of view.

- In chapter 3 we presented an experiment on a Brownian particle suspended in water and driven into a periodic nonequilibrium steady state by a toroidal op-

tical trap. We showed that the presence of a nonconservative force exerted by the scanning laser beam results in a strong deviation from the equilibrium fluctuation-dissipation theorem. As all the observables involved in the generalized fluctuation-dissipation relations presented in chapter 2 could be measured, we analyzed carefully the exact relation between fluctuations and linear response in the context of these formulations. We stressed the role of the probability current, the total entropy production and the breakdown of the time reversibility of the dynamics. Then, we found that when taking into account these quantities, the generalized fluctuation-dissipation formulae are satisfied. Due to the simplicity of the dynamics of the system, a clear interpretation of the link between the different approaches was accomplished in terms of the stochastic entropy production rate. Our work represents one of the first experimental test of these new theoretical approaches to fluctuation-dissipation around nonequilibrium steady states.

- In chapter 4 we described an experiment on a Brownian particle in an aqueous Laponite suspension. In this case the nonequilibrium nature of the system is due to the nonstationary dynamics created by the aging colloidal glass. Using simultaneously different microrheology techniques we checked that the particle position satisfies the equilibrium fluctuation-dissipation theorem for the timescales probed by optical tweezers even when the surrounding Laponite is in a nonequilibrium regime. Our results were supported by the measurement of the fluctuations of the heat transferred at different timescales between the Brownian particle and the suspension. We found that the probability density function of the heat fluctuations is symmetric and centered around zero. Therefore we could interpret these results as an equilibrium-like behavior of the trapped particle due to the slowdown of the heat fluxes as the colloidal glass ages.

- In chapter 5 we reported an experiment on a Brownian particle in a different kind of aging system: an aqueous gelatin solution undergoing the sol-gel transition. Unlike Laponite, in the case of gelatin we accurately controlled the initial condition of the solution by means of a heating laser, which allowed us to perform a very fast quench. Due to the gelatin microstructure and the fast quench, the typical length and timescales of the sol-gel transition became accessible by microrheology. Therefore the Brownian particle actually probed the relevant nonequilibrium degrees of freedom of the bath. Indeed, our experimental results show the presence of a significant heat flux from the particle to the bath due to the assemblage of the gel network. We found that the heat fluctuations satisfy the asymmetry relation quantified by the fluctuation theorem. This asymmetry decreases as the gelatin ages becoming negligible in a few seconds. Based on the statistical properties of the fluctuations of the particle position, we derived an analytical expression of the heat probability distribution which fits the experimental data. This anaytical expression satisfies a fluctuation relation similar to that for the entropy production of a stationary system in contact with two thermostats at

unequal temperatures. Hence, our results provide simultaneously experimental and analytical evidence that the fluctuation theorem is a very robust symmetry property of the entropy production that also holds for aging system. We also studied the connection between the mean heat flux from the particle to the bath with fluctuations and linear response. We found that the extent of the violation of the equilibrium fluctuation-dissipation relation is directly related to the heat which must flow from the particle to the bath in order for the system to reach thermal equilibrium.

From the results obtained in the three experiments, we accomplished a rather general comprehension of the relation between fluctuations and linear response for nonequilibrium processes. Our simple experimental results allowed us to identify several underlying concepts formulated originally for nonequilibrium steady states that can be naturally extended to nonstationary regimes slowly relaxing towards an equilibrium state. Unlike previous approaches to fluctuation-dissipation based on the concept of effective temperature, we showed that the violation of the fluctuation-dissipation theorem actually provides quantitative information on the irreversible heat exchanges in out-of-equilibrium processes. This prominent conclusion offers the possibility to implement useful protocols to quantify the broken detailed balance in nonequilibrium experiments on small systems. For example, the violation of the equilibrium fluctuation-dissipation theorem must be computed as the difference of independent measurements of the right correlation and response functions of interest. Then, the observables that quantify the broken detailed balance such as dissipation rates, heat fluxes, currents, total entropy production, etc., can be estimated by this difference. Reciprocally, if heat fluxes can be directly measured in an experiment, then the response of the system around a nonequilibrium state can be determined from the measurement of the right correlation functions involving heat fluctuations. So far, this approach has been exploited only once in a nonequilibrium steady state experiment to estimate the energetic efficiency of a rotary molecular motor [126]. However, based on the results of the thesis we claim that the same ideas can be applied to more complex systems involving multiple degrees of freedom or nonstationary states.

We point out that the explicit analysis on the connection between fluctuation-response and irreversible heat flows was always restricted to the regime where the elastic component of the surrounding fluid is sufficiently small, i. e. for Markovian dynamics. The viscoelastic case, which implies non-Markovian particle dynamics, was not analitically addressed in this thesis. This problem, although important for applications, is in general disregarded in theory. Indeed, until now almost all the generalized fluctuation-dissipation relations, except for that derived in [151, 152, 153], have been formulated for the Markovian case. On the other hand, the formulation of references [151, 152, 153] is very specific. It links the velocity fluctuations and its linear response for a Brownian particle in a viscoelastic bath, around a stationary or nonstationary state. It involves explicitly the viscoelastic kernel and the correlation of the stochastic force that appear in the Langevin equation (see for example equation (1.16)).The more

general case of the fluctuations and response for an arbitrary observable of a system with non-Markovian dynamics is still an open question. Some ideas have been loosely proposed to overcome this problem, such as extending the number of degrees of freedom of the system to render the dynamics Markovian. This is not evident at all in real experiments, though. At first glance a more suitable alternative is to develop a formulation involving a global quantity which quantifies the non-Markovianity of the system, such as the viscoelastic kernel or the shear modulus of the fluid. Nonetheless, it turns out that this also represents a difficult task in practice. For instance, for a single Brownian particle embedded in a highly viscoelastic fluid undergoing aging, the shear modulus of the fluid over a sufficiently broad bandwidth is not known a priori. Consequently, the non-Markovian dynamics can not be completely characterized and the energy exchanges can not be computed by means of the particle position only.

For the two different aging systems studied in this thesis, there are a number of interesting problems that could be addressed in the future in order to clarify some open questions:

- In chapters 4 and 5 we argued that the size and timescales of the trapped Brownian particle play a crucial role to probe the irreversible heat fluxes that give rise to the violation of the fluctuation-dissipation theorem. Then the dependence of the extent of the violation as a function of the particle size would be useful to offer a definitive answer to this question.

- For glassy systems, it has been widely discussed that the relaxation process is conducted by the rearrangement of mesoscopic regions into more stable configurations. In addition, glasses display a complex spatio-temporal structure, called dynamical heterogeneities. These phenomena, that generate long-range correlations in a glassy system, could be studied in a Laponite colloidal glass by means of the measurement of cross-correlation functions of sufficiently small tracers.

- In the experiment on gelatin described in chapter 5, we only studied the dynamics of the Brownian particle in the center of the droplet. A possible experiment that could help to understand how the gelation process takes place across the droplet is to measure the Brownian motion of a microbead at different places after the quench. The Brownian motion close to the sol-gel interface between the droplet and the bulk is particularly interesting. Indeed, it could provide information on the dynamics and surface tension fluctuations of the interface during the gelatin process

- We found that that during the first 20 second after the quench, the nonequilibrium assemblage of the gel strongly perturbs the Brownian motion of the trapped particle. Based on the spectral analysis of the particle position, this can be interepreted as a non-thermal noise at low frequencies. A more careful study on the statistical properties of this noise is interesting per se.

- Finally, it has been shown that the sol-gel transition in gelatin bulk occurs due to the percolation of the chains forming an infinite network. The cross-correlation study of free tracers inside the gelatin droplet after the quench could help to elucidate whether the same mechanism occurs at microscopic lengthscales.

Appendices

Appendix A

Fluctuation theorem

The *fluctuation theorem* (FT) is a very important achievement in nonequilibrium statistical mechanics because it represents a generalization of the second law of thermodynamics. It deals with symmetry properties of the entropy production of systems driven arbitrarily away from thermal equilibrium by an external driving and submitted to a source of fluctuations. According to the second law of thermodynamics, for a nonequilibrium system the mean entropy production is always positive. The FT quantifies the relative probability P of observing rare events, i.e. negative values of the entropy production S with respect to positive ones. For instance, for a system described by a set $\{x\}$ of degrees of freedom, in contact with a thermostat and driven by a time dependent force, the relation provided by the FT reads

$$\lim_{\tau\to\infty}\frac{1}{\tau}\ln\frac{P(\sigma_\tau=\sigma)}{P(\sigma_\tau=-\sigma)}=\frac{1}{k_B}\sigma\tau, \tag{A.1}$$

In equation (A.1), k_B is the Boltzmann constant whereas σ_τ is the average on a time τ of the entropy rate $\dot{S}(x_\tau)$, produced by the irreversible work done by the driving force

$$\sigma_\tau=\frac{1}{\tau}\int_0^\tau \dot{S}(x_t)\mathrm{d}t.$$

Note that in general, equation (A.1) is an asymptotic relation valid only for measurement times τ much larger than the correlation times of the system. As σ is an extensive quantity, the FT reduces to the second law of thermodynamics $\langle\sigma_\tau\rangle\geq 0$ as the size of the system increases. Equation (A.1) was observed for the first time in numerical simulations of a fluid driven by shear [8] and rigorously demonstrated for systems in nonequilibrium steady states [9, 127, 128]. Since then, several refinements on the formulation of FT have been developed. For example, equation (A.1) has been derived for Langevin dynamics [10] and general Markovian processes [129]. It has been demonstrated that for first order Langevin dynamics, quantities closely related to the entropy production, such as the work done by an external force [130] and the heat dissipated into the bath [131], also satisfy a symmetry property similar to equation (A.1). In reference [130] it was shown for the first time that the equality (A.1) holds for all $\tau\geq 0$

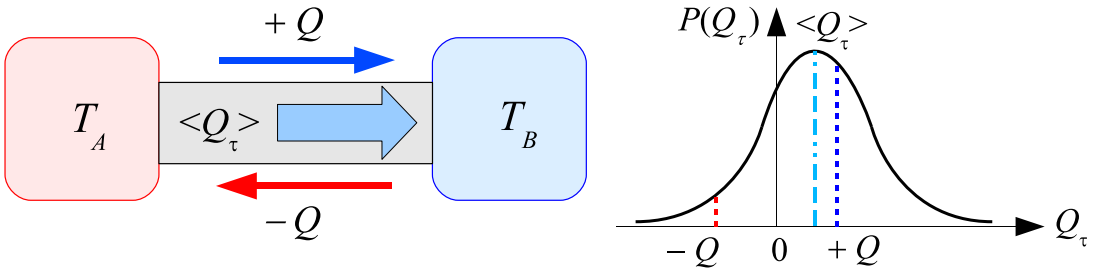

Figure A.1: Diagram of a thermally conductive system in contact with two reservoirs at different temperatures $T_A > T_B$. Due to the temperature difference, during a given time τ an amount of heat $\langle Q_\tau \rangle > 0$ flows in average from A to B (blue thick arrow). Extreme rare events when the heat flows from B to A can occur (thin red arrow), though, due to thermal fluctuations. The relative probability of a rare negative event with respect to that of the corresponding positive value (thin blue arrow) is quantified by the fluctuation theorem: the asymmetry of the profile of the probability density of the heat, $P(Q_\tau)$, is not arbitrary but it satisfies equation (A.3).

in the case of a first order Langevin system in a transient state after switching on a perturbing force. More recently, it was demonstrated that the equality is valid for all times as well in nonequilibrium steady states by introducting the concept of stochastic entropy [11], see appendix C. In such a case, equation (A.1) can be written as

$$\frac{P(\Delta S_\tau = \Delta S)}{P(\Delta S_\tau = -\Delta S)} = \exp\left(\frac{\Delta S}{k_B}\right). \tag{A.2}$$

where ΔS_τ is the *total* entropy variation of the system during a given stochastic realization x_τ.

FT for heat conduction

A different kind of nonequilibrium stationary process which exhibits a symmetry property similar to equation (A.1) is the heat flux between two thermostats at different temperatures. We consider a thermally conductive system in contact with two reservoirs A and B at unequal temperatures T_A and T_B, respectively, with $T_A > T_B$ (see figure A.1). Due to the temperature difference imposed at the boundaries, there is a mean heat flux from A to B. After a transient the sytem reaches a steady state: the mean heat flux becomes time-independent if the reservoirs are infinite. If the size of the system is sufficiently small, the stationary heat flux is a strongly fluctuating quantity: the heat can flow from B to A because of the thermal fluctuations but in average its direction is always from A to B. It has been demostrated that the probability $P(Q_\tau)$ of observing an amount of heat Q_τ flowing from A to B in a time τ, is related to that

of observing the quantity $-Q_\tau$ (from B to A) according to:

$$\ln \frac{P(Q_\tau)}{P(-Q_\tau)} = \Delta\beta \; Q_\tau, \tag{A.3}$$

where

$$\Delta\beta = \frac{1}{k_B}\left(\frac{1}{T_B} - \frac{1}{T_A}\right). \tag{A.4}$$

Note the strong similarity between equations (A.3) and (A.2): the logarithm of the probability ratio is a linear function of its argument. Indeed, it has been shown that the term $k_B \Delta\beta \; Q_\tau$ can be identified as the entropy production during the time τ [123, 124]. For $T_A = T_B$, equation (A.3) reduces to the equilibrium case $P(Q_\tau) = P(-Q_\tau)$ when the probability density of the heat is symmetric and $\langle Q_\tau \rangle = 0$ due to detailed balance and microscopic time-reversibility. Equation (A.3) was explicitly derived for several theoretical model systems in contact with two thermostats in the stationary regime: e.g. classical and quantum Hamiltonian systems [120], Ising models [121, 125], Langevin dynamics [122, 123], Markovian chains [124] and harmonic networks [132, 133].

FT for aging spin glasses

Finally, a third class of nonequilibrium process for which a similar symmetry property holds, corresponds to the aging in some models of spin glasses, prepared in an initial metastable state by a temperature quench. In this case, in order to reach more stable configurations there is a continuous heat release from the spin glass to the environment. The heat exchange occurs in two different ways: a fast heat exchange process due to the thermal fluctuations and an intermittent heat release taking place at much longer timescales. In references [116, 117] it was demonstrated and numerically checked that the fluctuations of the intermittent heat exchange satisfy the symmetry relation

$$\ln \frac{P_{t_w}(Q)}{P_{t_w}(-Q)} = \frac{Q}{k_B T_{eff}(t_w)} \tag{A.5}$$

where P_{t_w} stands for the probability density function of the intermittent released heat Q at aging time t_w, whereas $T_{eff}(t_w)$ is the value of the low-frequency *effective temperature* of the glass at time t_w (see section 4.1 for the definition of effective temperature in glassy systems). Note that, unlike equations (A.2) and (A.3), the relation given by equation (A.5) holds for a nonstationary regime that slowly evolves towards thermal equilibrium in which no external driving is applied to the system.

Appendix B

Work fluctuations for systems driven by an external random force

Introduction

As explained in appendix A, the FT is a very important result in nonequilibrium statistical mechanics because it quantifies the probability of observing rare extreme events in the energy exchange process of a rather broad class of nonequilibrium systems. According to equation (A.1), the FT applies formally to entropy production only, which in general can not be experimentally measured in a straightforward way. On the other hand, quantities such as heat, work, injected and dissipated power are more accessible in experiments. Hence, an important problem is to study how the FT is modified for such quantities. In particular, for overdamped Langevin dynamics it has been demonstrated that the fluctuations of the work W_τ injected by an external force into a thermostated system at temperature T and kept in a nonequilibrium stationary state, satisfy the symmetry relation [130]

$$\ln \frac{P(W_\tau = W)}{P(W_\tau = -W)} \to \frac{W}{k_B T}, \; \tau \gg \tau_c. \tag{B.1}$$

In equation (B.1) τ_c is the longest relaxation time of the system. Note the strong similarity between equation (B.1) and that directly provided by the fluctuation theorem (A.1). This is because the injected work, up to multiplicative constants and additive boundary terms, is closely related to the entropy production in this case.

Equation (B.1) has been tested in several experiments: e.g. a colloidal particle dragged by an optical trap [134], electrical circuits [135], mechanical harmonic oscillators [136] and a colloidal particle near the stochastic resonance [137]. In all of these examples the force which drives the system out of equilibrium is inherently deterministic. However, it has been recently argued that the nature (deterministic or stochastic) of the external forcing can play an important role in the distribution of the injected work, leading to possible deviations from the relation (B.1). Indeed, devations have been observed in different experiments and simulations: a Brownian particle in a Gaussian white [138] and colored [139] noise bath, turbulent thermal convection [140], wave

turbulence [141], a vibrating metalic plate [142], an RC electronic circuit [143] and a gravitational wave detector [144]. It is important to remark that in the systems previously cited the FT is violated because in such a case the external random force acts itself as a kind of thermal bath. Then the work W_τ is not a good estimator of the entropy production. One question which naturally arises is how equation (B.1) is modified when, in addition to the external random force, a true thermalization process is allowed, as occurs in the small systems discussed throughout this thesis. In this situation there are two sources of noise: the external force and the thermal bath.

In this appendix we address these questions in two experimental systems: a Brownian particle in an optical trap and a micro-cantilever used for atomic force microscopy (AFM). Both are in contact with a thermal bath and driven out of equilibrium by an external random force whose amplitude is tuned from a small fraction to several times the amplitude of the intrinsic thermal fluctuations exerted by the thermostat.

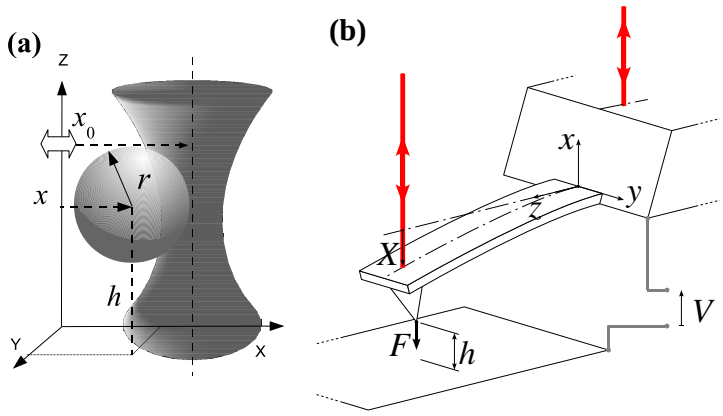

Figure B.1: a) Colloidal particle in the optical trap with modulated position. b) AFM cantilever close to a metallic surface. See text for explanation.

Colloidal particle in an optical trap

The first system we study consists on a spherical silica bead of radius $r = 1\,\mu$m immersed in ultrapure water which acts as a thermal bath. The experiment is performed at a room temperature of 27 ± 0.5°C at which the dynamic viscosity of water is $\eta = (8.52 \mp 0.10) \times 10^{-4}$ Pa s. The motion of the particle is confined by an optical trap using the experimental setup described in section 1.3. The trap stiffness is fixed at constant value $k = 5.4\,\mathrm{pN}/\mu\mathrm{m}$. The particle is kept at $h \approx 10\,\mu$m above the lower cell surface. Figure B.1(a) sketches the configuration of the bead in the optical trap. An external random force is applied to the particle by modulating the position of the trap $x_0(t)$ along a fixed direction x on the plane xy, using the XY AOD system (subsection 1.3.1). The modulation corresponds to a Gaussian Ornstein-Uhlenbeck noise of mean

$$\langle x_0(t) \rangle = 0,$$

and covariance

$$\langle x_0(s)x_0(t)\rangle = A\exp\left(-\frac{|t-s|}{\tau_0}\right).$$

The correlation time of the modulation is set to $\tau_0 = 25$ ms whereas the value of its amplitude A is tuned to control the driving intensity. We determine the particle barycenter (x, y) at a sampling rate of 1 kHz, as described in subsection 1.3.2. For the experimentally accessible timescales the dynamics of the coordinate x is described by the overdamped Langevin equation

$$\gamma\dot{x} = -kx + \zeta_T + f_0. \tag{B.2}$$

In equation (B.2) $\gamma = 6\pi r\eta$ is the viscous drag coefficient, ζ_T is a Gaussian white noise:

$$\langle\zeta_T\rangle = 0, \quad \langle\zeta_T(s)\zeta_T(t)\rangle = 2k_BT\gamma\delta(t-s),$$

which mimics the collisions of the thermal bath particles with the colloidal bead and $f_0(t) = kx_0(t)$ plays the role of the external stochastic force. The standard deviation δf_0 of f_0 is chosen as the main control parameter of the system. Besides the correlation time τ_0 of f_0, there is a second characteristic timescale in the dynamics of equation (B.2): the viscous relaxation time in the optical trap:

$$\tau_\gamma = \frac{\gamma}{k} = 3\,\text{ms} < \tau_0.$$

In order to quantify the relative strength of the external force with respect to the thermal fluctuations, we introduce a dimensionless parameter which measures the distance from equilibrium

$$\alpha = \frac{\langle x^2\rangle}{\langle x^2\rangle_{eq}} - 1. \tag{B.3}$$

In equation (B.3), $\langle x^2\rangle$ is the variance of x in the presence of $f_0 > 0$ whereas $\langle x^2\rangle_{eq} = k_BT/k$ is the corresponding variance at equilibrium ($f_0 = 0$). The dependence of α on δf_0 is quadratic, as shown in figure B.2(a). This quadratic dependence is a consequence of the linear response of the system to the external forcing described by the Langevin equation (B.2).

The work done by the external random force on the colloidal particle (in k_BT units) is

$$w_\tau = \frac{1}{k_BT}\int_t^{t+\tau}\dot{x}(t')f_0(t')\mathrm{d}t'. \tag{B.4}$$

Thus, by measuring simultaneously the time evolution of the barycenter position of the particle and the driving force we are able to compute directly the work injected into the system by the driving. In figures B.2(b)-(d) we show the probability density functions (PDF) of w_τ for different values of τ and α. We observe that for a fixed value of α, the PDFs have asymmetric exponential tails at short integration times and they become smoother as the value of τ increases. For $\alpha = 0.20$ they approach

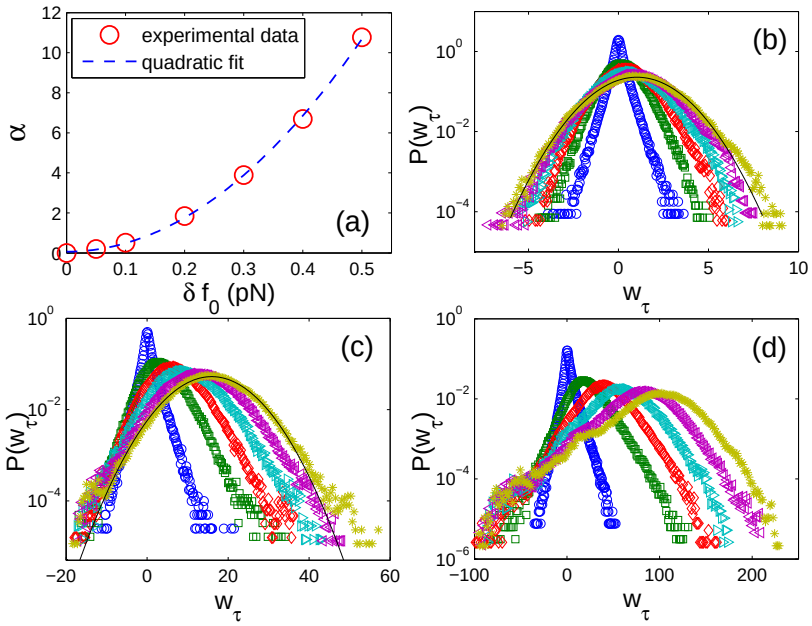

Figure B.2: (a) Dependence of the parameter α on the standard deviation of the Gaussian exponentially correlated external force f_0 acting on the colloidal particle. (b) Probability density functions of the work w_τ for $\alpha = 0.20$; (c) $\alpha = 3.89$; and (d) $\alpha = 10.77$. The symbols correspond to integration times $\tau = 5$ ms ($\circ$), 55 ms ($\square$), 105 ms ($\diamond$), 155 ms ($\triangleright$), 205 ms($\triangleleft$) and 255 ms ($*$). The solid black lines in (b) and (c) are Gaussian fits.

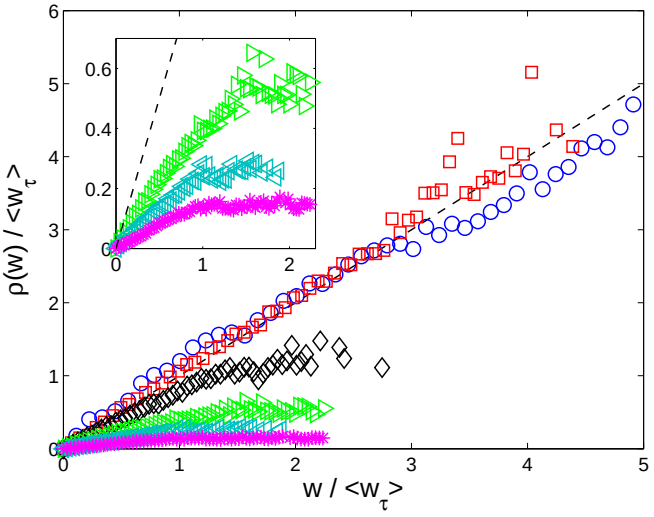

Figure B.3: Asymmetry function of the PDF of the work done by the external force on the colloidal bead computed at $\tau = 10\tau_0$ for different values of the parameter α: $0.20(\circ), 0.51(\square), 1.84(\diamond), 3.89(\triangleright), 6.69(\triangleleft), 10.77(*)$. The dashed line represents the prediction of the fluctuation theorem $\rho(w) = w$. Inset: Expanded view for $\alpha \geq 3.89$.

a Gaussian profile (figure B.2(b)) whereas asymmetric non-Gaussian tails remain for increasing values of α. Note that asymmetric non-Gaussian PDFs of the work are common in driven nonlinear systems [145, 137] and systems driven by a stochastic force [141, 142, 143, 144]. As shown in figures B.2(c)-(d), the asymmetry of these tails becomes very pronounced for large $\alpha > 1$ even for integration times as long as $\tau = 250\,\text{ms} = 10\tau_0$. We take τ_0 because it is the largest correlation time of the dynamics. The origin of this non-Gaussianity can be traced back to the strong correlation between the fluctuations of the particle motion and the stochastic external driving as α increases. As pointed out in [143], the deviations of the linear relation of equation (B.1) (with respect to w_τ) can occur for extreme values of the work fluctuations located on the non-Gaussian tails.

We define the asymmetry function of the PDF P as

$$\rho(w) = \lim_{\frac{\tau}{\tau_c}\to\infty} \ln \frac{P(w_\tau = w)}{P(w_\tau = -w)}, \tag{B.5}$$

so that eq. (B.1) reads

$$\rho(w) = w. \tag{B.6}$$

From the experimental PDFs of w_τ we compute $\rho(w)$ using equation (B.5) for an integration time $\tau = 10\tau_0$. We checked that for this value the limit of equation (B.5) has been reached within our experimental accuracy. Figure B.3 shows the profile of the asymmetry functions for different values of α. We notice that for sufficiently small values ($\alpha = 0.20, 0.51 < 1$), the FT given by equation (B.6) is verified by the

experimental data. To our knowledge, this is the first time that equation (B.6) holds for the work injected by a random force without introducing any prefactor in the linear relation of equation (B.6). It is important to point out that any deviation from the linear relation of eq. (B.6) for extreme fluctuations is unlikely since we probed values as large as $w_\tau/\langle w_\tau \rangle \sim 5$. Indeed it is argued [138, 139, 143, 146], that, for strongly dissipative systems driven by a random force, the deviations from FT may occur around $w_\tau/\langle w_\tau \rangle \sim 1$. Furthermore in the present case the validity of the FT for weak driving amplitudes $\alpha < 1$ is consistent with the fact that for integration times $\tau > 25$ ms, the ratio $\rho(w)/w$ has converged to its asymptotic value 1 for all measurable w. Note that this convergence to the FT prediction is quite similar to that measured in system driven out of equilibrium by deterministic forces [135, 136, 137]. For instance in the case of a harmonic oscillator driven by a sinusoidal external force the asymptotic value of $\rho(w)/w$ is reached for integration times larger than the forcing period [136].

In contrast, deviations from equaton (B.6) are expected to occur for $\alpha > 1$ because the fluctuations of injected energy produced by the external random force become larger than those injected by the thermal bath. Indeed figure B.3 shows that for values above $\alpha = 1.84$, equation (B.6) is not verified anymore but ρ becomes a nonlinear function of w_τ. For small values of w_τ it is linear with a slope which decreases as the driving amplitude increases whereas there is a crossover to a slower dependence around $w_\tau/\langle w_\tau \rangle \sim 1$. This behavior is qualitatively similar to those reported in [138, 141, 142, 143, 144]. We emphasize that we have clearly found that for an experimental system with first order Langevin dynamics in presence of thermal and external noises, the asymmetry described by the FT can be satisfied or not for the work fluctuations depending on the strength of the external driving. The details about how this deviations arise and the convergence to generic work fluctuation relations will be given further. We first analyze the experiment on the AFM.

AFM cantilever

A second example of a system for which thermal fluctuations are non-negligible in the energy injection process at equilibrium is the dynamics of the free end of a rectangular micro-cantilever used in AFM measurements. The cantilever is a mechanical clamped-free beam, which can be bended by an external force F and is thermalized with the surrounding air. The experiment is sketched in figure B.1(b).

We use conductive cantilevers from Nanoworld (PPP-CONTPt). They exhibit a nominal rectangular geometry: 450 μm long, 50 μm wide and 2 μm thick, with a 25 nm $PtIr_5$ conductive layer on both sides. The deflection is measured with a home made interferometric deflection sensor, inspired by the original design of Schonenberger [147] with a quadrature phase detection technique [148]. The interference between the reference laser beam reflecting on the chip of the cantilever and the sensing beam on the free end of the cantilever gives a direct measurement of the deflection X. Our detection system has a very low intrinsic noise, as low as 4 pm rms in the 100 kHz bandwidth we are probing [149].

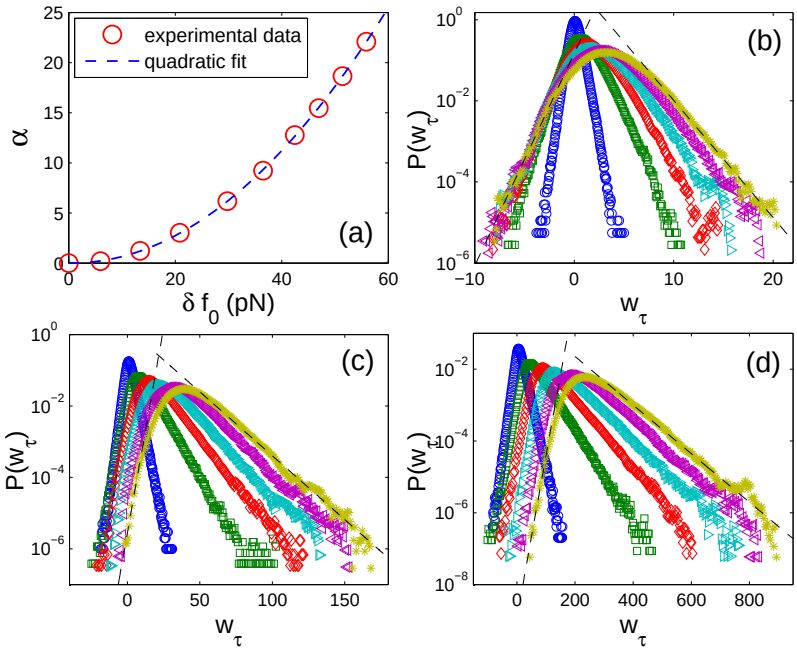

Figure B.4: (a) Dependence of the parameter α on the standard deviation of the Gaussian white external force f_0 acting on the cantilever. (b) Probability density functions of the work w_τ for $\alpha = 0.19$; (c) $\alpha = 3.03$; and (d) $\alpha = 18.66$. The symbols correspond to integration times $\tau = 97$ μs ($\circ$), 1.074 μs ($\square$), 2.051 ms ($\diamond$), 3.027 ms ($\triangleright$), 4.004 ms($\triangleleft$) and 4.981 ms ($*$). The black dashed lines in (b)-(d) represent the exponential fits of the corresponding tails.

From the power spectrum of the deflection fluctuations of the free end at equilibrium ($F = 0$) we verify that the cantilever dynamics can be reasonably modeled as a stochastic harmonic oscillator with viscous dissipation [149, 150]. Hence, in the presence of the external force the dynamics of the vertical coordinate X of the free end is described by the second order Langevin equation

$$m\ddot{X} + \gamma\dot{X} = -kX + \zeta_T + F, \tag{B.7}$$

where m is the effective mass, γ the viscous drag coefficient, k the stiffness associated to the elastic force on the cantilever and ζ_T models the thermal fluctuations. m, γ and k can be calibrated at zero forcing using the fluctuation-dissipation theorem, relating the observed power spectrum of X to the harmonic oscillator model. In our experiment we measure $m = 2.75 \times 10^{-11}$ kg, $\gamma = 4.35 \times 10^{-8}$ kg s^{-1} and $k = 8.0 \times 10^{-2}$ N/m. The amplitude of the equilibrium thermal fluctuations of the tip position (i.e. $\sqrt{\langle x^2 \rangle_{eq}} = \sqrt{k_B T/k} \simeq 2\ 10^{-10}$m) is two orders of magnitude larger then the detection noise (4 pm rms). The signal to noise ratio is even better when the system is driven by an external force F. The characteristic timescales of the deflection dynamics are the resonance period of the harmonic oscillator

$$\tau_k = 2\pi\sqrt{\frac{m}{k}} = 116\,\mu\text{s},$$

and the viscous relaxation time

$$\tau_\gamma = \frac{m}{\gamma} = 632\,\mu\text{s},$$

which is the longest correlation time.

When a voltage V is applied between the conductive cantilever and a metallic surface brought close to the tip ($h \approx 10\,\mu$m apart), an electrostatic interaction is created. The system behaves as a capacitor with stored energy

$$E_c = \frac{1}{2}C(X)V^2,$$

with C the capacitance of the cantilever-tip/surface system. Hence, the interaction between the cantilever and the opposite charged surface gives rise to an attractive external force

$$F = -\partial_X E_c = -aV^2,$$

on the free end, with $a = \partial_X C/2$. If we apply a static voltage $\overline{V}$, the force F can be deduced from the stationary solution of equation (B.7):

$$k\overline{X} = -a\overline{V}^2,$$

where $\overline{X}$ is the mean measured deflection. k being already calibrated, we validate this quadratic dependence[1] of forcing in V and measure $a = 1.49 \times 10^{-11}$N V^{-2}.

[1]The quadratic dependance is valid only after taking care to compensate for the contact potential between the tip and the sample, which gives a small correction of the order of a few tens of mV.

As the electrostatic force F is only attractive, its mean value cannot be chosen to be 0. We thus generated a driving voltage V designed to create a Gaussian white noise forcing f_0 around an offset $\overline{F}$:

$$F = \overline{F} + f_0.$$

The variance δf_0 of f_0 is the main control parameter of the system. In the absence of fluctuations ζ_T and f_0, equation (B.8) has the stationary solution $\overline{X} = \overline{F}/k$. This solution corresponds to the mean position reached by the free end in the presence of the zero mean fluctuating forces. Hence, we focus on the dynamics of the fluctuations $x = X - \overline{X}$ around $\overline{X}$ which are described by the equation

$$m\ddot{x} + \gamma\dot{x} = -kx + \zeta_T + f_0. \tag{B.8}$$

Figure B.4(a) shows the dependence between the parameter α defined in equation (B.3) for the stochastic variable x and the control parameter δf_0. We find that this dependence is quadatric verifying the linearity of the stochastic dynamics of the free end of the cantilever. On the other hand, the work done by the external random force during an integration time τ is computed from equation (B.4). The corresponding PDFs are shown in figures B.4(b)-(d). Unlike the colloidal particle, the PDFs do not converge to a Gaussian distribution but to a profile with asymmetric exponential tails even for the smallest driving amplitude ($\alpha = 0.19$) and for integration times as long as $\tau = 8\tau_\gamma$, as shown in figures B.4(b)-(d). Surprisingly, when computing the asymmetry function for $\alpha = 0.19 < 1$ and $\tau = 4\tau_\gamma$ the steady state FT is perfectly verified, as shown in figure B.5. Work fluctuations as large as 2.5 times their mean value located on the exponential tails are probed and hence deviations from FT are unlikely for the same reasons discussed for the case of the Brownian particle.

In figure B.5 we see that for $\alpha \geq 1.21$, the deviations from equation (B.6) appear as a nonlinear relation with a linear part for small fluctuations whose slope decreases as α increases and a crossover for larger fluctuations, qualitatively similar to the behavior observed for the colloidal particle, as shown clearly in the inset of figure B.5. In the following we discuss the properties of these deviations as the energy injection process becomes dominated by the external force.

Work fluctuation relation far from equilibrium

We address now the question of how the deviations from equation (B.6) arise as the external stochastic force drives the system far from equilibrium, i.e. $\alpha \gg 1$. As shown previously, for $\alpha \gtrsim 1$, the forcing amplitude is strong enough to destroy the conditions for the validity of equation (B.6) for w_τ. We note that there are two well defined limit regimes depending on the driving amplitude. One occurs at small values of α for which the FT is valid. The second corresponds to the limit $\alpha \gg 1$ for which the thermal bath is negligible in the energy injection process, which is completely dominated by the external stochastic force. In order to investigate whether the transition between these two regimes is abrupt or not, we proceed by noting that for the latter the stochastic

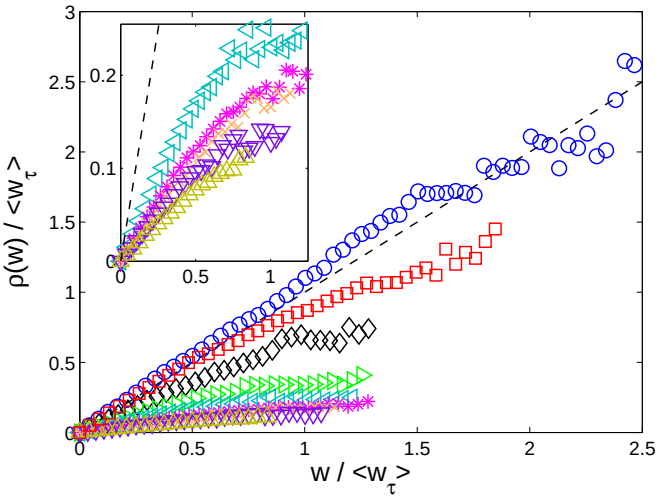

Figure B.5: Asymmetry function of the probability density function of the work done by the external force on the AFM cantilever computed at $\tau = 4\tau_\gamma$ for different values of the parameter α: $0.19(\circ), 1.21(\square), 3.03(\diamond), 6.18(\triangleright), 9.22(\triangleleft), 12.77(*)$, $15.46(\times), 18.66(\triangledown), 22.10(\triangle)$. The dashed line corresponds to the prediction of the fluctuation theorem $\rho(w) = w$. Inset: Expanded view for $\alpha \geq 9.22$.

force term ζ_T in equations (B.2) and (B.8) will be negligible compared to f_0. This implies that the resulting statistical time-integrated properties of the corresponding non-equilibrium steady state will be invariant under a normalization of the timescales and the temperature of the system as $\alpha \gg 1$. The information about the transition of the fluctuation relations to this regime is given by the convergence to a master curve.

We introduce the normalized work w_τ^* as

$$w_\tau^* = \frac{\tau_c}{\tau}\frac{w_\tau}{1+\alpha}. \tag{B.9}$$

The physical idea in equation (B.9) is that, for $\alpha \gg 1$, the thermal bath plays the role of a passive heat reservoir whereas most of the energy fluctuations injected into the system are provided by the external force. This can be interpreted as a bath kept at *effective temperature*:[2]

$$\frac{k\langle x^2\rangle}{k_B} = (1+\alpha)T \approx \alpha T.$$

The prefactor τ_c/τ is introduced in such a way that w_τ^* represents the average normalized work done during the largest correlation time of the system. Accordingly, the asymmetry function must be redefined as

$$\rho^*(w^*) = \lim_{\tau/\tau_c\to\infty} \frac{\tau_c}{\tau} \ln \frac{P(w_\tau^* = w^*)}{P(w_\tau^* = -w^*)}. \tag{B.10}$$

[2]The parameter α is an unambiguous choice to define the effective temperature out of equilibrium both for the harmonic oscillator and the trapped Brownian particle since $\langle x^2\rangle$ is finite. In this case the effective temperature is a measure of the *total* stochasticity of the system.

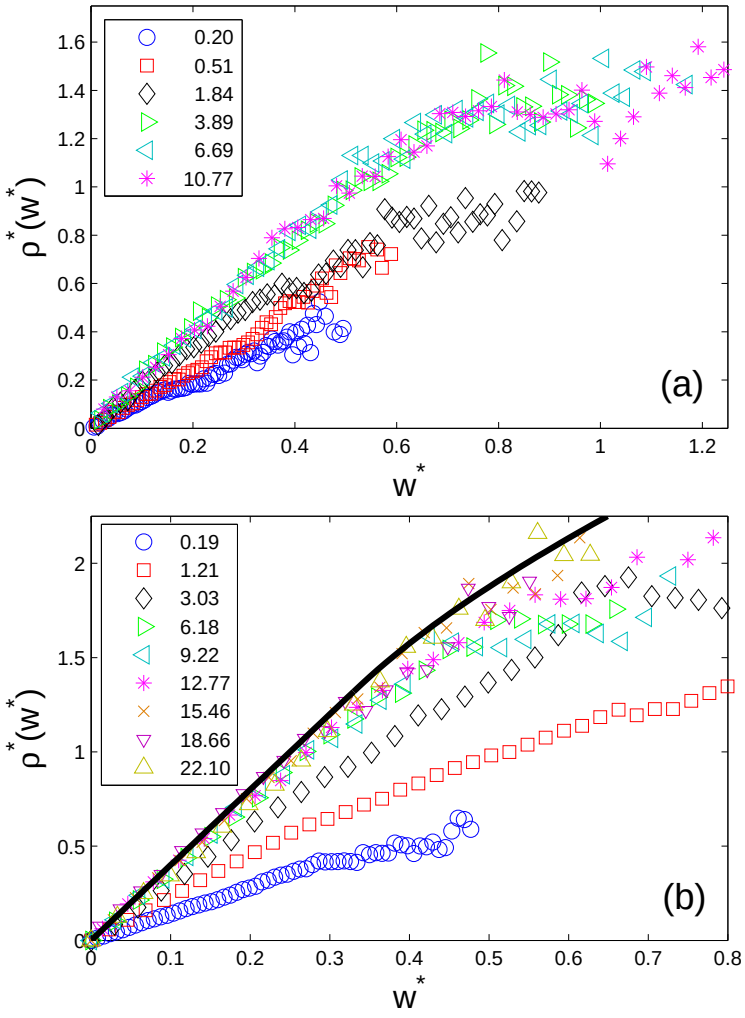

Figure B.6: (a) Asymmetry function of the PDF of the normalized work done by the Gaussian Ornstein-Uhlenbeck force on the colloidal particle for different values of the parameter α. (b) Asymmetry function of the PDF of the normalized work done by the Gaussian white force on the cantilever for different values of the parameter α. The thick solid line represents the analytical expression given by eq. (B.11).

Figure. B.6(a) shows the asymmetry function ρ^* for the normalized work w_τ^* on the colloidal particle at large values of α for which equation (B.6) is violated. The timescale τ_c in the computation of (B.9) and (B.10) is taken as the correlation time ($\tau_0 = 25$ ms) of the Ornstein-Uhlenbeck forcing of equation (B.2). For comparison we also show the corresponding curves at $\alpha = 0.20, 0.51$ as blue circles and red squares respectively, for which equation (B.6) holds. The convergence to a master curve is verified, which means that for a sufficiently strong forcing the thermal bath acts only as a passive reservoir for the energy dissipation without providing any important contribution to the energy injection into the system. Evidently, the normalized asymmetry function for the values α that verify equation (B.6) lie far from the master curve. We point out that the transition to the limit $\alpha \gg 1$ is rather continuous since intermediate regimes occur, as observed for $\alpha = 1.84$. In this case the strength of thermal noise is still comparable to that of the external noise.

The results for the normalized asymmetry function of the work done on the cantilever by the external force are shown in figure B.6(b). The curve corresponding to the verification of equation (B.6) for $\alpha = 0.19$ is also plotted for comparison. The convergence to a master curve is also checked as the value of α increases. Indeed, when comparing our normalized experimental curves with the analytic expression derived in reference [138] for the asymmetry of the work on a harmonic oscillator driven only by a Gaussian white noise

$$\rho^*(w^*) = \begin{cases} 4w^* & w^* < 1/3 \\ \frac{7}{4}w^* + \frac{3}{2} - \frac{1}{4w^*} & w^* \geq 1/3 \end{cases}, \tag{B.11}$$

we check the convergence to the function (B.11). Finite α corrections can be detected for large values of w_τ^*. This shows that the thermal bath still influences the energy injection into the cantilever. The corrections seem to vanish as the system is driven farther from equilibrium, as observed in figure B.6 for $\alpha = 22.10$.

Finally, we point out that the profile of the master curve strongly depends on: 1) the order (first or second) of the Langevin equation that models the dynamics and 2) the kind of stochastic force. Non-Gaussian extensions of the external random force are expected to lead to striking modification of the fluctuation relations in the limit $\alpha \gg 1$, as recently investigated for an asymmetric Poissonian shot noise [146].

Conclusions

We have studied, in the context of the FT, the symmetry properties of the fluctuations of the work fluctuations in two experimental systems in contact with a thermal bath and driven out of equilibrium by a stochastic force. The main result of our study is that the validity of the symmetry provided by the FT is controlled by the parameter α. For small $\alpha \lesssim 1$ we have shown that the validity of the FT is a very robust result regardless the details of the intrinsic dynamics of the system (first and second order Langevin dynamics) and the statistical properties of the forcing (white and colored

Gaussian noise). Indeed these specific features vanish when the integration of w_τ is performed for τ much larger than the largest correlation time of the system.

In contrast for large $\alpha \gtrsim 1$, when the randomness of the system becomes dominated by the external stochastic forcing, we have shown that the symmetry relation given by the FT is violated. We remark that this happens because in such a case the injected work is not a good measure of the entropy production of the system. Then the hypothesis for the validity of the FT are not satisfied. For $\alpha \gg 1$ the results at different driving amplitudes can be set on a master curve by defining a suitable effective temperature which is a function of α. We have shown that this master curve is system dependent. Therefore, some care must be taken when trying to apply directly the FT theorem to systems completely driven by random or chaotic forcing, such as in turbulent fluids and granular matter. For small systems this is not an issue as the stochasticity is in general dominated by the thermal fluctuations of the bath.

Appendix C

Stochastic thermodynamics for overdamped diffusion

Stochastic thermodynamics represents a refinement of classical thermodynmics. It provides a conceptual framework to describe fluctuating energy exchanges at thermal equilibrium or in simple nonequilibrium conditions. The fundamental idea is to extend the concepts of work, heat and entropy to single stochastic trajectories. This approach, initiated in [104] and widely developed in references [57, 58, 59, 60, 61, 62], has become very useful in soft and bio matter systems. The basic hypothesis for stochastic thermodynamics are: 1) the nonequilibrium behavior is due to an external conservative or nonconservative force or imbalanced chemical potentials; and 2) the systems are in contact with a heat bath at constant temperature.

Stochastic equations of motion

For simplicity, we consider an overdamped system described by a single degree of freedom x, evolving according to the first-order Langevin equation

$$\dot{x} = \mu F(x, \lambda) + \zeta, \tag{C.1}$$

where $F(x, \lambda)$ is the total deterministic force exerted on the system, μ is the mobility and ζ is a delta correlated white noise

$$\langle \zeta \rangle = 0, \quad \langle \zeta(t)\zeta(s) \rangle = 2D\delta(t - s), \tag{C.2}$$

which models the thermal fluctuations due to the coupling with a thermal bath at constant temperature T. We assume that detailed balance holds for the degrees of freedom of the bath, then the bare diffusivity D in equation (C.2) is linked to the mobility μ by

$$D = k_B T \mu.$$

The force $F(x, \lambda)$ is allowed to be time-dependent througth an external control parameter $\lambda(t)$, which is varied from $\lambda(0) = \lambda_0$ to $\lambda(\tau) = \lambda_\tau$ according to a prescribed

protocol. In addition, F it is allowed to have a nonconservative component, i.e. it can be expressed as

$$F(x,\lambda) = -\partial_x U(x,\lambda) + f(x),$$

where $U(x,\lambda)$ is a potential that represents the Hamiltonian part of the dynamics and $f(x)$ is a nonconservative force. The Fokker-Plank equation associated to equation (C.1), which describes the time evolution of the probability density $\rho(x,t)$ of x starting from an initial condition $\rho(x,0) = \rho_0(x)$, is

$$\begin{aligned} \partial_t \rho(x,t) &= -\partial_x j(x,t) \\ &= -\partial_x \left[\mu F(x,\lambda)\rho(x,t) - D\partial_x \rho(x,t)\right]. \end{aligned} \tag{C.3}$$

In equation (C.3), the current

$$j(x,t) = \mu F(x,\lambda)\rho(x,t) - D\partial_x \rho(x,t), \tag{C.4}$$

quantifies the breakdown the detailed balance. For example, at thermal equilibrium $j = 0$, whereas for steady states with nonvanishing nonconservative forces ($f \neq 0$), the current is $j = const. \neq 0$.

First law

We now proceed to show the extension of the first law in the context of stochastic thermodynamics to a system modeled by equation (C.1). We consider two different ways to perform work on the system. The first is by changing the potential U at fixed x while the second is by applying a nonconservative force. Then, the increment in work $\mathrm{d}W$ during an infinitesimal time $\mathrm{d}t$ is

$$\mathrm{d}W = (\partial_\lambda U)\dot{\lambda}\,\mathrm{d}t + f\,\mathrm{d}x. \tag{C.5}$$

On the other hand, during the same $\mathrm{d}t$, the heat dissipated into the medium can be identified by the quantity

$$\mathrm{d}Q = F\,\mathrm{d}x. \tag{C.6}$$

Integrating equations (C.5) and (C.6) along a single stochastic trajectory x_t defined over the time interval $0 \leq t \leq \tau$:

$$\begin{aligned} W_\tau &= \int_0^\tau \left[(\partial_\lambda U)\dot{\lambda} + f\dot{x}\right] \mathrm{d}t, \\ Q_\tau &= \int_0^\tau F\dot{x}\,\mathrm{d}t, \end{aligned} \tag{C.7}$$

we find

$$\begin{aligned} W_\tau - Q_\tau &= \int_0^\tau \left[(\partial_\lambda U)\dot{\lambda} + \partial_x U\dot{x}\right] \mathrm{d}t, \\ &= \int_0^\tau \mathrm{d}U, \\ &= \Delta U_\tau, \end{aligned} \tag{C.8}$$

where

$$\Delta U_\tau = U(x_\tau, \lambda_\tau) - U(x_0, \lambda_0),$$

is the change in the potential energy during the time τ. Therefore, equation (C.7) represents an extension of the first law of thermodynamics on the level of a single stochastic trajectory. As no hypothesis was done on the rate $\dot{\lambda}$ and on the strength of the nonconservative force f, it is valid arbitrarily away from equilibrium.

Stochastic entropy and second law

The second law of thermodynamics can be extended to single stochastic trajectories as well, by introducing the concept of *stochastic entropy*. Due to the stochastic evolution of x, modeled by equation (C.1), the instantaneous phase-space configuration of the system at time t, determined by the solution of the Fokker-Planck equation (C.3), depends on the trajectory x_t. The stochastic entropy, defined as

$$S_{st}(x_t) = -k_B \ln \rho(x_t, t), \tag{C.9}$$

measures this stochasticity as a contribution to the total entropy produced by the system. In equation (C.9), $\rho(x_t, t)$ is the solution of equation (C.3) evaluated along a given x_t. Note that $S_{st}(x_t)$ depends on the initial condition x_0. Then the stochastic entropy change along a given trajectory x_t in the time interval $0 \leq t \leq \tau$ is

$$\begin{aligned} \Delta S_{st}(\tau) &= S_{st}(x_\tau) - S_{st}(x_0), \\ &= -k_B \ln \frac{\rho(x_\tau, \tau)}{\rho(x_0, 0)}. \end{aligned} \tag{C.10}$$

On the other hand, a second contribution to the total entropy change originates from the heat dissipated into the environment during the same realization of x_t. The entropy change in the time interval $0 \leq t \leq \tau$ due to heat dissipation is

$$\Delta S_m(\tau) = \frac{Q_\tau}{T}, \tag{C.11}$$

where Q_τ is given by equation (C.7). The total entropy change is the sum of both contributions

$$\Delta S_{tot}(\tau) = \Delta S_{st}(\tau) + \Delta S_m(\tau). \tag{C.12}$$

We point out that these definitions of stochastic and total entropy arise naturally from the equations of motion (C.1) and (C.3). Indeed, taking the time derivative of equation (C.9), we obtain an expression for the stochastic entropy rate

$$\begin{aligned} \dot{S}_{st}(x_t) &= -k_B \left[\frac{\partial_t \rho(x,t)}{\rho(x,t)}\right]_{x_t} - k_B \left[\frac{\partial_x \rho(x,t)}{\rho(x,t)} \dot{x}\right]_{x_t}, \\ &= -k_B \left[\frac{\partial_t \rho(x,t)}{\rho(x,t)}\right]_{x_t} + k_B \left[\frac{j(x,t)\dot{x}}{D\rho(x,t)}\right]_{x_t} - k_B \left[\frac{\mu F(x,\lambda)\dot{x}}{D}\right]_{x_t}, \end{aligned} \tag{C.13}$$

where we used equation (C.4) in the second equality of (C.13). As we assume that the equilibrium bath is not perturbed by the external forces, $D = k_B T \mu$. Then, the last term in equation (C.13) can be identified as the entropy rate due to the power $\dot{Q} = F(x,\lambda)\dot{x}$ dissipated into the medium:

$$\dot{S}_m(x_t) = k_B \left[\frac{\mu F(x,\lambda)}{D} \dot{x} \right]_{x_t} = \frac{\dot{Q}(x_t)}{T}.$$

Consequently, the *total* entropy production rate is

$$\begin{aligned} \dot{S}_{tot}(x_t) &= \dot{S}_m(x_t) + \dot{S}_{st}(x_t), \\ &= -k_B \left[\frac{\partial_t \rho(x,t)}{\rho(x,t)} \right]_{x_t} + k_B \left[\frac{j(x,t)}{D\rho(x,t)} \dot{x} \right]_{x_t}. \end{aligned} \tag{C.14}$$

We remark that this is a good definition of total entropy rate because at thermal equilibrium ($j = 0$, $\partial_t \rho = 0$), one obtains $\dot{S}_{tot} = 0$, which is consistent with microscopic time reversibility. In the case of a nonequilibrium steady state with density $\rho_0(x)$ ($j = const. \neq 0$, $\partial_t \rho_0 = 0$), equation (C.14) allows one to write the total entropy rate in terms of the constant current j

$$\dot{S}_{tot}(x_t) = k_B \left[\frac{j}{D\rho_0(x)} \dot{x} \right]_{x_t}.$$

Finally, the total entropy rate defined by equation (C.14) reduces to the second law of thermodynamics upon averaging over an infinite number of realizations of the stochastic process x_t. Indeed, the average value of the total entropy rate $\langle \dot{S}_{tot}(t) \rangle$ at time t can be written as

$$\langle \dot{S}_{tot}(t) \rangle = \int \mathrm{d}x \, \rho(x,t) \langle \dot{S}_{tot}(x_t) | x, t \rangle, \tag{C.15}$$

where the ensemble average $\langle \ldots \rangle$ has been splitted into two steps. The first is a conditional average $\langle \ldots | x, t \rangle$ performed over all trajectories that are in a fixed x at time t. The second is perfomed over all the possible values of x. Taking into account the probability conservation

$$\partial_t \int \mathrm{d}x \, \rho(x,t) = 0,$$

equation (C.15) becomes

$$\langle \dot{S}_{tot}(t) \rangle = \int \mathrm{d}x \, \rho(x,t) \frac{j(x,t)}{D\rho(x,t)} \langle \dot{x} | x, t \rangle. \tag{C.16}$$

Furthermore, bearing in mind that, according to the definition of mobility, the ensemble average of the velocity $\dot{x}$ can be expressed as

$$\begin{aligned} \langle \dot{x} \rangle &= \mu \langle F(x,\lambda) \rangle, \\ &= \int \mathrm{d}x \, \rho(x,t) \mu F(x,\lambda), \\ &= \int \mathrm{d}x \, \rho(x,t) \left[\frac{\mu F(x,\lambda) - D\partial_x \rho(x,t)}{\rho(x,t)} \right], \end{aligned} \tag{C.17}$$

then the term between the square brakets in the last equality of (C.17) can be identified as

$$\frac{j(x,t)}{\rho(x,t)} = \langle \dot{x}|x,t\rangle. \tag{C.18}$$

By substituting (C.18) into (C.16), this yields

$$\langle \dot{S}_{tot}(t)\rangle = \int \mathrm{d}x \frac{j(x,t)^2}{D\rho(x,t)} \geq 0,$$

which is the second law of thermodynamics.

List of publications

- P. Jop, J. R. Gomez-Solano, A. Petrosyan, and S. Ciliberto, *"Experimental study of out-of-equilibrium fluctuations in a colloidal suspension of Laponite using optical traps"*, J. Stat. Mech. (2009) P04012.

- J. R. Gomez-Solano, A. Petrosyan, S. Ciliberto, R. Chetrite, and K. Gawędzki, *"Experimental Verification of a Modified Fluctuation-Dissipation Relation for a Micron-Sized Particle in a Nonequilibrium Steady State"*, Phys. Rev. Lett. **103**, 040601 (2009).

- J. R. Gomez-Solano, L. Bellon, A. Petrosyan, and S. Ciliberto, *"Steady-state fluctuation relations for systems driven by an external random force"*, EPL **89**, 60003 (2010).

- J. R. Gomez-Solano, A. Petrosyan, S. Ciliberto, and C. Maes, *"Fluctuations and response in a non-equilibrium micron-sized system"*, J. Stat. Mech. (2011) P01008.

- J. R. Gomez-Solano, A. Petrosyan, and S. Ciliberto, *"Heat Fluctuations in a Nonequilibrium Bath"*, Phys. Rev. Lett. **106**, 200602 (2011).

Bibliography

[1] T. Fukuda, F. Arai, and L. Dong, Proceedings of the IEEE **91**, 1803 (2003).

[2] Sandia National Laboratories website: http://mems.sandia.gov

[3] R. K. Soong, G. D. Bachand, H. P. Neves, A. G. Oikhovets, H. G. Craighead, and C. D. Montemagno, Science **290**, 1555 (2000).

[4] H. B. Callen and T. A. Welton, Phys. Rev. **83**, 34 (1951).

[5] C. Jarzynski, Phys. Rev. Lett. **78**, 2690 (1997).

[6] G. E. Crooks, Phys. Rev. E 60, 2721 (1999).

[7] T. Hatano and S. Sasa, Phys. Rev. Lett. **86**, 3463 (2001).

[8] D. J. Evans, E. G. D. Cohen, and G. P. Morris, Phys. Rev. Lett. **71**, 2401 (1993).

[9] G. Gallavotti and E. G. D. Cohen, J. Stat. Phys.**80**, 931 (1995).

[10] J. Kurchan, J. Phys. A: Math. Gen. **31**, 3719 (1998).

[11] U. Seifert, Phys. Rev. Lett. **95**, 040602 (2005).

[12] S. Ciliberto, S. Joubaud, and A. Petrosyan, J. Stat. Mech. (2010) P12003.

[13] D. Collin, F. Ritort, C. Jarzynski, S. B. Smith, I. Tinoco Jr, and C. Bustamante, Nature **437**, 231 (2005).

[14] I. Junier, A. Mossa, M. Manosas, and F. Ritort, Phys. Rev. Lett. **102**, 070602 (2009).

[15] K. Hayashi, H. Ueno, R. Iino, and H. Noji, Phys. Rev. Lett. **104**, 218103 (2010).

[16] G. S. Agarwal, Z. Phys. **252**, 25 (1972).

[17] P. Hänggi, Helv. Phys. Acta **51**, 202 (1978).

[18] T. Harada and S.-I. Sasa, Phys. Rev. Lett. **95**, 130602 (2005).

[19] T. Speck and U. Seifert, EPL **74**, 391 (2006).

[20] R. Chetrite, G. Falkovich, and K. Gawędzki, J. Stat. Mech. (2008) P08005.

[21] J. Prost, J.-F. Joanny and J. M. R. Parrondo, Phys. Rev. Lett. **103**, 090601 (2009).

[22] M. Baiesi, C. Maes, and B. Wynants, Phys. Rev. Lett. **103**, 010602 (2009).

[23] U. Seifert and T. Speck, EPL **89**, 10007 (2010).

[24] G. Verley, K. Mallick, and D. Lacoste, EPL **93**, 10002 (2011).

[25] L.F. Cugliandolo, J. Kurchan, and L. Peliti, Phys. Rev. E **55**, 3898 (1997).

[26] E. Lippiello, F. Corberi, and M. Zannetti, Phys. Rev. E **71**,036104 (2005).

[27] R. Chetrite, Phys. Rev. E **80**, 051107 (2009).

[28] G. Verley, R. Chetrite, and D. Lacoste, J. Stat. Mech. (2011) P10025.

[29] S. Joubaud, B. Percier, A. Petrosyan, and S. Ciliberto, Phys. Rev. Lett. **102**, 130601 (2009).

[30] A. Ashkin, Phys. Rev. Lett. **24**, 156 (1970).

[31] A. Ashkin, J. M. Dziedzic, J. E. Bjorkholm, and S. Chu, Opt. Lett. **11**, 288 (1986).

[32] T. Tlusty, A. Meller, and R. Bar-Ziv, Phys. Rev. Lett. **81**, 1738 (1998).

[33] A. Ashkin, Biophys. J. **61**, 569 (1992).

[34] Y. Harada and T. Asakura, Opt. Commun. **24**, 529 (1996).

[35] F. Merenda, G. Boer, J. Rohner, G. Delacrétaz, and R.-P. Salathé, Opt. Express **14**, 1685 (2006).

[36] Y. Roichman, B. Sun, A. Stolarski, and D. G. Grier, Phys. Rev. Lett. **101**, 128301 (2008).

[37] K. Berg-Sørensen and H. Flyvbjerg, Rev. Sci. Instrum., **75**, 594 (2004).

[38] S.F. Tolić-Nørrelykke, E. Schäffer, J. Howard, F. S. Pavone, F. Jülicher, and H. Flyvbjerg, Rev. Sci. Instrum. **77**, 103101 (2006).

[39] M. Fischer, A. C. Richardson, S. Nader, S. Reihani, L. B. Oddershede, and K. Berg-Soerensen, Rev. Sci. Instrum. **81**, 015103 (2010).

[40] S. S. Rogers, T. A. Waigh, X. Zhao, and J. R. Lu, Phys. Biol. **4** 220 (2007).

[41] G.. Pesce, G. Volpe, A. C. De Luca, G. Rusciano, and G. Volpe, 2009 EPL **86** 38002 .

[42] T. M Squires and T. G. Mason, Annu. Rev. Fluid Mech. **42**, 413 (2010).

[43] D. Mizuno, D. A. Head, F. C. MacKintosh, and C. F. Schmidt, Macromolecules **41**, 7194 (2008).

[44] A. Einstein, Annalen der Physik **17**, 549 (1905).

[45] M Smolochowski, Annalen der Physik **21** 756 (1906).

[46] P. Langevin, C. R. Acad. Sci. (Paris) **146**, 530 (1908).

[47] J. Perrin, Ann. Chim. Phys. **18**, 5 (1909).

[48] J. Johnson, Phys. Rev. **32**, 97 (1928).

[49] H. Nyquist, Phys. Rev. **32**, 110 (1928).

[50] L. Onsager, Phys. Rev. **37**, 405 (1931); L. Onsager, Phys. Rev. **38**, 2265 (1931).

[51] M. S. Green, J. Chem. Phys **22**, 398 (1954).

[52] R. Kubo, J. Phys. Soc. Jpn. **12**, 570 (1957).

[53] R. Chetrite and K. Gawędzki, J. Stat. Phys. **137**, 890 (2009).

[54] C. Maes, K. Netocny, and B. Wynants, Physica A **387**, 2675 (2008).

[55] M. Baiesi, C. Maes, and B. Wynants, J. Stat. Phys. **137**, 1094 (2009).

[56] M. Baiesi, E. Boksenbojm, C. Maes and B. Wynants, J. Stat. Phys. **139**, 492 (2010).

[57] U. Seifert, Phys. Rev. Lett **95**, 040602 (2005).

[58] T. Speck and U. Seifert, J. Stat. Mech. (2007) L09002.

[59] U. Seifert, Eur. Phys. J. B **64**, 423 (2008).

[60] T. Speck, J. Mehl, and U. Seifert, Phys. Rev. Lett. **100**, 178302 (2008).

[61] U. Seifert. Lecture Notes: 'Soft Matter. From Synthetic to Biological Materials', 39th Spring School 2008. Institute of Solid State Research, Forschungszentrum Jülich (2008). ISBN 978-3-89336-517-3.

[62] U. Seifert, Eur. Phys. J. E **34**, 26 (2011).

[63] L. P. Faucheux, G. Stolovitzky, and A. Libchaber, Phys. Rev. E **51**, 5239 (1995).

[64] H. Faxen, Ark. Mat. Astron. Fys. **18**, 1 (1924).

[65] L. P. Faucheux and A. Libchaber, Phys. Rev. E **49**, 5158 (1994).

[66] R. Chetrite and K. Gawędzki, Commun. Math. Phys. **282**, 469 (2008).

[67] H. Risken, *The Fokker-Planck equation*, 2nd edition, Springer, Berlin (1989).

[68] V. Blickle, T. Speck, U. Seifert, and C. Bechinger, Phys. Rev. E **75**, 060101 (R) (2007).

[69] V. Blickle, T. Speck, C. Lutz, U. Seifert, and C. Bechinger, Phys. Rev. Lett. **98**, 210601 (2007).

[70] V. Blickle, J. Mehl, and C. Bechinger, Phys. Rev. E **79**, 060104 (R) (2009).

[71] J. Mehl, V. Blickle, U. Seifert, and C. Bechinger, Phys. Rev. E **82**, 032401 (2010).

[72] P. Reimann, C. Van den Broeck, H. Linke,4, P. Hänggi, J. M. Rubi, and A. Pérez-Madrid, Phys. Rev. Lett. **87**, 010602 (2001).

[73] S.-H. Lee and D. G. Grier, Phys. Rev. Lett. **96**, 190601 (2006).

[74] L. Berthier and G. Biroli, Rev. Mod. Phys. **83**, 587 (2011).

[75] G. Parisi, Phys. Rev. Lett. **79**, 3660 (1997).

[76] J.-L. Barrat and W. Kob, EPL **46**, 637 (1999).

[77] D. Hérisson and M. Ocio, Phys. Rev. Lett. **88**, 257202 (2002).

[78] D. Hérisson and M. Ocio, Eur. Phys. J. B **40**, 283 (2004).

[79] J. Kurchan, Nature **433** (2005).

[80] L. Berthier and J.-L. Barrat, Phys. Rev. Lett. **89**, 095702 (2002).

[81] S. Jabbari-Farouji, H. Tanaka, G. H. Wegdam, and D. Bonn Phys. Rev E **78**, 061405 (2008).

[82] B Abou, D. Bonn, and J. Meunier Phys. Rev. E **64**, 021510 (2001).

[83] S. Jabbari-Farouji, E. Eiser, G. H. Wegdam, and D. Bonn, J. Phys.: Condens. Matter **16**, (2004)

[84] N. Ghofraniha, C. Conti, and G. Ruocco, Phys. Rev. B **75**, 224203 (2007).

[85] B. Ruzicka and E. Zaccarelli, Soft Matter **7**, 1268 (2011).

[86] B. Ruzicka, E. Zaccarelli, L. Zulian, R. Angelini, M. Sztucki, A. MoussaÃ¯d, T. Narayanan, and F. Sciortino, Nature Materials **10**, 56 (2011).

[87] L. Bellon, S. Ciliberto, and C. Laroche, Europhys. Lett. **53**, 511 (2001);

[88] L. Bellon and S. Ciliberto, Physica D **168-169**, 325 (2002)

[89] L. Buisson, L. Bellon, and S. Ciliberto, J. Phys. Cond. Matt. **15**, S1163 (2003).

[90] B. Abou and F. Gallet, Phys. Rev. Lett. **93**, 160603 (2003).

[91] S. Jabbari-Farouji, D. Mizuno, M. Atakhorrami, F. C. MacKintosh, C. F. Shmidt, E. Eiser, G. H. Wegdam, and D. Bonn, Phys. Rev. Lett. **98**, 108302 (2007).

[92] N. Greinert, T. Wood, and P. Bartlett, Phys. Rev. Lett. **97**, 265702 (2006).

[93] S. Jabbari-Farouji, D. Mizuno, G. H. Wegdam, F. C. MacKintosh, C. F., and D. Bonn, EPL **84**, 20006 (2008).

[94] H. Z. Cummins, Journal of Non-Crystalline Solids **353**, (2007).

[95] D. Bonn, H. Kellay, H. Tanaka, G. Wegdam, and J. Meunier, Langmuir **15** (1999).

[96] P. Jop, A. Petrosyan, and C. Ciliberto, Phylosophical Magazine published online.

[97] F. Douarche, S. Joubaud, N. B. Garnier, A. Petrosyan, and S. Ciliberto Phys. Rev. Lett. **97**, 140603 (2006).

[98] S. Joubaud, N. B. Garnier, S. Ciliberto, J. Stat. Mech. (2007) P09018.

[99] P. Jop, S. Ciliberto, A. Petrosyan, Eur. Phys. Lett. **81**, 50005 (2008)

[100] A. Imparato, P. Jop, A. Petrosyan, S. Ciliberto, J. Stat. Mech. (2008) P10017.

[101] J. Kurchan, J. Stat. Mech., P07005 (2007).

[102] A. Crisanti and F. Ritort, Europhys. Lett. **66**, 253 (2004).

[103] F. Zamponi, F. Bonetto, L. F. Cugliandolo, and J. Kurchan, J. Stat. Mech. (2005) P09013.

[104] K. Sekimoto, Prog. Theor. Phys. Suppl. **130**, 17 (1998).

[105] J. Russo and F. Sciortino, Phys. Rev. Lett. **104**, 195791 (2010).

[106] C. Maggi, R. Di Leonardo, J. C. Dyre, and C. Ruocco, Phys. Rev. B **81**, 104201 (2010).

[107] O. Ronsin, C. Caroli, and T. Baumberger, Phys. Rev. Lett. **103**, 138302 (2009).

[108] A. Parker and V. Normand, Soft Matter **6**, 4916 (2010).

[109] V. Normand, S. Muller, J.-C. Ravey, and A. Parker, Macromolecules **33**, 1063 (2000).

[110] E. J. G. Peterman, F. Gittes, and C. F. Schmidt, Biophys. J **84**, 1308 (2003).

[111] M. Djabourov, J. Leblond, and P. Papon, J. Phys. France **49**, 319 (1988).

[112] M. Djabourov, J. Leblond, and P. Papon, J. Phys. France **49**, 333 (1988).

[113] C. Joly-Duhamel, D. Hellio, A. Ajdari, and M. Djabourov, Langmuir **18**, 7158 (2002)

[114] J. C. Reid, D. M. Carberry, G. M. Wang, E. M. Sevick, D. J. Evans, and D. J. Searles, Phys. Rev. E **70**, 016111 (2004);

[115] R. Chetrite, Phys. Rev. E **80**, 051107 (2009).

[116] A. Crisanti and F. Ritort, EPL **66**, 253 (2004)

[117] F. Ritort, J. Phys. Chem. B **108**, 6893 (2004).

[118] A. Imparato *et al.*, Phys. Rev. E **76**, 050101(R) (2007).

[119] D. Chatterjee and B. J. Cherayil, Phys. Rev. E **82**, 051104 (2010).

[120] C. Jarzynski and D. K. Wojcik, Phys. Rev. Lett. **92**, 230602 (2004).

[121] V. Lecomte, Z. Racz, and F. van Wijland, J. Stat. Mech. (2005) P02008.

[122] P. Visco, J. Stat. Mech. (2006) P06006.

[123] C. Maes and M. H. van Wieren, Phys. Rev Lett. **96**, 240601 (2006).

[124] T. Bodineau and B. Derrida, C. R. Physique **8**, 540 (2007).

[125] A. Piscitelli, F. Corberi, and G. Gonnella, J. Phys. A: Math. Theor. **41** 332003 (2008).

[126] S. Toyabe, T. Okamoto, T. Watanabe-Nakayama, H. Taketani, S. Kudo, and E. Muneyuki, Phys. Rev. Lett. **104**, 198103 (2010).

[127] D. J. Evans and D. Searles, Phys. Rev. E **50**, 1645 (1994).

[128] G. Gallavotti and E. G. D. Cohen, Phys. Rev. Lett. **74**, 2694 (1995).

[129] J. Lebowitz and H. Spohn, J. Stat. Phys. **95**, 333 (1999).

[130] R. van Zon and E. G. D. Cohen, Phys. Rev. E **67**, 046102 (2003).

[131] R. van Zon and E. G. D. Cohen, Phys. Rev. Lett. **91**, 110601 (2003).

[132] K. Saito and A. Dhar, Phys. Rev. E **83**, 041121 (2011).

[133] A. Kundu, S. Sabhapandit, and A. Dhar, J. Stat. Mech. (2011) P03007.

[134] G. M. Wang, J. C. Reid, D. M. Carberry, D. R. M. Williams, E. M. Sevick, and D. J. Evans, Phys. Rev. E **71**, 046142 (2005).

[135] N. Garnier and S. Ciliberto, Phys. Rev. E **71**, 060101(R) (2005).

[136] S. Joubaud, N. B. Garnier, and S. Ciliberto, J. Stat. Mech. (2007) P09018.

[137] P. Jop, A. Petrosyan, and S. Ciliberto, EPL **81**, 50005 (2008).

[138] J. Farago, J. Stat. Phys. **107**, 781 (2002).

[139] J. Farago, Physica A **331**, 69 (2004).

[140] X.-D. Shang, P. Tong, and K.-Q. Xia, Phys. Rev. E **72**, 015301(R) (2005).

[141] E. Falcon, S. Aumaître, C. Falcón, C. Laroche, and S. Fauve, Phys. Rev. Lett. **100**, 064503 (2008).

[142] O. Cadot, A. Boudaoud, and C. Touzé, Eur. Phys. J. B **66**, 399 (2008).

[143] C. Falcón and E. Falcon, Phys. Rev. E **79**, 041110 (2009).

[144] M. Bonaldi, L. Conti, P. De Gregorio, L. Rondoni, G. Vedovato, A. Vinante, M. Bignotto, M. Cerdonio, P. Falferi, N. Liguori, S. Longo, R. Mezzena, A. Ortolan, G. A. Prodi, F. Salemi, L. Taffarello, S. Vitale, and J.-P. Zendri, Phys. Rev. Lett **103**, 010601 (2009).

[145] V. Blickle, T. Speck, L. Helden, U. Seifert, and C. Bechinger, Phys. Rev. Lett. **96**, 070603 (2006).

[146] A. Baule and E. G. D. Cohen, Phys. Rev. E **80**, 011110 (2009).

[147] C. Schonenberger and S. F. Alvarado, Rev. Sci. Instrum. **60**, 3131 (1989).

[148] L. Bellon, S. Ciliberto, H. Boubaker, and L. Guyon, Opt. Comm. **207**, 49 (2002).

[149] P. Paolino and L. Bellon, Nanotechnology **20**, 405705 (2009).

[150] L. Bellon, J. Appl. Phys. **104**, 104906 (2008).

[151] J. M. Deutsch and O. Narayan, Phys. Rev. E **74**, 026112 (2006).

[152] T. Ohkuma and T. Ohta, J. Stat. Mech. (2007) P10010.

[153] S. Toyabe and M. Sano, Phys. Rev. E **77**, 041403 (2008).